8-13-2019

Quantifying Feedback from Narrow Line Region Outflows in Nearby Active Galaxies

Mitchell Revalski
Georgia State University

QUANTIFYING FEEDBACK FROM NARROW LINE REGION OUTFLOWS IN NEARBY ACTIVE GALAXIES

by

MITCHELL D. REVALSKI

Under the Direction of D. Michael Crenshaw, PhD

ABSTRACT

Observations reveal that supermassive black holes (SMBHs) grow through the accretion of gas at the centers of galaxies as luminous active galactic nuclei (AGN), releasing radiation that drives powerful outflows of ionized and molecular gas. These winds are thought to play a critical role in galaxy evolution by regulating star formation and the growth of galaxies and their SMBHs. To test this model, we must quantify the dynamic impact of outflows by measuring their mass outflow rates and energetics. Using spatially resolved spectroscopy and imaging from the *Hubble Space Telescope* and Cloudy photoionization models we mapped the ionized gas kinematics and mass distributions of narrow line region (NLR) outflows in nearby active galaxies. We find that the outflows contain up to several million solar masses of ionized gas and are limited to distances of $1-2$ kiloparsecs from the nucleus. The maximum mass outflow rates are $\dot{M}_{max} \approx 3-12\ M_{\odot}\ \mathrm{yr}^{-1}$ and the outflow gas mass, velocity, radial extent, and energetics are positively correlated with AGN luminosity. We use our results to test simplified techniques with less stringent data requirements and find that they significantly overestimate the gas mass. These results are crucial for modeling powerful outflows at higher redshift that may considerably influence star formation rates and the formation of galactic structure.

INDEX WORDS: Seyfert Galaxies, SMBH, AGN, Feedback, Outflows, Kinematics, Photoionization Modeling, Hubble Space Telescope, Spatially Resolved, Spectroscopy

QUANTIFYING FEEDBACK FROM NARROW LINE REGION OUTFLOWS IN NEARBY ACTIVE GALAXIES

by

MITCHELL D. REVALSKI

A Dissertation Submitted in Partial Fulfillment of the Requirements for the Degree of

Doctor of Philosophy

in the College of Arts and Sciences

Georgia State University

2019

QUANTIFYING FEEDBACK FROM NARROW LINE REGION OUTFLOWS IN NEARBY ACTIVE GALAXIES

by

MITCHELL D. REVALSKI

Committee Chair: D. Michael Crenshaw

Committee: Misty C. Bentz

Steven B. Kraemer

Alexander Kozhanov

Electronic Version Approved:

Office of Graduate Studies

College of Arts and Sciences

Georgia State University

August 2019

DEDICATION

I dedicate this dissertation to my family, my loving fiancée, and to my teachers, for their unwavering support, encouragement, and generosity in my pursuit of answers.

ACKNOWLEDGEMENTS

I would like to thank my family, fiancée, friends, mentors, and colleagues for their support. I cannot imagine having completed this pursuit without them. Any attempt to acknowledge all those who have helped me to achieve my goals will invariably result in omissions and to these wonderful people I apologize. My passion for astronomy was ignited by my inspiring teachers Deborah Szmaida and Teri Bellows. They introduced me to the New Jersey Astronomical Association where I learned much from its many kind and generous members. I am indebted to my undergraduate mentors Dr. Paul Wiita and Dr. Thulsi Wickramasinghe for introducing me to the challenges and excitement of original research and preparing me for a graduate program. I am thankful to my collaborators including Dr. Steve Kraemer, Dr. Travis Fischer, and Dr. Henrique Schmitt for their tutelage and advice on numerous drafts of papers that have culminated in this dissertation.

I would like to thank my committee members including Dr. Steve Kraemer, Dr. Misty Bentz, and Dr. Alexander Kozhanov for their suggestions that greatly improved this manuscript. Many of the stunning images in this dissertation were created by Judy Schmidt, who dedicated her time and talent to create true to life images of these galaxies that capture the imagination. I would also like to acknowledge Justin Cantrell and Sushant Mahajan for cluster computing assistance, Kathryn Lester and Wesely Peters for helpful conversations, and Gary Ferland, Peter van Hoof, and Eric Pellegrini for Cloudy support. Finally, I would like to thank my advisor Dr. Mike Crenshaw for dedicating his time and experience to ensure my success, and whose good-humored style of advising reminded me to always see the big picture and enjoy the journey along the way.

"Success depends in a very large measure upon individual initiative and exertion, and cannot be achieved except by a dint of hard work."

- Anna Pavlova, 1881-1931

Mitchell Revalski gratefully acknowledges support from the National Science Foundation through the Graduate Research Fellowship Program (GRFP). This material is based upon work supported by the National Science Foundation Graduate Research Fellowship Program under Grant No. DGE-1550139. Any opinions, findings, and conclusions or recommendations expressed in this material are those of the author(s) and do not necessarily reflect the views of the National Science Foundation.

TABLE OF CONTENTS

LIST OF TABLES

LIST OF FIGURES

LIST OF ABBREVIATIONS

AD	Accretion Disk
AGN	Active Galactic Nuclei
ALMA	Atacama Large Millimeter Array
AO	Adaptive Optics
APO	Apache Point Observatory
ARC	Astrophysical Research Consortium
BPT	Baldwin–Phillips–Terlevich
BLR	Broad Line Region
CCD	Charged Coupled Device
Chandra	Chandra X-ray Observatory
DIS	Dual Imaging Spectrograph
ENLR	Extended Narrow Line Region
EW	Equivalent Width
eV	Electronvolt
FWHM	Full Width at Half Maximum
HST	Hubble Space Telescope
IRAF	Image Reduction and Analysis Facility
IDL	Interactive Data Language
IFU	Integral Field Unit
IR	Infrared

IPAC	Infrared Processing and Analysis Center
IUE	International Ultraviolet Explorer
ISM	Interstellar Medium
IP	Ionization Potential
JWST	James Webb Space Telescope
keV	Kiloelectronvolt
kpc	Kiloparsec
LUVOIR	Large UV/Optical/IR Surveyor
MAST	Mikulski Archive for Space Telescopes
MCG	Morphological Catalogue of Galaxies
Mpc	Megaparsec
Mrk	Markarian
NASA	National Aeronautics and Space Administration
NGC	New General Catalog
NIFS	Near-Infrared Integral Field Spectrometer
NLR	Narrow Line Region
pc	Parsec
PA	Position Angle
QSO	Quasar or Quasi-stellar Object
SDSS	Sloan Digital Sky Survey
SED	Spectral Energy Distribution
SFR	Star Formation Rate
SIMBAD	Set of Identifications Measurements & Bibliography for Astro. Data
SMBH	Supermassive Black Hole
STIS	Space Telescope Imaging Spectrograph
S/N	Signal-to-Noise

UFO	Ultra-fast Outflow
UGC	Uppsala General Catalogue
UM	University of Michigan Objective-Prism Survey
UT	Universal Time
UV	Ultraviolet
WFC3	Wide Field Camera 3
WFPC2	Wide Field and Planetary Camera 2
XMM-Newton	X-ray Multi-Mirror Mission

LIST OF CONSTANTS

Quantity	**Symbol**	**Value**	**Units**
Speed of Light	c	2.989×10^{10}	cm s^{-1}
Solar Mass	$M_\odot$	1.989×10^{33}	g
Solar Luminosity	$L_\odot$	3.826×10^{33}	erg s^{-1}
Hubble's Constant	H_0	71.0	km s^{-1} Mpc^{-1}
Planck's Constant	h	6.626×10^{-27}	erg s
Proton Mass	m_p	1.673×10^{-24}	g
Electron Mass	m_e	9.109×10^{-28}	g
Parsec	pc	3.086×10^{18}	cm
Pi	π	3.14159	unitless
Degree	$^\circ$	1.745×10^{-2}	radian
Arcminute	$'$	2.909×10^{-4}	radian
Arcsecond	$''$	4.848×10^{-6}	radian

CHAPTER 1

INTRODUCTION

1.1 Galaxies and Supermassive Black Holes

Galaxies are collections of stars, gas, and dust that form the basis of large scale structure in the universe. They are generally categorized into spiral, elliptical, or irregular galaxy types based on their appearance, which is related to their age and the distribution of their gas and stars. Most spiral galaxies contain a central stellar bulge, which is an approximately spherical distribution of stars and gas that may vary in size from hundreds of parsecs (1 pc $\approx$ 3.26 light-years) to several kiloparsecs (kpc) depending on their mass (Oohama et al. 2009). The bulge is embedded in a stellar disk that is rich in gas and dust, with a visually-stunning example of the galaxy NGC 5643 shown in Figure 1.1.

A profound discovery of observational astronomy in the last several decades is that nearly all massive galaxies host a supermassive black hole (SMBH) with masses that are millions to billions of times larger than that of the Sun. Despite their great masses, these SMBHs only gravitationally dominate their immediate vicinity that extends a few parsecs from the galactic center. While the majority of SMBHs in the present day universe are quiescent, they can interact dramatically with their galaxies on much larger scales when they are growing through the accretion of gas as luminous active galactic nuclei (AGN).

At some time in their evolution, all galaxies are believed to have experienced one or more AGN phases where gas reaches the SMBH (Heckman & Best 2014). As this material falls into the SMBH's gravitational potential it liberates immense amounts of energy, which is converted into ionizing radiation that propagates out into the host galaxy. This radiation

Figure 1.1 A color-composite image of NGC 5643 produced from multiple *Hubble Space Telescope* exposures taken with different filters. The SMBH is hidden within the bright central knot of emission that is surrounded by the yellow bulge of older stars. At larger radial distances the spiral arms are visible, traced out by the hot, young, blue stars that are embedded in the darker, gas rich dust lanes. In this case, the spiral arms and bulge are connected by a stellar bar. The image spans 2.′69, or approximately 13.2 kpc when adopting a distance of $D \approx 17$ Mpc to NGC 5643. Image credit: NASA / ESA / Judy Schmidt. Used with the permission of Judy Schmidt.

ionizes gas in the host galaxy's interstellar medium (ISM), which can drive powerful outflows of ionized and molecular gas away from the SMBH and further out into the galaxy. Outflows

that originate near the vicinity of the SMBH were some of the first to be characterized through spectroscopic observations and have come to be known as "AGN winds" (Crenshaw et al. 2003; Veilleux et al. 2005; Fabian 2012; Kormendy & Ho 2013; Heckman & Best 2014; Combes 2015; King & Pounds 2015).

AGN winds may hold the key to understanding the observed positive correlations between the masses of SMBHs and their host galaxies. Specifically, they are thought to play a critical role in regulating SMBH and galactic bulge growth by clearing the nucleus of star-forming gas (Ciotti & Ostriker 2001; Hopkins et al. 2005; Kormendy & Ho 2013; Heckman & Best 2014; Fiore et al. 2017), thereby establishing the observed galaxy luminosity function (Madau & Dickinson 2014). This process may also explain the relationships between the mass of the SMBH and the stellar mass and stellar velocity dispersion of the galactic bulge. These are the well-known black hole mass – stellar bulge mass ($M_{\rm BH} - M_{\rm Bulge}$, Magorrian et al. 1998; Häring & Rix 2004) and black hole mass – stellar velocity dispersion ($M_{\rm BH} - \sigma_\star$, Ferrarese & Merritt 2000; Gebhardt et al. 2000; Batiste et al. 2017; Baron & Netzer 2019) relationships. Outflows may also affect chemical enrichment of the intergalactic medium (Hamann & Ferland 1999; Khalatyan et al. 2008) and the overall development of large-scale structure in the early universe (Scannapieco & Oh 2004; Di Matteo et al. 2005; Yang et al. 2019). This process whereby the SMBH grows through the accretion of matter (*feeding*) and impacts its environment (*feedback*) has become a central tenet of galaxy evolution models (Begelman 2004; Hopkins et al. 2005; Storchi-Bergmann & Schnorr-Müller 2019).

Exploring the evolutionary role of outflows is a complex topic, as observations across the electromagnetic spectrum reveal that AGN winds manifest in multiple gas phases on a variety of spatial scales that can only be fully characterized with several different telescopes and instruments from the ground and in space. These multiphase outflows include so-called ultra-fast outflows in the X-rays (UFOs, e.g. Tombesi et al. 2013), absorbers in the X-rays and ultraviolet (UV, e.g. Crenshaw et al. 1999; Laha et al. 2016), narrow line region (NLR) outflows in the optical and infrared (IR, e.g. Fischer et al. 2013, 2017), and molecular outflows

in the IR and radio (e.g. Rupke et al. 2017). These winds produce nonrelativistic, wide angle outflows known as "quasar mode" feedback (or AGN winds). This is in comparison to "jet mode" feedback from narrow, relativistic jets of low density plasma in radio galaxies (Urry & Padovani 1995) that are present in $\sim$ 5-10% of AGN (Rafter et al. 2009), or outflows driven by stellar winds (Rupke 2018; Zhang 2018).

In order to understand whether feeding and feedback from outflows is a viable evolutionary model that can explain our observations, we must first answer the following question: *Are the mass outflows energetic enough to provide significant feedback to their host galaxies by enhancing or suppressing star formation and/or evacuating gas reservoirs from the galactic bulge?* Answering this question poses a number of observational challenges.

1.2 The Unified Model of Active Galaxies

Before we attempt to answer this question, it is important to have a firm understanding of active galaxies, the physical processes that power them, and how the energy they release interacts with the host galaxy to drive mass outflows. Our current knowledge and understanding has developed from interpreting two fundamental types of observational data; namely, imaging and spectroscopy. While imaging gathers long exposure pictures that reveal faint galaxy structure, spectroscopy allows us to further analyze the composition of the light by dispersing it as a function of wavelength and recording its intensity. This reveals the physical processes responsible for the emission and allows us to draw fundamental conclusions about the structure of active galaxies. Spectra for two of the most well-studied active galaxies, NGC 4151 and NGC 1068, are shown in Figure 1.2.

These spectra reveal three fundamental features of the light that we observe from active galaxies: continuum emission, broad and narrow emission lines, and absorption lines. The continuum is an underlying flux level produced by the combined emission of many individual stars within the galaxy as well as emission from the AGN. The emission lines are produced by gas in which individual electrons transition between discrete energy levels surrounding

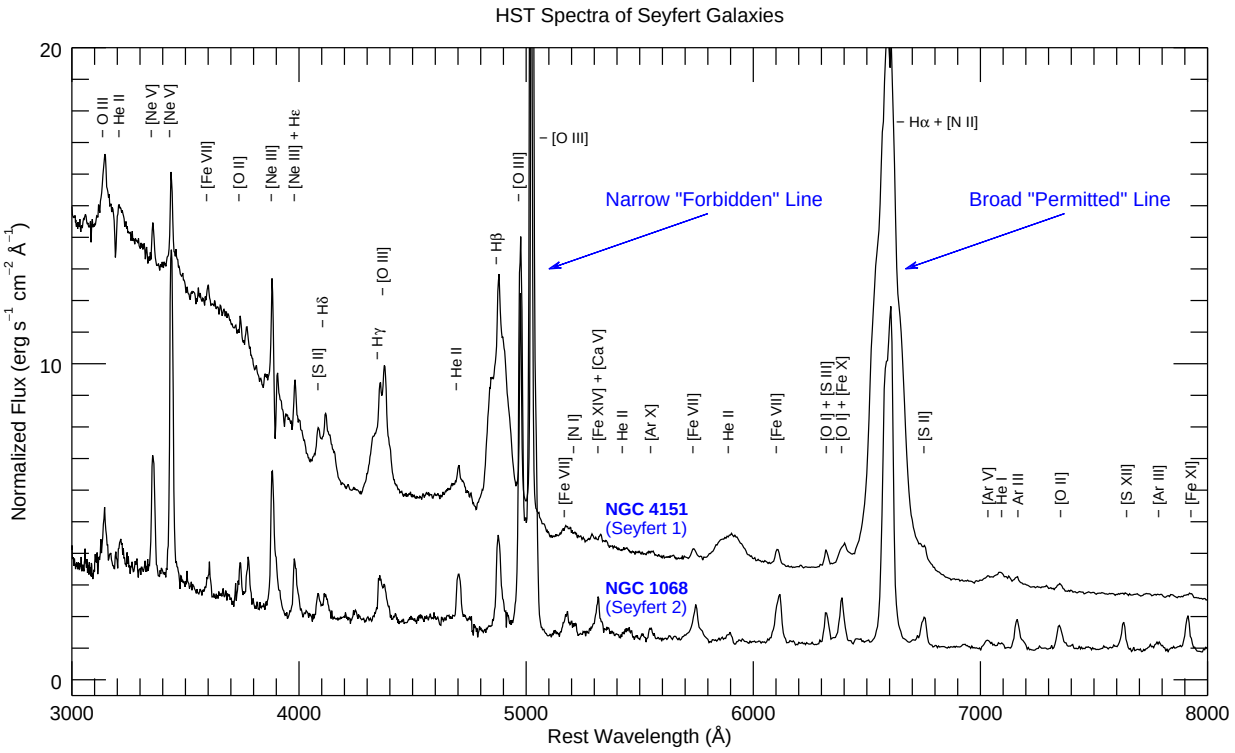

Figure 1.2 Spectra of the proto-typical Seyfert 1 galaxy NGC 4151 and Seyfert 2 galaxy NGC 1068. These *Hubble Space Telescope* spectra were gathered with the Space Telescope Imaging Spectrograph using the G140L, G230L, G430L, and G750L gratings (Kraemer et al. 2000a; Kraemer & Crenshaw 2000b). These spectra were extracted from emission near the nucleus, which encompasses light from the central engine, BLR, and inner NLR. Type 1 AGN display broad and narrow emission lines while Type 2 display only narrow lines due to orientation effects. The fluxes for NGC 4151 and NGC 1068 are multiplied by 10^{14} and 10^{15}, respectively.

an atom, releasing photons with specific energies at a single wavelength (or color). These emission lines that are attributed to the transitions of electrons around atoms are denoted by their element and ionization state. Emission lines are further divided into forbidden lines (long transition lifetime) and permitted lines (short transition lifetime) that are denoted with and without brackets, respectively. The permitted lines are created through electron recombination or collisional excitation. For example, the permitted optical recombination emission lines of hydrogen are Hα (level 3 $\rightarrow$ 2), Hβ (level 4 $\rightarrow$ 2), Hδ (level 5 $\rightarrow$ 2), and so on. The forbidden optical emission lines of oxygen are [O I], [O II], and [O III], for neutral, single, and doubly ionized states (O^{+0}, O^{+1}, O^{+2}). These so-called "forbidden lines"

have earned their name from the fact that the electron transitions violate various quantum mechanical selection rules and are difficult to produce in the laboratory, and would be more aptly described as "low-probability" lines. The relative strength of each permitted and forbidden line contains diagnostic information about the physical conditions in the gas such as its ionization state, temperature, density, elemental abundances, and the source of ionizing radiation.

The wavelength of each line is determined by its energy, which will shift to shorter (bluer) or longer (redder) wavelengths due to the Doppler effect if the gas has a nonzero velocity toward or away from us. The redshifts and blueshifts are used to measure the velocity of the gas, while the width of the emission line tells us about the range of velocities present. This is important for our study as gas that is rotating in the galaxy disk will have a different velocity profile than gas in the outflows.

Observations suggest that an energetic source of ionizing radiation is present to excite gas in the galaxy and produce the emission lines, which has led to a "unified model" of active galaxy structure (see Figure 1.3, Antonucci 1993; Urry & Padovani 1995; Netzer 2015; Padovani et al. 2017). At their centers, active galaxies host a SMBH with masses that span a range from $\sim 10^6$ to $\sim 10^9$ solar masses ($M_\odot$) that is contained within a volume comparable to that of the solar system. This gives rise to the strongest gravitational fields in the universe that allow SMBHs to draw in gas, dust, and the occasional star that passes within a few light-years of the galactic center.

Gravity compresses and heats the material through dynamical friction, which forms an accretion disk (AD) of material that can reach temperatures of $\sim 10^5$ Kelvin (K) and is responsible for the high energy UV and soft X-ray emission observed in AGN (the hard X-rays are thought to originate in a "corona" above the disk). The ionizing radiation propagates away from the SMBH until it encounters gas in the broad line region (BLR), which is highly irradiated and dense gas ($n_H > 10^9$ cm^{-3}) that absorbs and reprocesses the AD emission. Spectroscopy reveals broad emission lines due to the convolution of emission from many

individual gas clouds that each have a unique line-of-sight velocity as they orbit the SMBH at velocities of several thousand km s^{-1}. Time resolved spectroscopy of the BLR can be used to measure the black hole mass based on the light travel time-lag between changes in the AGN continuum and the corresponding response of the BLR luminosity (Peterson et al. 2004; Bentz et al. 2006, 2009). The SMBH, AD, and BLR are spatially unresolved in images due to their small angular size ($\sim$ milliarcseconds), with the exception of recent observations revealing the SMBH in a nearby AGN (Event Horizon Telescope Collaboration et al. 2019).

As radiation escapes to distances of parsecs and kiloparsecs it continues to ionize gas within the host galaxy disk that gives rise to the narrow line region (NLR), which is composed of ionized gas at distances of $\sim 1 - 1000$ pc from the AGN with densities of $n_{\rm H} \approx 10^2 - 10^6$ cm^{-3} (Peterson 1997). This gas gives rise to the narrow emission lines observed in spectra, because the gas is moving more slowly and with a smaller range of velocities than in the BLR. The NLR encompasses the smallest spatial scale that can be resolved into individual, extended gas structures in nearby active galaxies, which provides a direct measurement for the distance of the gas from the SMBH.

Spectroscopic observations over the past several decades have revealed that some AGN display both broad and narrow emission lines (Type 1), while others display only the narrow lines (Type 2, Khachikian & Weedman 1974). Detailed spectropolarimetry of Type 2 AGN revealed that some exhibit weak BLRs in scattered light, which led to the idea that Type 1 and 2 AGN are intrinsically similar objects with the observed differences mainly due to the viewpoint of the observer (Osterbrock 1978; Antonucci & Miller 1985). It is generally accepted that this is explained by the presence of a thick obscuring disk of gas and dust known as the torus. This toroidal shaped structure obscures the view to the central AD and BLR depending on the viewpoint of the observer and the solid angle subtended by the torus, which resides at an intermediate distance between the BLR and NLR. This structure collimates the escaping emission into two anti-parallel "cones" of emission that propagate into the host galaxy and produce the NLR emission. This unification of different AGN classes

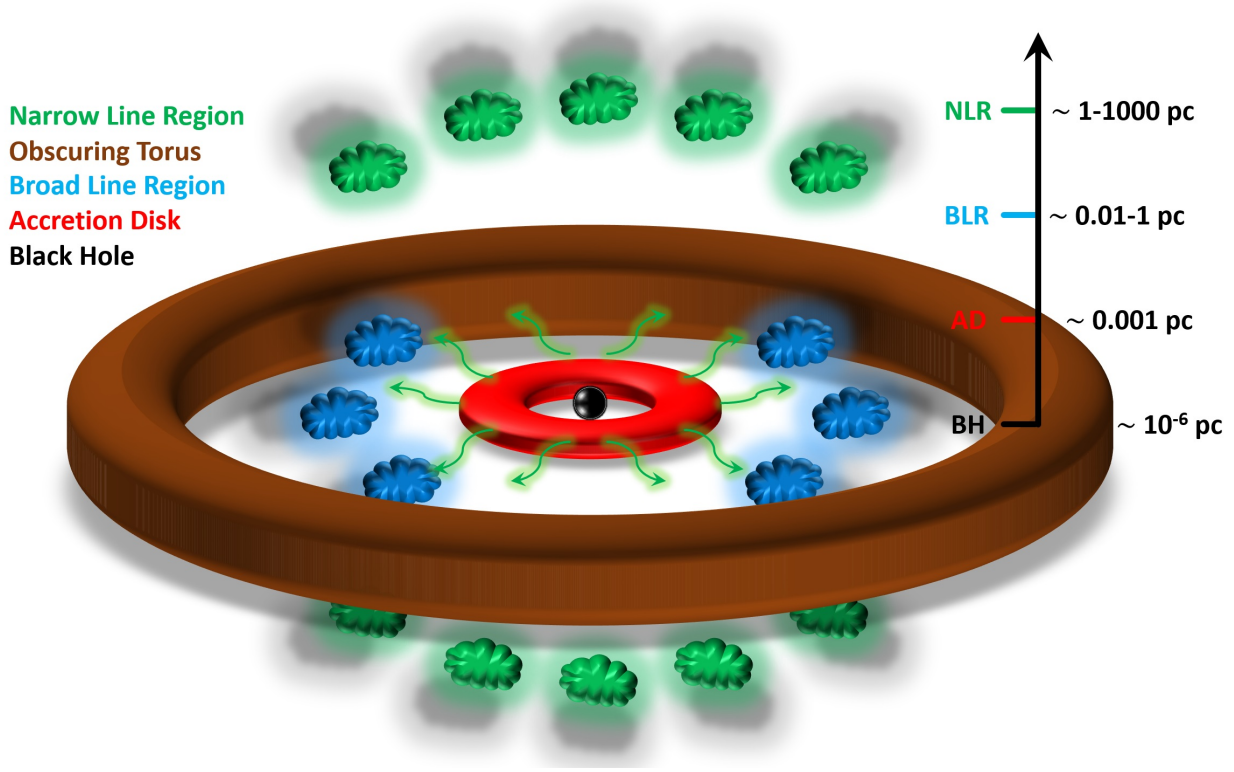

Figure 1.3 The unified model of active galaxy structure on a logarithmic scale for a SMBH of $M \sim 10^7 M_\odot$. Material from the accretion disk (red) falls onto the SMBH (black), producing energetic photons (green arrows). This radiation propagates out into the broad line region (blue clouds) and narrow line region (green clouds) where it is reprocessed. In this model, Type 1 AGN are those viewed "pole-on" such that the observer can see the AD and BLR, while our view of Type 2 AGN intersects the torus that obscures the central engine and only allows us to view the NLR. The above diagram presents a simplified view, as the various components are likely clumpy and inhomogeneous. This image is based on an illustration created by Claudio Ricci.

has become known as the "unified model" (Antonucci 1993; Urry & Padovani 1995; Netzer 2015; Padovani et al. 2017).

With these observational similarities and differences, it is useful to characterize all AGN based on shared and fundamental physical properties. The first of these is the mass of the SMBH, which can be directly measured from reverberation mapping in Type 1 AGN (Peterson et al. 2004; Bentz et al. 2006, 2009). For Type 2 AGN where the BLR is obscured, this can be inferred from the velocity dispersion of stars in the bulge, which is correlated with the mass of the SMBH that establishes their orbital velocities (Ferrarese & Merritt

2000; Gebhardt et al. 2000; Batiste et al. 2017). Another fundamental parameter is the AGN's bolometric luminosity (L_{bol}), which is a measure of the total energy radiated by the AGN integrated across all wavelengths. This parameter encapsulates the total power output of the AGN and is useful for measuring its potential impact relative to other AGN. The bolometric luminosity generally increases with the accretion rate up to a theoretical maximum for spherically symmetric accretion given by the Eddington luminosity, which is $L_{Edd} \approx 1.26 \times 10^{38} \, (M/M_{\odot})$ erg s^{-1}. The relative accretion rates of AGN may then be compared through the Eddington ratio, L_{bol}/L_{Edd}, which has a value of zero in the case of no accretion and one in the case of a maximum accretion rate. There are circumstances where a black hole may exceed this theoretical maximum accretion rate based on the geometry of the inflowing gas.

1.3 Narrow Line Region Mass Outflows

With this model of AGN structure and their fundamental parameters we are now equipped to investigate the impact of outflows on their host galaxies. As discussed above, the SMBH, AD, and BLR are all so compact that their emission and physical structure are contained within a single spatially unresolved point. The NLR is the first link between the AGN central engine and the host galaxy that we may probe as a function of radial distance from the galactic center, which provides important constraints on the motion and physical conditions of the gas. The NLR also spans more than three orders of magnitude in spatial extent from parsecs to kiloparsecs, indicating that NLR outflows may potentially provide feedback on the critical scale of galaxy bulges.

Kinematic studies of the NLR reveal outflows of ionized gas, often with a biconical geometry (Crenshaw et al. 2010; Müller-Sánchez et al. 2011; Fischer et al. 2013, 2014; Bae & Woo 2016; Müller-Sánchez et al. 2016; Nevin et al. 2016), that exhibit wide opening angles as compared to narrow relativistic radio jets. Following the precedent of others, we define the NLR to be ionized gas with outflow kinematics driven by the AGN, while the extended

Figure 1.4 An enlarged portion of Figure 1.1 highlighting the nuclear region of NGC 5643. The red-green emission extending from the nucleus to the lower left is gas that has been ionized by the central AGN and is being driven away from the SMBH at hundreds to thousands of km s^{-1}. The image spans $37\farcs2$, or approximately 3 kpc when adopting a distance of $D \approx 17$ Mpc to NGC 5643. Image credit: NASA / ESA / Judy Schmidt. Used with the permission of Judy Schmidt.

narrow line region (ENLR) is ionized gas at larger radii that primarily exhibits galactic rotation (Unger et al. 1987). An example of the NLR-galaxy interaction for the nearby active galaxy NGC 5643 is highlighted in Figure 1.4.

To better understand whether or not these outflows provide effective feedback, especially in spatially unresolved and powerful high redshift quasars, it is helpful to perform detailed studies of nearby Seyfert galaxies ($z \leq 0.1$, $L_{bol} \approx 10^{43} - 10^{45}$ erg s^{-1}, Seyfert 1943) because

their NLRs are bright and spatially resolved. The impact of these outflows must be quantified to determine whether or not they deliver feedback capable of altering star formation rates and/or evacuating gas reservoirs from the galactic bulge (Harrison 2017).

We can assess the impact of spatially resolved NLR outflows by determining the outflowing mass (M), and velocity (v) across a spatial resolution element (δr), which are then used to calculate outflow energetics such as mass outflow rates ($\dot{M} = Mv/\delta r$), kinetic luminosities ($\dot{E} = \frac{1}{2}\dot{M}v^2$), and momenta flow rates ($\dot{p} = \dot{M}v$). Determining these quantities is greatly aided by spatially resolved observations that constrain the physical extent and location of the outflowing material, making nearby AGN prime targets for this type of study as observations can resolve structures on the scale of tens of parsecs.

Studies of NLR outflows have traditionally measured "global" outflow rates that average over the spatial extent of the NLR by determining a single mass, velocity, and outflow extent. These studies find a wide range of outflow rates and energetics using two main techniques. The first is a geometric-based technique that determines the gas mass based on the volume of a modeled bicone that encompasses the observed NLR emission and a filling factor that accounts for the fact that the bicone is not a solid gaseous structure (Barbosa et al. 2009; Riffel et al. 2009; Storchi-Bergmann et al. 2010; Müller-Sánchez et al. 2011; Riffel & Storchi-Bergmann 2011a; Riffel et al. 2013; Schönell et al. 2014, 2017; Schnorr-Müller et al. 2014; Gofford et al. 2015; Müller-Sánchez et al. 2016; Nevin et al. 2018; Wylezalek et al. 2017). The second method is a luminosity-based technique that determines the gas mass based on the luminosity of an emission line and an estimate of the gas density (Liu et al. 2013; Förster Schreiber et al. 2014; Genzel et al. 2014; Harrison et al. 2014; McElroy et al. 2015; Karouzos et al. 2016; Schnorr-Müller et al. 2016; Villar-Martín et al. 2016; Bae et al. 2017; Bischetti et al. 2017; Leung et al. 2017).

These global techniques provide measurements relatively quickly; however, detailed spatial information is lost and global measurements may suffer from large uncertainties if the sizes and kinematic profiles of the NLRs are not well constrained (Kang & Woo 2018) and/or the

proper techniques for determining gas masses are not employed (Karouzos et al. 2016; Perna et al. 2017; Revalski et al. 2018a). We can leverage the power of spatially resolved NLR observations to not only quantify feedback from the outflows, but also reveal in detail where energy and material are deposited (Venturi et al. 2018; Durré, & Mould 2018, 2019). The lack of spatially resolved NLR outflow measurements combined with the unknown and possibly large uncertainties of current global estimates provides the motivation for the current study.

1.4 Study Overview and Goals

The goal of this study is to quantify the impact of spatially resolved NLR outflows in nearby active galaxies. The success of the study will be measured by the completion of specific scientific objectives and our ability to critically examine and answer the following questions.

1.4.1 Scientific Objectives

1. *Do properties of the outflows scale with fundamental AGN parameters?*

   We will quantify the ionized gas mass distributions, mass outflow rates, and outflow energetics of NLR outflows in a sample of AGN that span a range of black hole masses (M_{BH}), bolometric luminosities (L_{bol}) and Eddington ratios (L_{bol}/L_{Edd}).

2. *Are the outflows energetic enough to measurably impact the host galaxy?*

   We will determine if the NLR outflows are providing effective feedback by constraining the timescale for removing potential star-forming gas from the host galaxy bulge and by comparing our outflow energetics with theoretical models.

3. *Can ionized gas masses be calculated accurately without photoionization modeling?*

   We will use our spatially resolved measurements to explore the assumptions of simplified gas mass estimate techniques to gauge the reliability and systematic uncertainties of mass outflow rate and energetic measurements in the literature.

1.4.2 Data Requirements

Accomplishing these objectives requires us to constrain the mass and velocity of the NLR outflows as a function of radial distance from the SMBH. These properties can be determined using the fundamental observational tools of spectroscopy and imaging, in conjunction with photoionization modeling.

Spectroscopy of the NLR reveals emission lines that are produced by individual atomic transitions that can be used to trace the velocity of the gas via their Doppler shifts. Previous studies have found outflow velocities of $\sim 250 - 2000$ km s^{-1} (Fischer et al. 2013, 2014), which requires that our spectroscopic observations have a minimum spectral resolution of $R = \lambda/\delta\lambda \approx 1000$ in order to resolve the intrinsic widths of the emission lines and separate the kinematics of rotational and outflowing gas.

The NLRs of nearby AGN typically subtend $\sim 1 - 5''$ on the sky, which requires that our observations have a spatial resolution of $\sim 0\farcs1$ to provide sufficient sampling that will allow us to map changes in the kinematics and physical conditions of the gas as a function of radial distance. As a result, normal seeing-limited observations from the ground that have spatial resolutions of $\sim 1''$ due to the blurring effects of the Earth's atmosphere are insufficient for this study.

The need for high spatial and spectral resolution observations was a primary science driver for the development of NASA's *Hubble Space Telescope* (*HST*, Figure 1.5). Since its launch in 1990, *HST* has become one of the most scientifically productive telescopes ever constructed. Orbiting above Earth's atmosphere, *HST* provides diffraction-limited observations with superior sensitivity to faint and extended emission such as that found in the NLR. While the advent of adaptive optics (AO, Babcock 1953) that distort a telescopes optical elements in real time to partially counteract the blurring effect of the Earth's atmosphere now allows for high spatial resolution spectroscopy and imaging from the ground, optical aberrations remain that reduce contrast and sensitivity as compared to space-based observations.

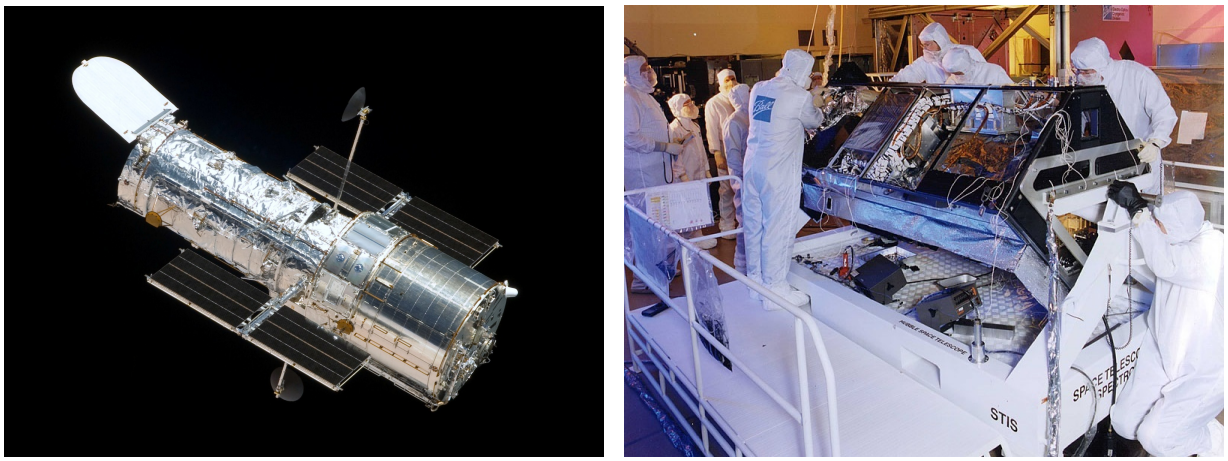

Figure 1.5 The *Hubble Space Telescope* (left) and Space Telescope Imaging Spectrograph (right). *HST* STIS enables high spatial and spectral resolution observations of AGN, without the blurring effects introduced by the Earth's atmosphere. Credit: NASA / STScI.

Through an array of cameras and spectrographs *HST* has accumulated an immense archive of data that are accessible through the The Mikulski Archive for Space Telescopes (MAST) database. Most importantly for this study, numerous spectroscopic and imaging campaigns of nearby AGN have been conducted, which alleviates the time-consuming need to acquire new observations for many galaxies. *HST's* variety of cameras and spectrographs gives it the versatility to tackle a multitude of scientific inquiries. Based on the data requirements needed to accomplish our scientific objectives, the spectrograph of choice is the Space Telescope Imaging Spectrograph (STIS, Woodgate et al. 1998).

STIS has multiple interchangeable gratings that can be used to disperse different portions of the spectrum by varying amounts depending on the science requirements. In general, low dispersion spectroscopy provides a larger swath of the spectrum with coverage of many emission lines for photoionization modeling, but with reduced velocity resolution. Medium and high dispersion spectroscopy provides superior velocity resolution for determining gas velocities, at the expense of a narrower spectral range that encompasses relatively few emission lines. This study requires both high velocity precision and a large number of emission lines for modeling, which can be accomplished by using multiple observations with different gratings. The *HST* STIS gratings are labeled according to their central wavelength in nanometers, with

Figure 1.6 The Astrophysical Research Consortiums 3.5 meter telescope and enclosure (left) located at the Apache Point Observatory in Sunspot, New Mexico. The right panel shows the Dual Imaging Spectrograph mounted to one of the telescope's Nasmyth focal points. Image Credit: D. Michael Crenshaw.

a letter indicating high (H), medium (M), or low (L) dispersion. The primary gratings for optical spectroscopy are the G430L, G430M, G750L, and G750M. At a minimum, we require at least one spectrum from each of the G430 and G750 series that are spatially coincident such that the observations sample different wavelengths emitted by the same gas at the same spatial location along the NLR.

Finally, despite the superior sensitivity and spatial resolution of *HST*, ground-based observations of AGN can provide useful measurements of the large scale properties of the ionized gas in the host galaxy. This includes determining the radial extent of the ionized gas and outflows, and constraining the host galaxy rotation, orientation, and inclination from faint extended emission on scales of tens of arcseconds to arcminutes. We took advantage of guaranteed time on the Astrophysical Research Consortiums 3.5 meter telescope at the Apache Point Observatory (APO) to obtain supplementary spectroscopy with the Dual Imaging Spectrograph (DIS, Figure 1.6).

1.4.3 Active Galaxy Sample

The selection of a suitable galaxy sample for this study was aided significantly by the studies of Fischer et al. (2013, 2014). These authors examined the *HST* STIS long-slit spectra of every AGN with a redshift of $z < 0.035$ in the MAST archive, resulting in kinematic measurements for the NLRs of 53 Seyfert galaxies and quasars. They found clear kinematic signatures of biconical outflow in 17/53 galaxies, with the remainder showing primarily rotational, compact, or complex kinematics that could not easily be identified as outflows.

Starting with the 17 galaxies exhibiting biconical outflows, we examined the quantity and quality of their STIS long-slit spectra and [O III] imaging in the MAST archive. While the studies of Fischer et al. (2013, 2014) only required spectral coverage of either the strong [O III] λ5007 or Hα λ6563 emission line to characterize the gas kinematics, we require multiple emission lines for photoionization modeling as well as an [O III] image to determine the NLR gas mass. We initially identified 10 galaxies with the required spectroscopy and imaging, but upon careful examination we discovered that several of these did not have co-spatial spectroscopy in each grating and/or had exceedingly low signal-to-noise (S/N) in the emission lines. Ultimately, we selected six galaxies with the required spectroscopy and imaging for this study. The selected AGN and their physical characteristics are provided in Table 1.1, with uncertainties in the bolometric luminosities and black hole masses $\sim 0.3 - 0.5$ dex (Heckman et al. 2004; Bentz et al. 2006). The availability of spectroscopy and [O III] imaging for each target, as well as the number of long-slit observations that we obtained with APO DIS, are summarized in Table 1.2.

The final column of Table 1.1 indicates whether the analysis for each galaxy is complete or in-progress. One of our scientific objectives is to determine whether or not a simplified methodology that does not utilize photoionization models can be used to determine accurate gas masses. This would greatly expedite the analysis for individual targets. As discussed in Chapter 4, we were unable to find a suitable simplified process. Thus, we present the results

Table 1.1. Nearby Active Galaxies with Archival *HST* STIS Observations

Catalog Name (1)	Redshift (21 cm) (2)	Distance (Mpc) (3)	Scale (pc/″) (4)	V (mag) (5)	$\log(L_{bol})$ (erg s^{-1}) (6)	$\log(M_{BH})$ ($M_\odot$) (7)	L_{bol}/L_{Edd} (unitless) (8)	Refs. (Col. 6,7) (9)	Analysis Status (10)
NGC 4151	0.0033	13.3	67.4	11.5	43.9	7.6	0.01	1, 2	Complete
MRK 573	0.0172	72.0	349.1	14.0	45.5	7.3	0.75	3, 4	Complete
MRK 34	0.0505	207.9	1007.7	14.7	46.2	7.5	3.98	5, 6	Complete
NGC 1068	0.0038	16.0	77.6	10.0	45.0	7.2	0.50	4, 4	In-progress
MRK 3	0.0135	56.6	274.5	13.0	45.3	8.7	0.04	7, 4	In-progress
MRK 78	0.0372	154.2	747.4	14.6	44.6	7.9	0.04	4, 4	In-progress

Note. — Columns are (1) target name, (2) 21 cm redshift from the NASA/IPAC Extragalactic Database, (3) Hubble distance and (4) spatial scale assuming $H_0 = 71$ km s^{-1} Mpc^{-1}, (5) apparent V band magnitude from SIMBAD, (6) bolometric luminosity estimated from [O III] imaging, (7) black hole mass, and (8) the corresponding Eddington ratio. Column (9) gives the references for columns (6) and (7). References are: (1) Crenshaw & Kraemer 2012, (2) Bentz et al. 2006, (3) Revalski et al. 2018a, (4) Woo & Urry 2002, (5) Revalski et al. 2018b, (6) Oh et al. 2011, (7) Collins et al. 2009.

Table 1.2. Spectroscopic and Imaging Observations

Target (1)	Type (2)	G430L (3)	G430M (4)	G750M (5)	G750L (6)	[O III] (7)	APO (8)
NGC 4151	1	2	5	3	2	3	4
Mrk 573	2	1	...	1	...	2	4
Mrk 34	2	2	3	...	1	1	8
NGC 1068	2	2	7	3	1	3	5
Mrk 3	2	1	...	...	1	3	8
Mrk 78	2	5	4	4	...	1	6

Note. — *HST* data available in the MAST archive for the targets in Table 1.1. Columns are: (1) target name, (2) AGN Type, followed by the availability of *HST* STIS data for the following gratings: (3) G430L, (4) G430M, (5) G750M, (6) G750L, and (7) [O III] imaging. Column (8) lists the number of APO DIS long-slit spectral observations that we obtained along different position angles and/or with different grating configurations.

for the first three AGN in this dissertation and the analysis for the remaining three will be presented in a future publication.

1.4.4 Pilot Study of NGC 4151

To begin tackling this investigation, Crenshaw et al. (2015) conducted a pilot study to quantify the mass outflow rate at each location along the NLR in the nearby Seyfert 1 galaxy NGC 4151 ($z = 0.00332$, $D = 13.3$ Mpc, Figure 1.7, 1.8). The spatially resolved techniques developed by Crenshaw et al. (2015) form the foundation of the methods applied in the current study and we provide an overview in this section. The analysis requires determining the velocity and mass of the outflowing gas as a function of spatial position in order to quantify the mass outflow rates and outflow energetics.

The physical conditions in the ionized gas were constrained by Kraemer et al. (2000a), who employed a spectral synthesis code to develop photoionization models of the NLR (Kraemer 1985). This requires providing the AGN spectral energy distribution (SED), luminosity, and gas composition and dust content, along with any other relevant ionization sources. The models then predict the observed emission line spectrum, which were compared with the measured emission line strengths. The physical conditions in the gas such as the number and column density were then varied until an acceptable match was found for all the emission lines. These models predict the parameters needed to calculate the gas mass.

The kinematics of the ionized gas were then measured by Das et al. (2005) by fitting multiple Gaussian profiles to the strong [O III] λ5007 emission line at each location along the *HST* slit. By comparing the observed wavelength with its laboratory measured rest wavelength they calculated the line-of-sight Doppler velocity of the gas at each position. Das et al. (2005) then used these measurements to develop a geometric model for NGC 4151 that is composed of a host galaxy disk and a biconical NLR outflow component. This model provides a projection factor that allows the outflow velocities to be deprojected to true radial outflow velocities, independent of the system inclination (Fischer et al. 2013, 2014).

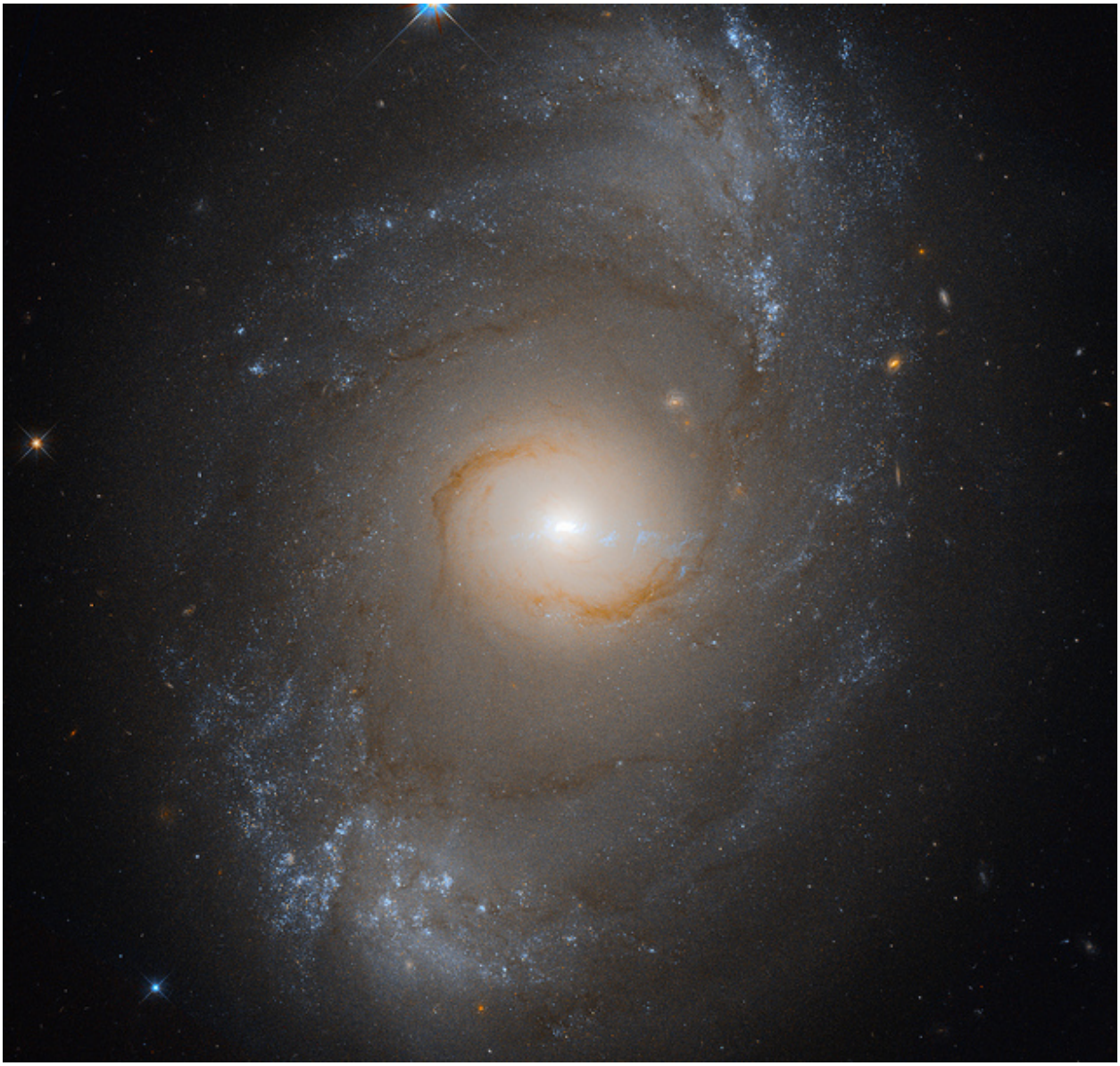

Figure 1.7 The nearby Seyfert 1 galaxy NGC 4151 used as a pilot study by Crenshaw et al. (2015). The image spans $2\farcm69 \times 2\farcm56$, or approximately 10.9×10.3 kpc when adopting a distance of $D \approx 13.3$ Mpc to NGC 4151. Image credit: NASA / ESA / Judy Schmidt. Used with the permission of Judy Schmidt.

The photoionization models provide key parameters about the gas that allowed Crenshaw et al. (2015) to calculate the gas mass at each position along the spectral slit. These masses and observed fluxes were then used to calculate a luminosity-to-mass scale factor that was applied to an [O III] emission line image of the entire NLR to determine the total ionized gas

Figure 1.8 An enlarged portion of Figure 1.7 highlighting the nuclear region of NGC 4151. The white-blue emission represents the AGN ionized gas of the NLR and ENLR. Note the biconical shape of the emission and the clumpy, inhomogeneous nature of the gas. The image spans $57\farcs4 \times 44\farcs7$, or approximately 3.9×3.0 kpc when adopting a distance of $D \approx 13.3$ Mpc to NGC 4151. Image credit: NASA / ESA / Judy Schmidt. Used with the permission of Judy Schmidt.

mass as a function of distance from the SMBH. The techniques and results of Crenshaw et al. (2015) are summarized in Figure 1.9.

For the NLR outflows in NGC 4151 Crenshaw et al. (2015) concluded that the peak mass outflow rate is $\dot{M}_{out} \approx 3.0\ M_{\odot}\ \mathrm{yr}^{-1}$ at a distance of 70 pc from the SMBH, with the outflow extending to ~ 140 pc from the nucleus. This outflow rate exceeds that of the UV/X-ray absorbers by a factor of $\sim 5-10$, and also exceeds the calculated mass accretion rate onto the SMBH by a factor of ~ 230 based on the AGN's bolometric luminosity (Crenshaw & Kraemer

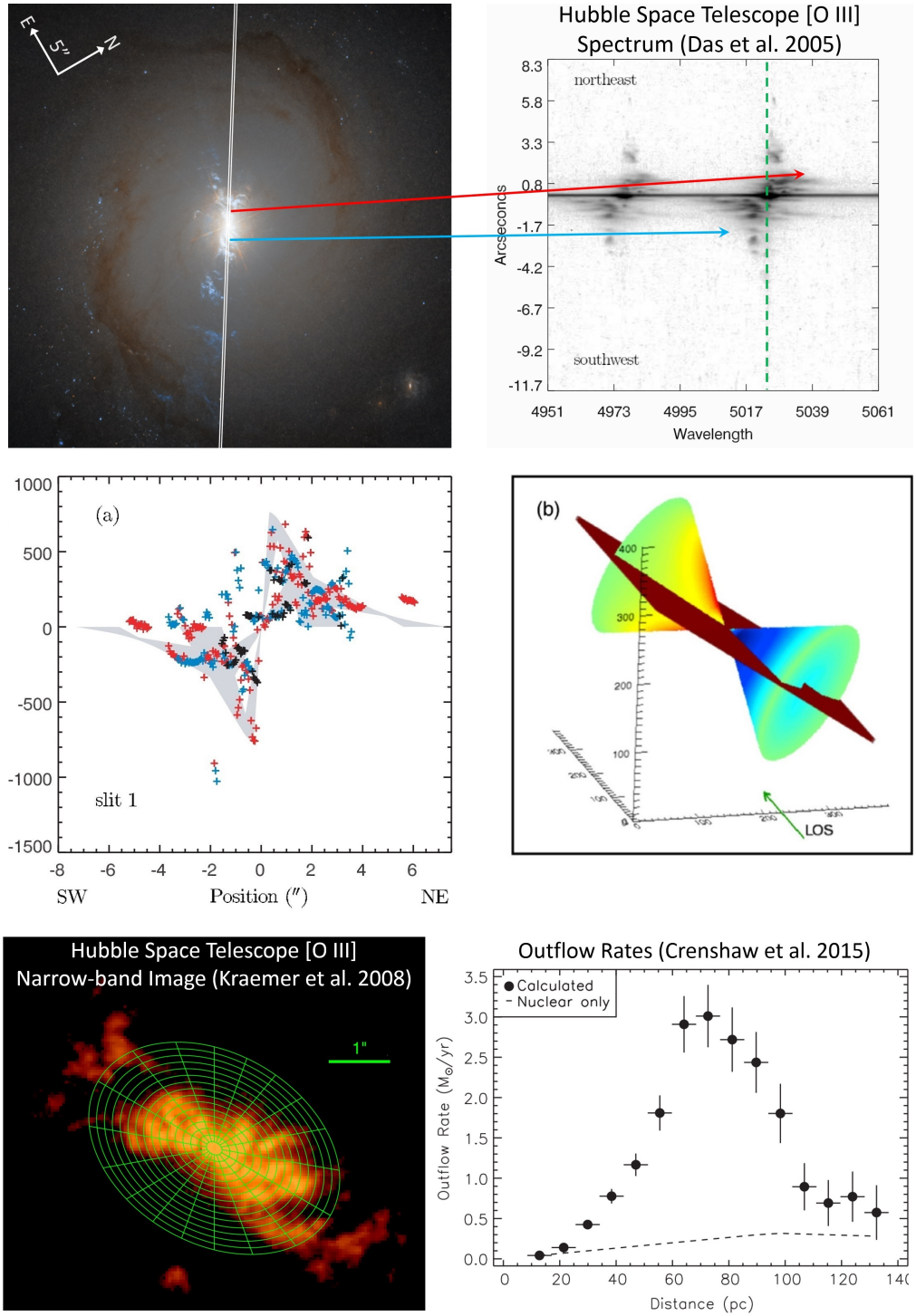

Figure 1.9 The pilot study of NGC 4151 by Crenshaw et al. (2015, ApJ, 799, 83, doi: 10.1088/0004-637X/799/1/83). The top panel shows (left) the position of the 0.″2 *HST* STIS slit and (right) the resulting dispersed image that reveals strong red and blueshifted velocities (arrows) that are much larger than the systemic rotational velocities (green dashed line). Measurements of the outflowing gas yield the outflow velocity law (middle-left) and resulting bicone model (middle-right, Das et al. 2005, AJ, 130, 945, doi: 10.1086/432255). The lower-left panel is an [O III] image of the NLR (Kraemer et al. 2008, ApJ, 679, 1128, doi: 10.1086/587802). The mass (M) and velocity (v) across each image extraction (δr) were used to calculate the mass outflow rates ($\dot{M} = Mv/\delta r$) at each distance (lower-right). © AAS. Reproduced with permission.

2012). The calculated energetics reach benchmark values for effective feedback, indicating that NLR outflows may significantly impact their host galaxies. Following this result, we chose to begin our analysis with the AGN known as Markarian 573 and Markarian 34. Together with NGC 4151, these targets span the largest range in bolometric luminosity and radial outflow extent of all the galaxies in our sample (Table 1.1).

CHAPTER 2

MARKARIAN 573[1]

The investigation of NGC 4151 by Crenshaw et al. (2015) suggests that NLR outflows may significantly impact their host galaxies and demonstrated the power of using spatially resolved observations to quantify outflow properties. We chose the Seyfert 2 galaxy Markarian 573 (Mrk 573, UGC 01214, UM 363) to refine the techniques of Crenshaw et al. (2015), as high quality spectroscopy and imaging are readily available and previous studies have provided results that are relevant for creating precise photoionization models. The central AGN is also more luminous and rapidly accreting than in NGC 4151, which allows us to probe NLR outflows in a more energetic environment.

2.1 Physical Characteristics of Markarian 573

Morphological studies of Mrk 573 reveal a spatially extended NLR that is approximately biconical in shape. Strong emission lines from a wide range of ionized species such as [O I] and [Fe XIV] are observed near the nucleus, with ionized gas in the ENLR reaching distances of ~ 8 kpc (Koski 1978; Tsvetanov et al. 1989a; Haniff et al. 1991; Kinney et al. 1991; Tsvetanov & Walsh 1992; Pogge & De Robertis 1993; Erkens et al. 1997; Alonso-Herrero et al. 1998; Storchi-Bergmann et al. 1998a; Mullaney & Ward 2008; Dopita et al. 2015). Observations from space and with adaptive optics have unveiled rich structure, including ionized arcs of emission, spiral dust lanes, and a so dubbed "linear feature" of emission line knots extending

[1]This chapter was originally published in the Astrophysical Journal, Volume 856, Pages 46-69 on 2018 March 20, under the title "Quantifying Feedback from Narrow Line Region Outflows in Nearby Active Galaxies. I. Spatially Resolved Mass Outflow Rates for the Seyfert 2 Galaxy Markarian 573" by Revalski et al. (2018a). doi:10.3847/1538-4357/aab107.

along a position angle (PA) of $\sim 125^\circ$ (Pogge & De Robertis 1995; Malkan et al. 1998; Ferruit et al. 1999; Martini et al. 2001; Pogge & Martini 2002). This feature is coincident with a triple-lobed radio source that displays possible interaction with the ENLR (Ulvestad & Wilson 1984; Unger et al. 1987; Haniff et al. 1988; Whittle et al. 1988; Tsvetanov 1989b; Capetti et al. 1996; Falcke et al. 1998; Ferruit 2002). Several of these features can be seen in our structure map in Figure 2.1. Additional studies focusing on the kinematics (Tsvetanov 1989b; Afanasiev et al. 1996; Ruiz et al. 2005; Fischer et al. 2010, 2017) and physical conditions of the ionized gas (Tsvetanov & Walsh 1992; Kraemer et al. 2009; Schlesinger et al. 2009) are discussed throughout this chapter.

As a Type 2 AGN under the unified model (Khachikian & Weedman 1974; Osterbrock 1981; Antonucci & Miller 1985; Antonucci 1993; Netzer 2015), Mrk 573 displays narrow permitted and forbidden lines and was suspected to house a hidden BLR (Kay 1994; Tran 2001) that was detected with deep spectropolarimetric observations (Nagao et al. 2004a,b; but see also Ramos Almeida et al. 2008, 2009a). The central SMBH has a mass of $\log(M_{BH}/M_\odot) = 7.28$ (Woo & Urry 2002; Bian & Gu 2007) and radiates at a bolometric luminosity of $\log(L_{bol}/\mathrm{erg\ s^{-1}}) = 45.5 \pm 0.6$ (Meléndez et al. 2008a,b; Kraemer et al. 2009). This corresponds to an Eddington ratio of $L_{bol}/L_{Edd} \approx 0.75$.

The central AGN resides in an S0 host galaxy with an (R)SAB(rs) classification (de Vaucouleurs et al. 1995). There are measured redshifts from stellar kinematics ($z = 0.01718$, Nelson & Whittle 1995) and 21 cm observations ($z = 0.01721$, Springob et al. 2005). The former is most consistent with the NLR gas kinematics and corresponds to $cz \approx 5150$ km s^{-1}. We adopt $H_0 = 71$ km s^{-1} Mpc^{-1}, corresponding to a Hubble distance of 72 Mpc and a spatial scale of ~ 350 pc/$''$ on the sky.

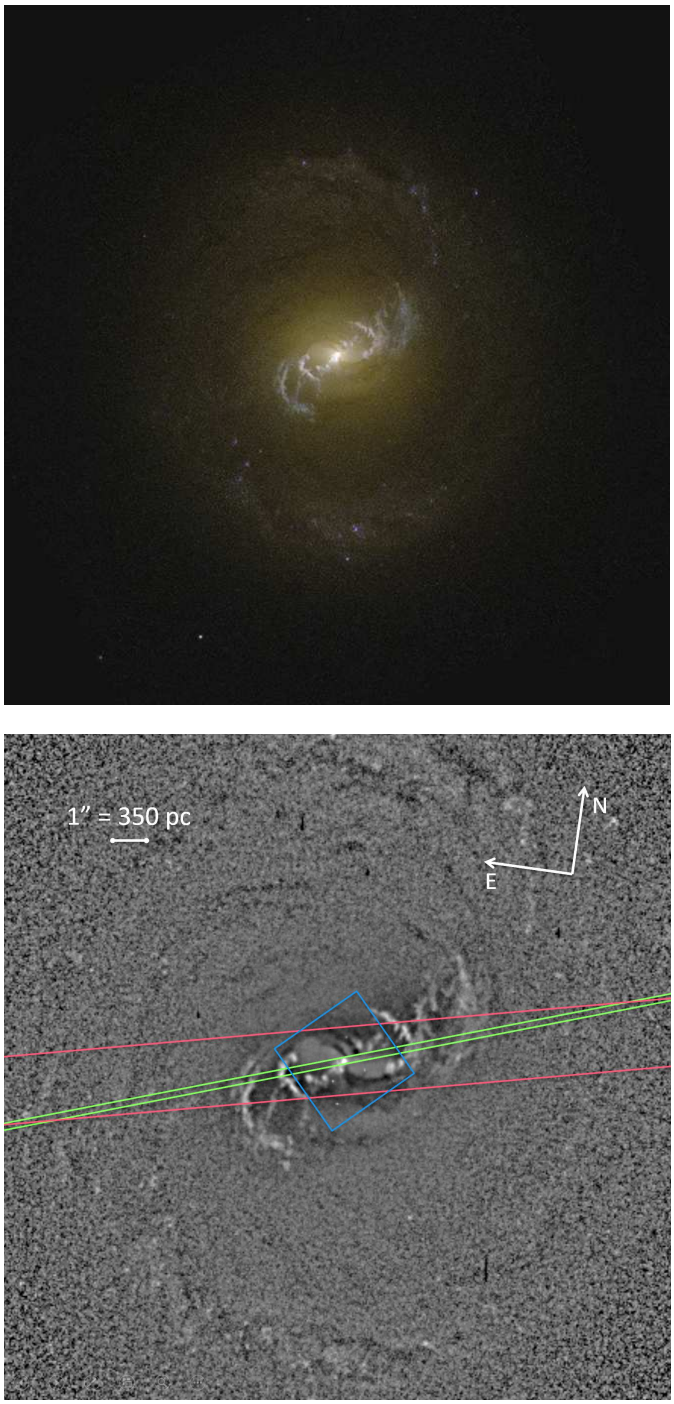

Figure 2.1 The top panel is an *HST* color-composite image of Mrk 573 created by Judy Schmidt, with North up and East to the left (Red: WFPC2/PC F675W, Green: WFPC2/PC F569W, Blue: ACS/HRC F330WA). The bottom panel is a $20'' \times 20''$ contrast enhanced structure map from the *HST* WFPC2 image of Mrk 573 using the F606W filter (Pogge & Martini 2002; Fischer et al. 2010). Bright regions correspond to [O III] and continuum emission, while darker regions are dust lanes. The position of the $0\farcs2$ *HST* STIS slit is shown in green, the APO DIS $2\farcs0$ slit is shown in red, and the central *Gemini* NIFS $3'' \times 3''$ field from Fischer et al. (2017) is shown in blue. Image credit: NASA / ESA / Judy Schmidt. Used with the permission of Judy Schmidt.

2.2 Observations

2.2.1 Hubble Space Telescope

The archival Space Telescope Imaging Spectrograph spectra were retrieved from the Mikulski Archive at the Space Telescope Science Institute and calibrated as part of a detailed study that classified the NLR kinematics in a large sample of Seyfert galaxies (Fischer et al. 2013, 2014). The observations were obtained on 2001 October 17 as a part of Program ID 9143 (PI: R. Pogge) utilizing the 52″ x 0.″2 slit with G430L and G750M gratings. The G430L observations span $2845 - 5760$ Å at a dispersion of 2.744 Å pixel^{-1}, and the G750M observations span $6285 - 6875$ Å at a dispersion of 0.555 Å pixel^{-1}. Both data sets have a spatial resolution of 0.″05078 pixel^{-1}. Data reduction consisted of aligning the spatially offset exposures using the peaks of the underlying continua to within half a pixel, median combining, and hot pixel removal. We extracted spectra spatially summed over two pixel intervals to match the angular resolution along the slit, and further data reduction details are given by Kraemer et al. (2009) and Fischer et al. (2010).

The slit position of $-71.^{\circ}2$ spatially samples the bright nuclear emission and extended arcs, but misses the linear feature of bright emission line knots extending roughly parallel to the radio feature along PA $\sim 125^{\circ}$. The position of the *HST* STIS slit relative to the NLR is shown in Figure 2.1 and the extracted spectra are shown in Figure 2.2.

The [O III] imaging observations were conducted on 1995 November 12 with the *HST* Wide Field and Planetary Camera 2 (WFPC2) on the WF2 camera with a plate scale of 0.″0996 pixel^{-1} as part of Program ID 6332 (PI: A. Wilson). Two 600 s exposures were taken through the FR533N ramp filter with a wavelength center of 5093 Å, centering on the [O III] λ5007 emission line at the redshift of Mrk 537. The images were retrieved and calibrated by Schmitt et al. (2003a,b) to study the extended [O III] morphologies of Seyfert galaxies, and data reduction details are given in those papers.

2.2.2 Apache Point Observatory

To characterize NLR emission that falls outside of the narrow STIS slit, we utilized supplementary observations taken with the Dual Imaging Spectrograph (DIS) on the Astrophysical Research Consortium's Apache Point Observatory (ARC's APO) 3.5 meter telescope in Sunspot, New Mexico. The DIS employs a dichroic element that splits light into blue and red channels, allowing for simultaneous data collection in the Hβ and Hα portions of the spectrum. Here we focus on our observations along PA = 103° with a 2.″0 slit and B/R1200 gratings that were originally presented in our study of the NLR and ENLR kinematics of Mrk 573 (Fischer et al. 2017).

These data consist of two 900 s exposures taken on 2013 December 3 at a mean airmass of 1.214 with 1.″6 seeing. The blue channel spans 4190 − 5455 Å at a dispersion and spatial resolution of 0.6148 Å pixel^{-1} and 0.″42 pixel^{-1}, respectively. The red channel spans 5995−7180 Å at a dispersion and spatial resolution of 0.5796 Å pixel^{-1} and 0.″40 pixel^{-1}, respectively. The corresponding spectral resolutions are approximately 1.23 and 1.16 Å in the blue and red channels, respectively, yielding resolving powers of $R \approx 3400$ – 6200 across the spectra.

We completed a new reduction of the data using the latest calibrations following standard techniques in IRAF[2] (Tody 1986). This consisted of bias subtraction, image trimming, bad pixel replacement, flat fielding, Laplacian edge cosmic ray removal (van Dokkum 2001), and image combining. Wavelength calibration was completed using comparison lamp images taken immediately before the science exposures, and flux calibration with the airmass at mid exposure using the standard stars Feige 110 and BD+28 (Oke 1990). The DIS dispersion and spatial directions are not precisely perpendicular, so we fit a line to the underlying galaxy continuum and resampled the data to a new grid to ensure that measurements of different emission lines from the same pixel row sample the same spatial location. We extracted spectra over single pixel spatial intervals to probe large-scale NLR gradients.

[2]IRAF is distributed by the National Optical Astronomy Observatories, which are operated by the Association of Universities for Research in Astronomy, Inc., under cooperative agreement with the National Science Foundation.

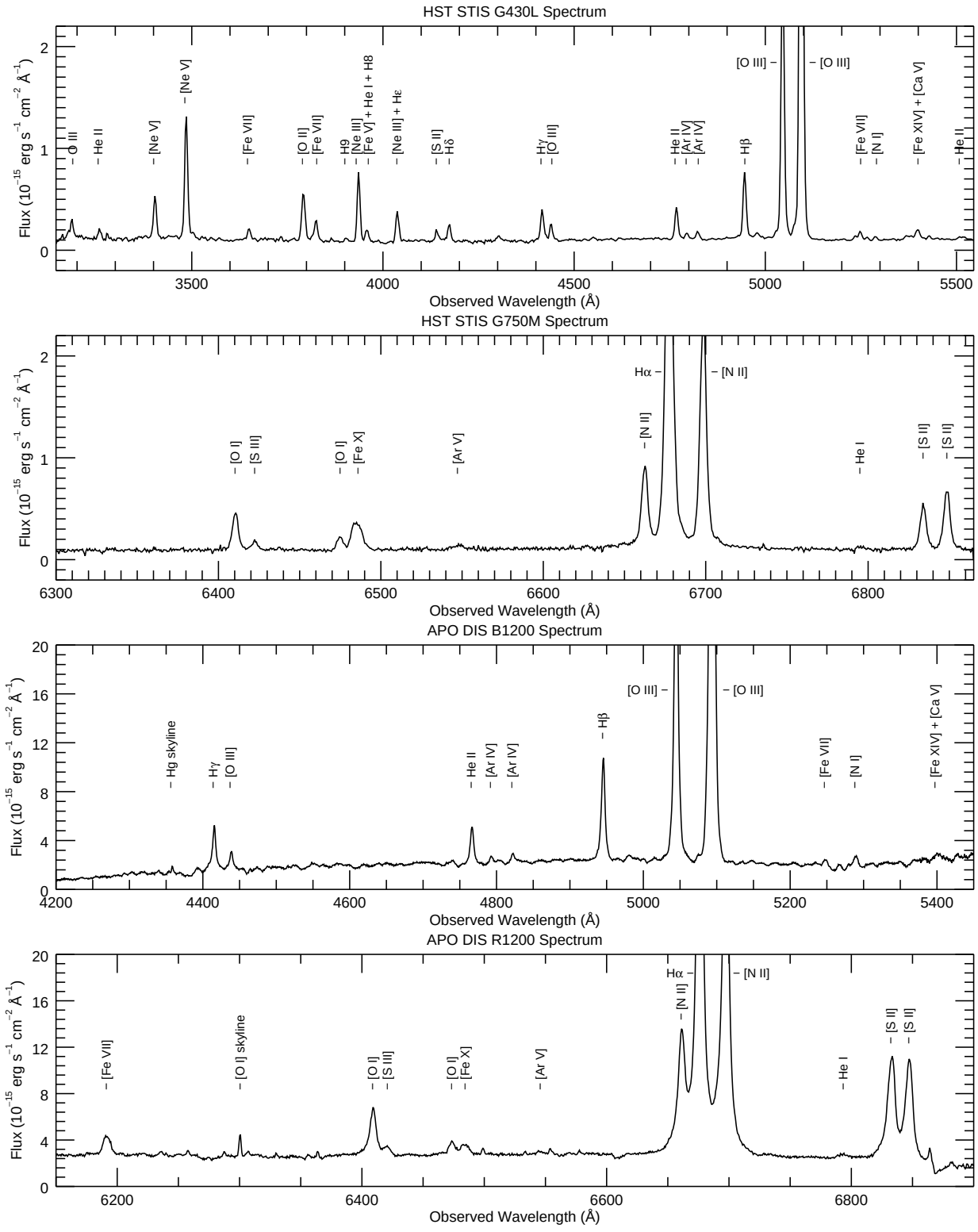

Figure 2.2 Spectral traces of the nucleus spatially summed over 0.″2 and 2.″0 for the STIS and DIS data, respectively. From top to bottom are *HST* STIS G430L, *HST* STIS G750M, APO DIS B1200, and APO DIS R1200 spectra. The spectra are shown at observed wavelengths, and emission line ratios relative to Hβ are given in Table 2.1.

2.3 Analysis

2.3.1 Gaussian Template Fitting

We identified emission lines in the spectra using previous studies and photoionization model predictions. Care was taken to measure weak lines that serve as temperature or density diagnostics to constrain the physical conditions in the NLR gas. We fit all emission lines with S/N > 2, and tentatively identified lines that fell below this threshold at all positions, including He I+Fe II λ4923, [Fe VII] λ5158, [Fe VI] λ5176, [N I] λ5199, [Fe XIV] λ5303, [Ca V] λ5310, and [Ar X] λ5536 (Storchi-Bergmann et al. 1996).

Photoionization modeling requires accurate emission line flux ratios for comparison. To accomplish this we fit gaussian profiles to all emission lines at each spatial extraction using a template method that calculates the centroids and widths of all lines based on the best fit to the strong, velocity resolved Hα emission line. We found that Hα produced more accurate centroid predictions than the stronger [O III] emission line due to the higher spectral resolution of the G750M data, and we corrected the line widths to maintain the same intrinsic velocity width as the template and account for the different line-spread functions of the gratings. The height was free to vary to encompass the total line flux, with errors calculated from the residuals between the data and fits.

This method has the flexibility to fit multiple kinematic components and heavily blended lines; however, information is lost about intrinsic differences in the radial velocity and full width at half maximum (FWHM) of individual lines. While studies have shown that the radial velocity or FWHM can correlate with the critical density or ionization potential of an emission line (Whittle 1985; De Robertis & Osterbrock 1986; Kraemer & Crenshaw 2000b; Rodríguez-Ardila et al. 2006), our goal was to obtain accurate emission line fluxes. We conducted tests and found the integrated fluxes from free versus template fitting methods differed by $\sim 2 - 8\%$, and that the template method produced more accurate fits to weak emission lines in noisy regions. A single exception is the [Fe X] λ6375 line that is blue shifted

relative to all other lines, as noted by Kraemer et al. (2009) and Schlesinger et al. (2009). In this case the fluxes agree to within 15%.

2.3.2 Ionized Gas Kinematics

Calculating mass outflow rates requires knowing the NLR mass and its radial velocity at each location. The kinematics of Mrk 573 have been studied extensively, exhibiting a linearly increasing velocity profile with distance from the nucleus, followed by a turnover and linear decrease (Tsvetanov & Walsh 1992; Afanasiev et al. 1996; Schlesinger et al. 2009; Fischer et al. 2010, 2017).

To determine accurate outflow velocity laws, we fit a series of linear functions to single row extractions of the [O III] emission line velocity centroids. We used these fits to derive the observed velocity of the gas at each projected radial distance, as shown in Figure 2.3. The outflow terminates at $\sim 1\farcs7$ (600 pc), beyond which galactic rotation dominates (Fischer et al. 2017). The spectra display a single kinematic component at all locations, except for a weak secondary line at $+0\farcs25$ that was not fit.

From our results presented in Fischer et al. (2017) we adopt a host disk inclination of $i = 38^\circ$ with the northeast (NE) side of the disk closest to us, a revision from our earlier model (Fischer et al. 2010), and in agreement with previous findings (Pogge & De Robertis 1995). We assume the NLR gas is approximately coplanar with the stellar disk (Keel 1980; Afanasiev et al. 1996; Xanthopoulos 1996; Afanasiev et al. 1998; Schmitt & Kinney 2000) and is flowing radially along the disk (Fischer et al. 2017). The PAs of the inner disk and NLR are approximately 97° and 128°, respectively. This yields an offset of $\varphi = 31^\circ$ between the disk and NLR major axes. While the *HST* spectral slit is not exactly parallel to the NLR major axis, all material out to $\sim 0\farcs6$ can travel along the NLR major axis and remain within the spectral slit, so we adopt this angle ($\varphi = 31^\circ$) for deprojecting the velocities. With this model of radial outflow, the observed Doppler velocities were deprojected to their intrinsic

values via

$$V_{\rm int}(i,\varphi) = \left(\frac{V_{\rm obs}}{sin(i)sin(\varphi)}\right), \tag{2.1}$$

where $V_{\rm int}$ and $V_{\rm obs}$ are the intrinsic and observed velocities for an inclination i and phase angle φ from the major axis. This is similar to the expression for rotational velocities, with the final term sine instead of cosine. The true distance from the SMBH is calculated from the observed distance and inverting the equation for distance from the center of an ellipse,[3]

$$R_{\rm int}(i,\varphi) = \sqrt{R_{\rm obs}^2\left(cos^2(\varphi) + \frac{sin^2(\varphi)}{cos^2(i)}\right)}, \tag{2.2}$$

where $R_{\rm int}$ and $R_{\rm obs}$ are the intrinsic and observed distances for an inclination i and phase angle φ from the major axis. We adopt the convention that $i = 0°$ is face on and $i = 90°$ is edge on. The phase angle φ is defined such that $\varphi = 0°$ is along the major axis and $\varphi = 90°$ is along the minor axis.

With our adopted angles ($i = 38°$, $\varphi = 31°$) the intrinsic velocities are ~ 3.15 times larger than the observed values. Thus the peak observed outflow velocity of ~ 350 km s^{-1} corresponds to an intrinsic velocity of 1100 km s^{-1}, typical of Seyferts (Fischer et al. 2013, 2014).

2.3.3 Emission Line Ratios

We used the integrated line fluxes to calculate emission line ratios relative to the standard hydrogen Balmer (Hβ) emission line at each position along the NLR (Table 2.1). Near the nucleus, lines with a wide range of ionization potentials (IPs) are seen, from neutral [O I] to [Fe X] with an IP of 234 eV. The number and fluxes of detectable lines decreases steadily with increasing distance from the nucleus until the bright arcs of emission are encountered at $\sim 1\farcs8$. Fits were made to all visible emission lines across the NLR, but only emission within

[3]Our terminology assumes that the distances from the central SMBH and the "nucleus", as defined by the peak [O III] emission, are the same; however, there is evidence that AGN nuclei and their SMBHs can be offset by tens of pc (Kraemer et al. 2010; Comerford et al. 2017).

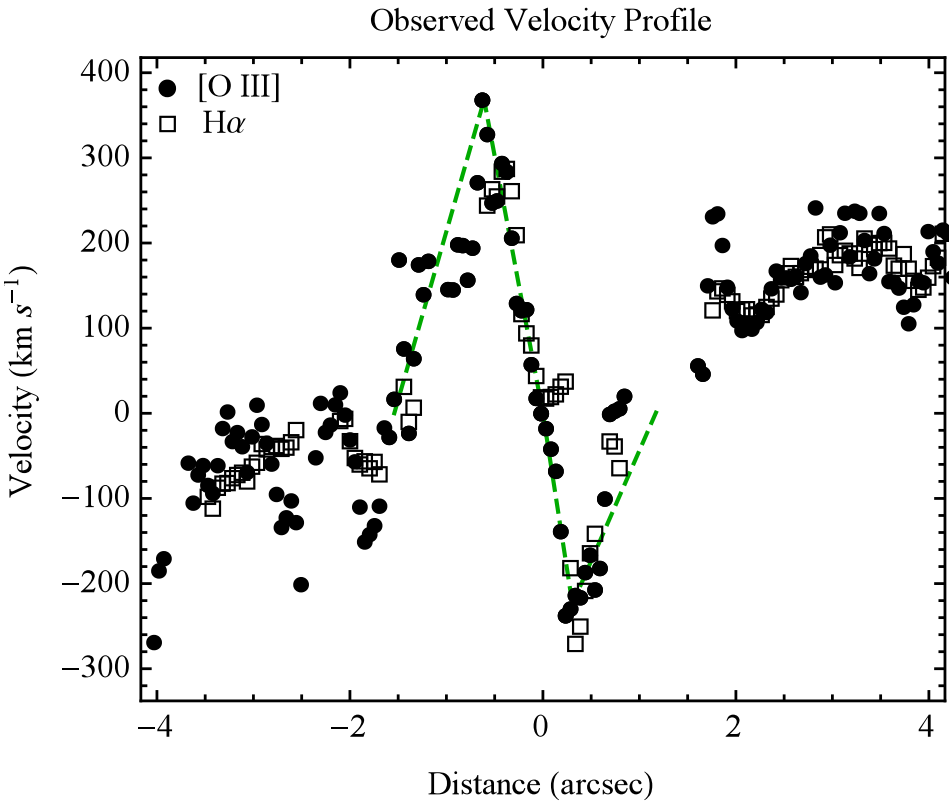

Figure 2.3 Observed *HST* STIS [O III] and Hα kinematics shown with filled circles and empty squares, respectively. The best fit linear velocity laws are shown as dashed green lines. The maximum velocity centroid uncertainties are $\sim$ 50 and 21 km s^{-1} for the [O III] and Hα kinematics, respectively (Fischer et al. 2013). SE is to the left and NW is to the right.

$\sim 1\farcs7$ of the nucleus displays kinematic signatures of outflow and are included in our tables and models presented here. All measurements are available by request to M.R.

Before interpreting the line ratios, we applied a reddening correction using a standard Galactic reddening curve (Savage & Mathis 1979) and color excesses calculated from the observed Hα/Hβ ratios, assuming an intrinsic recombination value of 2.90 (Osterbrock & Ferland 2006). The extinction was calculated from

$$E(B-V) \equiv \frac{A_\lambda}{R_\lambda} = -\frac{2.5log\left(\frac{F_o}{F_i}\right)}{R_\lambda} = \frac{2.5log\left(\frac{(\mathrm{H}\alpha/\mathrm{H}\beta)_i}{(\mathrm{H}\alpha/\mathrm{H}\beta)_o}\right)}{R_{\mathrm{H}\alpha} - R_{\mathrm{H}\beta}}, \tag{2.3}$$

where $E(B-V)$ is the color excess, A_λ is the extinction in magnitudes, R_λ is the reddening value at a particular wavelength, and F_o and F_i are the observed and intrinsic fluxes,

respectively. The flux ratios can be expanded to the intrinsic and observed Hα/Hβ ratios, and the Galactic reddening values are $R_{\rm H\alpha} \approx 2.497$ and $R_{\rm H\beta} \approx 3.687$. Corrected line ratios relative to Hβ are then given by

$$H_{int} = H_{obs} \cdot 10^{[0.4 \cdot E(B-V) \cdot (R_j - R_{\rm H\beta})]}, \tag{2.4}$$

where $H_{\rm int}$ and $H_{\rm obs}$ are the intrinsic and observed emission line ratios and R_j is the reddening value at the wavelength of the emission line being corrected. Uncertainties were propagated from the Hα and Hβ fit errors.

Several extractions had Hα/H$\beta \leq 2.90$ within errors, and for these locations we assumed no reddening. At two locations, 0.″15 and 0.″25 NW of the nucleus, this procedure derived large extinctions, and the resulting corrected line ratios were unphysically large in the blue portion of the spectrum. Our investigations concluded that residual sub-pixel offset in the spatial direction between the G430L and G750M spectra, combined with an extremely steep flux gradient at those locations, was the most plausible explanation. Another possibility is preferential absorption of Hβ, which can be enhanced by a young-intermediate age ($10 - 100$ Myr) stellar population. Stellar population modeling of Mrk 573 is consistent with an old nuclear stellar population (Alonso-Herrero et al. 1998; González Delgado et al. 2001; Raimann et al. 2003; Ramos Almeida et al. 2009a), although some studies have found evidence of recent star formation within the inner few hundred pc (Riffel et al. 2006, 2007; Diniz et al. 2017).

To quantify any absorption, we measured the equivalent width (EW) of Hβ by comparing the integrated line flux to the surrounding continuum level. For most nuclear extractions ($r < 0.''5$) we measured EWs > 30 Å. For positions $+0.''15$ through $+0.''46$ we found EWs $\approx 6-12$ Å, indicating possible absorption at the $\leq 10\%$ level. These studies and measurements, together with a lack of visible absorption in the higher order Balmer lines, suggests that stellar absorption is a minor secondary affect.

Table 2.1. Observed *HST* STIS Emission Line Ratios

Emission Line	+0.″46	+0.″36	+0.″25	+0.″15	+0.″05	–0.″05	–0.″15	–0.″25	–0.″36	–0.″46
O III λ3133	... ± ...	... ± ...	... ± ...	... ± ...	0.25 ± 0.06	0.25 ± 0.03	0.28 ± 0.02	0.20 ± 0.05	... ± ...	... ± ...
He II λ3203	... ± ...	... ± ...	... ± ...	... ± ...	0.12 ± 0.02	0.15 ± 0.02	0.22 ± 0.03	0.10 ± 0.05	... ± ...	... ± ...
[Ne V] λ3346	... ± ...	... ± ...	... ± ...	... ± ...	0.65 ± 0.05	0.64 ± 0.04	0.81 ± 0.05	0.40 ± 0.05	... ± ...	... ± ...
[Ne V] λ3426	1.92 ± 0.30	2.44 ± 0.78	... ± ...	1.78 ± 0.47	1.88 ± 0.15	1.79 ± 0.12	1.96 ± 0.19	1.22 ± 0.08	0.87 ± 0.07	... ± ...
[Fe VII] λ3586	... ± ...	... ± ...	... ± ...	... ± ...	0.16 ± 0.02	0.17 ± 0.03	0.15 ± 0.02	... ± ...	... ± ...	... ± ...
[O II] λ3727	1.75 ± 0.28	1.55 ± 0.20	2.24 ± 1.01	1.67 ± 0.28	0.86 ± 0.05	0.68 ± 0.06	0.87 ± 0.04	1.11 ± 0.07	1.53 ± 0.10	1.85 ± 0.36
[Fe VII] λ3759	... ± ...	... ± ...	... ± ...	0.33 ± 0.05	0.36 ± 0.03	0.28 ± 0.02	0.18 ± 0.01	0.06 ± 0.02	... ± ...	... ± ...
[Ne III] λ3869	1.44 ± 0.30	0.90 ± 0.20	... ± ...	1.26 ± 0.17	1.09 ± 0.10	0.85 ± 0.06	1.06 ± 0.10	1.02 ± 0.07	0.94 ± 0.06	1.50 ± 0.18
He I λ3889[a]	... ± ...	... ± ...	... ± ...	0.24 ± 0.07	0.22 ± 0.02	0.16 ± 0.02	0.18 ± 0.02	0.10 ± 0.01	0.24 ± 0.03	... ± ...
[Ne III] λ3969[b]	... ± ...	... ± ...	... ± ...	0.35 ± 0.07	0.52 ± 0.04	0.37 ± 0.03	0.44 ± 0.06	0.38 ± 0.04	0.43 ± 0.07	... ± ...
[S II] λ4074	... ± ...	... ± ...	... ± ...	... ± ...	0.18 ± 0.05	0.10 ± 0.02	0.08 ± 0.03	... ± ...	... ± ...	... ± ...
Hδ λ4102	... ± ...	... ± ...	... ± ...	... ± ...	0.26 ± 0.03	0.25 ± 0.02	0.25 ± 0.02	0.22 ± 0.03	... ± ...	... ± ...
Hγ λ4340	... ± ...	... ± ...	0.40 ± 0.30	0.59 ± 0.11	0.52 ± 0.03	0.45 ± 0.03	0.48 ± 0.05	0.42 ± 0.03	0.42 ± 0.05	0.64 ± 0.09
[O III] λ4363	... ± ...	... ± ...	... ± ...	0.28 ± 0.08	0.27 ± 0.02	0.22 ± 0.02	0.22 ± 0.03	0.19 ± 0.03	... ± ...	... ± ...
He II λ4686	... ± ...	... ± ...	... ± ...	0.39 ± 0.07	0.46 ± 0.03	0.50 ± 0.03	0.51 ± 0.04	0.46 ± 0.03	0.40 ± 0.03	... ± ...
[Ar IV] λ4711	... ± ...	... ± ...	... ± ...	... ± ...	0.07 ± 0.01	0.11 ± 0.01	0.12 ± 0.02	0.10 ± 0.01	... ± ...	... ± ...
[Ar IV] λ4740	... ± ...	... ± ...	... ± ...	... ± ...	0.12 ± 0.01	0.11 ± 0.01	0.12 ± 0.02	0.07 ± 0.01	... ± ...	... ± ...
Hβ λ4861	1.00 ± 0.13	1.00 ± 0.11	1.00 ± 0.38	1.00 ± 0.13	1.00 ± 0.05	1.00 ± 0.05	1.00 ± 0.04	1.00 ± 0.05	1.00 ± 0.04	1.00 ± 0.08
[O III] λ4959	5.25 ± 0.69	4.00 ± 0.52	5.09 ± 2.10	4.87 ± 0.73	4.45 ± 0.27	4.40 ± 0.28	4.72 ± 0.29	4.52 ± 0.38	4.53 ± 0.22	5.36 ± 0.59
[O III] λ5007	15.55 ± 2.01	11.44 ± 1.58	13.05 ± 5.58	14.06 ± 2.14	13.49 ± 0.81	13.53 ± 0.86	13.93 ± 0.79	13.53 ± 1.11	13.17 ± 0.65	16.07 ± 1.58
[O I] λ6300	... ± ...	... ± ...	... ± ...	1.48 ± 0.21	0.38 ± 0.02	0.17 ± 0.01	0.18 ± 0.01	... ± ...	... ± ...	... ± ...
[S III] λ6312	... ± ...	... ± ...	... ± ...	0.15 ± 0.03	0.08 ± 0.01	0.05 ± 0.01	0.06 ± 0.01	... ± ...	... ± ...	... ± ...
[O I] λ6363	... ± ...	... ± ...	... ± ...	0.47 ± 0.07	0.14 ± 0.01	0.07 ± 0.00	0.05 ± 0.00	... ± ...	... ± ...	... ± ...
[Fe X] λ6375	... ± ...	... ± ...	... ± ...	1.20 ± 0.17	0.39 ± 0.03	0.16 ± 0.01	0.06 ± 0.00	... ± ...	... ± ...	... ± ...
[N II] λ6548	1.31 ± 0.20	0.57 ± 0.09	2.16 ± 0.84	3.22 ± 0.42	0.91 ± 0.05	0.42 ± 0.02	0.47 ± 0.02	0.57 ± 0.05	0.63 ± 0.05	0.21 ± 0.17
Hα λ6563	5.69 ± 0.75	2.85 ± 0.31	7.09 ± 2.70	13.70 ± 1.81	4.51 ± 0.23	2.53 ± 0.14	2.69 ± 0.14	2.32 ± 0.15	2.26 ± 0.12	2.57 ± 0.21
[N II] λ6584	3.79 ± 0.49	2.35 ± 0.26	5.06 ± 1.94	8.71 ± 1.17	2.35 ± 0.15	1.25 ± 0.08	1.27 ± 0.06	1.49 ± 0.11	1.56 ± 0.11	1.71 ± 0.15
[S II] λ6716	... ± ...	... ± ...	1.25 ± 0.50	1.70 ± 0.24	0.45 ± 0.03	0.22 ± 0.01	0.27 ± 0.02	0.33 ± 0.03	0.49 ± 0.03	0.53 ± 0.06
[S II] λ6731	... ± ...	... ± ...	1.21 ± 0.48	2.18 ± 0.30	0.59 ± 0.04	0.32 ± 0.02	0.35 ± 0.02	0.40 ± 0.04	0.59 ± 0.05	0.53 ± 0.12
F(Hβ) $\times 10^{-15}$	0.119±0.015	0.234±0.025	0.113±0.043	0.447±0.058	3.172±0.152	3.350±0.166	2.101±0.078	1.205±0.062	0.534±0.020	0.154±0.012

Note. — Observed emission line ratios relative to Hβ at each spatial distance from the nucleus in arcseconds, with positive numbers corresponding to the NW direction and negative to the SE. Emission lines were fit using widths and centroids calculated from fits to Hα and error bars are the quadrature sum of the fractional flux uncertainty in Hβ and each respective line. Rows marked with "... ± ..." represent nondetections. Wavelengths are approximate vacuum values used as markers in Cloudy. [a] blend of He I 3889 + [Fe V] 3892 + H8. [b] blend of [Ne III] 3968 + Hϵ 3970.

Table 2.2. Reddening-Corrected *HST* STIS Emission Line Ratios

Emission Line	+0.″46	+0.″36	+0.″25†	+0.″15†	+0.″05	−0.″05	−0.″15	−0.″25	−0.″36	−0.″46
O III λ3133	... ± ...	... ± ...	... ± ...	... ± ...	0.46 ± 0.07	0.25 ± 0.06	0.28 ± 0.04	0.20 ± 0.08	... ± ...	... ± ...
He II λ3203	... ± ...	... ± ...	... ± ...	... ± ...	0.21 ± 0.02	0.15 ± 0.03	0.22 ± 0.04	0.10 ± 0.06	... ± ...	... ± ...
[Ne V] λ3346	... ± ...	... ± ...	... ± ...	... ± ...	1.07 ± 0.08	0.64 ± 0.11	0.81 ± 0.09	0.40 ± 0.11	... ± ...	... ± ...
[Ne V] λ3426	3.93 ± 0.63	2.44 ± 0.83	... ± ...	4.96 ± 1.00	3.01 ± 0.22	1.79 ± 0.29	1.96 ± 0.25	1.22 ± 0.31	0.87 ± 0.24	... ± ...
[Fe VII] λ3586	... ± ...	... ± ...	... ± ...	... ± ...	0.24 ± 0.02	0.17 ± 0.04	0.15 ± 0.02	... ± ...	... ± ...	... ± ...
[O II] λ3727	2.97 ± 0.42	1.55 ± 0.24	4.09 ± 3.20	3.55 ± 0.54	1.21 ± 0.07	0.68 ± 0.09	0.87 ± 0.07	1.11 ± 0.21	1.53 ± 0.32	1.85 ± 0.40
[Fe VII] λ3759	... ± ...	... ± ...	... ± ...	0.69 ± 0.10	0.50 ± 0.04	0.28 ± 0.04	0.18 ± 0.01	0.06 ± 0.02	... ± ...	... ± ...
[Ne III] λ3869	2.28 ± 0.36	0.90 ± 0.21	... ± ...	2.44 ± 0.33	1.47 ± 0.11	0.85 ± 0.10	1.06 ± 0.11	1.02 ± 0.17	0.94 ± 0.17	1.50 ± 0.22
He I λ3889[a]	... ± ...	... ± ...	... ± ...	0.46 ± 0.09	0.30 ± 0.02	0.16 ± 0.02	0.18 ± 0.02	0.10 ± 0.02	0.24 ± 0.05	... ± ...
[Ne III] λ3969[b]	... ± ...	... ± ...	... ± ...	0.64 ± 0.10	0.68 ± 0.05	0.37 ± 0.04	0.44 ± 0.06	0.38 ± 0.07	0.43 ± 0.10	... ± ...
[S II] λ4074	... ± ...	... ± ...	... ± ...	... ± ...	0.23 ± 0.05	0.10 ± 0.02	0.08 ± 0.03	... ± ...	... ± ...	... ± ...
Hδ λ4102	... ± ...	... ± ...	... ± ...	... ± ...	0.33 ± 0.03	0.25 ± 0.03	0.25 ± 0.02	0.22 ± 0.04	... ± ...	... ± ...
Hγ λ4340	... ± ...	... ± ...	0.54 ± 0.36	0.86 ± 0.12	0.62 ± 0.03	0.45 ± 0.04	0.48 ± 0.05	0.42 ± 0.05	0.42 ± 0.07	0.64 ± 0.10
[O III] λ4363	... ± ...	... ± ...	... ± ...	0.40 ± 0.08	0.32 ± 0.02	0.22 ± 0.02	0.22 ± 0.03	0.19 ± 0.03	... ± ...	... ± ...
He II λ4686	... ± ...	... ± ...	... ± ...	0.44 ± 0.07	0.49 ± 0.03	0.50 ± 0.03	0.51 ± 0.04	0.46 ± 0.03	0.40 ± 0.03	... ± ...
[Ar IV] λ4711	... ± ...	... ± ...	... ± ...	... ± ...	0.07 ± 0.01	0.11 ± 0.01	0.12 ± 0.02	0.10 ± 0.01	... ± ...	... ± ...
[Ar IV] λ4740	... ± ...	... ± ...	... ± ...	... ± ...	0.12 ± 0.01	0.11 ± 0.01	0.12 ± 0.02	0.07 ± 0.01	... ± ...	... ± ...
Hβ λ4861	1.00 ± 0.13	1.00 ± 0.11	1.00 ± 0.38	1.00 ± 0.13	1.00 ± 0.05	1.00 ± 0.05	1.00 ± 0.04	1.00 ± 0.05	1.00 ± 0.04	1.00 ± 0.08
[O III] λ4959	5.02 ± 0.69	4.00 ± 0.52	4.84 ± 2.12	4.57 ± 0.73	4.32 ± 0.27	4.40 ± 0.28	4.72 ± 0.29	4.52 ± 0.39	4.53 ± 0.23	5.36 ± 0.59
[O III] λ5007	14.53 ± 2.02	11.44 ± 1.59	11.93 ± 5.60	12.02 ± 2.15	12.90 ± 0.81	13.53 ± 0.88	13.93 ± 0.80	13.53 ± 1.15	13.17 ± 0.73	16.07 ± 1.59
[O I] λ6300	... ± ...	... ± ...	... ± ...	0.38 ± 0.21	0.26 ± 0.02	0.17 ± 0.02	0.18 ± 0.02	... ± ...	... ± ...	... ± ...
[S III] λ6312	... ± ...	... ± ...	... ± ...	0.04 ± 0.03	0.05 ± 0.01	0.05 ± 0.01	0.06 ± 0.01	... ± ...	... ± ...	... ± ...
[O I] λ6363	... ± ...	... ± ...	... ± ...	0.12 ± 0.07	0.09 ± 0.01	0.07 ± 0.01	0.05 ± 0.00	... ± ...	... ± ...	... ± ...
[Fe X] λ6375	... ± ...	... ± ...	... ± ...	0.29 ± 0.17	0.26 ± 0.03	0.16 ± 0.02	0.06 ± 0.00	... ± ...	... ± ...	... ± ...
[N II] λ6548	0.67 ± 0.22	0.57 ± 0.11	0.89 ± 0.92	0.69 ± 0.43	0.59 ± 0.06	0.42 ± 0.06	0.47 ± 0.04	0.57 ± 0.14	0.63 ± 0.17	... ± ...
Hα λ6563	2.90 ± 0.84	2.85 ± 0.44	2.91 ± 2.95	2.91 ± 1.85	2.90 ± 0.27	2.53 ± 0.38	2.69 ± 0.25	2.32 ± 0.55	2.26 ± 0.58	2.57 ± 0.38
[N II] λ6584	1.92 ± 0.55	2.35 ± 0.37	2.06 ± 2.12	1.82 ± 1.20	1.51 ± 0.17	1.25 ± 0.19	1.27 ± 0.11	1.49 ± 0.36	1.56 ± 0.41	1.71 ± 0.26
[S II] λ6716	... ± ...	... ± ...	0.48 ± 0.54	0.33 ± 0.24	0.28 ± 0.03	0.22 ± 0.03	0.27 ± 0.03	0.33 ± 0.09	0.49 ± 0.14	0.53 ± 0.09
[S II] λ6731	... ± ...	... ± ...	0.47 ± 0.52	0.41 ± 0.31	0.37 ± 0.04	0.32 ± 0.05	0.35 ± 0.03	0.40 ± 0.11	0.59 ± 0.17	0.53 ± 0.14
E(B-V)	0.61 ± 0.12	0.00 ± 0.10	0.70 ± 0.80	0.88 ± 0.15	0.40 ± 0.05	0.00 ± 0.13	0.00 ± 0.07	0.00 ± 0.21	0.00 ± 0.23	0.00 ± 0.11

Note. — Same as in Table 2.1 with line ratios corrected for galactic extinction using a Galactic reddening curve (Savage & Mathis 1979). The Hα/Hβ ratios were fixed at 2.90 and negative E(B-V) values were set to zero. Error bars are the quadrature sum of the fractional flux uncertainty in Hβ and each respective line along with the reddening uncertainty. "†" indicates a row with secondary correction to the reddening (§2.3.3); original values for +0.″15 and +0.″25 were E(B-V) = 1.42 ± 0.12 and 0.82 ± 0.37, respectively.

For positions +0.″15 and +0.″25 we used the Hα/Hγ ratios to calculate the extinction values for the blue spectrum to obtain more physically realistic line ratios to compare with our models. The shortest wavelength lines such as [O II] and [Ne V] at these two positions retain a minor residual over correction.

2.3.4 Emission Line Diagnostics

The dereddened line ratios allow us to limit our photoionization model parameter ranges by constraining the abundances, ionization, temperature, and density of the gas at each location. We ultimately used these diagnostics to extrapolate a density law to larger distances where there are not sufficient emission lines to create detailed photoionization models.

2.3.4.1 Ionization

To properly model the NLR, we confirmed that our *HST* and APO spectra, which have vastly different spatial resolutions and slit widths, both sample completely AGN ionized gas using Baldwin–Phillips–Terlevich (BPT) diagrams shown in Figure 2.4 (Baldwin et al. 1981; Veilleux & Osterbrock 1987). These diagrams exploit ratios of emission lines with small wavelength separations to avoid the effects of extinction. Specifically, the diagrams use the ratio of [O III] λ5007/Hβ λ4861 compared to [N II] λ6584, [S II] $\lambda\lambda$6716, 6731, and [O I] λ6300, relative to Hα λ6563.

These tests indicate that all of the NLR gas participating in the outflow is ionized by the central AGN, in agreement with previous findings (Unger et al. 1987; Kraemer et al. 2009; Schlesinger et al. 2009; Fischer et al. 2017). All of the line ratios fall in the AGN/Seyfert regions of the diagrams using the explored separation criteria (Kewley et al. 2001, 2006; Kauffmann et al. 2003, see also Stasińska et al. 2006; Schawinski et al. 2007; Kewley et al. 2013a,b; Meléndez et al. 2014; Bär et al. 2017). [S II] arises from low ionization gas, and we interpret the points near the AGN/LINER border as emission from gas that is subject to a partially absorbed, or "filtered", ionizing spectrum, as discussed in §2.5.1.

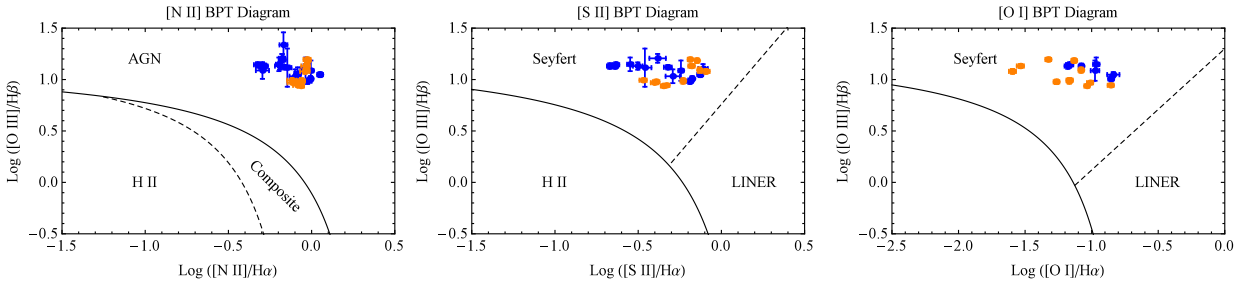

Figure 2.4 BPT ionization diagrams for [N II], [S II], and [O I] for all measurements within 2″ of the nucleus. *HST* STIS and APO DIS points are in blue and orange circles, respectively. Further extended emission also shows AGN ionization (Fischer et al. 2017). The demarcation lines for distinguishing ionization mechanisms are from Kewley et al. (2001, 2006); Kauffmann et al. (2003).

In addition, He II λ4686/Hβ λ4861 is useful for constraining the column density of the gas (N_H cm^{-2}). As radiation propagates through the NLR gas, both emission lines strengthen until He II ionizing photons ($E > 54.4$ eV) are exhausted. As a result, He II/Hβ is ~ 1 in optically thin (matter-bounded) gas and reduces to ~ 0.2 in optically thick (radiation-bounded) gas, with the exact values dependent on the SED. Intermediate values indicate a mixture of these cases and are representative of our ratios in Table 2.2.[4]

2.3.4.2 Abundances

Elemental abundances play an important role in determining the heating and cooling balance within the gas and are determined by the true abundances and the fraction of each element trapped in dust grains. NLR abundances are typically solar or greater, but are observed to vary between objects over the range $Z \approx 0.6 - 1.8\ Z_\odot$ (Storchi-Bergmann et al. 1998b; Hamann & Ferland 1999; Nagao et al. 2006; Dors et al. 2014, 2015; Castro et al. 2017).

We determined the abundances of elements across the NLR of Mrk 573 by first finding the abundance of oxygen and then scaling other elements by that factor. We adopt solar abundances ($Z_\odot$) from Asplund et al. (2009), which lists oxygen as log(O/H)+12 = 8.69.

[4]Note that there is a minor error in the y-intercept of the diagonal Seyfert/LINER line on the [S II] diagram in Figure 4 of the published paper. The displayed intercept is 1.30, and the correct value is 0.76. This does not affect the results or interpretation, and has been corrected in the above figure.

For Mrk 573 we determined the oxygen abundance using equations 2 and 4 from Storchi-Bergmann et al. (1998b) and Castro et al. (2017), respectively, which compare the ratios of strong emission lines in the spectra. These yield a mean oxygen abundance of log(O/H)+12 = 8.78, or $Z = 1.29 \pm 0.26\ Z_{\odot}$. The distributions are shown in Figure 2.5, with errors propagated from the individual uncertainties in the equations. This result neglects a minor density-dependent correction that would decrease points near the nucleus and increase outer points by ≤ 0.04 dex.

This abundance is in excellent agreement with the global NLR value found by Dors et al. (2015) and Castro et al. (2017) for Mrk 573. Other relationships in Storchi-Bergmann et al. (1998b) and Dors et al. (2015) yielded higher and lower abundances, respectively, and were not included due to their sensitivities to the ionizing spectrum and temperature, as discussed in those papers.

From this result we adopted a NLR metallicity of $Z \approx 1.3\ Z_{\odot}$ for all elements, with nitrogen scaled by Z^2 as it is enhanced by secondary nucleosynthesis processes (Hamann et al. 2002; Nagao et al. 2006).

2.3.4.3 Temperature

Density sensitive line ratios that are useful for determining masses also exhibit a weak temperature dependence that must be accounted for to derive accurate densities (Osterbrock & Ferland 2006; Draine 2011). The strongest indicator of the electron density (n_e cm^{-3}) in our data is the [S II] $\lambda\lambda$6716/6731 ratio. We employed the available temperature dependent ratio of [O III] $\lambda\lambda$4363/5007 that may come from hotter gas and scaled it to derive a temperature of the [S II] gas (Wilson et al. 1997). The measured [O III] ratios and photoionization model predictions are shown in Figure 2.6.

The temperature sensitive [O III] line ratio only changes appreciably due to density affects for $n_e > 10^4$ cm^{-3} as [O III] λ5007 begins to be collisionally suppressed. For the APO DIS data the observed [S II] $\lambda\lambda$6716/6731 ratios do not drop below 0.5, indicating $n_e < 10^4$ cm^{-3}

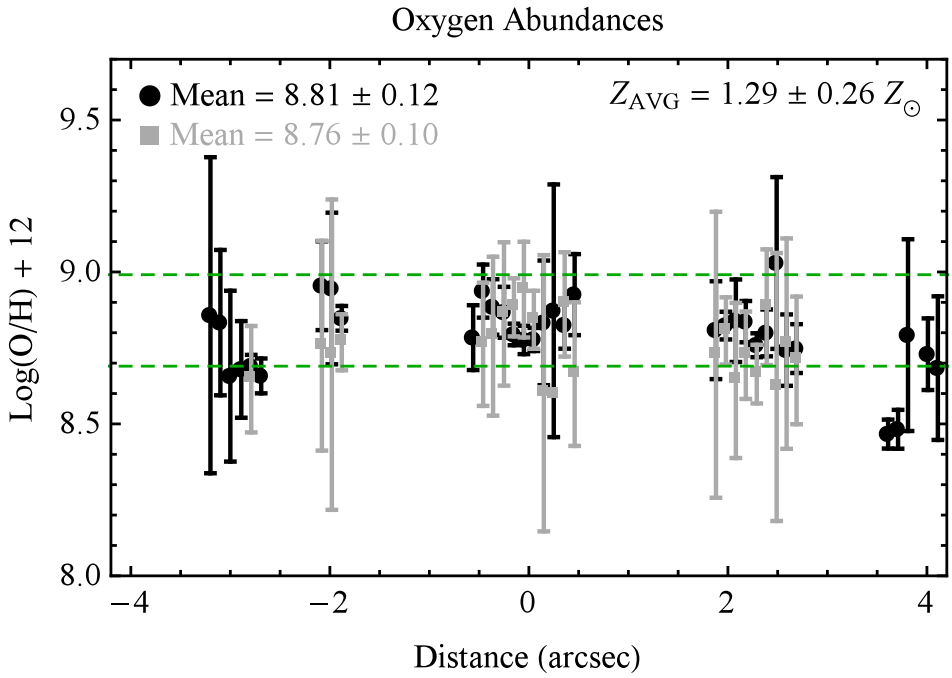

Figure 2.5 Oxygen abundance as a function of distance from the nucleus using the methods of Storchi-Bergmann et al. (1998b) and Castro et al. (2017) in black circles and gray squares, respectively, for the *HST* STIS data. The lower and upper dotted green lines represent one and two times solar abundance values, respectively. SE is to the left and NW is to the right.

over any range of temperatures typically seen in NLRs, so we derived temperatures from [O III] in the low density limit.

We calculated Cloudy (Ferland et al. 2013) photoionization models over a wide range of parameters and found the mean [S II] temperature to be $\sim 0.18 - 0.25$ dex cooler than the mean [O III] emitting gas. We adopted the upper end of this range for scaling because the [S II] emissivity peaks deeper within a cloud as the gas begins to become neutral. The uncertainty in this scaling from model to model variation is ~ 0.1 dex.

Using this scaling procedure we determined the mean temperature of $T_{[O\ III]} = 13,500 \pm 650$ K for our APO data (corresponding to an Hγ reddening-corrected flux ratio of $\lambda4363/\lambda5007 = 0.0175 \pm 0.0017$) and $T_{[O\ III]} = 13,450 \pm 750$ K for the *HST* data. These values are in excellent agreement with previous studies (Tsvetanov & Walsh 1992; Spinoglio et al. 2000; Schlesinger et al. 2009). Adopting $T_{[S\ II]} = T_{[O\ III]} - 0.25$ dex we find $T_{[S\ II]} = 7590 \pm 375$ K, with uncertainties calculated from the variation in the derived temperatures.

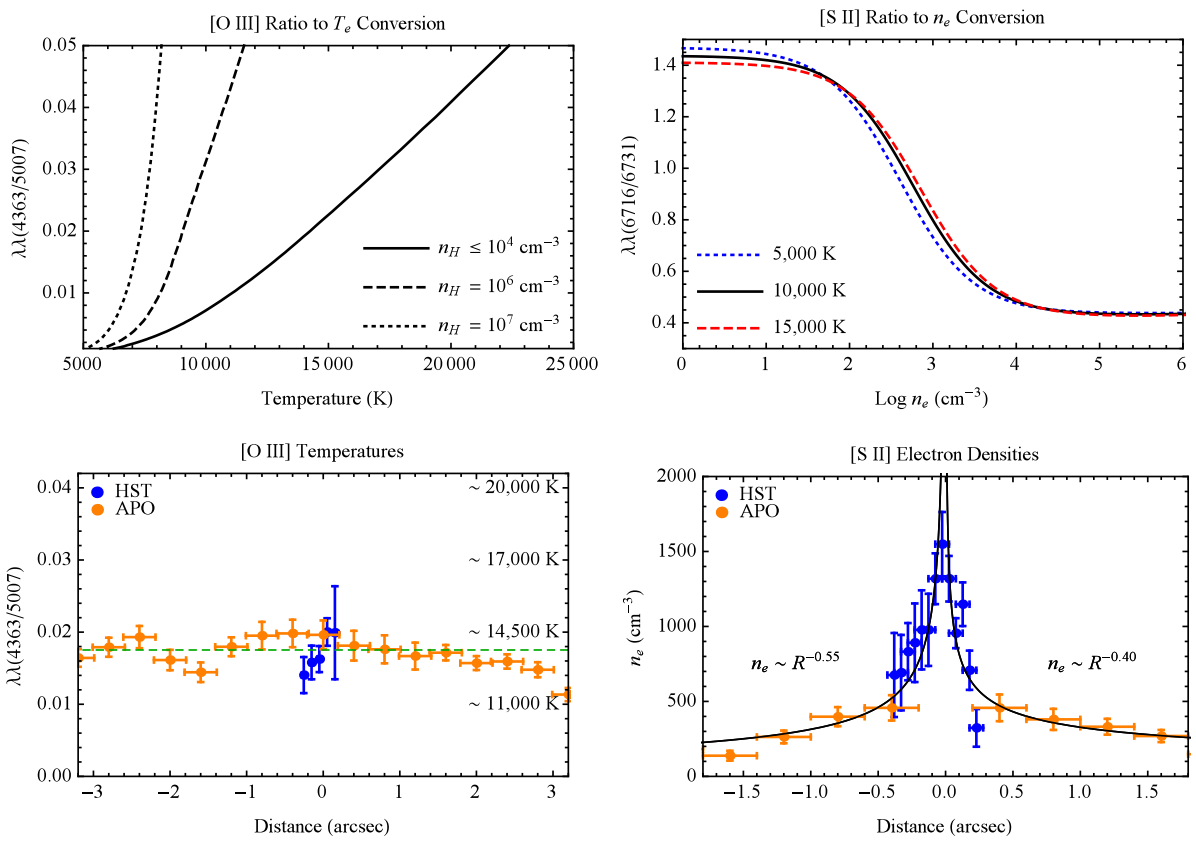

Figure 2.6 Top left: The theoretical behavior of the [O III] $\lambda\lambda$4363/5007 line ratio as a function of temperature for several densities calculated using Cloudy. Bottom left: The derived temperature of the [O III] emitting gas for the *HST* STIS and APO DIS data sets in blue and orange circles, respectively. The mean of $T_{[O\ III]} = 13,500 \pm 650$ K was calculated for all points within $\pm 1\farcs7$ of the nucleus. Top right: The theoretical conversion of the [S II] $\lambda\lambda$6716/6731 ratios to electron density for several temperatures calculated using Cloudy. Bottom right: The derived [S II] electron densities and power law fits with SE to the left and NW to the right.

2.3.4.4 Density

We derived the electron density (n_e cm^{-3}) at each location using the observed [S II] $\lambda\lambda$6716/6731 line ratios, aforementioned temperature, and photoionization model grids. Each ratio was matched to the closest grid value and corresponding density, and the results are shown in Figure 2.6. Errors were propagated from the original fit residuals, temperature uncertainties, and grid step size.

We fit independent power laws to the density profiles in either direction from the nucleus, with points beyond the outflow ($r > 1\farcs7$) not included in the fit. Interestingly, the density profiles have shallow power law indexes with $n_e \propto r^{-0.4} - r^{-0.6}$. This overall decreasing profile is consistent with the previous study by Tsvetanov & Walsh (1992); however, we derive a peak nuclear density that is 2–3× higher due to the lack of atmospheric smearing in the high spatial resolution *HST* spectra. This is a clear demonstration of the powerful selection effects that arise in blended ground based observations.

Finally, within the NLR some elements heavier than hydrogen will contribute more than one electron per nuclei, and the electron density will be higher than the hydrogen density. From photoionization models we adopt the conversion $n_H = 0.85 \times n_e$ (Crenshaw et al. 2015).

2.3.5 [O III] Image Analysis

To account for the NLR mass outside of our spectral slit observations, we employ [O III] imaging and use the physical quantities derived from the spectra and models to convert [O III] fluxes to mass at each point along the NLR. Here we improve on the methodology of Crenshaw et al. (2015) by dividing the NLR in half, which is necessary due to the asymmetry of the velocity laws and NLR flux distribution on either side of the nucleus.

We determined the total [O III] flux as a function of distance from the nucleus by analyzing an *HST* WFPC2 [O III] image of Mrk 573 using the Elliptical Panda routine within the SAOImage DS9 image software (Joye & Mandel 2003). We constructed a series of concentric semi-ellipses centered on the nucleus with spacings equal to the spatial sampling of our extracted *HST* spectra (2 pixels, or $0\farcs10156$). The ellipticity for each ring was calculated based on our adopted inclination of 38° via $b/a = cos(i)$, where a and b are the major and minor axis lengths, respectively. A portion of the [O III] image with overlaid semi-annuli and the resulting azimuthally summed flux profile are shown in Figure 2.7. Errors were calculated from the standard deviation of flux values in line-free regions of the image, and we derived $\sigma \approx 2 \times 10^{-17}$ erg s^{-1} cm^{-2} pixel^{-1}, in agreement with that found by Schmitt et al. (2003a).

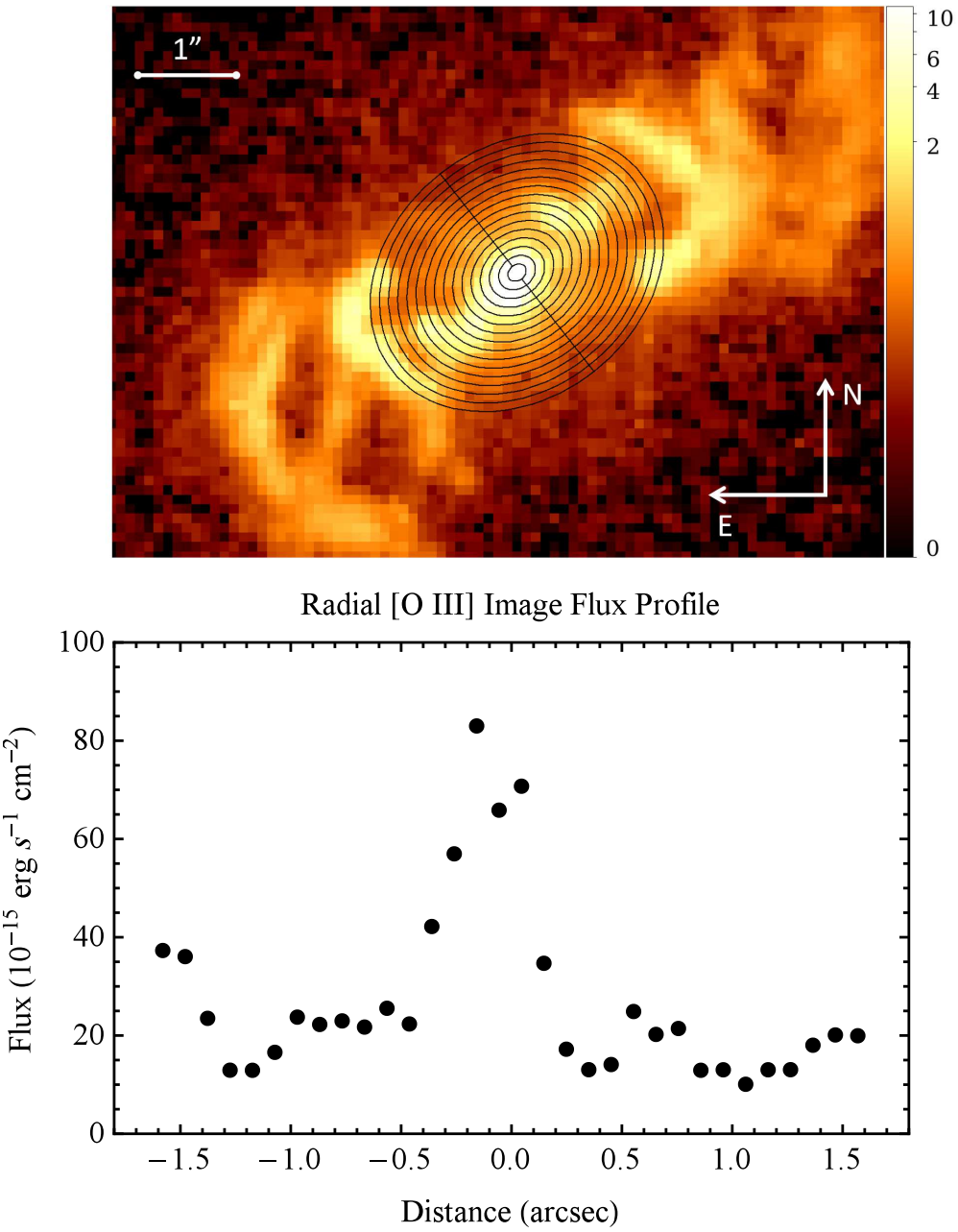

Figure 2.7 Top: A portion of the *HST* WFPC2 [O III] image with overlaid elliptical semi-annuli representing rings of constant distance from the nucleus in black. The color bar gives fluxes in units of 10^{-15} erg s^{-1} cm^{-2}. Bottom: The azimuthally summed [O III] semi-annuli fluxes; SE is to the left and NW is to the right. Typical errors are smaller than the size of the points.

The error in any given annulus was calculated as $\sqrt{N_{\rm pix}} \times \sigma$, where $N_{\rm pix}$ is the number of pixels in the annulus. Typical fractional errors are $< 1\%$.

2.4 Photoionization Models

To accurately convert the [O III] image fluxes (Figure 2.7) to the amount of mass at each position in the NLR, we created photoionization models that match the physical conditions of the emitting clouds in our high spatial resolution *HST* STIS spectra. This is critical because the emissivity of the gas will depend on the physical conditions at each location, and detailed models are needed to derive a scale factor between [O III] flux and mass. To model our dereddened line ratios (Table 2.2), we employed the Cloudy photoionization code version 13.04 and all hotfixes (Ferland et al. 2013).

2.4.1 Input Parameters

To create a physically consistent model, Cloudy must be able to determine the number and energy distribution of photons striking the face of a cloud of known composition and geometry. The first of these is described by the ionization parameter (U), which is a ratio of the number of ionizing photons to the number of atoms at the face of the cloud, and is given by (Osterbrock & Ferland 2006, §13.6)

$$U = \frac{1}{4\pi r^2 n_H c} \int_{\nu_0}^{\infty} \frac{L_\nu}{h\nu} d\nu, \tag{2.5}$$

where r is the radial distance of the emitting cloud from the AGN, n_H is the hydrogen number density cm^{-3}, and c is the speed of light. The integral represents the number of ionizing photons s^{-1} emitted by the AGN, $Q(H)$, across the spectral energy distribution (SED). Specifically, $Q(H) = \int_{\nu_0}^{\infty} (L_\nu / h\nu) d\nu$, where L_ν is the luminosity of the AGN as a function of frequency, h is Planck's constant, and $\nu_0 = 13.6eV/h$ is the ionization potential of hydrogen (Osterbrock & Ferland 2006, §14.3).[5]

[5]Within the X-ray community the ionization parameter is frequently described by $\xi = L_i / n_H r^2$, where L_i is the radiation energy density between 1 and 1000 Rydbergs (13.6 eV–13.6 keV). A close approximation for typical Seyfert power law SEDs is $\log(U) = \log(\xi) - 1.5$ (Crenshaw & Kraemer 2012).

For our SED we adopted the broken power law of Kraemer et al. (2009), with $L_\nu \propto \nu^\alpha$ and $\alpha = -1.0$ for energies < 13.6 eV, $\alpha = -1.5$ for 13.6 $eV \leq h\nu <$ 0.5 keV, and $\alpha = -0.8$ for energies above 0.5 keV, with low and high energy cutoffs at 1 eV and 100 keV, respectively. Kraemer et al. (2009) determined $Q(H) \approx 6 \times 10^{54}$ photons s^{-1}, similar to earlier studies (Wilson et al. 1988).

With this ionizing photon luminosity it is difficult to explain the presence of strong low ionization lines such as [S II] at small distances from the nucleus that form at low ionization parameters $\sim \log(U) =$ –3. In order to maintain physical continuity in Equation 2.5 the resulting densities would be much higher than the critical density of [S II], and these lines would be collisionally suppressed. Two possible explanations are that either the gas is high out of the NLR plane and only close to the nucleus in projection, or that some of the NLR gas is exposed to a heavily filtered continuum where much of the ionizing flux has been removed by a closer in absorber (Ferland & Mushotzky 1982; Binette et al. 1996; Alexander et al. 1999; Collins et al. 2009; Kraemer et al. 2009). Our previous studies concluded that the NLR material is approximately coplanar with the host disk (Fischer et al. 2017), and we adopt the latter explanation that was successfully modeled by Kraemer et al. (2009). Using a filter with $\log(U) =$ –1.50 the best fitting column densities for the absorber were $\log(N_H)$ = 21.50–21.60 cm^{-2}, similar to Kraemer et al. (2009).

To fully model the gas, we use multiple components with different ionization states, which we refer to as "HIGH", "MED" and "LOW" ION ionization components. The HIGH and MED ION components were directly ionized by the AGN SED, while the LOW ION component was calculated using the filtered SED. The intrinsic SED and filtered continua for several absorber column densities are shown in Figure 2.8.

The composition of the gas is specified by the abundances, dust content, and corresponding depletions of certain heavy elements out of gas phase into dust grains. We adopt abundances of $\sim$ 1.3 $Z_\odot$, as determined in §2.4.2. The inclusion of dust is important, as it removes coolants from the gas and contributes to photoelectric heating (van Hoof et al. 2001, 2004;

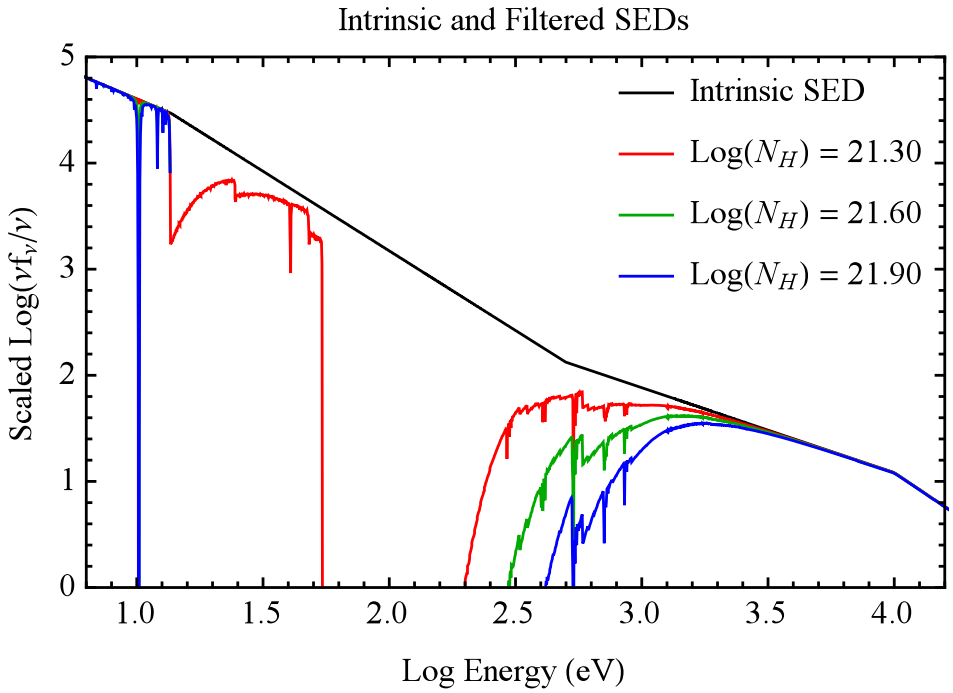

Figure 2.8 A portion of the intrinsic and transmitted SEDs for different absorber column densities, with $\log(N_H) = 21.50 - 21.60$ best matching the observations.

Weingartner & Draine 2001; Draine 2003, 2011; Weingartner et al. 2006; Krügel 2008). In more highly ionized gas, strong iron emission indicates the gas is primarily dust free (Nagao et al. 2003). In addition, we examined the *International Ultraviolet Explorer* (IUE) spectrum of Mrk 573 (MacAlpine 1988). The IUE aperture encompasses a large portion of the NLR such that the spectrum is heavily weighted toward the denser gas that is emitting most efficiently. Nonetheless, MacAlpine (1988) reports Lyα/C IV λ1549 = 8.0. Our dusty models predict this ratio to be $\sim$ 0.6 for a typical HIGH ION component, while for a dust free and optically thin model, it is $\sim$ 7. This indicates dust free gas, as there is little to no suppression of Lyα, and was further motivation to adopt a dust free HIGH ION component. From previous studies a dust content of approximately half the levels seen in the ISM reproduce the observed medium and low ionization lines seen in the spectra (Collins et al. 2009; Kraemer et al. 2009), and we adopt that for MED and LOW ION.

The exact logarithmic abundances relative to hydrogen by number for dust free models are: He = -1, C = -3.47, N = -3.92, O = -3.17, Ne = -3.96, Na = -5.76, Mg = -4.48 Al = -5.55,

Si = -4.51, P = -6.59, S = -4.82, Ar = -5.60, Ca = -5.66, Fe = -4.40, and Ni = -5.78. For models with a dust level of 0.50 relative to the Galactic ISM, we accounted for the depletion of certain heavy elements onto graphite and silicate grains. Nitrogen is not depleted, as it is deposited onto ice mantles in grains that dissociate in the NLR (Seab & Shull 1983; Snow & Witt 1996; Collins et al. 2009). The logarithmic abundances relative to hydrogen by number for these dusty models are: He = -1, C = -3.59, N = -3.92, O = -3.21, Ne = -3.96, Na = -5.76, Mg = -4.74, Al = -5.81, Si = -4.76, P = -6.59, S = -4.82, Ar = -5.60, Ca = -5.92, Fe = -4.66, and Ni = -6.04. We consider only the effects of the default atomic data within Cloudy on our predictions (see, e.g. Juan de Dios & Rodríguez 2017; Laha et al. 2017 for discussions).

2.4.2 Model Selection

With these input parameters, we ran grids of models over a range of ionization parameters for each location along the slit located a distance r from the nucleus. From Equation 2.5 the only unknown quantities are U and n_H, so for each U we solved for the corresponding density to maintain physical continuity. If U and n_H are allowed to vary independently, then the corresponding distance r would be incorrect. The number density of the LOW ION component was constrained to a small range encompassing typical errors around the power law fits in Figure 2.6, while a range of densities were explored for the HIGH and MED ION components, as they are less constrained. Using the limits from our diagnostics in §2.3.4, we explored a range of parameters for number and column density, column density of the filter, and number of components. We then add fractional combinations of the multiple components to create a final composite model that matches the total observed Hβ luminosity.

To determine the best fit model at each location, we employed a simple numerical scheme that computed the model line ratios for all possible fractional combinations of our HIGH, MED, and LOW ION components across our range of parameters. No assumptions were made about the number of components, and the technique could find that one, two, or three

components was a best fit to the observations. Model/dereddened line ratios were calculated for each composite model, with an ideal match having a ratio of one.

Our criteria for a successful fit were the following. The sensitive diagnostics lines of [O III], [N II], and [S II] must match the observations to within 30%. In addition, the column density sensitive He II λ4686 line ratios must match within 10%. Furthermore, we imposed the limits that all remaining lines must match their predicted value within a factor of five, and the global model/dereddened ratios must center on a mean of unity to within 20%.

In cases where a position was well matched by two or more similar models, we chose the composite model that best matched the strong emission lines and those sensitive to column density, as these should provide the most realistic mass determination. For all but one position ($-0\farcs25$) three components produced the best fit. The best fit absorber column density was $\log(N_H) = 21.50$ for positions $+0\farcs15$, $-0\farcs05$, $-0\farcs15$, and $-0\farcs25$, and $\log(N_H) = 21.60$ for all other positions. The input and output parameters for these best fit models are given in Tables 2.3 and 2.4, respectively. The final predicted emission line ratios from all components weighted by their fractional contributions are given in Table 2.5.

2.4.3 Comparison to the Observations

The comparison between our dereddened and model emission line ratios is shown in Figure 2.9. The dashed unity line indicates an exact match, and all points between the dotted lines represent agreement to within better than a factor of three. A variety of factors contribute to the deviations of each line from an exact match, including a poor gaussian fit, low S/N, accuracy of atomic data, and the accuracy of our multi-component models. Here we discuss deviations greater than a factor of three within errors for the important diagnostic lines at each position.

Table 2.3. Cloudy Model Input Parameters

Distance from Nucleus (arcsec) (1)	Comp ION Name (2)	Ionization Parameter log(U) (unitless) (3)	Column Density log(N_H) (cm^{-2}) (4)	Number Density log(n_H) (cm^{-3}) (5)	Dust Content Relative to ISM (6)	Input SED Type (I/F) (7)
0.46	High	-0.70	21.90	2.44	0.0	I
0.46	Med	-1.40	21.60	3.14	0.5	I
0.46	Low	-2.83	22.10	2.20	0.5	F
0.36	High	-1.20	21.30	3.16	0.0	I
0.36	Med	-1.50	21.00	3.46	0.5	I
0.36	Low	-2.82	21.80	2.40	0.5	F
0.25	High	-1.10	19.70	3.37	0.0	I
0.25	Med	-1.50	21.30	3.77	0.5	I
0.25	Low	-2.70	22.00	2.60	0.5	F
0.15	High	-0.60	22.00	3.32	0.0	I
0.15	Med	-1.40	20.20	4.12	0.5	I
0.15	Low	-1.82	21.80	3.70	0.5	F
0.05	High	-0.70	19.80	4.37	0.0	I
0.05	Med	-1.40	21.40	5.07	0.5	I
0.05	Low	-2.61	22.60	3.90	0.5	F
-0.05	High	-1.10	22.20	4.77	0.0	I
-0.05	Med	-1.60	20.20	5.27	0.5	I
-0.05	Low	-0.96	22.70	3.80	0.5	F
-0.15	High	-0.70	20.10	3.42	0.0	I
-0.15	Med	-1.70	20.20	4.42	0.5	I
-0.15	Low	-1.92	21.70	3.80	0.5	F
-0.25	High	...	...	...	...	I
-0.25	Med	-1.80	20.20	4.07	0.5	I
-0.25	Low	-2.16	21.60	3.60	0.5	F
-0.36	High	-0.60	19.80	2.56	0.0	I
-0.36	Med	-1.70	21.90	3.66	0.5	I
-0.36	Low	-2.48	21.72	2.80	0.5	F
-0.46	High	-0.70	21.90	2.44	0.0	I
-0.46	Med	-1.40	21.50	3.14	0.5	I
-0.46	Low	-2.83	22.10	2.20	0.5	F

Note. — The Cloudy photoionization model input parameters. The columns are: (1) distance from the nucleus to the center of each $0\farcs1 \times 0\farcs2$ bin, (2) component name, (3) log ionization parameter, (4) log column density, (5) log number density, (6) dust fraction relative to ISM, and (7) the implemented SED (Intrinsic/Filtered, see §2.5.1). The ionization parameters for LOW ION models are computed by Cloudy using the filtered SED.

Table 2.4. Cloudy Model Output Parameters

Distance from Nucleus (arcsec) (1)	Comp ION Name (2)	Fraction of Total Model (3)	log($F_{H\beta}$) Model Flux (cgs) (4)	Cloud Surface Area (pc^2) (5)	Cloud Model Thickness (pc) (6)	Cloud Model Depth (pc) (7)
0.46	High	0.10	-0.80	39.	9.3	0.6
0.46	Med	0.65	-0.47	120.	0.9	1.7
0.46	Low	0.25	-1.51	502.	25.7	7.2
0.36	High	0.30	-0.60	18.	0.4	0.3
0.36	Med	0.45	-0.58	26.	0.1	0.4
0.36	Low	0.25	-1.39	93.	8.1	1.3
0.25	High	0.20	-2.00	1618.	<0.1	23.1
0.25	Med	0.50	0.08	33.	0.1	0.5
0.25	Low	0.30	-1.02	252.	8.1	3.6
0.15	High	0.25	0.15	103.	1.6	1.5
0.15	Med	0.15	-0.76	498.	<0.1	7.1
0.15	Low	0.60	-0.03	374.	0.4	5.3
0.05	High	0.25	-1.01	2057.	<0.1	29.4
0.05	Med	0.60	1.43	18.	<0.1	0.3
0.05	Low	0.15	0.57	33.	1.6	0.5
-0.05	High	0.55	1.82	2.	0.1	<0.1
-0.05	Med	0.30	0.40	26.	<0.1	0.4
-0.05	Low	0.15	0.70	7.	2.6	0.1
-0.15	High	0.05	-1.66	311.	<0.1	4.4
-0.15	Med	0.45	-0.42	164.	<0.1	2.3
-0.15	Low	0.50	-0.02	71.	0.3	1.0
-0.25	High	0.00	...	...	...	...
-0.25	Med	0.40	-0.75	177.	<0.1	2.5
-0.25	Low	0.60	-0.42	124.	0.3	1.8
-0.36	High	0.25	-2.85	6173.	0.1	88.2
-0.36	Med	0.60	-0.10	26.	0.6	0.4
-0.36	Low	0.15	-1.35	117.	2.7	1.7
-0.46	High	0.05	-0.80	3.	9.3	<0.1
-0.46	Med	0.70	-0.48	21.	0.7	0.3
-0.46	Low	0.25	-1.51	81.	25.7	1.2

Note. — The best fitting Cloudy model output parameters. The columns are: (1) distance from the nucleus to the center of each $0\farcs1 \times 0\farcs2$ bin, (2) component name, (3) fraction of model contributing to the final Hβ luminosity, (4) log Hβ model flux (erg s^{-1} cm^{-2}), (5) surface area of the emitting gas, (6) gas cloud thickness (N_H/n_H), and (7) depth into the plane of the sky.

Table 2.5. Predicted Cloudy Model Emission Line Ratios

Line	0.″46	0.″36	0.″25	0.″15	0.″05	–0.″05	–0.″15	–0.″25	–0.″36	–0.″46
He II λ3203	0.15	0.28	0.17	0.19	0.21	0.19	0.23	0.18	0.18	0.14
[Ne V] λ3346	0.48	0.85	0.55	0.59	0.63	0.76	0.70	0.44	0.32	0.44
[Ne V] λ3426	1.32	2.32	1.50	1.63	1.73	2.09	1.91	1.20	0.87	1.22
[Fe VII] λ3586	0.22	0.36	0.30	0.43	0.40	0.31	0.23	0.11	0.29	0.17
[O II] λ3727	2.20	1.48	2.24	0.84	0.88	0.52	0.66	0.99	1.13	2.20
[Fe VII] λ3759	0.30	0.50	0.42	0.60	0.56	0.43	0.32	0.15	0.40	0.23
[Ne III] λ3869	1.56	0.95	1.36	1.42	1.56	1.36	1.20	1.21	1.13	1.62
He I λ3889	0.35	0.49	0.31	0.23	0.33	0.38	0.33	0.35	0.29	0.36
[Ne III] λ3969	0.63	0.45	0.57	0.59	0.63	0.58	0.53	0.53	0.50	0.65
[S II] λ4074	0.10	0.05	0.08	0.09	0.11	0.09	0.08	0.09	0.09	0.09
Hδ λ4102	0.26	0.26	0.26	0.27	0.26	0.26	0.27	0.26	0.26	0.26
Hγ λ4340	0.47	0.47	0.47	0.48	0.47	0.48	0.48	0.47	0.47	0.47
[O III] λ4363	0.25	0.25	0.19	0.20	0.37	0.30	0.20	0.19	0.17	0.26
He II λ4686	0.37	0.68	0.40	0.45	0.48	0.44	0.54	0.44	0.42	0.35
[Ar IV] λ4711	0.06	0.07	0.04	0.04	0.01	0.03	0.05	0.05	0.04	0.07
[Ar IV] λ4740	0.06	0.07	0.05	0.06	0.07	0.10	0.09	0.08	0.05	0.06
Hβ λ4861	1.00	1.00	1.00	1.00	1.00	1.00	1.00	1.00	1.00	1.00
[O III] λ4959	5.05	3.63	4.01	5.06	4.63	5.08	4.52	4.71	4.07	5.38
[O III] λ5007	15.21	10.93	12.07	15.23	13.94	15.28	13.61	14.17	12.24	16.19
[O I] λ6300	1.68	1.12	1.48	0.79	1.09	0.74	0.59	0.56	1.12	1.60
[S III] λ 6312	0.05	0.03	0.05	0.04	0.04	0.02	0.04	0.05	0.04	0.05
[O I] λ6363	0.54	0.36	0.47	0.25	0.35	0.23	0.19	0.18	0.36	0.51
[Fe X] λ6375	0.03	0.01	0.02	0.26	0.23	0.01	0.05	0.00	0.40	0.01
[N II] λ6548	0.76	0.62	0.79	0.48	0.41	0.25	0.40	0.44	0.60	0.74
Hα λ6563	2.88	2.84	2.86	2.83	2.82	2.82	2.82	2.85	2.81	2.88
[N II] λ6584	2.25	1.82	2.33	1.42	1.21	0.73	1.19	1.30	1.78	2.18
[S II] λ6716	0.72	0.39	0.50	0.32	0.22	0.17	0.23	0.33	0.57	0.68
[S II] λ6731	0.56	0.29	0.41	0.40	0.32	0.25	0.30	0.39	0.52	0.53

Note. — The predicted Cloudy emission line ratios for our final composite models with the fractional weightings of each component given in Table 2.4. Cloudy version 13.04 does not predict O III λ3133.

The positions at larger radial distances from the nucleus ($\pm0\farcs46$, $\pm0\farcs36$, $\pm0\farcs25$) all show excellent agreement between the observations and models. The apparent under-prediction of lines in the blue at $+0\farcs46$, $+0\farcs25$, and $+0\farcs15$ is indicative of the residual over-extinction correction discussed in §2.3.3. As the ratios are over-corrected by a factor of $\sim 1.5-2$, their apparent under-prediction by a similar factor indicates a good fit. The large errors in the red at $+0\farcs25$ and $+0\farcs15$ are due to the large reddening uncertainties (§2.3.3).

For positions at small radial distances from the nucleus ($\pm0\farcs15$ and $\pm0\farcs05$) with up to 28 emission lines, we also find excellent agreement between the observations and models. The sole exception is the over-prediction of the neutral oxygen doublet [O I] $\lambda\lambda$6300,6363. For these positions, we explored using less stringent criteria on [O III], [N II], [S II], and He II, which decreased the over-prediction from ~ 4.5 times to ~ 3.8 times, at the expense of other line fits.

The collisionally excited [O I] emission line is strongest in the neutral zone of a cloud, and is sensitive to the temperature (Kraemer et al. 2000a) and gas turbulence (Moy & Rocca-Volmerange 2002). This may indicate an excess of X-rays transmitted by the absorbing filter, increasing the temperature in the neutral zone. Because the extraction bin is $\sim 0\farcs1 \times 0\farcs2$ (2×4 pixels, $\sim 36 \times 72$ pc) some of the lower ionization material could be slightly offset from the peak [O III] emission, but still within the spectral extraction bin, as seen in Mrk 3 (Collins et al. 2009). As the centers of these two extractions are just $\sim$18 pc from the nucleus, the X-ray flux could be artificially high if the material is located toward the extremes of the bins. Given the excellent agreement of all other diagnostic lines at these locations, we opted against further fine tuning.

Our multi-component photoionization models are consistent with pure AGN ionization from the central source. As noted by others (Schlesinger et al. 2009), we do not see any evidence for shock ionization in the outflow regions (see, e.g. Schlesinger et al. 2009; Maksym et al. 2016, 2017; Terao et al. 2016, and references therein for discussions on shocks). Our composite models generally agree with the IUE UV line ratios, indicating that we are likely

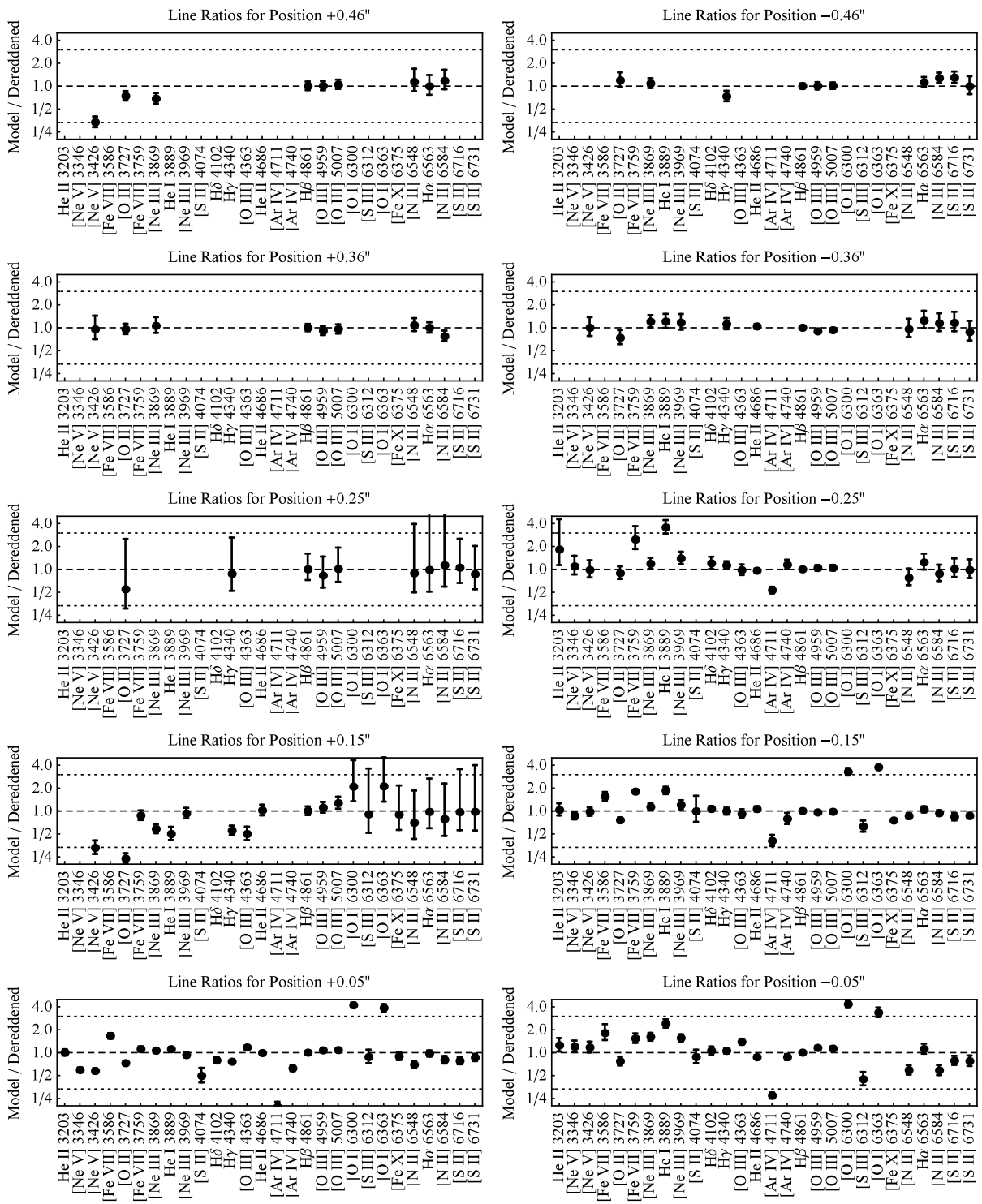

Figure 2.9 The composite Cloudy model line ratios divided by the dereddened values for each position. The dashed unity lines indicate an exact match, while the dotted lines are factor of three difference intervals (tick marks are logarithmically spaced for even ratio distributions above and below the unity line). Points above the unity line are over-predicted by the models, while points below the unity line are under-predicted. Lines with no data point were too weak to measure at that location.

encompassing a significant portion of the UV emitting gas in our models and resulting outflow rates.

2.4.4 Physical Implications of the Models

Using the best-fit models, we derived several physical quantities at each position that are given in Table 2.4. First, there is the surface area of the emitting clouds ($A = L_{\mathrm{H}\beta}/F_{\mathrm{H}\beta}$). Next, we confirmed that the physical thicknesses of the clouds (N_H/n_H) were smaller than our bin size to ensure they fit within the slit extraction (2 pixels). Finally, we calculated the summed depths of the clouds into the plane of the sky by dividing the cloud area by the projected slit width ($\sim$ 70 pc), to verify they were smaller than the scale height of the disk and ionizing bicone. It is important to note that each component may not be co-located within the extraction bin, as the emission is spread across $0\farcs2$ (4 pixels) in the spectral direction (Collins et al. 2009).

2.5 Calculations

We calculate the mass at each point along the *HST* STIS slit using the extinction-corrected Hβ and Cloudy model Hβ fluxes. For our multi-component models, the mass in each photoionized component is calculated separately by dividing up the Hβ luminosity in each component, and then they are summed.

2.5.1 Ionized Mass in the Slit

The ionized gas mass in each slit extraction (M_{slit}) for a given Hβ luminosity is given by (Peterson 1997; Crenshaw et al. 2015)

$$M_{\mathrm{slit}} = N_{\mathrm{H}} \mu m_p \left(\frac{L(\mathrm{H}\beta)}{F(\mathrm{H}\beta)_m} \right), \tag{2.6}$$

where N_H is the total model hydrogen column density (predominantly ionized, with only trace amounts of neutral and molecular phases), μ is the mean mass per proton (~ 1.36 for solar, ~ 1.40 for our abundances), m_p is the mass of a proton, $F(\mathrm{H}\beta)_m$ is the Hβ model flux, and $L(\mathrm{H}\beta)$ is the luminosity of Hβ calculated from the observed flux and distance. That is,

$$L(\mathrm{H}\beta) = 4\pi D^2 F(\mathrm{H}\beta)_i, \tag{2.7}$$

where D is the distance to the galaxy and $F(\mathrm{H}\beta)_i$ is the intrinsic flux corrected for extinction at each point (§2.3). Conceptually, Equation 2.6 determines the area of the emitting clouds through the ratio of the luminosity and flux, and then multiplies this by the column density, or projected number of particles per unit area, to yield the total number of particles. Multiplying this by the mean mass per particle gives the total ionized mass.

2.5.2 Ionized Mass Profile from [O III] Imaging

These calculations yield a direct conversion between the luminosity of the Hβ emission line and the ionized gas mass, specifically, the number of Hβ photons emitted per unit mass at a given density. If high quality Hβ emission line imaging of the NLR were available, then those fluxes and our model densities could be used to directly calculate the gas mass at all spatial locations. For Mrk 573, only high spatial resolution [O III] imaging is available. The flux of Hβ and [O III] are related simply by the [O III]/Hβ ratio, and thus the mass per unit Hβ luminosity is also proportional to the observed [O III] flux within a scale factor. Specifically,

$$S = \left(\frac{M_{\mathrm{slit}} n_H}{F_{\lambda 5007}} \right), \tag{2.8}$$

where M_{slit} is the ionized mass in the slit calculated from Equation 2.6, n_H is the fractional weighted mean hydrogen number density (cm^{-3}) for all components, and $F_{\lambda 5007}$ is the extinction-corrected [O III] emission line flux from our spectra. We take an average value of the scale factors from each location (Figure 2.10), which exhibit some scatter due to variations

in the [O III]/Hβ ratios across the NLR. This scale factor allows us to derive masses from observed [O III] image fluxes rather than Hβ luminosities. The total ionized mass for a given image flux is then

$$M_{\rm ion} = S\left(\frac{F_{[\rm O\ III]}}{n_H}\right). \tag{2.9}$$

For this analysis, $F_{[\rm O\ III]}$ is the flux in each image semi-annulus of width δr (Figure 2.7) and n_H is the hydrogen number density.

The calculated scale factors are shown in Figure 2.10. The mean scale factor is S $= 1.25 \pm 0.14 \times 10^{21}$ $M_\odot$ cm^{-1} erg^{-1} s, and the 1σ error corresponds to a fractional uncertainty of 11.3%. For position $-0\farcs36$ the calculated scale factor was $> 3\sigma$ from the mean, possibly due to an anomalous corrected Hβ flux, and was replaced with a mean value. The scale factor uncertainty in Crenshaw et al. (2015) was calculated using a standard error, while we have adopted the standard deviation. This can result in larger fractional errors for the mass outflow rates, but should yield a more realistic estimate of the uncertainty at any individual point given the [O III]/Hβ variations across the NLR.

Ideally our density law and resulting masses would be determined from detailed photoionization models at all locations along the NLR. However, at distances of $r > 0\farcs5$ from the nucleus, only the [O III] and Hα emission lines are strong enough to get reliable measurements in our high spatial resolution *HST* data. This is due to intrinsically lower fluxes further from the nucleus, in combination with the PA of the *HST* slit that does not follow the linear feature of bright emission line knots.

To obtain masses for $r = 0\farcs5 - 1\farcs7$ from the nucleus, we derived a hybrid technique employing our scale factor and then derived the gas density at each distance from our power law fits to the [S II] lines in our APO DIS data, as shown in Figure 2.6. The APO observations have lower spatial resolution, but the wider slit encompasses significantly more NLR emission. Our testing showed that at distances of $r \geq 0\farcs5$ from the nucleus the ionization state of the gas drops enough such that the density derived from [S II] is approximately equal to that of

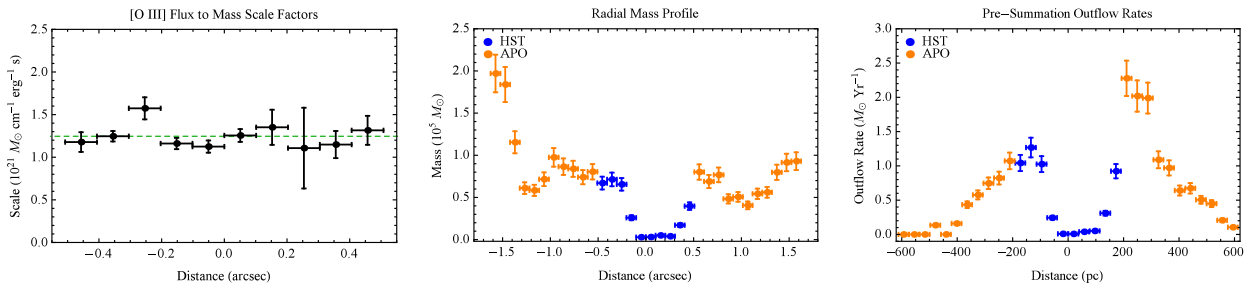

Figure 2.10 Left: The derived scale factor at each location for converting [O III] image fluxes to mass. The mean is indicated by the green dashed line. Middle: The derived mass profile in units of 10^5 $M_\odot$ across the NLR. Right: The calculated mass outflow rates before azimuthal summation. The *HST* STIS and APO DIS data are in blue and orange, respectively. SE is to the left and NW is to the right.

a multi-component model. In this way we were able to extend our mass outflow calculations from 175 pc to 600 pc.

Using our scale factor and the densities from our photoionization models (for $r < 0\farcs5$) and [S II] power law fits (for $r = 0\farcs5 - 1\farcs7$), we calculated the total mass in each image semi-annulus from Equation 2.9. The NLR mass profile is shown before (Figure 2.10) and after (Figure 2.11) azimuthal summation. The bump in the mass profile between 500 and 600 pc is due to the partial inclusion of the bright arc of emission in the southwest. The total mass of ionized gas in the NLR for $r < 1\farcs7$ is $\sim 2.2 \times 10^6$ $M_\odot$ with $\sim 10\%$ of that contained in the *HST* spectral slit used to create our photoionization models and scale factor.

2.5.3 Outflow Parameters

Finally, we calculate the mass outflow rates ($\dot{M}_{out}$) in units of $M_\odot$ yr^{-1} at each position along the NLR using

$$\dot{M}_{out} = \left(\frac{Mv}{\delta r}\right), \tag{2.10}$$

where M is the semi-annular mass, v is the deprojected velocity corrected for inclination and position angle on the sky (§2.2), and δr is the deprojected width for each extraction. Deprojecting the distances results in a bin width that is 7.8% larger than the observed value; thus each deprojected measurement spans $\delta r \approx 38.3$ pc.

In addition to mass outflow rates, a variety of energetic quantities can be determined, including kinetic energies, momenta, and their flow rates. These quantites yield information about the amount of AGN energy deposited into the NLR. The kinetic energy is given by

$$E = \frac{1}{2} M_{out} v^2, \tag{2.11}$$

The time derivative of this is the kinetic luminosity (also referred to as the energy injection or flow rate),

$$L_{KE} = \dot{E} = \frac{1}{2} \dot{M}_{out} v^2, \tag{2.12}$$

where we only include contributions from pure radial outflow (a σ_v term is sometimes added to the energy budget to account for gas turbulence). Finally, the momenta ($p = M_{out} v$) and momenta flow rates ($\dot{p} = \dot{M}_{out} v$) are useful quantities that can be compared to the AGN bolometric luminosity, as well as the photon momentum (L/c), to quantify the efficiency of the NLR in converting radiation from the AGN into the radial motion of the outflows (Zubovas & King 2012; Costa et al. 2014).

We obtain a single radial profile for each quantity by azimuthally summing the values derived for the SE and NW semi-annuli. The mass outflow rates prior to summation can be seen in Figure 2.10, with the asymmetry due to the nature of the velocity laws and mass distributions.

2.6 Results

2.6.1 Mass Outflow Rates & Energetics

In Figure 2.11 and Table 2.6 we present our mass outflow rates and energetics as functions of distance from the nucleus for Mrk 573. We also show the results for NGC 4151 from Crenshaw et al. (2015) for comparison. The outflow has a maximum radial extent of 600 pc from the nucleus and contains a total ionized gas mass of $M \approx 2.2 \times 10^6\ M_\odot$. This mass is

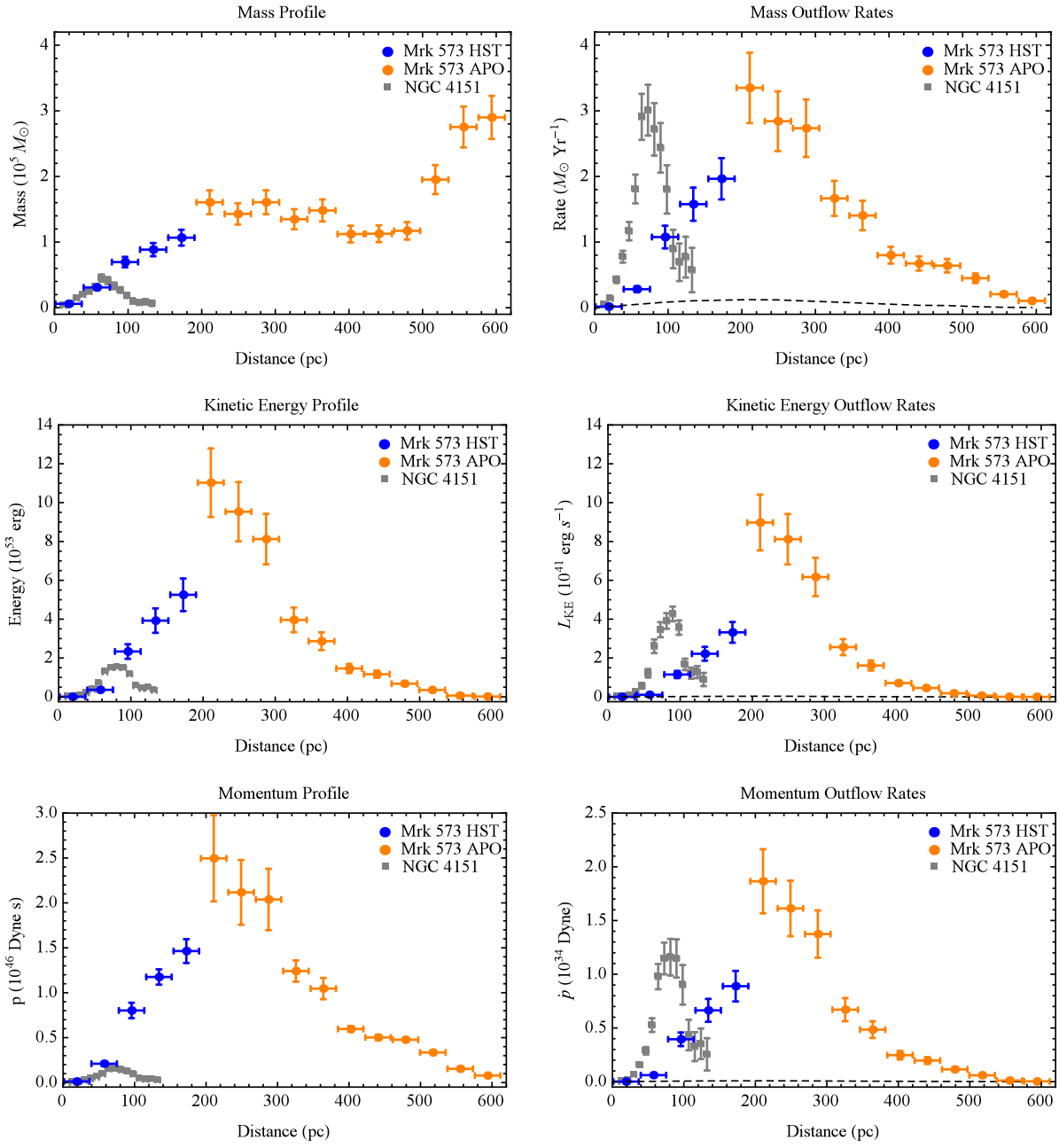

Figure 2.11 From top left to bottom right are the azimuthally summed mass profiles, mass outflow rates, kinetic energy profiles, kinetic energy outflow rates, momentum profiles, and momentum outflow rates for Mrk 573 and NGC 4151 (Crenshaw et al. 2015). The dashed lines represent the profiles that would result from the mass in the center bin ($M \approx 5.9 \times 10^3\ M_\odot$) traveling through the velocity profile. The value at each distance is the quantity contained within that extraction bin of width $\delta r = 38.3$ pc.

similar to other Seyfert galaxies such as Mrk 3 (Collins et al. 2009). The total kinetic energy summed over all distances is $E \approx 5.1 \times 10^{54}$ erg.

The mass outflow rates rise to a peak value of $\dot{M}_{out} \approx 3.4 \pm 0.5\ M_{\odot}\ \mathrm{yr}^{-1}$ at a distance of 210 pc from the nucleus and then steadily decrease to zero at ~ 600 pc, which is the extent of our velocity law exhibiting outflow. The kinematics at further distances are consistent with rotation. The overall shapes of the profiles are a convolution of the velocity laws and mass profiles, exhibiting minor fluctuations on top of the overall increasing followed by decreasing trends. The dashed lines represent the mass outflow rates and energetics that would be observed if the amount of mass in the central bin ($M \approx 5.9 \times 10^3\ M_{\odot}$) was allowed to propagate through the velocity profile. At 210 pc where the outflow peaks, this is ~ 27 times smaller than the observed value, indicating that the outflow is not a steady state nuclear outflow, but that material is accelerated in-situ from its local location in the NLR.

The mass profiles for the SE and NW semi-annuli (Figure 2.10) are asymmetric, such that their summed radial mass outflow rates (Table 2.6) are not represented by a simple average of the velocity laws, but by a mass weighted mean. The appropriate mean velocity profile is found by solving Equation 2.10 with the final mass and mass outflow rates (Table 2.6). The mean velocity profile does not reach the peak deprojected velocity of 1100 km s^{-1}, as the two halves of the velocity law peak at different radial distances (Figure 2.3).

Compared to the AGN bolometric luminosity of Mrk 573, $\log(L_{bol}) = 45.5 \pm 0.6$ erg s^{-1} (Kraemer et al. 2009), the peak kinetic luminosity reaches $< 0.1\%$ of L_{bol}, but see also the discussion in §2.7.2. The momentum flow rate can be compared to the photon momentum (L/c) of ionizing flux emanating from the AGN. The photon momentum from the bolometric luminosity is $\dot{p} \approx 1.05 \times 10^{35}$ dyne, and the peak momentum flow rate is $\dot{p} \approx 2.5 \times 10^{34}$ dyne. Thus the peak outflow momentum rate is $\sim 25\%$ of the AGN's photon momentum.

The outflow velocities trending to zero near the nucleus naturally leads to small outflow rates at small radial distances. In Fischer et al. (2017) we found evidence of multiple high velocity (FWHM ~ 1000 km s^{-1}) kinematic components near the nucleus using high spatial

Table 2.6. Radial Mass Outflow and Energetic Results

Distance (pc) (1)	Velocity (km s^{-1}) (2)	Mass (10^5 $M_\odot$) (3)	$\dot{M}$ ($M_\odot$ yr^{-1}) (4)	Energy (10^{53} erg) (5)	$\dot{E}$ (10^{41} erg s^{-1}) (6)	Momentum (10^{46} dyne s) (7)	$\dot{P}$ (10^{34} dyne) (8)
19.2	106.7	0.06 ± 0.01	0.02 ± 0.00	0.01 ± 0.00	0.00 ± 0.00	0.01 ± 0.00	0.00 ± 0.00
57.5	342.0	0.31 ± 0.03	0.28 ± 0.05	0.36 ± 0.06	0.11 ± 0.02	0.21 ± 0.02	0.06 ± 0.01
95.8	580.7	0.69 ± 0.08	1.08 ± 0.17	2.33 ± 0.37	1.15 ± 0.18	0.80 ± 0.09	0.39 ± 0.06
134.1	667.8	0.89 ± 0.10	1.58 ± 0.25	3.92 ± 0.63	2.22 ± 0.35	1.18 ± 0.08	0.66 ± 0.11
172.4	689.8	1.07 ± 0.12	1.96 ± 0.31	5.25 ± 0.84	3.32 ± 0.53	1.46 ± 0.13	0.89 ± 0.14
210.7	781.3	1.61 ± 0.18	3.35 ± 0.54	11.03 ± 1.76	8.98 ± 1.44	2.50 ± 0.48	1.87 ± 0.30
249.1	744.7	1.43 ± 0.16	2.84 ± 0.45	9.53 ± 1.52	8.11 ± 1.30	2.12 ± 0.36	1.61 ± 0.26
287.4	637.7	1.61 ± 0.18	2.74 ± 0.44	8.12 ± 1.30	6.17 ± 0.99	2.04 ± 0.34	1.37 ± 0.22
325.7	463.0	1.35 ± 0.15	1.67 ± 0.27	3.96 ± 0.63	2.56 ± 0.41	1.24 ± 0.12	0.67 ± 0.11
364.0	355.1	1.48 ± 0.17	1.40 ± 0.22	2.86 ± 0.46	1.61 ± 0.26	1.05 ± 0.12	0.48 ± 0.08
402.3	267.3	1.12 ± 0.13	0.80 ± 0.13	1.46 ± 0.23	0.71 ± 0.11	0.60 ± 0.03	0.25 ± 0.04
440.6	224.0	1.13 ± 0.13	0.67 ± 0.11	1.16 ± 0.19	0.46 ± 0.07	0.50 ± 0.03	0.20 ± 0.03
478.9	204.8	1.17 ± 0.13	0.64 ± 0.10	0.68 ± 0.11	0.18 ± 0.03	0.48 ± 0.02	0.11 ± 0.02
517.3	86.3	1.95 ± 0.22	0.45 ± 0.07	0.35 ± 0.06	0.06 ± 0.01	0.33 ± 0.01	0.06 ± 0.01
555.6	28.0	2.75 ± 0.31	0.21 ± 0.03	0.06 ± 0.01	0.00 ± 0.00	0.15 ± 0.00	0.01 ± 0.00
593.9	13.6	2.90 ± 0.33	0.10 ± 0.02	0.02 ± 0.00	0.00 ± 0.00	0.08 ± 0.00	0.00 ± 0.00

Note. — Numerical results for the mass and energetic quantities as a function of radial distance. Columns are (1) deprojected distance from the nucleus, (2) mass weighted mean velocity, (3) gas mass in units of 10^5 $M_\odot$, (4) mass outflow rates, (5) kinetic energies, (6) kinetic energy outflow rates, (7) momenta, and (8) momenta flow rates. These results, shown in Figure 2.11, are the sum of the individual radial profiles calculated for the SE and NW semi-annuli (see Figures 2.7 and 2.10). The value at each distance is the quantity contained within the annulus of width $\delta r = 38.3$ pc.

resolution Gemini Near-Infrared Field Spectrograph (NIFS) observations. If the FWHM is taken to be a more representative signature of the outflow velocities near the nucleus, then the three innermost outflow rates would increase to ~ 2.2, 3.6, and 4.8 $M_\odot$ yr^{-1}, respectively.

We also assumed that the NLR material is moving radially along the NLR major axis (PA = 128°), rather than the STIS slit PA. If this angle were used, the projection effects would be more significant ($\varphi = 12°$), with the peak deprojected velocities reaching ~ 2700 km s^{-1}, and the mass outflow rates would increase by a factor of ~ 2.48. From our modeling in Fischer et al. (2017), and the typical observed velocities in Seyferts, we consider this to be less probable and retain our conservative result.

Furthermore, we have neglected contributions to the mass outflow rates and energetics from ablation of gas off the spiral dust lanes at distances of $600 - 750$ pc. Here the kinematics are generally consistent with rotation; however, the [O III] and Hα velocity centroids show a systematic separation ~ 100 km s^{-1} that is not seen at larger radial distances. This separation is most likely due to ablation of material off the faces of the ionized arcs in rotation, and we do not include it in our results.

Finally, our assumptions about outflows and the specific velocity and density laws may not be accurate for material outside of the nominal bicone, along the NLR minor axis. If we restrict our semi-annuli to azimuthal angles within the ionizing bicone, which has a large opening angle (§2.7.1.1), the mass and outflow rates decrease by $\sim 20\%$.

In the ENLR ($r > 1\farcs7$), the density drops very slowly and $n_e \approx 150 - 200$ cm^{-3}. Adopting this density range, our scale factor, and extended [O III] image fluxes, we find the ENLR mass is $\sim 6 - 7{\times}10^6$ $M_\odot$. Thus the mass of the NLR+ENLR is $\sim 8 - 9{\times}10^6$ $M_\odot$, indicating that $\sim 25\%$ of the ionized gas exhibits outflow kinematics.

2.6.2 Comparison with NGC 4151

The mass outflows in Mrk 573 are significantly more powerful than those in NGC 4151, as shown by the energetics in Figure 2.11. This is because the total ionized NLR mass

participating in the outflow is $\sim 2.2{\times}10^6\ M_\odot$ in Mrk 573, a factor of seven greater than NGC 4151's $\sim 3{\times}10^5\ M_\odot$ (Crenshaw et al. 2015). Another notable difference is the extent of the outflows, which reach ~ 600 pc in Mrk 573, but only ~ 140 pc for NGC 4151.

These results can be understood by comparing the physical properties of these two AGN. Mrk 573 has a SMBH mass of $\log(M_{BH}) = 10^{7.28}\ M_\odot$ (Woo & Urry 2002; Bian & Gu 2007), a bolometric luminosity of $L_{bol} \approx 10^{45.5}$ erg s^{-1}, and a corresponding accretion rate of $\dot{m}_{\rm acc} \approx 0.44\ M_\odot$ yr^{-1} (assuming $\dot{m}_{\rm acc} = L/\eta c^2$ with $\eta = 0.1$, Peterson 1997). For NGC 4151 these values are $\log(M_{BH}) = 10^{7.66}\ M_\odot$ (Bentz et al. 2006), $L_{bol} \approx 10^{43.9}$ erg s^{-1} for $D = 13.3$ Mpc, and $\dot{m}_{\rm acc} \approx 0.013\ M_\odot$ yr^{-1}. Thus despite the similar SMBH masses in these two objects their bolometric luminosities and corresponding accretion rates differ by ~ 1.6 dex, yielding $L_{bol}/L_{Edd} \approx 0.75$ for Mrk 573 and $L_{bol}/L_{Edd} \approx 0.01$ for NGC 4151.

Mrk 573 is releasing significantly more energy into the NLR, allowing for higher velocity outflows containing more mass that are driven to larger distances. Interestingly, the masses, velocities, and extraction sizes conspire so both objects have peak outflow rates $\sim 3\ M_\odot$ yr^{-1}. For this reason, comparing the outflow energetics between AGN may be more insightful.

2.7 Discussion

2.7.1 Comparison with Global Outflow Rates

We refer to single value mass outflow rates that are derived from mean conditions across the entire NLR as "global" outflow rates. There are two common techniques for obtaining global outflow rates. The first is to derive a geometric model, typically an ionized bicone, and fill it with material diluted by a filling factor to account for clumpiness. The second converts the observed luminosity of a hydrogen recombination line (e.g. Hβ, Pβ) to mass based on a mass-luminosity scaling relationship. We examine our results in the context of these techniques to explore systematics and uncertainties, and to compare with other AGN in a broader framework.

2.7.1.1 Geometric Approach

The geometric approach can take the form $\dot{M}_{out} = 2m_p n_e v A f$, where m_p is the proton mass, n_e is the electron density, v is the outflow velocity, A is the area of the bicone, f is a volume filling factor, and the factor of two accounts for two symmetric bicones (e.g. Müller-Sánchez et al. 2011). The filling factor accounts for the clumpiness of the gas and the fact that it does not fill the entire volume of the ionization cone. This method has the advantage of yielding quick estimates once a geometric model is adopted, but variations in the filling factor from object to object and across the NLR can result in uncertainties > 1 dex. This is compounded by assuming the outflow rates of each bicone are symmetric, which is not accurate for Mrk 573 (Figure 2.10). When photoionization models are not available, this discrepancy might be reduced by estimating the filling factor observationally for individual objects, which can be done using the luminosity of $P\beta$ when spectra are available (Riffel & Storchi-Bergmann 2011b; Müller-Sánchez et al. 2016).

For comparing with this technique, we adopt a mean velocity (rather than a maximum) that is representative of the majority of the outflow. We also adopt the hydrogen number density as compared to the electron density, with the two related by $n_H \approx 0.85 \times n_e$ (§2.4.4). We use our range of observed [S II] densities, a biconical geometry with a half opening angle of 38°, and radial extent of 600 pc to encompass the observed emission, and a range of NLR filling factors from the literature ($f \approx 0.001 - 0.1$, Storchi-Bergmann et al. 2010; Müller-Sánchez et al. 2011; Nevin et al. 2018). We find $\dot{M}_{out} \approx 8 - 800\ M_\odot\ \mathrm{yr}^{-1}$ for $n_e = 200$ cm^{-3}, and $\dot{M}_{out} \approx 65 - 6500\ M_\odot\ \mathrm{yr}^{-1}$ for $n_e = 1500$ cm^{-3}. These values are significantly higher than those derived using our photoionization models.

This discrepancy can be traced to the filling factors. From the volume of our biconical geometry intercepted by the slit, and the volumes of our model clouds, we calculate a mean filling factor of $f \approx 5.9 \times 10^{-5}$. Using this filling factor, we find $\dot{M}_{out} \approx 0.5 - 4\ M_\odot\ \mathrm{yr}^{-1}$ for $n_e = 200 - 1500$ cm^{-3}, which comfortably encompass our model derived outflow rates. It is important to note that our filling factor is arbitrarily low as compared to values in the

literature. If we adopted a geometry with material constrained to a disk, the filling factor would increase as the corresponding volume decreases, yielding the same mass outflow rates. For these reasons it is critical to calculate filling factors for individual objects.

Using the geometric technique to estimate mass outflow rates for the NLR of NGC 4151, Storchi-Bergmann et al. (2010) found a global outflow rate of $\sim 2.4\ M_{\odot}\ \mathrm{yr}^{-1}$ using $f = 0.11$ (biconical) or $f = 0.025$ (spherical). Similarly, Müller-Sánchez et al. (2011) found $\sim 9\ M_{\odot}\ \mathrm{yr}^{-1}$ using $f = 0.001$. These values are in overall agreement with the peak value of $\sim 3.0\ M_{\odot}\ \mathrm{yr}^{-1}$ from Crenshaw et al. (2015). This indicates that the two techniques can derive comparable mass outflow rates when calculated from physically motivated choices for the velocity, density, geometry, and filling factor of the system.

2.7.1.2 Luminosity Approach

The second technique that is closer to the methodology employed here is to convert an observed luminosity (e.g. Hβ, Hα, [O III]) to mass using a simple relationship that assumes uniform NLR conditions and that scales with density. This type of relationship is the same as that given in Equation 2.6, with the mass typically determined using a scaling relationship based on a single emission line and density, in contrast to our multi-component models that account for material of different densities and ionization states at the same spatial location. Employing the techniques of Nesvadba et al. (2006) and Bae et al. (2017), we calculate the NLR mass as $M = (9.73 \times 10^8\ M_{\odot}) \times L_{\mathrm{H}\alpha,43} \times n_{e,100}^{-1}$, where $L_{\mathrm{H}\alpha,43}$ is the Hα luminosity in units of 10^{43} erg s^{-1}, and $n_{e,100}^{-1}$ is the electron density in units of 100 cm^{-3}. Here we used the [O III] luminosity scaled by the average Hα/[O III] ratio as a proxy for $L_{\mathrm{H}\alpha}$. From this we derive $\dot{M}_{out} \approx 5 - 35\ M_{\odot}\ \mathrm{yr}^{-1}$ for $n_e = 1500 - 200$ cm^{-3}, the full range of our observed [S II] densities. The corresponding NLR mass estimate is $\sim 1 - 7$ times larger than that found from our models ($\sim 2.2 \times 10^6\ M_{\odot}$), highlighting the difference between employing a single density and multi-density gas phases at each location.

This method can have the advantage of deriving mass outflow rates with smaller systematic uncertainties than the geometric approach, but requires an accurate Balmer emission line luminosity or proxy obtained from spectroscopy or narrow-band imaging. As luminosity and density are physical indicators of the total gas mass (Peterson 1997), we strongly encourage the use of luminosity based methods for deriving total masses and outflow rates to avoid uncertain filling factors and geometries.

2.7.1.3 Recommendations for Comparison

The methodology used here that was modeled after Crenshaw et al. (2015) has the advantage of deriving spatially resolved mass outflow rates with small uncertainties that are critical for probing AGN feedback on scales of tens of parsecs in the NLRs of nearby AGN. However, this requires high quality spectroscopy and imaging, or optical Integral Field Unit (IFU) spectroscopy and detailed, time-intensive photoionization modeling. For targets where these data are unavailable, both of the techniques above can provide estimates of the global mass outflow rate with larger uncertainties.

The derived mass outflow rates will depend strongly on the choices of velocity, density, and geometry of the system. Different conventions throughout the literature can result in estimated mass outflow rates spanning ~ 3 orders of magnitude for individual objects! (see, e.g Karouzos et al. 2016; Bischetti et al. 2017; Perna et al. 2017; Nevin et al. 2018 for discussions).

When spatially resolved kinematics and density profiles are unfeasible, we would recommend using an average or flux weighted average velocity, as this will be more representative of the majority of the outflow than the peak velocity. In addition, densities should be determined from spectra whenever possible, as individual objects can vary significantly from typical NLR values, and the density profile as a function of radius can span more than a factor of 10 as shown here. [S II] is typically a strong choice in optical spectra, with the caveat that it will generally yield a lower limit to the electron density, as [S II] is a lower ionization line with

a peak emissivity toward the neutral zone of a cloud such that additional material can be hiding in the neutral phase because it is not contributing electrons to the ionized gas. In addition, higher ionization gas will generally have a lower density that is not probed by [S II]. Finally, the radial extent of the outflow must be determined precisely, which is only possible with spatially resolved spectroscopy.

The mass, kinetic energy, and momentum at each distance (Figure 2.11) may be added to obtain enclosed totals; however, the rates cannot. A continuous flow originating near the nucleus, shown by the dotted line in Figure 2.11, represents the minimum outflow rate. When in-situ acceleration is included, gas is driven at all distances and the total mass reaching the outer boundary will be larger. This requires an integration over time, assuming the gas travels without being destroyed, and is not equivalent to summing the mass outflow rates. The average outflow rate across all bins, and the area under the outflow curve representing the total momentum, are invariant to the number of bins. For these reasons, comparing the total outflow energetics between objects is more straightforward.

For a direct comparison with global outflow rates, we consider larger spatial extractions such that each bin contains more mass and must travel a larger δr. Reducing this to a single point with $M \approx 2.2 \times 10^6\ M_\odot$ and $\delta r = 600$ pc results in a global mass outflow rate of $\sim 2\ M_\odot\ \mathrm{yr}^{-1}$ for a mean velocity of 550 km s^{-1}.

2.7.2 Implications for Feedback

The global kinetic luminosity ($M = 2.2 \times 10^6\ M_\odot$, $\delta r = 600$ pc, $V = 550$ km s^{-1}) of the outflow in Mrk 573 is $L_{KE}/L_{bol} \approx 0.4 - 0.8\%$ of the AGN bolometric luminosity ($L_{bol} \approx 10^{45.5}$ erg s^{-1}, Kraemer et al. 2009). This is in the range of $0.5\% - 5\%$ used in some models of efficient feedback (Di Matteo et al. 2005; Hopkins & Elvis 2010) and is similar to the values reported for NGC 4151 (Storchi-Bergmann et al. 2010; Müller-Sánchez et al. 2011; Crenshaw et al. 2015). However, it is important to note that local AGN already have well-established

bulges, so comparing to models of effective feedback for higher redshift AGN requires further investigation.

Our results indicate that most of the outflow is accelerated in-situ within the NLR and does not originate from near the nucleus. This is seen in that the peak mass outflow rate is much greater than what would result from the amount of mass near the nucleus following the radial velocity law, as shown by the dashed line in Figure 2.11. The only nuclear outflow scenario that could produce the observed result would be if the nuclear outflow rate decreased and increased in a fashion exactly matching the shape and travel time of a cloud along the velocity profile, requiring inordinate fine tuning.

Our modeling is consistent with the conclusions of Fischer et al. (2017) that the NLR outflows are radiatively driven, with force multipliers $\sim 2000 - 3000$. Recently, Mou et al. (2017) also explored the possibility that these outflows are circumnuclear clouds accelerated by an accretion disk wind. Their numerical simulations of the NLR outflows in NGC 4151 match the mass outflow rates and kinetic luminosities, with some discrepancy in the velocity turnover at larger radii. The high temperatures of the model winds indicate they may be difficult to detect observationally. The comparison of these types of models to radiative driving for the more powerful outflows in Mrk 573 and other AGN should yield valuable physical insight into the launching mechanisms responsible for NLR outflows.

A variety of metrics are employed in the literature to determine if outflows deliver "effective" feedback to their host galaxies by impacting star formation (Leung et al. 2017). This can include triggering star formation through positive feedback (Silk 2013; Mahoro et al. 2017), quenching star formation through negative feedback (Wylezalek & Zakamska 2016), or more complex interactions (Zubovas & Bourne 2017). These comparisons require accurate star formation rates (SFRs), which are typically estimated through Hα luminosities. Determining SFRs for AGN is difficult due to the contamination by AGN ionized gas (Imanishi et al. 2011). Successful techniques include using estimates in wavebands where the AGN is weakly emitting, utilizing high spatial resolution optical IFU data to separate the emission (Davies

et al. 2016), and the emission from hydrocarbons that are excited by star forming regions (Shipley et al. 2013, 2016). A detailed investigation of the SFR is beyond the scope of this work, and future observations with the *James Webb Space Telescope* (JWST) will enable spatially resolved distribution studies of star-forming excited hydrocarbons (Kirkpatrick et al. 2017). However, it is worth noting that AGN can also excite hydrocarbons (Jensen et al. 2017).

2.7.3 Missing Mass: X-ray & Molecular Outflows

These results account for the optical and some UV emission line gas; however, AGN outflows are also seen in more highly ionized UV/X-ray gas that is not accounted for in our mass outflow rates. For NGC 4151, Wang et al. (2011) found a mass outflow rate of $\dot{M}_{out} \approx 2.1\ M_{\odot}$ yr^{-1} for the X-ray emitting gas, while Crenshaw & Kraemer (2012) derived a mass outflow rate of $\dot{M}_{out} \approx 0.3 - 0.7\ M_{\odot}$ yr^{-1} for the UV/X-ray absorbers, indicating two additional important outflow components. The presence of an ultrafast outflow (UFO) traveling at $0.1c$ with a much smaller mass outflow rate ($\dot{M}_{out} \approx 0.003 - 0.04\ M_{\odot}$ yr^{-1}) than the NLR outflows, but comparable kinetic luminosity ($\dot{E} \sim 10^{42} - 10^{43}$ erg s^{-1}), underscores the need to study outflows across all spatial scales and energy regimes (Schurch et al. 2003; Kraemer et al. 2005, 2006; Piro et al. 2005; Tombesi et al. 2010, 2011, 2012).

Studies of Mrk 573 in the UV and X-rays (Ferland & Osterbrock 1986; Awaki et al. 1991) with *Chandra* and *XXM-Newton* (Guainazzi et al. 2005; Paggi et al. 2012; Reynaldi et al. 2012) have found very highly ionized gas including the Fe XXV Kα line. Photoionization modeling by Bianchi et al. (2010) and Gonzalez-Martin et al. (2010) found that two high ionization components were needed to describe the X-ray gas. It is interesting to note that the ionization parameters of our highest ionization components begin to approach the conditions of the components modeled in the X-rays, suggesting a natural continuum of physical conditions in the NLR, as mentioned by Gonzalez-Martin et al. (2010). If this X-ray material is outflowing, it may contribute significantly to feedback.

At much lower temperatures, AGN driven outflows of molecular hydrogen (H_2) have been observed (Sturm et al. 2011; Feruglio et al. 2015; Janssen et al. 2016; Rupke et al. 2017). There are several H_2 lines present in near infrared spectra of Mrk 573 (Veilleux et al. 1997; Fischer et al. 2017) that probe warmer molecular gas, and we presented a kinematic map showing signatures of outflow in Fischer et al. (2017). In future work we will address the contribution of warm molecular outflows to the overall feedback and energetics of Mrk 573. While the total mass in the warm molecular gas phase is significantly smaller than the optical emission line gas, it may represent the warm skin of the more massive cold molecular reservoirs that form stars. Probing the cold H_2 in detail will require radio observations with observatories such as the Atacama Large Millimeter Array (ALMA).

2.8 Conclusions

We used long-slit spectroscopy, [O III] imaging, and Cloudy photoionization models to determine the mass outflow rates and energetics as functions of distance from the nucleus in the Seyfert 2 galaxy Mrk 573. This is the second spatially resolved outflow rate for an AGN, and the first for a Type 2. Our conclusions are as follows:

1. The outflow contains $M \approx 2.2 \times 10^6\ M_\odot$ of ionized gas, with a total kinetic energy of $E \approx 5.1 \times 10^{54}$ erg. This is significantly more ionized gas and energy than the NLR outflow in the lower luminosity Seyfert 1 galaxy NGC 4151 (Crenshaw et al. 2015).

2. We find that the outflows extend to ~ 600 pc, reaching a peak mass outflow rate of $\dot{M}_{out} \approx 3.4 \pm 0.5\ M_\odot\ \mathrm{yr}^{-1}$ at a distance of 210 pc from the SMBH. Our spatially resolved measurements are consistent with in-situ acceleration of the circumnuclear gas.

3. The global kinetic luminosity of the outflow is $L_{KE}/L_{bol} \approx 0.4 - 0.8\%$ of the AGN bolometric luminosity. This is similar to values used in feedback models and those reported for NGC 4151.

4. Methods for determining global outflow rates are subject to larger uncertainties if photoionization models are not used, and luminosity-based methods are preferred over geometric, as they invoke physical tracers of the gas mass. All techniques require accurate gas densities, mean velocities, and system geometry. Spatially resolved outflow rates cannot be co-added to obtain global estimates.

5. Our results account for the UV/optical emission line gas, and multi-wavelength studies of individual AGN are needed to understand the importance of additional outflow components including hot X-ray and cold molecular gas phases.

CHAPTER 3

MARKARIAN 34[1]

3.1 Physical Characteristics of Markarian 34

We selected the Type 2 quasar (QSO2) Markarian 34 (Mrk 34, SDSS J103408.58+600152.1, MCG+10-15-104) to extend our sample to higher redshifts, bolometric luminosities, and outflow radii, complementing our studies in Crenshaw et al. (2015) and Revalski et al. (2018a), which was presented in Chapter 2. The central AGN resides in an Sa-type galaxy with spiral arms and a weak bar structure (Nair & Abraham 2010) that are visible in Figure 3.1. Using our observations, we derive (§3.3.2) a new heliocentric redshift of $z = 0.05080$, a recessional velocity of 14,843 km s^{-1}, a Hubble distance of 209 Mpc, and a spatial scale of 1014 pc arcsec^{-1}, assuming $H_0 = 71$ km s^{-1} Mpc^{-1}.

In Fischer et al. (2018) we found that the host galaxy major axis is along a position angle (PA) of $\approx 30°$, with an ellipticity of $e = 1 - b/a = 0.25$, and an inclination of $i = cos^{-1}(b/a) = 41°$, in agreement with previous studies (Haniff et al. 1988). The NLR major axis is along PA $\approx 150°$, which is similar to the observed radio jet that displays a double-lobed structure, and enhanced emission in regions of low gas excitation (Ulvestad & Wilson 1984; Unger et al. 1987; Baum et al. 1993; Falcke et al. 1998; Nagar & Wilson 1999). The ionized gas displays multiple kinematic components, and emission has been traced to

[1]This chapter was originally published in the Astrophysical Journal, Volume 867, Pages 88-117 on 2018 November 2, under the title "Quantifying Feedback from Narrow Line Region Outflows in Nearby Active Galaxies. II. Spatially Resolved Mass Outflow Rates for the QSO2 Markarian 34" by Revalski et al. (2018b). doi:10.3847/1538-4357/aae3e6. Note: A calculation error was discovered following publication in the Astrophysical Journal and amended numerical values are reflected in Table 3.9, Figure 3.9, Figure 3.10, and in the discussion and conclusions.

radial distances of $\sim$ 12 kpc (Whittle et al. 1988). These details are explored extensively in Rosario (2007).

As discussed by Gandhi et al. (2014), Mrk 34 is the nearest Compton-thick QSO2, and a firm black hole mass estimate is not currently available. A water maser has been detected (Henkel et al. 2005; Liu et al. 2017), but a resolved velocity map has not yet been obtained. Estimates from the $M_{BH} - \sigma_\star$ method using proxies for $\sigma_\star$ (Wang et al. 2007; Oh et al. 2011) yield a mass range of $M_{BH} \approx 10^{6.8-7.5}\ M_\odot$, resulting in a wide range of Eddington ratios with $L_{bol}/L_{Edd} \sim 1 - 10$. We adopt a bolometric luminosity of $\log(L_{bol}/\mathrm{erg\ s^{-1}}) = 46.2 \pm 0.4$ (§3.3.2). The host galaxy morphology and ionized gas distribution within the NLR are shown in Figure 3.1.

3.2 Observations

3.2.1 Hubble Space Telescope

The *Hubble Space Telescope* spectroscopy and imaging used in this study were obtained with the Space Telescope Imaging Spectrograph (STIS), Wide Field Camera 3 (WFC3), and Wide Field and Planetary Camera 2 (WFPC2/PC). We employ low and medium-dispersion spectra to characterize the physical conditions and kinematics of the emission line gas, as well as [O III] imaging to determine the ionized gas mass. The calibrated data were retrieved from the Mikulski Archive at the Space Telescope Science Institute, and the multiple spatially dithered exposures were combined using the Interactive Data Language (IDL). These data are summarized in Table 3.1, and all spectral observations employed the $52'' \times 0\farcs2$ slit.

In Fischer et al. (2018) we used the G430M observations with a resolving power of $R \approx 9400$ to characterize the NLR kinematics of Mrk 34. These slits are labeled A, B, and C in Figure 3.1, and additional details are given in Fischer et al. (2013, 2018). To characterize the physical conditions of the gas, we obtained new STIS spectroscopy with a larger wavelength range and resolving powers of $R \approx 900 - 1000$ using the G430L/G750L gratings under Program ID 14360 (PI: M. Elvis). The position of these observations is

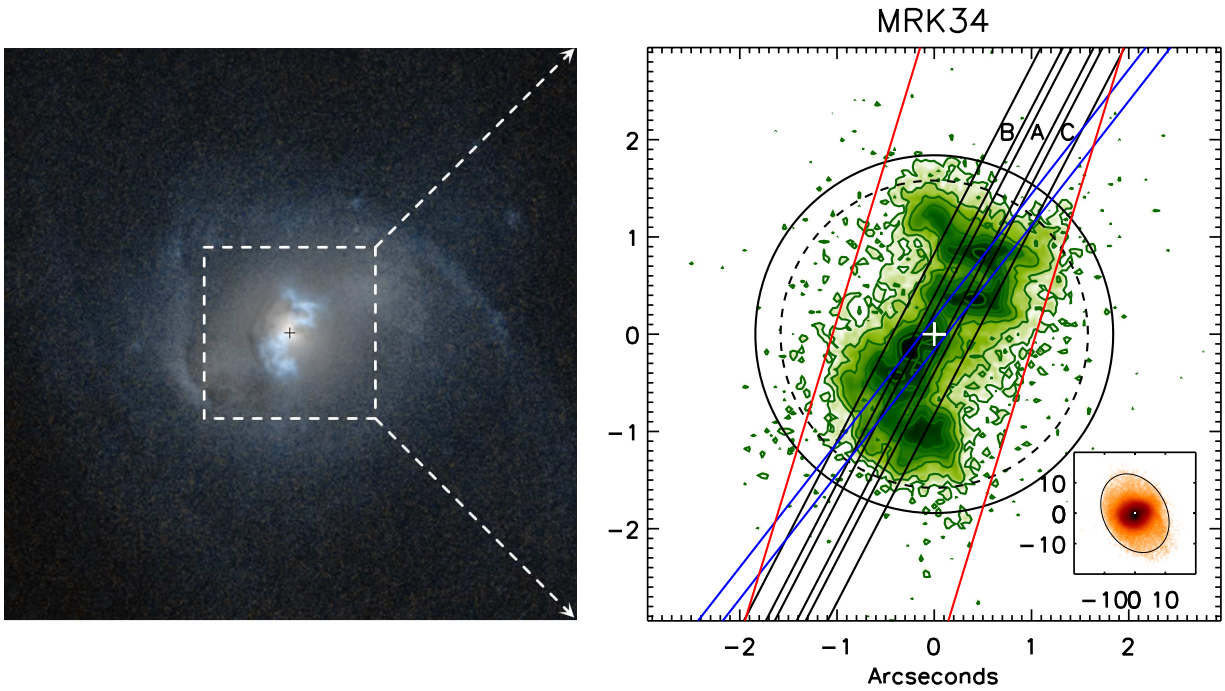

Figure 3.1 The left panel is a 20″ × 20″ composite image of Mrk 34 with a 6″ × 6″ inset square. The individual color channels are composed of *HST* WFC3/UVIS F814W (red) and WFPC2/PC F547M (blue) images, which are dominated by galaxy continuum and [O III] emission, respectively. The right panel shows an [O III] flux contour map of the NLR of Mrk 34 modified from Fischer et al. (2018), where the dashed and solid circles are the outflow radius and 3σ flux detection limit, respectively. The solid lines delineate the locations and slit widths of the observations, with *HST* STIS using the G430M grating and 0.″2 slit in black, *HST* STIS using the G430L/G750M gratings and 0.″2 slit in blue, and our APO DIS observations along PA = 163° with a 2.″0 slit in red. The inset panel is a 40″ × 40″ SDSS r-band image of Mrk 34 with the best-fitting elliptical isophote used to derive the ellipticity and inclination of the host galaxy disk. North is up and east is to the left in both panels. This image was created with the help of the ESA/ESO/NASA FITS Liberator.

represented by a blue slit in Figure 3.1, and extracted spectra are shown in Figure 3.2. The corollary X-ray observations obtained with *Chandra* to investigate shocks associated with the outflows will be presented in a future paper (Fischer et al. in prep).

To examine the NLR structure, we created a color-composite image using *HST* WFC3/UVIS images with the F814W and F547M filters. An ArcSinh(x) stretch function was applied to reveal faint details in each image, and then they were combined into a single color average. The "Z-shaped" NLR structure and its continuation into the spiral arms are visible in the left panel of Figure 3.1. The [O III] emission line image used to calculate the ionized gas

mass was taken from our study in Fischer et al. (2018), which consists of the F547M images discussed previously, in combination with an F467M image for continuum subtraction.

3.2.2 Apache Point Observatory

We obtained additional spectra using the Dual Imaging Spectrograph on the Astrophysical Research Consortium's Apache Point Observatory 3.5 meter telescope in Sunspot, New Mexico. The DIS uses a dichroic element to split light into blue and red channels, allowing for simultaneous data collection in the Hβ and Hα regions of the spectrum. The spectral resolution is 1.23 Å in the blue and 1.16 Å in the red, corresponding to resolving powers of $R \approx 3400 - 6200$. These spectra have lower spatial resolution than the *HST* data, but allow us to search for outflow signatures outside of the narrow *HST* slits, probe the ENLR kinematics, and detect important diagnostic emission lines with greater S/N out to larger distances from the nucleus. We obtained observations at four evenly spaced position angles of $\sim 73°$, $118°$, $163°$, and $208°$, using a $2\farcs0$ slit at low air masses (Table 3.1). While the slits were not at the ideal parallactic angle, we compared with available SDSS spectra and found no evidence for loss of blue light due to atmospheric refraction.

We reduced the data using IRAF (Tody 1986, 1993)[2] following the standard techniques of bias subtraction, image trimming, bad pixel replacement, flat-fielding, Laplacian edge cosmic ray removal (van Dokkum 2001), image combining, and sky line subtraction. Wavelength calibration was completed using comparison lamp images taken before the science exposures, and velocities were converted to heliocentric values. Flux calibration was completed using Oke standard stars (Oke 1990) and the air mass at mid-exposure. The DIS dispersion and spatial axes are not perpendicular, so we fit a line to the galaxy continuum and resampled the data to ensure that measurements of emission lines from the same pixel row sample the same spatial location. We focus on our observations at PA = $163°$, closest to the NLR major axis.

[2]IRAF is distributed by the National Optical Astronomy Observatories, which are operated by the Association of Universities for Research in Astronomy, Inc., under cooperative agreement with the National Science Foundation.

Table 3.1. Summary of Observations

Observing Facility	Instrument Name	Observation ID	Program ID	Date (UT)	Exposure Time (s)	Grating / Filter	Spectral Dispersion (Å pix^{-1})	Wavelength Centroid (Å)	Wavelength Range (Å)	Spatial Scale ($''$ pix^{-1})	Position Angle (deg)	Mean Air Mass	Seeing ($''$)
HST	STIS CCD	O5G404010	8253	2000-02-17	1500	G430M	0.28	5216	5076-5357	0.051	152.5	...	...
HST	STIS CCD	O5G404030	8253	2000-02-17	1460	G430M	0.28	5216	5076-5357	0.051	152.5*	...	...
HST	STIS CCD	O5G404040	8253	2000-02-18	1460	G430M	0.28	5216	5076-5357	0.051	152.5*	...	...
HST	STIS CCD	OD2501010	14360	2016-02-24	437	G430L	2.73	4300	2900-5700	0.051	143.1	...	...
HST	STIS CCD	OD2501020	14360	2016-02-24	437	G430L	2.73	4300	2900-5700	0.051	143.1	...	...
HST	STIS CCD	OD2501030	14360	2016-02-24	437	G430L	2.73	4300	2900-5700	0.051	143.1	...	...
HST	STIS CCD	OD2501040	14360	2016-02-24	143	G750L	4.92	7751	5240-10270	0.051	143.1	...	...
HST	STIS CCD	OD2501050	14360	2016-02-24	143	G750L	4.92	7751	5240-10270	0.051	143.1	...	...
HST	STIS CCD	OD2501060	14360	2016-02-24	143	G750L	4.92	7751	5240-10270	0.051	143.1	...	...
HST	WFC3/UVIS	IBY80U020	12903	2013-10-09	75	F814W	...	8030	1536	0.04	...	...	...
HST	WFC3/UVIS	IBY80U030	12903	2013-10-09	75	F814W	...	8030	1536	0.04	...	...	...
HST	WFPC2/PC	U9PM0201M	10873	2007-06-07	1300	F547M	...	5468	483	0.046	...	...	...
HST	WFPC2/PC	U9PM0202M	10873	2007-06-07	1300	F547M	...	5468	483	0.046	...	...	...
HST	WFPC2/PC	U9PM0203M	10873	2007-06-07	1300	F547M	...	5468	483	0.046	...	...	...
HST	WFPC2/PC	U9PM0204M	10873	2007-06-07	1300	F547M	...	5468	483	0.046	...	...	...
HST	WFPC2/PC	U9PM0207M	10873	2007-06-07	1300	F547M	...	5468	483	0.046	...	...	...
HST	WFPC2/PC	U9PM0208M	10873	2007-06-07	1300	F547M	...	5468	483	0.046	...	...	...
HST	WFPC2/PC	U9PM0205M	10873	2007-06-07	1300	F467M	...	5468	483	0.046	...	...	...
HST	WFPC2/PC	U9PM0206M	10873	2007-06-07	1300	F467M	...	5468	483	0.046	...	...	...
HST	WFPC2/PC	U9PM0209M	10873	2007-06-07	1300	F467M	...	5468	483	0.046	...	...	...
HST	WFPC2/PC	U9PM020AM	10873	2007-06-07	1300	F467M	...	5468	483	0.046	...	...	...
APO	DIS	...	...	2017-01-31	900	B1200	0.615	4898	4257-5517	0.42	73	1.13	1.22
APO	DIS	...	...	2017-01-31	900	R1200	0.580	6600	6006-7192	0.40	73	1.13	1.22
APO	DIS	...	...	2017-04-23	900	B1200	0.615	4900	4273-5545	0.42	118	1.14	1.80
APO	DIS	...	...	2017-04-23	900	R1200	0.580	6600	5996-7183	0.40	118	1.14	1.80
APO	DIS	...	...	2017-01-31	900	B1200	0.615	4898	4257-5517	0.42	163	1.17	1.22
APO	DIS	...	...	2017-01-31	900	R1200	0.580	6600	6005-7191	0.40	163	1.17	1.22
APO	DIS	...	...	2014-11-19	900	B1200	0.615	5380	4734-5584	0.42	208	1.20	1.13
APO	DIS	...	...	2014-11-19	900	R1200	0.580	6582	5990-7179	0.40	208	1.20	1.13

Note. — A summary of the observations and data used in this study. The columns list the observing facility, instrument, MAST archive dataset name, *HST* Program ID, observation date, exposure time, grating (for spectra) or filter (for imaging), spectral dispersion, wavelength centroid, wavelength range (for spectra) or bandpass (for imaging), spatial resolution, position angle (for spectra), air mass, and seeing. All *HST* values are defined in their respective instrument handbooks (Riley 2017; McMaster & et al. 2008; Dressel 2012), with the exact STIS spatial scale quoted as 0.05078$''$ pix^{-1}. *These observations are spatially offset from the nucleus by $\pm 0\farcs28$ (see Figure 3.1).

3.3 Analysis

3.3.1 Spectral Fitting

We fit Gaussian profiles to all emission lines in our spectra to obtain the gas kinematics and emission line flux ratios for comparison with photoionization models. Some of the extracted spectra are shown in Figure 3.2. We employ a Bayesian fitting routine developed for our recent kinematic studies (Fischer et al. 2017, 2018) based on the Importance Nested Sampling algorithm in MultiNest[3] (Feroz & Hobson 2008; Feroz et al. 2009, 2013; Buchner et al. 2014), and a detailed description is given in the Appendix of Fischer et al. (2017). We require an emission line to have a height signal-to-noise ratio (S/N) of > 2 in our *HST* spectra, and S/N > 3 in our APO spectra, for a positive detection.

As in Chapter 2, we use a spectral template method by first fitting the strong [O III] emission line, and then use the Gaussian fit parameters to calculate the centroids and widths for all other lines at each location. This ensures that we are sampling the same kinematic components in each line, although minor differences in the intrinsic line widths may be neglected (see §2.3.1). The widths are scaled to maintain the same intrinsic velocity and account for the instrumental line-spread functions. The height of each component is then allowed to vary to encompass the total line flux.

We further improve the fitting procedure by fixing the relative height ratios of doublet lines to their theoretical values (Osterbrock & Ferland 2006). Specifically, [O III] $\lambda\lambda$5007/4959 = 3.01, [O I] $\lambda\lambda$6300/6363 = 3.0, and [N II] $\lambda\lambda$6584/6548 = 2.95. The resulting fits to key emission lines are shown in Figure 3.3 and the Appendix.

The uncertainty in flux for each line is calculated from the residuals between the data and fit. As we detect multiple kinematic components, we scale the uncertainty for each component based on its fractional contribution. If $F = \sum f_i$ is the total flux of all N Gaussians, each of flux f_i, and δF is the difference in flux between the data and fit, then the fractional flux

[3] `https://ccpforge.cse.rl.ac.uk/gf/project/multinest/`

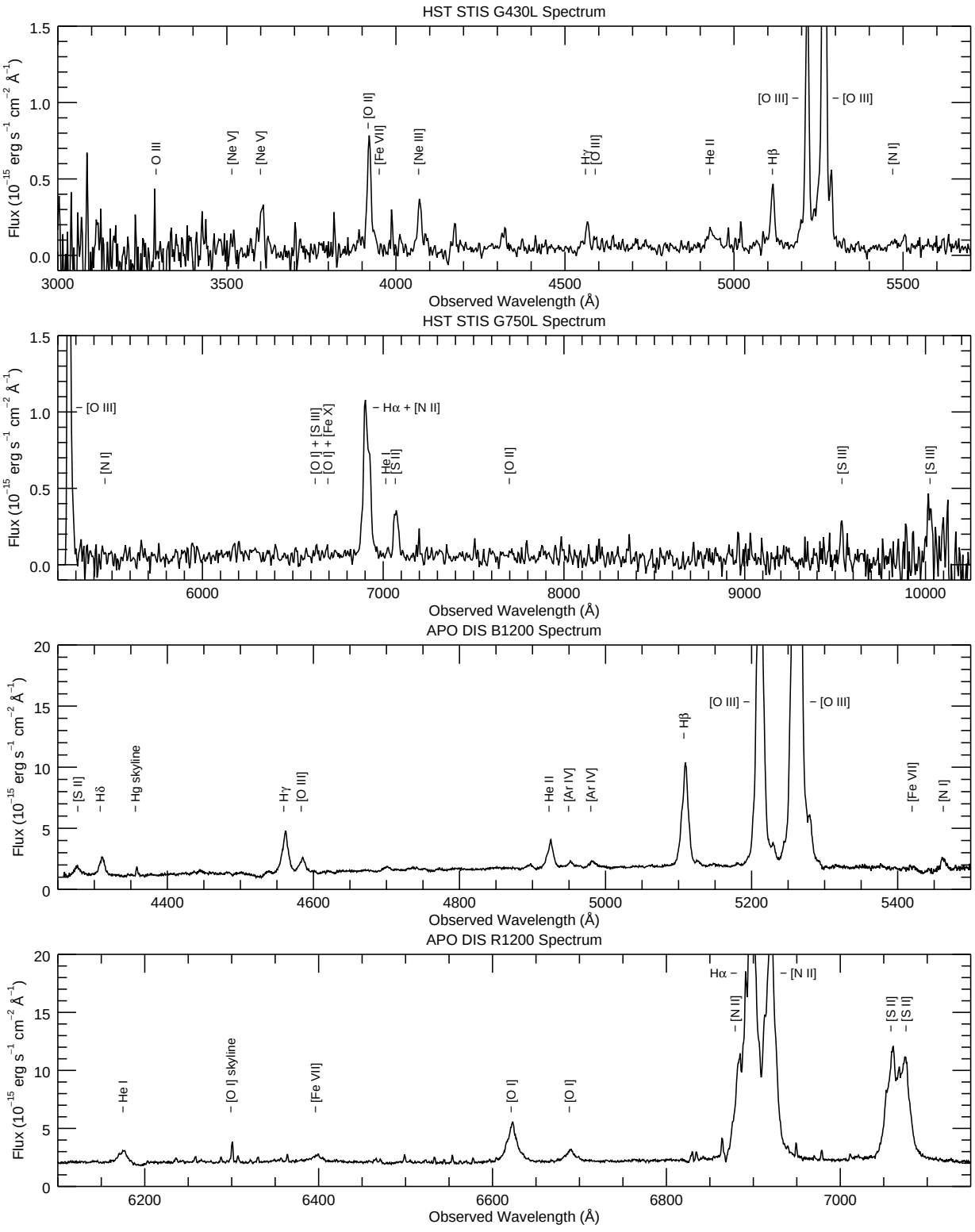

Figure 3.2 Spectral traces centered on the nucleus and spatially summed over $\sim 1\farcs3$ and $\sim 2\farcs9$ for the *HST* and APO data, respectively, with the positions of common emission lines labeled. The spectra are shown at observed wavelengths, and from top to bottom are: *HST* STIS G430L, *HST* STIS G750L, APO DIS B1200, and APO DIS R1200.

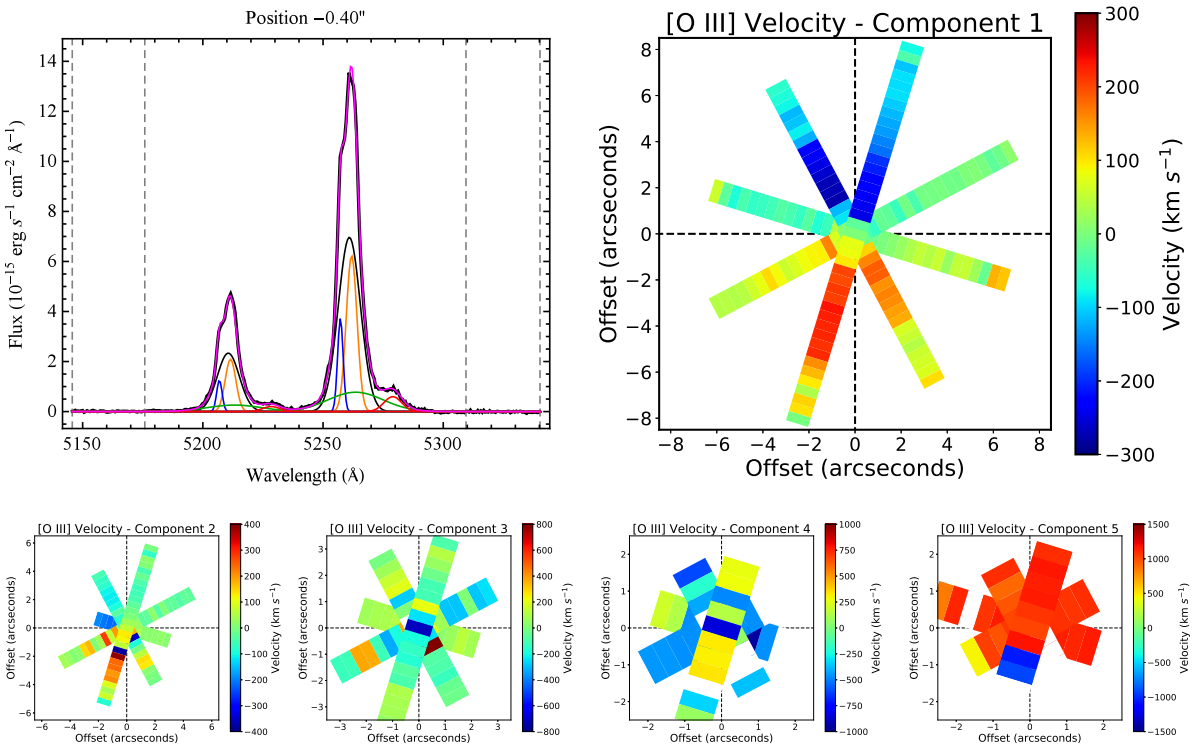

Figure 3.3 The left panel is a spectral trace of the [O III] doublet from our APO DIS observations along PA = 163° at a position 0.″4 SE of the nucleus, overlaid with a multi-component fit. The data are represented by a thick black line, and the composite model by magenta. The individual kinematic components are color-coded from strongest to weakest peak flux in the following order: black, orange, blue, green, and red. See the Appendix for additional fits. The right panel shows the observed velocities at each position for the strongest [O III] λ5007 emission line component in each of the four APO observations. The redshifts and blueshifts are a signature of galactic rotation. The lower row shows the observed velocities for the second, third, fourth, and fifth components. Note the different spatial range displayed in each panel. The observations employed a 2″ wide slit and are represented by 1″ wide rectangles for visibility. North is up, and East is to the left.

uncertainty for each i-th component is

$$\sigma f_i = \left(\frac{\delta F}{f_i \sqrt{N}} \right). \tag{3.1}$$

3.3.2 Ionized Gas Kinematics

The observed gas kinematics are significantly more complex than those seen in Mrk 573 (Chapter 2). In that target, we observed a single outflowing component that transitioned

to rotation at a radial distance of $\sim$ 600 pc. Here, we observe a combination of rotational and outflow kinematics at all radial distances $\lesssim 1\farcs6$ from the nucleus. To derive a velocity law that describes the intrinsic outflow velocity at each position, we created a flux-weighted mean velocity profile from the three parallel *HST* STIS G430M observations (Rosario et al. 2008; Fischer et al. 2013, 2018). This yields a better average velocity profile over the spatial extent of the NLR than was available with our single slit position for Mrk 573. As the two offset observations do not pass through the nucleus, there is no zero point, and the nuclear distance of each pixel is a function of position along the slit. The projected nuclear distance in arcseconds for each pixel is then represented by Pythagorean's theorem,

$$D = \sqrt{(\delta N \times S)^2 + (\delta R)^2} \tag{3.2}$$

where δN is the number of pixels from the pixel passing closest to the nucleus as defined by the continuum peak, S is the STIS pixel scale of $0\farcs05078$ pixel^{-1}, and $\delta R = 0\farcs28$ is the offset distance of the parallel slits. The results of this procedure are shown in the left panel of Figure 3.4. Next, we grouped the resulting kinematic components at each distance into either rotation or outflow based on their velocities, and created a single flux-weighted velocity profile with one rotational and outflow component at each distance, shown in the middle panel of Figure 3.4. This also allows us to derive the fraction of flux in the outflowing component relative to the total flux. Finally, the velocities and positions were corrected for projection effects using Equations 2.1 and 2.2, with $i = 41^\circ$ and $\varphi = 77^\circ$. This technique assumes that the outflows are moving radially outward along the galactic disk as suggested by Fischer et al. (2017). The resulting maximum deprojected velocities are $\sim$ 2000 km s^{-1}. This provides us with the intrinsic outflow velocity and the fraction of flux in outflow that are needed to calculate the mass outflow rates and energetics. Further discussion of the kinematics is presented in Fischer et al. (2018).

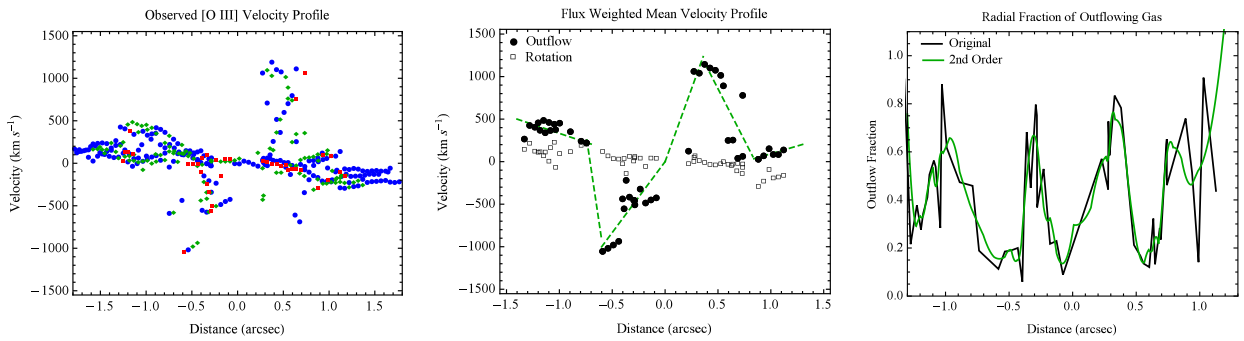

Figure 3.4 Left: The measured kinematics from the three parallel G430M slits (Fischer et al. 2018) after spatial alignment. The components are sorted from largest to smallest flux as blue circles, green diamonds, and red squares, respectively. Middle: The flux-weighted average velocity profile with components classified as rotation (open squares) or outflow (filled black circles), with the best linear fit in dashed green. Right: The ratio of the outflowing flux to the total flux as a function of distance, with the data in black and a second-order fit in green. Southeast is to the left and Northwest is to the right in all figures.

We also applied our fitting routine to the multiple APO DIS long-slit observations to trace the kinematics and physical conditions of the gas at larger radii. We require up to five Gaussian components to match the observed line profiles near the nucleus, in agreement with the study by Whittle et al. (1988). Assigning a physical meaning to each component must be done cautiously, as a wide, low-flux component may represent a superposition of the non-Gaussian emission line wings, rather than a physical component of gas with a unique velocity (Peterson 1997). An example of our multi-component emission line fitting is shown in Figure 3.3, with additional fits provided in the Appendix. In Figure 3.3 we also show the observed velocities for the strongest emission line component along each of our APO DIS observations in the form of a pseudo-integral field unit (IFU) velocity field, which shows characteristic redshifts and blueshifts indicating that the underlying galactic rotation is traced by at least one emission line component at all radii.

We present the observed velocities, full width at half maxima (FWHM), and integrated line fluxes for all components in our four APO DIS observations in Figure 3.5. Due to the 2″ wide slit, the inner regions of all four slits sample the same gas and kinematic components. The maximum rotational velocity is seen for PA = 208°, along the host galaxy major axis.

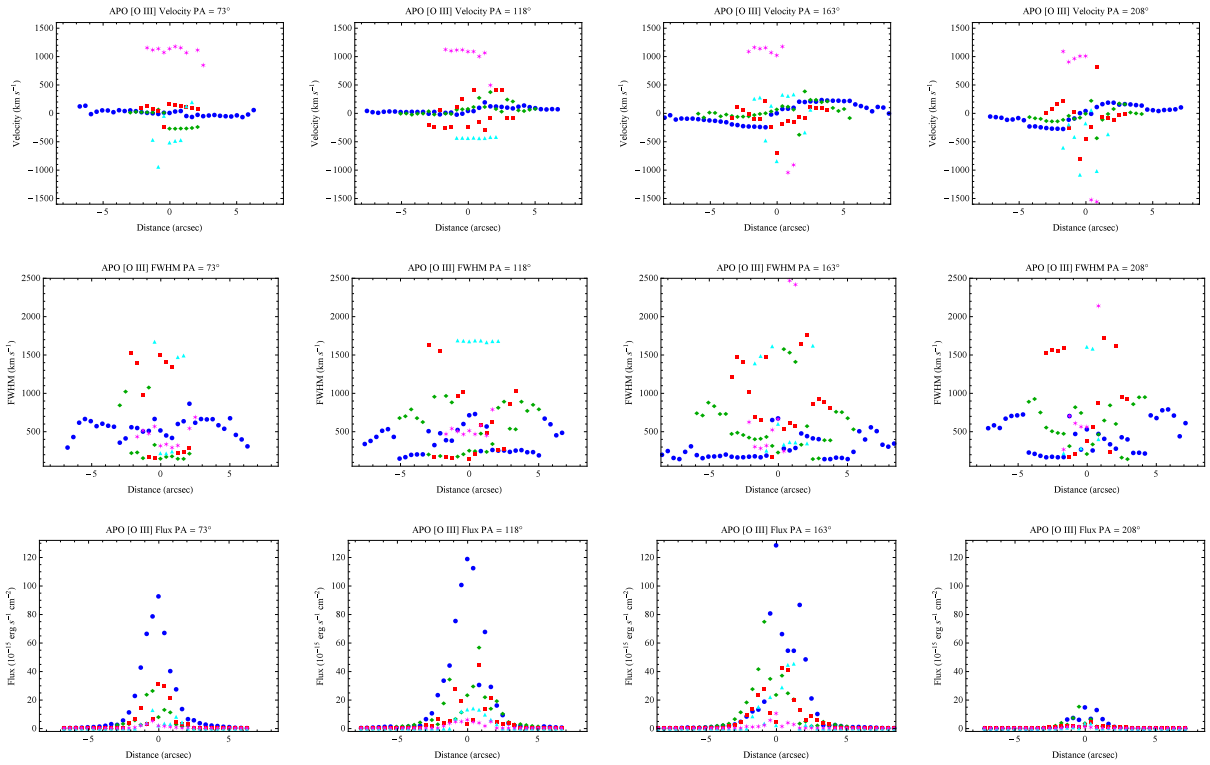

Figure 3.5 The observed velocities (top), FWHM (middle), and integrated line fluxes (bottom) for the [O III] λ5007 emission line in each of the four long-slit APO observations. The points are color-coded from strongest to weakest flux in the order: blue circles, green diamonds, red squares, cyan triangles, and magenta stars. Left to right are position angles 73°, 118°, 163°, and 208°, East of North.

The large velocity amplitude of the strongest component along PA = 163°, combined with the weak but highly redshifted $\sim$ 1000 km s^{-1} component seen in all slits, suggests that the outflows extend to larger distances than seen in the *HST* data.

Using our APO observations, we derive a new heliocentric redshift, recessional velocity, Hubble distance, and spatial scale for Mrk 34. These are based on the centroids of the rotational component of the [O III] emission line from the central pixel of each PA. The quoted errors are purely instrumental, and the true uncertainty in distance and spatial scale will be dominated by peculiar motion of the galaxy relative to the Hubble flow, which can be up to $\sim$ 600 km s^{-1}. For $H_0 = 71$ km s^{-1} Mpc^{-1},

$$z = \left(\frac{\lambda - \lambda_0}{\lambda_0}\right) = 0.05080 \pm 0.00005, \tag{3.3}$$

$$\frac{v}{c} = \frac{(1+z)^2 - 1}{(1+z)^2 + 1} = 14843 \pm 21 \text{ km/s}, \tag{3.4}$$

$$D = \left(\frac{v}{H_0}\right) = 209.1 \pm 0.3 \text{ Mpc}, \tag{3.5}$$

$$R = \left(\frac{D(pc)}{206265}\right) = 1013.5 \pm 1.4 \text{ pc}/'', \tag{3.6}$$

where λ is the observed wavelength, and λ_0 is the rest wavelength of [O III] λ5007 (5006.843 Å in air, 5008.240 Å in vacuum). This uses the relativistic velocity expression, and the mean Hubble velocity ($v \approx cz$) and distance are 15,229 km s^{-1} and 214.5 Mpc, respectively, consistent with the literature (Whittle et al. 1988). Finally, we derive the bolometric luminosity using $L_{bol} = 3500 \times L_{[\text{O III}]}$, with a scatter of 0.38 dex (Heckman et al. 2004). Using an observed [O III] luminosity[4] of $\log(L_{[\text{O III}]}) = 42.64 \pm 0.24$ erg s^{-1}, we find $\log(L_{bol})$ $= 46.2 \pm 0.4$ erg s^{-1}.

3.3.3 Emission Line Ratios

We used the Gaussian fit parameters to calculate integrated emission line fluxes and their ratios relative to Hβ. We determined line ratios with the fluxes of all kinematic components added together for the highest possible S/N, as well as for each individual component to probe differences in the physical conditions between rotational and outflowing gas. The observed and reddening-corrected line ratios for the sum of all components are given in Tables 3.2 and 3.3 for the *HST* data, and in Tables 3.4 and 3.5 for the APO data, respectively. The observed emission line ratios for the individual components with a S/N > 2 are given in the Appendix. The procedure for reddening correction is described in §2.3.3.

[4]Published values span $\log(L_{[\text{O III}]}) \approx 42.39 - 42.83$ erg s^{-1} (Reyes et al. 2008; Heckman et al. 2005, this work). The luminosity is higher but consistent with the relationship of Netzer (2009), which with a reddening correction yields $\log(L_{bol}) = 45.8 \pm 0.4$ erg s^{-1}.

There are a maximum of two components for the *HST* data, sorted into rotation and outflow based on velocity, and up to five components for the APO data, sorted from highest to lowest peak flux. The larger number of components in the APO observations can be attributed to the wider slit that encompasses additional emission line knots, and spatial blending across adjacent pixels due to atmospheric smearing. The weakest components likely encompass the non-Gaussian wings of the combined profile, and we caution against a physical interpretation for these ratios. Only emission within $\lesssim 2''$ of the nucleus displays outflow kinematics and are included in our tables.

The *HST* data have detectable emission over a limited spatial extent with modest S/N and large uncertainties due to the relatively short exposure times of the G430L/G750L observations, allowing us to place some constraints on the physical conditions in the gas at very high spatial resolution. The APO observations yield emission line ratios over a larger spatial extent with higher S/N and smaller uncertainties, but at lower spatial resolution, allowing us to probe conditions on large scales.

To first order, our flux-to-mass scale factor and the resulting ionized gas masses depend solely on the gas density and the ratio of [O III]/Hβ, and the latter does not vary by more than a factor of ~ 2 between components at each location. The similarity between the [O III]/Hβ ratios in the *HST* and APO observations suggests that both sample gas with similar physical conditions and ionization states. The mildly larger [O III]/Hβ ratios in the *HST* observations are likely due to the noisy continuum regions surrounding Hβ and/or isolating individual knots of emission. In addition, the consistency between the [O III]/Hβ ratios in all five components of the APO data suggests that modeling the combined emission line ratios yields a sufficiently accurate representation of the conditions in the photoionized gas.

Table 3.2. Observed Emission Line Ratios - Markarian 34 *HST* STIS Spectrum - Sum of All Components

Emission Line	−0.″66	−0.″56	−0.″46	−0.″36	−0.″25	−0.″15	−0.″05	+0.″05	+0.″15	+0.″46	+0.″56	+0.″66
[Ne V] λ3426	... ± ...	0.67 ± 0.25	0.98 ± 0.43	0.80 ± 0.35	1.21 ± 0.74	1.13 ± 0.50	0.70 ± 0.22	... ± ...	... ± ...	... ± ...	... ± ...	... ± ...
[O II] λ3728	2.92 ± 1.20	1.96 ± 0.73	2.02 ± 0.89	1.61 ± 0.71	1.19 ± 0.73	1.28 ± 0.56	1.61 ± 0.51	1.30 ± 0.44	1.95 ± 1.28	1.14 ± 0.89	1.34 ± 0.74	1.96 ± 0.62
[Ne III] λ3870	1.50 ± 0.62	0.91 ± 0.34	0.96 ± 0.42	0.95 ± 0.42	0.75 ± 0.46	0.80 ± 0.35	0.63 ± 0.20	0.36 ± 0.12	0.68 ± 0.45	0.79 ± 0.61	0.62 ± 0.34	1.29 ± 0.41
[Ne III] λ3968	0.63 ± 0.26	0.27 ± 0.10	0.31 ± 0.13	0.39 ± 0.17	0.17 ± 0.11	0.39 ± 0.17	0.34 ± 0.11	0.30 ± 0.10	... ± ...	0.19 ± 0.15	0.18 ± 0.10	0.31 ± 0.10
Hδ λ4102	... ± ...	0.16 ± 0.06	0.25 ± 0.11	0.25 ± 0.11	... ± ...	... ± ...	0.18 ± 0.06	... ± ...	0.52 ± 0.34	... ± ...	... ± ...	0.32 ± 0.10
Hγ λ4341	0.31 ± 0.13	0.46 ± 0.17	0.70 ± 0.31	0.29 ± 0.13	0.24 ± 0.15	0.47 ± 0.20	0.20 ± 0.07	0.26 ± 0.09	... ± ...	0.27 ± 0.21	0.22 ± 0.12	0.38 ± 0.12
[O III] λ4364	0.27 ± 0.11	0.07 ± 0.02	... ± ...	... ± ...	... ± ...	... ± ...	... ± ...	... ± ...	... ± ...	0.39 ± 0.31	... ± ...	... ± ...
He II λ4687	0.35 ± 0.14	0.45 ± 0.17	0.44 ± 0.19	0.26 ± 0.12	0.42 ± 0.26	... ± ...	0.20 ± 0.06	... ± ...	0.52 ± 0.35	0.28 ± 0.22	0.41 ± 0.23	0.36 ± 0.11
Hβ λ4862	1.00 ± 0.29	1.00 ± 0.26	1.00 ± 0.31	1.00 ± 0.31	1.00 ± 0.43	1.00 ± 0.31	1.00 ± 0.23	1.00 ± 0.24	1.00 ± 0.47	1.00 ± 0.55	1.00 ± 0.39	1.00 ± 0.22
[O III] λ4960	6.96 ± 2.87	5.28 ± 1.96	5.07 ± 2.23	4.42 ± 1.96	4.31 ± 2.65	6.06 ± 2.65	4.44 ± 1.42	3.15 ± 1.08	4.90 ± 3.23	3.53 ± 2.75	4.34 ± 2.40	5.51 ± 1.74
[O III] λ5008	20.94 ± 8.63	15.89 ± 5.91	15.26 ± 6.71	13.32 ± 5.90	12.96 ± 7.97	18.24 ± 7.99	13.37 ± 4.28	9.47 ± 3.24	14.74 ± 9.71	10.63 ± 8.26	13.08 ± 7.23	16.58 ± 5.22
[O I] λ6302	... ± ...	... ± ...	... ± ...	... ± ...	... ± ...	... ± ...	... ± ...	... ± ...	... ± ...	... ± ...	0.25 ± 0.14	... ± ...
[N II] λ6549	0.99 ± 0.41	0.94 ± 0.35	0.75 ± 0.33	1.08 ± 0.48	0.68 ± 0.42	0.69 ± 0.30	0.71 ± 0.23	0.62 ± 0.21	1.57 ± 1.03	... ± ...	0.54 ± 0.30	0.81 ± 0.26
Hα λ6564	5.28 ± 2.18	3.50 ± 1.30	2.91 ± 1.28	2.36 ± 1.04	3.45 ± 2.12	4.39 ± 1.92	3.98 ± 1.27	3.91 ± 1.34	8.49 ± 5.59	3.10 ± 2.41	2.41 ± 1.33	3.75 ± 1.18
[N II] λ6585	2.92 ± 1.20	2.76 ± 1.03	3.07 ± 1.35	3.18 ± 1.41	2.02 ± 1.24	3.39 ± 1.49	2.11 ± 0.67	2.29 ± 0.78	4.63 ± 3.05	2.04 ± 1.59	2.03 ± 1.12	2.40 ± 0.76
[S II] λ6718	0.52 ± 0.22	0.65 ± 0.24	0.66 ± 0.29	0.55 ± 0.25	0.66 ± 0.40	0.70 ± 0.31	0.82 ± 0.26	0.77 ± 0.26	... ± ...	0.58 ± 0.45	0.84 ± 0.47	0.41 ± 0.13
[S II] λ6732	1.01 ± 0.42	0.94 ± 0.35	0.79 ± 0.35	0.78 ± 0.35	0.90 ± 0.56	1.19 ± 0.52	0.51 ± 0.16	0.66 ± 0.23	... ± ...	0.49 ± 0.38	0.59 ± 0.33	0.53 ± 0.17
F(Hβ) $\times 10^{-15}$	0.28 ± 0.08	0.49 ± 0.13	0.46 ± 0.14	0.61 ± 0.19	0.56 ± 0.24	0.30 ± 0.09	0.59 ± 0.13	0.78 ± 0.19	0.21 ± 0.10	0.38 ± 0.21	0.55 ± 0.22	0.42 ± 0.09

Note. — *HST* STIS observed emission line ratios relative to Hβ with the flux of all kinematic components summed together at each spatial distance from the nucleus in arcseconds. Positive is toward the NW and negative is to the SE. Emission lines were fit using widths and centroids calculated from fits to [O III] λ5007 and error bars are the quadrature sum of the fractional flux uncertainty in Hβ and each respective line. Rows marked with "... ± ..." represent nondetections. Wavelengths are approximate vacuum values, and the last row lists the observed Hβ flux in units of 10^{-15} erg s^{-1} cm^{-2}.

Table 3.3. Reddening-Corrected Emission Line Ratios - Markarian 34 *HST* STIS Spectrum - Sum of All Components

Emission Line	−0.″66	−0.″56	−0.″46	−0.″36	−0.″25	−0.″15	−0.″05	+0.″05	+0.″15	+0.″46	+0.″56	+0.″66
[Ne V] λ3426	... ± ...	0.82 ± 0.43	0.98 ± 0.67	0.80 ± 0.55	1.46 ± 1.42	1.75 ± 1.03	0.98 ± 0.41	... ± ...	... ± ...	... ± ...	... ± ...	... ± ...
[O II] λ3728	4.67 ± 2.03	2.27 ± 1.01	2.03 ± 1.17	1.61 ± 0.94	1.37 ± 1.09	1.77 ± 0.87	2.06 ± 0.74	1.64 ± 0.64	4.51 ± 3.23	1.20 ± 1.40	1.34 ± 1.01	2.40 ± 0.88
[Ne III] λ3870	2.26 ± 0.92	1.04 ± 0.44	0.96 ± 0.53	0.95 ± 0.52	0.85 ± 0.63	1.06 ± 0.49	0.78 ± 0.27	0.45 ± 0.17	1.42 ± 0.92	0.83 ± 0.89	0.62 ± 0.43	1.54 ± 0.53
[Ne III] λ3968	0.91 ± 0.36	0.31 ± 0.13	0.31 ± 0.16	0.39 ± 0.21	0.19 ± 0.14	0.51 ± 0.23	0.41 ± 0.14	0.37 ± 0.13	... ± ...	0.20 ± 0.20	0.18 ± 0.12	0.37 ± 0.12
Hδ λ4102	... ± ...	0.17 ± 0.07	0.25 ± 0.13	0.25 ± 0.13	... ± ...	... ± ...	0.22 ± 0.07	... ± ...	0.92 ± 0.53	... ± ...	... ± ...	0.37 ± 0.12
Hγ λ4341	0.39 ± 0.14	0.50 ± 0.19	0.70 ± 0.34	0.29 ± 0.14	0.25 ± 0.16	0.55 ± 0.23	0.23 ± 0.07	0.29 ± 0.10	... ± ...	0.28 ± 0.24	0.22 ± 0.13	0.42 ± 0.13
[O III] λ4364	0.34 ± 0.12	0.07 ± 0.03	... ± ...	... ± ...	... ± ...	... ± ...	... ± ...	... ± ...	... ± ...	0.40 ± 0.35	... ± ...	... ± ...
He II λ4687	0.38 ± 0.15	0.46 ± 0.17	0.44 ± 0.19	0.26 ± 0.12	0.43 ± 0.26	... ± ...	0.21 ± 0.07	... ± ...	0.60 ± 0.35	0.29 ± 0.22	0.41 ± 0.23	0.37 ± 0.11
Hβ λ4862	1.00 ± 0.29	1.00 ± 0.26	1.00 ± 0.31	1.00 ± 0.31	1.00 ± 0.43	1.00 ± 0.31	1.00 ± 0.23	1.00 ± 0.24	1.00 ± 0.47	1.00 ± 0.55	1.00 ± 0.39	1.00 ± 0.22
[O III] λ4960	6.68 ± 2.87	5.21 ± 1.97	5.07 ± 2.23	4.42 ± 1.97	4.26 ± 2.65	5.90 ± 2.66	4.35 ± 1.42	3.08 ± 1.08	4.56 ± 3.23	3.52 ± 2.76	4.34 ± 2.41	5.41 ± 1.74
[O III] λ5008	19.71 ± 8.67	15.59 ± 5.94	15.26 ± 6.75	13.32 ± 5.93	12.74 ± 8.02	17.50 ± 8.03	12.95 ± 4.30	9.19 ± 3.26	13.23 ± 9.77	10.56 ± 8.34	13.08 ± 7.27	16.15 ± 5.25
[O I] λ6302	... ± ...	... ± ...	... ± ...	... ± ...	... ± ...	... ± ...	... ± ...	... ± ...	... ± ...	... ± ...	0.25 ± 0.19	... ± ...
[N II] λ6549	0.54 ± 0.47	0.78 ± 0.47	0.75 ± 0.49	1.08 ± 0.71	0.58 ± 0.61	0.46 ± 0.37	0.52 ± 0.29	0.46 ± 0.27	0.54 ± 1.13	... ± ...	0.54 ± 0.46	0.63 ± 0.33
Hα λ6564	2.90 ± 2.54	2.90 ± 1.75	2.90 ± 1.91	2.36 ± 1.56	2.90 ± 3.10	2.90 ± 2.38	2.90 ± 1.61	2.90 ± 1.71	2.91 ± 6.14	2.90 ± 4.31	2.41 ± 2.08	2.90 ± 1.52
[N II] λ6585	1.59 ± 1.40	2.28 ± 1.38	3.06 ± 2.03	3.18 ± 2.12	1.69 ± 1.82	2.24 ± 1.85	1.53 ± 0.85	1.69 ± 1.00	1.57 ± 3.35	1.91 ± 2.86	2.03 ± 1.76	1.85 ± 0.98
[S II] λ6718	0.28 ± 0.25	0.53 ± 0.33	0.65 ± 0.45	0.55 ± 0.38	0.55 ± 0.61	0.45 ± 0.39	0.58 ± 0.34	0.56 ± 0.34	... ± ...	0.54 ± 0.86	0.84 ± 0.76	0.31 ± 0.17
[S II] λ6732	0.53 ± 0.49	0.77 ± 0.48	0.78 ± 0.54	0.78 ± 0.54	0.75 ± 0.84	0.76 ± 0.66	0.37 ± 0.21	0.48 ± 0.29	... ± ...	0.46 ± 0.73	0.59 ± 0.54	0.40 ± 0.22
E(B-V)	0.55 ± 0.40	0.17 ± 0.36	0.00 ± 0.43	0.00 ± 0.43	0.16 ± 0.65	0.38 ± 0.43	0.29 ± 0.30	0.27 ± 0.33	0.98 ± 0.72	0.06 ± 0.95	0.00 ± 0.57	0.24 ± 0.30

Note. — Same as in Table 3.2, but with line ratios corrected for galactic extinction using a Galactic reddening curve (Savage & Mathis 1979). The $H\alpha/H\beta$ ratios were fixed at 2.90 and negative E(B-V) values were set to zero. Error bars are the quadrature sum of the fractional flux uncertainty in Hβ and each respective line along with the reddening uncertainty. The last row lists the color excess E(B-V).

Table 3.4. Observed Emission Line Ratios - Markarian 34 APO DIS Spectrum - Sum of All Components

Emission Line	−2.″0	−1.″6	−1.″2	−0.″8	−0.″4	0.″0	+0.″4	+0.″8	+1.″2	+1.″6	+2.″0
[S II] λ4072	0.17 ± 0.03	0.14 ± 0.02	0.12 ± 0.01	0.10 ± 0.01	0.08 ± 0.01	0.07 ± 0.01	0.08 ± 0.01	0.08 ± 0.01	0.10 ± 0.01	0.05 ± 0.01	... ± ...
Hδ λ4101	0.23 ± 0.04	0.18 ± 0.03	0.19 ± 0.02	0.16 ± 0.02	0.16 ± 0.02	0.14 ± 0.02	0.14 ± 0.01	0.14 ± 0.02	0.14 ± 0.02	0.11 ± 0.01	... ± ...
Hγ λ4340	0.47 ± 0.08	0.44 ± 0.06	0.40 ± 0.04	0.41 ± 0.04	0.40 ± 0.04	0.30 ± 0.03	0.38 ± 0.04	0.39 ± 0.04	0.39 ± 0.05	0.39 ± 0.05	0.38 ± 0.07
[O III] λ4363	0.15 ± 0.03	0.13 ± 0.02	0.14 ± 0.01	0.15 ± 0.02	0.15 ± 0.02	0.21 ± 0.02	0.14 ± 0.01	0.15 ± 0.02	0.17 ± 0.02	0.18 ± 0.03	0.20 ± 0.04
He II λ4685	0.24 ± 0.04	0.23 ± 0.03	0.26 ± 0.03	0.25 ± 0.03	0.23 ± 0.02	0.22 ± 0.02	0.23 ± 0.02	0.23 ± 0.03	0.23 ± 0.03	0.24 ± 0.03	0.26 ± 0.05
Hβ λ4861	1.00 ± 0.13	1.00 ± 0.10	1.00 ± 0.07	1.00 ± 0.07	1.00 ± 0.08	1.00 ± 0.08	1.00 ± 0.07	1.00 ± 0.08	1.00 ± 0.08	1.00 ± 0.10	1.00 ± 0.13
[O III] λ4958	4.01 ± 0.73	3.95 ± 0.57	3.93 ± 0.38	3.92 ± 0.41	3.80 ± 0.41	3.65 ± 0.41	3.66 ± 0.34	3.58 ± 0.39	3.51 ± 0.41	3.47 ± 0.49	3.55 ± 0.67
[O III] λ5006	12.08 ± 2.20	11.88 ± 1.72	11.82 ± 1.13	11.81 ± 1.24	11.44 ± 1.23	10.99 ± 1.23	11.00 ± 1.03	10.77 ± 1.18	10.57 ± 1.25	10.44 ± 1.47	10.68 ± 2.02
[N I] λ5199	... ± ...	... ± ...	... ± ...	0.08 ± 0.01	0.11 ± 0.01	... ± ...	... ± ...	... ± ...	... ± ...	... ± ...	... ± ...
He I λ5875	0.27 ± 0.05	0.18 ± 0.03	0.17 ± 0.02	0.14 ± 0.01	0.13 ± 0.01	0.13 ± 0.01	0.11 ± 0.01	0.10 ± 0.01	0.08 ± 0.01	0.11 ± 0.01	0.11 ± 0.02
[Fe VII] λ6086	... ± ...	0.09 ± 0.01	0.12 ± 0.01	0.13 ± 0.01	0.10 ± 0.01	0.10 ± 0.01	0.09 ± 0.01	0.08 ± 0.01	0.06 ± 0.01	... ± ...	... ± ...
[O I] λ6300	0.60 ± 0.11	0.56 ± 0.08	0.56 ± 0.05	0.54 ± 0.06	0.54 ± 0.06	0.51 ± 0.06	0.54 ± 0.05	0.56 ± 0.06	0.62 ± 0.07	0.64 ± 0.09	0.68 ± 0.13
[O I] λ6363	0.20 ± 0.04	0.19 ± 0.03	0.19 ± 0.02	0.18 ± 0.02	0.18 ± 0.02	0.17 ± 0.02	0.18 ± 0.02	0.19 ± 0.02	0.21 ± 0.02	0.21 ± 0.03	0.23 ± 0.04
[N II] λ6548	1.77 ± 0.32	1.39 ± 0.20	1.23 ± 0.12	1.14 ± 0.12	1.09 ± 0.12	0.88 ± 0.10	0.89 ± 0.08	0.94 ± 0.10	0.89 ± 0.10	0.90 ± 0.13	1.00 ± 0.19
Hα λ6562	5.24 ± 0.95	4.78 ± 0.69	4.03 ± 0.38	3.60 ± 0.38	3.36 ± 0.36	3.78 ± 0.42	3.80 ± 0.36	3.54 ± 0.39	3.72 ± 0.44	3.95 ± 0.56	3.98 ± 0.75
[N II] λ6583	5.21 ± 0.95	4.10 ± 0.59	3.63 ± 0.35	3.37 ± 0.36	3.21 ± 0.34	2.58 ± 0.29	2.62 ± 0.25	2.79 ± 0.31	2.61 ± 0.31	2.66 ± 0.37	2.96 ± 0.56
[S II] λ6716	2.49 ± 0.45	2.20 ± 0.32	1.26 ± 0.12	1.28 ± 0.13	1.13 ± 0.12	1.18 ± 0.13	1.18 ± 0.11	1.26 ± 0.14	1.14 ± 0.13	1.09 ± 0.15	1.22 ± 0.23
[S II] λ6730	3.04 ± 0.55	1.90 ± 0.28	2.14 ± 0.20	1.78 ± 0.19	1.64 ± 0.18	1.29 ± 0.14	1.12 ± 0.11	1.04 ± 0.11	1.00 ± 0.12	1.01 ± 0.14	1.05 ± 0.20
F(Hβ) $\times 10^{-15}$	5.09 ± 0.65	8.65 ± 0.89	12.10 ± 0.82	14.27 ± 1.06	15.36 ± 1.16	15.41 ± 1.22	13.99 ± 0.93	11.78 ± 0.91	8.93 ± 0.74	5.96 ± 0.59	3.44 ± 0.46

Note. — The same as Table 3.2 for the APO DIS observed emission line ratios along PA = 163° with the flux of all kinematic components summed together. Wavelengths are approximate air values, and the last row lists the observed Hβ flux in units of 10^{-15} erg s^{-1} cm^{-2}.

Table 3.5. Reddening-Corrected Emission Line Ratios - Markarian 34 APO DIS Spectrum - Sum of All Components

Emission Line	−2.″0	−1.″6	−1.″2	−0.″8	−0.″4	0.″0	+0.″4	+0.″8	+1.″2	+1.″6	+2.″0
[S II] λ4072	0.23 ± 0.04	0.18 ± 0.02	0.14 ± 0.01	0.11 ± 0.01	0.09 ± 0.01	0.08 ± 0.01	0.09 ± 0.01	0.09 ± 0.01	0.11 ± 0.01	0.06 ± 0.01	... ± ...
Hδ λ4101	0.31 ± 0.05	0.24 ± 0.03	0.23 ± 0.02	0.17 ± 0.02	0.17 ± 0.02	0.16 ± 0.02	0.16 ± 0.01	0.16 ± 0.02	0.16 ± 0.02	0.13 ± 0.02	... ± ...
Hγ λ4340	0.59 ± 0.09	0.54 ± 0.07	0.46 ± 0.04	0.45 ± 0.05	0.42 ± 0.05	0.34 ± 0.04	0.43 ± 0.04	0.42 ± 0.05	0.43 ± 0.05	0.44 ± 0.06	0.44 ± 0.08
[O III] λ4363	0.18 ± 0.03	0.16 ± 0.02	0.16 ± 0.01	0.16 ± 0.02	0.16 ± 0.02	0.23 ± 0.03	0.16 ± 0.01	0.17 ± 0.02	0.19 ± 0.02	0.21 ± 0.03	0.23 ± 0.04
He II λ4685	0.26 ± 0.04	0.25 ± 0.03	0.27 ± 0.03	0.25 ± 0.03	0.23 ± 0.02	0.23 ± 0.03	0.23 ± 0.02	0.24 ± 0.03	0.24 ± 0.03	0.25 ± 0.03	0.27 ± 0.05
Hβ λ4861	1.00 ± 0.13	1.00 ± 0.10	1.00 ± 0.07	1.00 ± 0.07	1.00 ± 0.08	1.00 ± 0.08	1.00 ± 0.07	1.00 ± 0.08	1.00 ± 0.08	1.00 ± 0.10	1.00 ± 0.13
[O III] λ4958	3.86 ± 0.73	3.82 ± 0.57	3.84 ± 0.38	3.87 ± 0.41	3.76 ± 0.41	3.59 ± 0.41	3.59 ± 0.34	3.53 ± 0.39	3.45 ± 0.41	3.40 ± 0.49	3.47 ± 0.67
[O III] λ5006	11.38 ± 2.21	11.29 ± 1.73	11.44 ± 1.13	11.56 ± 1.25	11.27 ± 1.23	10.70 ± 1.23	10.71 ± 1.04	10.56 ± 1.19	10.31 ± 1.25	10.12 ± 1.48	10.34 ± 2.03
[N I] λ5199	... ± ...	... ± ...	... ± ...	0.08 ± 0.01	0.11 ± 0.01	... ± ...	... ± ...	... ± ...	... ± ...	... ± ...	... ± ...
He I λ5875	0.18 ± 0.05	0.13 ± 0.03	0.14 ± 0.02	0.12 ± 0.02	0.12 ± 0.02	0.11 ± 0.02	0.09 ± 0.01	0.09 ± 0.01	0.07 ± 0.01	0.09 ± 0.02	0.09 ± 0.02
[Fe VII] λ6086	... ± ...	0.06 ± 0.01	0.09 ± 0.01	0.11 ± 0.02	0.09 ± 0.01	0.08 ± 0.01	0.07 ± 0.01	0.07 ± 0.01	0.05 ± 0.01	... ± ...	... ± ...
[O I] λ6300	0.36 ± 0.12	0.36 ± 0.09	0.42 ± 0.06	0.44 ± 0.07	0.47 ± 0.07	0.40 ± 0.07	0.43 ± 0.06	0.47 ± 0.08	0.49 ± 0.09	0.49 ± 0.11	0.51 ± 0.15
[O I] λ6363	0.12 ± 0.04	0.12 ± 0.03	0.14 ± 0.02	0.15 ± 0.02	0.16 ± 0.02	0.13 ± 0.02	0.14 ± 0.02	0.16 ± 0.03	0.16 ± 0.03	0.16 ± 0.04	0.17 ± 0.05
[N II] λ6548	0.98 ± 0.37	0.85 ± 0.24	0.89 ± 0.14	0.92 ± 0.15	0.94 ± 0.15	0.67 ± 0.12	0.68 ± 0.10	0.78 ± 0.13	0.69 ± 0.13	0.66 ± 0.16	0.73 ± 0.24
Hα λ6562	2.90 ± 1.09	2.90 ± 0.81	2.90 ± 0.47	2.90 ± 0.49	2.90 ± 0.48	2.90 ± 0.53	2.90 ± 0.45	2.90 ± 0.50	2.90 ± 0.56	2.90 ± 0.69	2.90 ± 0.94
[N II] λ6583	2.87 ± 1.09	2.48 ± 0.70	2.61 ± 0.43	2.71 ± 0.46	2.76 ± 0.46	1.98 ± 0.37	1.99 ± 0.31	2.28 ± 0.40	2.03 ± 0.39	1.95 ± 0.47	2.15 ± 0.70
[S II] λ6716	1.33 ± 0.52	1.29 ± 0.38	0.89 ± 0.15	1.01 ± 0.18	0.97 ± 0.16	0.89 ± 0.17	0.88 ± 0.14	1.02 ± 0.18	0.87 ± 0.17	0.79 ± 0.19	0.87 ± 0.29
[S II] λ6730	1.61 ± 0.64	1.12 ± 0.33	1.51 ± 0.26	1.41 ± 0.25	1.40 ± 0.24	0.97 ± 0.19	0.84 ± 0.13	0.84 ± 0.15	0.76 ± 0.15	0.73 ± 0.18	0.74 ± 0.25
E(B-V)	0.54 ± 0.17	0.46 ± 0.13	0.30 ± 0.09	0.20 ± 0.10	0.14 ± 0.10	0.24 ± 0.10	0.25 ± 0.09	0.18 ± 0.10	0.23 ± 0.11	0.28 ± 0.13	0.29 ± 0.17

Note. — The same as in Table 3.4, but with line ratios corrected for galactic extinction using a Galactic reddening curve (Savage & Mathis 1979). The $H\alpha/H\beta$ ratios were fixed at 2.90 and negative E(B-V) values were set to zero. Error bars are the quadrature sum of the fractional flux uncertainty in Hβ and each respective line along with the reddening uncertainty. Wavelengths are approximate air values, and the last row lists the color excess E(B-V).

In Chapter 2 the *HST* spectra had sufficient S/N for the key diagnostic emission lines, and we did not model the APO data, as they offered similar insights at lower spatial resolution. For Mrk 34, the larger uncertainties of the *HST* observations would yield models with limited constraints on the conditions in the gas; however, the similarity of the ratios between the *HST* and APO observations means we can be confident that photoionization models of the APO data will yield an equivalent scale factor for converting [O III] flux to mass, while the higher spatial resolution *HST* observations help to constrain the density profile using the [S II] doublet.

3.3.4 Emission Line Diagnostics

As in Chapter 2, we use the dereddened emission line ratios to constrain the physical conditions in the emission line gas, including the ionization mechanism, elemental abundances, temperature, and electron density. In Figure 3.6 and the Appendix, we present Baldwin-Phillips-Terlevich (BPT) diagrams (Baldwin et al. 1981; Veilleux & Osterbrock 1987) that confirm the gas sampled by our observations is ionized by the central AGN, in agreement with Stoklasová et al. (2009). The AGN ionized gas extends to at least 8 kpc, with emission detected out to 12 kpc from the nucleus (Whittle et al. 1988).

We determined the elemental abundances in gas phase using Equation (2) of Storchi-Bergmann et al. (1998b), and adopt a solar abundance of $\log(\mathrm{O/H})+12 = 8.69$ from Asplund et al. (2009). We find a mean oxygen abundance of $\log(\mathrm{O/H})+12 = 8.84 \pm 0.08$, or $Z = 1.40 \pm 0.26\ Z_{\odot}$, with the spatial distribution shown in Figure 3.6. This value is ~ 0.4 dex higher than that found by Castro et al. (2017); however, our spectra do not contain the required emission lines for a direct comparison with that method.

We also derived the electron temperature and density, and the results are shown in Figure 3.6. We find typical NLR temperatures of $\sim 10,000 - 15,000$ K, in agreement with Koski (1978). Unlike Mrk 573, we do not observe a strong, centrally peaked density profile with a characteristic power-law index. The abundance, temperature, and density profiles display a

curious dichotomy across the nucleus, following a systematic decrease in [O III]/Hβ across the NLR from the SE to the NW.

3.3.5 [O III] Image Analysis

We use an [O III] emission line image of the entire NLR to account for mass outside of our spectral slit observations. To ensure proper flux calibration, we compared our integrated [O III] emission line fluxes to extracted regions of the image covering the same area. Owing to the excellent calibration of *HST* observations, the [O III] fluxes agree to better than 5% after scaling the image by the filter bandpass.

We determined the total [O III] flux as a function of distance from the nucleus using the Elliptical Panda routine within the SAOImage DS9 software (Joye & Mandel 2003). We divide the image into two concentric semi-ellipses to better account for NLR asymmetries in the flux, density, and velocity profiles. The semi-ellipses are centered on the nucleus, with spacings equal to the spatial sampling of our extracted *HST* observations for determining the mass profile. The ring ellipticity is calculated from the adopted inclination of $i = 41^{\circ}$ using $b/a = cos(i)$ where a and b are the major and minor-axis lengths, respectively.

The [O III] image and azimuthally summed flux profile are shown in Figure 3.7. An error of $\sigma \approx 8.77 \times 10^{-18}$ erg s^{-1} cm^{-2} pixel^{-1} was calculated from line-free regions in the image, with the error in each annulus equal to $\sqrt{N_{\rm pix}} \times \sigma$, where N_{pix} is the number of pixels.

3.4 Photoionization Models

Ultimately, our techniques rely on an accurate scale factor for converting [O III] flux to ionized gas mass. The most accurate method requires detailed photoionization models, as the emission coefficient of the gas will vary across the NLR due to changing physical conditions, such as density. Our process for creating multi-component photoionization models is described in §2.4, and we summarize here the most pertinent details.

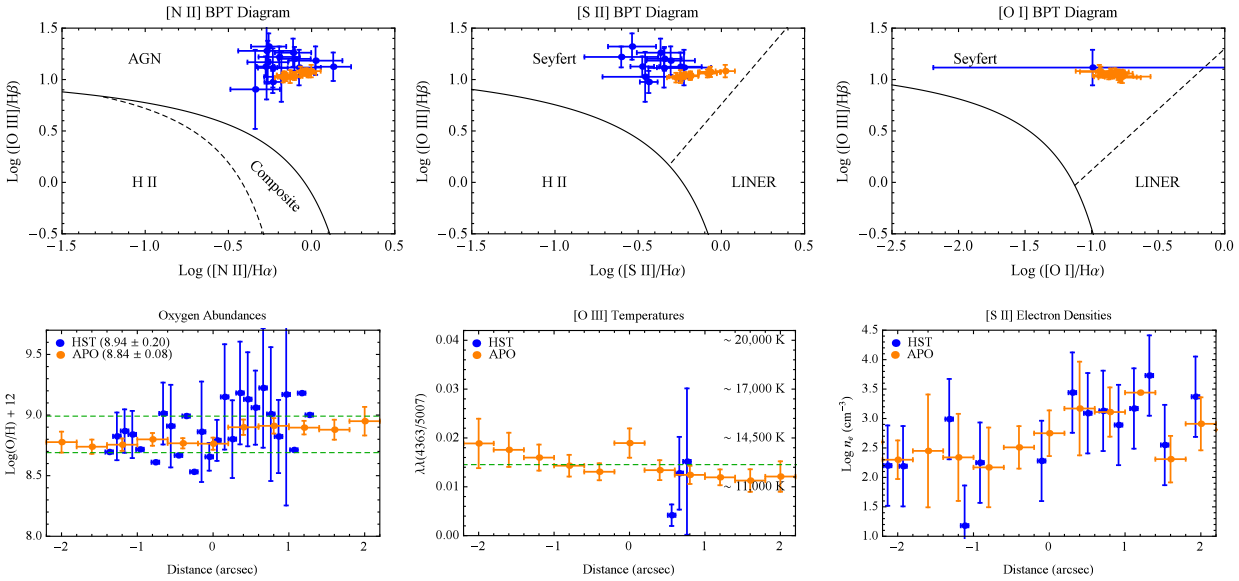

Figure 3.6 Top: BPT ionization diagrams for [N II], [S II], and [O I] using ratios calculated from the fluxes of all kinematic components summed together (Tables 3.3 and 3.5). *HST* STIS and APO DIS points are shown with blue and orange circles, respectively. The demarcation lines for distinguishing ionization mechanisms are from Kewley et al. (2001, 2006); Kauffmann et al. (2003). Diagrams for the individual kinematic components and the other APO slit positions are given in the appendix. Bottom: The left panel shows the derived oxygen abundances using the method of Storchi-Bergmann et al. (1998b). The lower and upper dotted green lines represent one and two times solar abundances, respectively, with the average values provided in parentheses. The middle panel shows the electron temperatures, with the dotted green line representing the mean. The right panel shows the electron densities as derived from [S II], with uncertainties propagated from the individual errors in the line ratios for all figures.

3.4.1 Input Parameters

We construct models using version 13.04 of the photoionization code Cloudy (Ferland et al. 2013). A self-consistent model requires supplying the quantity and energy distribution of photons intercepting a cloud of known composition and geometry. These quantities are encapsulated by the ionization parameter (U), which is the ratio of the number of ionizing photons to atoms at the cloud face (Osterbrock & Ferland 2006, §13.6),

$$U = \frac{1}{4\pi r^2 n_H c} \int_{\nu_0}^{\infty} \frac{L_\nu}{h\nu} d\nu, \tag{3.7}$$

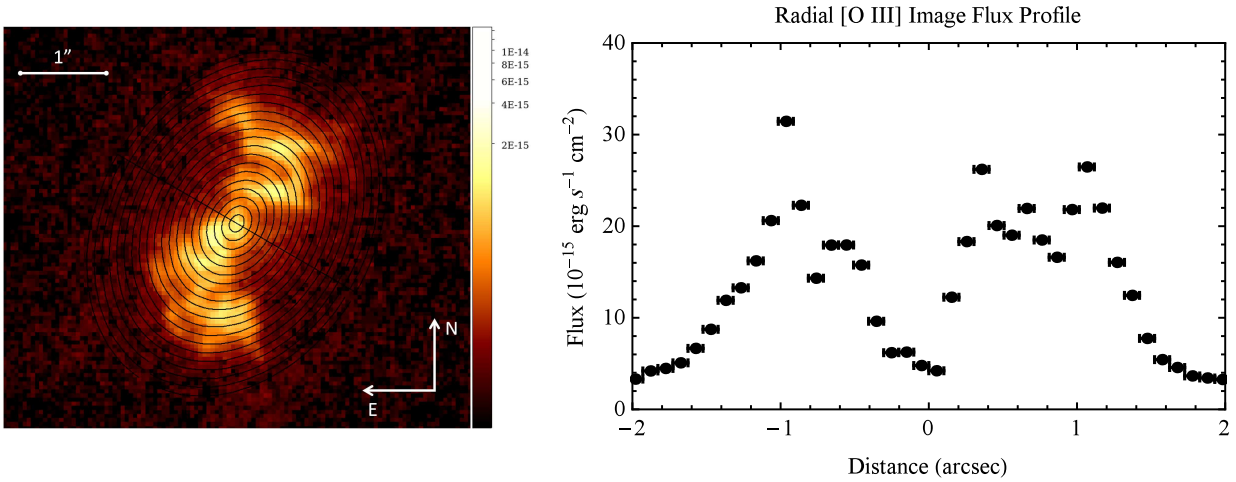

Figure 3.7 The left panel is a portion of the *HST* [O III] image with overlaid elliptical semi-annuli representing rings of constant distance from the nucleus. The color bar gives fluxes in units of erg s^{-1} cm^{-2}. The right panel is the azimuthally summed [O III] semi-annuli fluxes oriented along the major axis of the ellipse, with typical errors smaller than the size of the points. SE is to the left and NW is to the right.

where r is the radial distance from the AGN, n_H is the hydrogen number density cm^{-3}, and c is the speed of light. The integral is the number of ionizing photons s^{-1}, $Q(H) = \int_{\nu_0}^{\infty}(L_\nu/h\nu)d\nu$, where L_ν is the luminosity of the AGN as a function of frequency as determined from the spectral energy distribution, h is Planck's constant, and $\nu_0 = 13.6eV/h$ is the ionization potential of hydrogen (Osterbrock & Ferland 2006, §14.3).

We adopt a typical power-law SED that has worked well in previous studies (Kraemer & Crenshaw 2000b,c), taking into consideration the X-ray modeling of Gandhi et al. (2014). For $L_\nu \propto \nu^\alpha$ we adopt slopes of $\alpha = -0.5$ from 1 eV to 13.6 eV, $\alpha = -1.4$ from 13.6 eV to 0.5 keV, $\alpha = -1$ from 0.5 keV to 10 keV, and $\alpha = -0.5$ from 10 keV to 100 keV, with low and high energy cutoffs below 1 eV and above 100 keV, respectively. Normalizing this SED to the 2-10 keV luminosity from Gandhi et al. (2014), $L_{2-10} = 9(\pm3) \times 10^{43}$ erg s^{-1}, we numerically compute the above integral and find $Q(H) = 7.8(\pm2.6) \times 10^{54}$ photons s^{-1}, or equivalently, $\log(Q(H)) \approx 54.89$, in approximate agreement with Wilson et al. (1988). We also investigated scaling the 2-10 keV luminosity to our adopted distance, a difference of $\sim 22\%$, but this did not noticeably improve the model fits.

The gas composition is determined by the elemental abundances, dust content, and corresponding depletions of elements into dust grains. We adopt abundances of $\sim 1.3\ Z_{\odot}$, and the exact logarithmic values relative to hydrogen by number for dust free models are: He = -0.96, C = -3.46, N = -3.94, O = -3.20, Ne = -3.96, Na = -5.65, Mg = -4.29, Al = -5.44, Si = -4.38, P = -6.48, S = -4.77, Ar = -5.49, Ca = -5.55, Fe = -4.39, Ni = -5.67. The strong low ionization lines are more easily reproduced by including a dusty component, and for models with a dust level of 0.5 relative to the Galactic interstellar medium we accounted for depletion of certain elements in graphite and silicate grains (Seab & Shull 1983; Snow & Witt 1996; Collins et al. 2009). The logarithmic abundances relative to hydrogen by number for the dusty models are: He = -0.96, C = -3.63, N = -3.94, O = -3.32, Ne = -3.96, Na = -5.65, Mg = -4.57, Al = -5.70, Si = -4.66, P = -6.48, S = -4.77, Ar = -5.49, Ca = -5.81, Fe = -4.67, Ni = -5.93.

3.4.2 Model Selection

To account for gas in multiple ionization states with different densities at each location, we use up to three model components referred to as HIGH, MED, and LOW ION. At each location along the slit, the only unknown quantities in Equation 3.7 are U and n_H, so for a grid of models we choose a range of U values to produce the observed emission and solve for the corresponding density to maintain physical consistency. We then add fractional combinations of the components to create a composite model that matches the Hβ luminosity.

To determine the best model for each location, we use a simple numerical scheme that compares the model line ratios to the dereddened values for all fractional combinations of HIGH, MED, and LOW ION, with an ideal match having a ratio of unity. Similar to Chapter 2, our limiting criteria for a successful fit were the following. First, the He II ratio that is critically sensitive to the column density, and the [O III] doublet that determines our flux to mass scaling, must match the observations within 10%. We then aim to constrain [O I], [N II], and [S II] within 30%. We loosened this criterion up to a factor of ~ 2 for [S II] at

some locations to find a match. Finally, all remaining lines in the spectra must match within a factor of three.

In contrast to our modeling of Mrk 573, we find that simpler two-component models are able to match the line ratios, in agreement with the general conclusions of Rosario (2007). This could be in part due to the fewer number of emission lines available in the spectra, in combination with the significantly larger APO extraction areas that will tend to blend the conditions of various emission line knots. The models employ pure AGN ionization, and we do not see evidence for shock excitation, in agreement with the findings of Jackson & Beswick (2007). We will explore this in more detail using *Chandra* data in a forthcoming paper (Fischer et al., in prep). The Cloudy model input and output parameters for our best-fitting models are given in Tables 3.6 and 3.7, respectively. The predicted emission line ratios for the final composite models are given in Table 3.8.

3.4.3 Comparison to the Observations

The comparison of our model and dereddened emission line ratios is presented in Figure 3.8. The dashed unity line indicates an exact match, and points between the dotted lines agree to within better than a factor of three. A variety of factors contribute to the observed deviations, such as a poor Gaussian fit, the S/N, the quality of atomic data, and the accuracy of our models. We discuss here systematics discrepancies and those greater than a factor of two for important diagnostic lines at each position.

Qualitatively, the [S II] λ4072 line should be treated with skepticism, as it is an unresolved doublet and at the extreme edge of the spectral coverage. The agreement of the Hγ line is indicative of a proper reddening correction, while the mild overprediction of Hδ may be due to a noisy continuum. The slight underprediction of [O III] λ4363 is a minor concern as it indicates an underprediction of the temperature in more highly ionized zones and may be partially attributed to blending with Hγ.

Table 3.6. Cloudy Model Input Parameters

Distance from Nucleus (arcsec) (1)	Comp ION Name (2)	Ionization Parameter log(U) (unitless) (3)	Column Density log(N_H) (cm^{-2}) (4)	Number Density log(n_H) (cm^{-3}) (5)	Dust Content Relative to ISM (6)
2.00	High	...	...	...	...
2.00	Med	-2.00	21.20	1.46	0.5
2.00	Low	-4.00	19.40	3.46	0.5
1.60	High	...	...	...	...
1.60	Med	-2.00	21.40	1.64	0.5
1.60	Low	-3.80	19.40	3.44	0.5
1.20	High	...	...	...	...
1.20	Med	-2.00	21.30	1.86	0.5
1.20	Low	-3.90	19.60	3.76	0.5
0.80	High	...	...	...	...
0.80	Med	-2.00	21.40	2.14	0.5
0.80	Low	-3.20	20.30	3.34	0.5
0.40	High	-0.80	22.20	1.28	0.0
0.40	Med	-2.80	20.80	3.28	0.5
0.40	Low	...	...	...	...
0.00	High	-0.90	22.00	1.59	0.0
0.00	Med	-2.80	20.80	3.49	0.5
0.00	Low	...	...	...	...
-0.40	High	-1.40	21.60	1.88	0.0
-0.40	Med	-2.90	20.60	3.38	0.5
-0.40	Low	...	...	...	...
-0.80	High	...	...	...	...
-0.80	Med	-2.00	21.40	2.14	0.5
-0.80	Low	-3.50	20.00	3.64	0.5
-1.20	High	...	...	...	...
-1.20	Med	-2.00	20.90	1.86	0.5
-1.20	Low	-4.00	19.70	3.86	0.5
-1.60	High	...	...	...	...
-1.60	Med	-2.00	21.40	1.64	0.5
-1.60	Low	-3.70	19.90	3.34	0.5
-2.00	High	...	...	...	...
-2.00	Med	-2.00	21.20	1.46	0.5
-2.00	Low	-4.00	19.60	3.46	0.5

Note. — The Cloudy photoionization model input parameters. The columns are: (1) distance from the nucleus to the center of each $0\farcs1 \times 0\farcs2$ bin, (2) component name, (3) log ionization parameter, (4) log column density, (5) log number density, and (6) dust fraction relative to ISM.

Table 3.7. Cloudy Model Output Parameters

Distance from Nucleus (arcsec) (1)	Comp ION Name (2)	Fraction of Total Model (3)	log($F_{H\beta}$) Model Flux (cgs) (4)	Cloud Surface Area (10^3 pc^2) (5)	Cloud Model Thickness (pc) (6)	Cloud Model Depth (pc) (7)
2.00	High	...	...	...	...	...
2.00	Med	0.70	-2.54	4292	18	2117
2.00	Low	0.30	-2.46	1506	<0.1	742
1.60	High	...	...	...	...	...
1.60	Med	0.70	-2.35	3527	19	1739
1.60	Low	0.30	-2.28	1278	<0.1	630
1.20	High	...	...	...	...	...
1.20	Med	0.65	-2.14	1644	9	811
1.20	Low	0.35	-2.05	714	<0.1	352
0.80	High	...	...	...	...	...
0.80	Med	0.40	-1.75	347	6	171
0.80	Low	0.60	-1.85	657	<0.1	324
0.40	High	0.05	-1.47	20	269.6	10
0.40	Med	0.95	-1.42	330	<0.1	163
0.40	Low	...	...	...	...	...
0.00	High	0.05	-1.38	23	83	11
0.00	Med	0.95	-1.21	294	<0.1	145
0.00	Low	...	...	...	...	...
-0.40	High	0.10	-1.44	49	17.0	24
-0.40	Med	0.90	-1.42	418	<0.1	206
-0.40	Low	...	...	...	...	...
-0.80	High	...	...	...	...	...
-0.80	Med	0.60	-1.85	513	6	253
-0.80	Low	0.40	-1.75	272	<0.1	134
-1.20	High	...	...	...	...	...
-1.20	Med	0.60	-2.18	956	4	471
-1.20	Low	0.40	-2.04	467	<0.1	230
-1.60	High	...	...	...	...	...
-1.60	Med	0.65	-2.35	1246	19	615
-1.60	Low	0.35	-2.25	534	<0.1	264
-2.00	High	...	...	...	...	...
-2.00	Med	0.65	-2.54	1149	18	567
-2.00	Low	0.35	-2.45	494	<0.1	244

Note. — The best-fitting Cloudy model output parameters. The columns are: (1) distance from the nucleus to the center of each $0\farcs1 \times 0\farcs2$ bin, (2) component name, (3) fraction of model contributing to the Hβ luminosity, (4) log Hβ model flux (erg s^{-1} cm^{-2}), (5) surface area of the gas in units of 10^3, (6) gas cloud thickness (N_H/n_H), and (7) depth into the plane of the sky.

Table 3.8. Predicted Cloudy Model Emission Line Ratios

Line	–2.″0	–1.″6	–1.″2	–0.″8	–0.″4	0.″0	+0.″4	+0.″8	+1.″2	+1.″6	+2.″0
[S II]	0.20	0.17	0.30	0.21	0.18	0.18	0.15	0.19	0.25	0.17	0.18
Hδ	0.26	0.26	0.26	0.26	0.26	0.26	0.26	0.26	0.26	0.26	0.26
Hγ	0.47	0.47	0.47	0.47	0.47	0.47	0.47	0.47	0.47	0.47	0.47
[O III]	0.13	0.13	0.13	0.13	0.09	0.10	0.09	0.10	0.13	0.13	0.14
He II	0.26	0.27	0.26	0.27	0.25	0.25	0.25	0.26	0.26	0.27	0.27
Hβ	1.00	1.00	1.00	1.00	1.00	1.00	1.00	1.00	1.00	1.00	1.00
[O III]	3.44	3.46	3.47	3.49	3.41	3.64	3.52	3.21	3.48	3.67	3.70
[O III]	10.37	10.41	10.43	10.51	10.26	10.95	10.60	9.68	10.46	11.05	11.15
[N I]	0.22	0.21	0.12	0.18	0.13	0.13	0.14	0.18	0.20	0.18	0.20
He I	0.14	0.14	0.14	0.14	0.15	0.15	0.14	0.14	0.14	0.13	0.14
[Fe VII]	0.05	0.05	0.05	0.05	0.05	0.05	0.04	0.03	0.05	0.06	0.06
[O I]	0.52	0.47	0.45	0.48	0.39	0.41	0.38	0.44	0.55	0.43	0.47
[O I]	0.17	0.15	0.14	0.15	0.12	0.13	0.12	0.14	0.17	0.14	0.15
[N II]	0.68	0.71	0.67	0.79	0.81	0.76	0.74	0.85	0.73	0.66	0.63
Hα	2.90	2.91	2.89	2.90	2.90	2.89	2.90	2.90	2.90	2.90	2.90
[N II]	2.00	2.09	1.99	2.34	2.39	2.25	2.18	2.52	2.14	1.95	1.85
[S II]	0.72	0.69	0.50	0.54	0.45	0.39	0.45	0.59	0.58	0.58	0.63
[S II]	0.88	0.78	0.77	0.68	0.61	0.55	0.58	0.72	0.76	0.68	0.76

Note. — The predicted Cloudy emission line ratios for our final composite models with the fractional weight of each component given in Table 3.6. The emission lines are in the same order as Tables 3.2–3.5.

Finally, there is the general underprediction of [S II] $\lambda\lambda$6716, 6731, which may indicate the need for more dust, or exposure to a partially-absorbed SED from a closer in absorber as found for the NLRs of Mrk 573 (Revalski et al. 2018a) and Mrk 3 (Collins et al. 2009). The issue is most severe near the nucleus, which may also indicate that some of the [S II] emission arises from the edges of the ionized NLR bicone, at larger distances from the nucleus than those adopted in our models. Specifically, our models use a distance corresponding to the midpoint between the pixel center and the edge of the slit, calculated using Equation 3.2 for each position (e.g. the central extraction uses a distance of $\pm$0.″5, while the pixel covers an area of 2.″0 $\times$ 0.″4).

The introduction of additional dust brought the [S II] emission lines into agreement with the observations for the extractions at larger distances, but degraded the overall fit in some cases and introduced significant scatter into the scale factors. Allowing the low ionization component to be at larger distances near the edge of the slit, rather than in the middle,

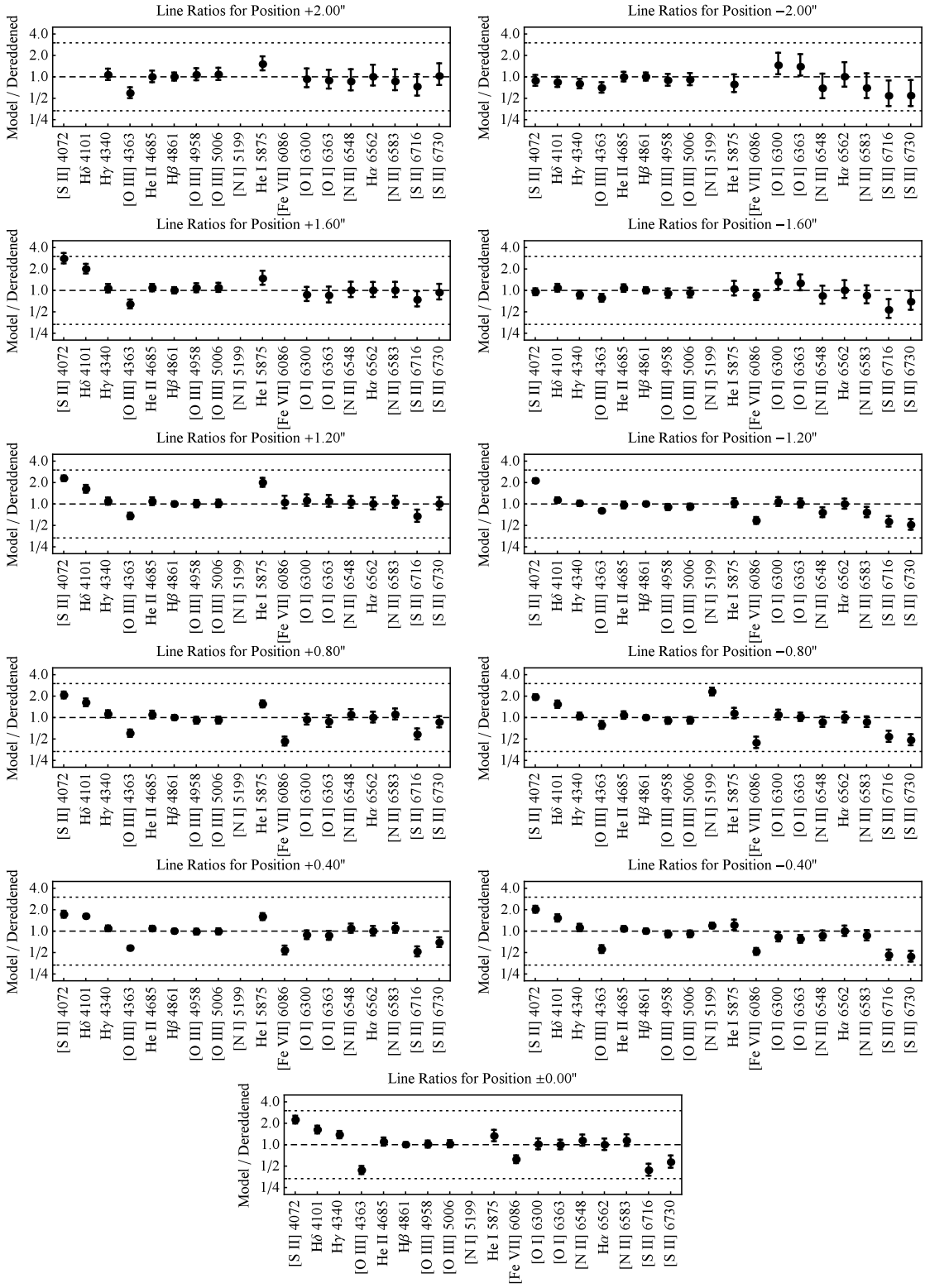

Figure 3.8 The composite model line ratios divided by the dereddened values, where the spatial distance is that from the nucleus to the center of the pixel extraction. The dashed unity lines indicate an exact match, while the dotted lines are factor of three boundaries. The tick marks are logarithmically spaced for even distributions above and below the unity line. Points above this line are overpredicted, while points below are underpredicted by the models.

marginally improved the fits at the $\sim$ 10–20% level. Considering the limited constraints we are able to place on the physical conditions in the gas from the small number of emission lines, and the ability of the models to accurately reproduce all other lines in the spectrum, we decided against further fine-tuning. Overall, our models are able to successfully match all emission lines within a factor of three or better at all locations in the NLR.

To check the physical reality of our models, we also derived several quantities at each location. These include the surface areas ($A = L_{\mathrm{H}\beta}/F_{\mathrm{H}\beta}$) and thicknesses ($N_H/n_H$) of the emitting clouds, which must fit within the slit. Finally, we calculated the depths of the clouds into the plane of the sky by dividing the cloud area by the projected slit width ($\sim$ 2 kpc) to verify that they were within the scale height of a typical disk. It is important to note that each ionized component may not be co-located in the slit, as the emission is spread across 2″ in the spectral direction.

3.5 Calculations

3.5.1 Mass of the Ionized Gas

Calculating gas masses from our observed spectra and photoionization models is summarized here as described in §2.5. For multi-component models, the mass in each component is calculated separately by dividing up the Hβ luminosity, and then the masses are summed. This involves first determining the mass in the slit from

$$M_{\mathrm{slit}} = N_H \mu m_p \left(\frac{L(H\beta)}{F(H\beta)_m} \right), \tag{3.8}$$

where N_H is the model hydrogen column density, μ is the mean mass per proton ($\sim$ 1.4 for our abundances), m_p is the proton mass, $F(H\beta)_m$ is the Hβ model flux, and $L(H\beta)$ is the luminosity of Hβ calculated from the extinction-corrected flux and distance. This establishes a direct relationship describing the number of Hβ photons emitted per unit mass at a specific density. To determine the ionized gas mass at all radii we use available [O III] imaging, so

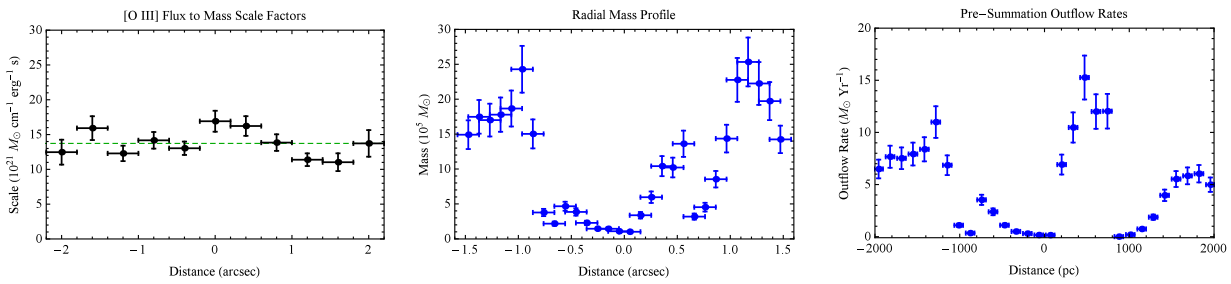

Figure 3.9 The left panel shows the [O III] flux to mass scale factors, with the mean indicated by the green dashed line. The middle panel shows the ionized mass profile in units of 10^5 $M_\odot$ calculated from the total flux in each semi-ellipse. The right panel shows the mass outflow rates assuming that all of the material is in outflow. Distances in arcseconds are observed, and distances in pc are corrected for projection.

we derive a scale factor that allows us to calculate mass from observed [O III] flux rather than Hβ luminosity. Specifically,

$$S = \left(\frac{M_{\rm slit} n_H}{F_{\lambda 5007}} \right), \tag{3.9}$$

where M_{slit} is the ionized mass in the slit from Equation 3.8, n_H is the fractional weighted mean hydrogen number density (cm^{-3}) for all components, and $F_{\lambda 5007}$ is the extinction-corrected [O III] emission line flux from our spectra. Figure 3.9 shows the mean scale factor, with S = $(1.37 \pm 0.20) \times 10^{22}$ M$_\odot$ cm^{-1} erg^{-1} s, and the 1σ error corresponding to a fractional uncertainty of 14.3%. For position $-2\farcs0$ the scale factor was discrepantly low and was replaced with a mean value. We take an average value of the scale factors and then calculate the ionized gas mass for each image flux using

$$M_{ion} = S \left(\frac{F_{[\rm O\ III]}}{n_H} \right), \tag{3.10}$$

where $F_{[\rm O\ III]}$ is the image flux in each semi-annulus of width δr (Figure 3.7) and n_H is the hydrogen number density found by interpolating between our model points.

3.5.2 Outflow Parameters

The goal of our study is to quantify the power and impact of the NLR outflows. This is encapsulated by mass outflow rates, kinetic energy and luminosity, and momenta. The mass outflow rate ($\dot{M}_{out}$) is given by

$$\dot{M}_{out} = \left(\frac{Mv}{\delta r} \right), \tag{3.11}$$

where M is the mass in each semi-annulus, v is the deprojected velocity corrected for inclination and position angle on the sky (§2.3.2), and δr is the deprojected width for each extraction. Deprojecting the distances results in a bin width that is 31% larger than the observed value, thus each observed 103 pc bin spans $\delta r \approx 135$ pc after deprojection. The kinetic energy (E), kinetic energy flow rate ($\dot{E}$), momentum (p), and momentum flow rate ($\dot{p}$) are given by

$$E = \frac{1}{2} M_{out} v^2, \tag{3.12}$$

$$\dot{E} = \frac{1}{2} \dot{M}_{out} v^2, \tag{3.13}$$

$$p = M_{out} v, \tag{3.14}$$

$$\dot{p} = \dot{M}_{out} v. \tag{3.15}$$

We do not include contributions from velocity spread, such as turbulence, which would add a σ_v term to these expressions. We obtain a single profile for each of these quantities by radially summing the values derived for each of the semi-annuli, and the mass profile and outflow rates for each semi-ellipse can be seen in Figure 3.9.

3.6 Results

In Figure 3.10 and Table 3.9 we present our mass outflow rates and energetics as functions of distance from the nucleus for Mrk 34. We also show the results for NGC 4151 (Crenshaw et

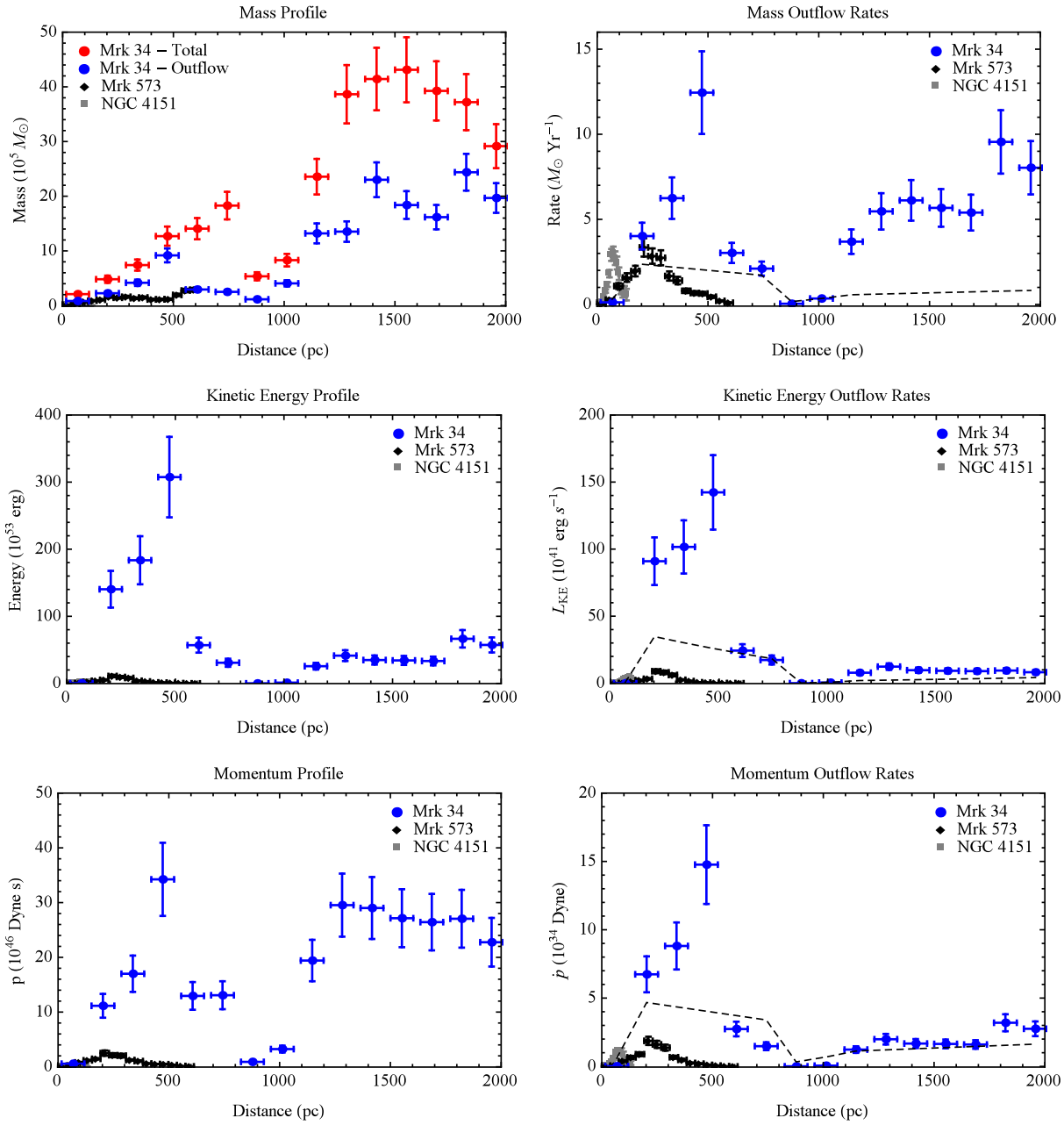

Figure 3.10 Top left to bottom right are the azimuthally summed mass profiles, mass outflow rates, kinetic energy profiles, kinetic energy outflow rates, momentum profiles, and momentum outflow rates for Mrk 34, Mrk 573 (Revalski et al. 2018a), and NGC 4151 (Crenshaw et al. 2015). The red points represent the result that is obtained assuming that all of the mass is in outflow, and the blue points show the net result after multiplying by the fraction of flux in outflow as shown in Figure 3.5. The dashed lines represent the profiles that would result from the mass in the center bin ($M \approx 2.1 \times 10^5$ $M_\odot$) traveling through the velocity profile. Quantities are per bin, and targets have different bin sizes.

al. 2015) and Mrk 573 (Revalski et al. 2018a) for comparison. The quantities displayed are the value within each bin of width δr, and each target has a different bin size.

The outflow reaches a maximum radial extent of ~ 2 kpc from the nucleus and contains an ionized gas mass of $M \approx 1.6 \times 10^7\ M_\odot$. The mass of ionized gas in the rotational component is nearly equal (Figure 3.10), yielding a total ionized gas mass of $M \approx 3.3 \times 10^7\ M_\odot$ for the NLR. The total kinetic energy of the outflow over all distances is $E \approx 1.0 \times 10^{56}$ erg. The mass outflow rate reaches a peak value of $\dot{M}_{out} \approx 12.5 \pm 2.4\ M_\odot\ \mathrm{yr}^{-1}$ at a distance of 470 pc from the nucleus and then decreases to nearly zero at ~ 900 pc before rising slightly out to distances of ~ 2 kpc. As discussed in Fischer et al. (2017) and §3.7, points beyond 1.5 kpc represent disturbed kinematics that may not be in radial outflow and should be considered upper limits. Beyond these distances, the observed *HST* kinematics are generally consistent with rotation (Fischer et al. 2018).

The dashed lines in Figure 3.10 represent the mass outflow rates and energetics that would be observed if the mass in the central bin ($M \approx 2.1 \times 10^5\ M_\odot$) propagated through the velocity profile. At 470 pc, where the outflow peaks, this is ~ 5 times smaller than the observed value, indicating that the outflow is likely accelerated in-situ such that material does not originate at small radii and travel large distances, but is actually host galaxy material driven by the nuclear radiation field.

Compared to the AGN bolometric luminosity of Mrk 34, $\log(L_{bol}) = 46.2 \pm 0.4$ erg s^{-1}, the peak kinetic luminosity reaches $\sim 0.1 - 0.3\%$ of L_{bol}. The photon momentum (L/c) from the bolometric luminosity is $\dot{p} \approx 5.3 \times 10^{35}$ dyne, and the peak momentum flow rate is $\dot{p} \approx 1.5 \times 10^{35}$ dyne. Thus, the peak outflow momentum rate is $\sim 28\%$ of the AGN photon momentum.

Table 3.9. Radial Mass Outflow and Energetic Results

Distance (pc) (1)	Velocity (km s^{-1}) (2)	Mass (10^5 $M_\odot$) (3)	$\dot{M}$ ($M_\odot$ yr^{-1}) (4)	Energy (10^{53} erg) (5)	$\dot{E}$ (10^{41} erg s^{-1}) (6)	Momentum (10^{46} dyne s) (7)	$\dot{P}$ (10^{34} dyne) (8)
67.5	191.8	0.84 ± 0.12	0.12 ± 0.02	0.31 ± 0.06	0.03 ± 0.01	0.57 ± 0.11	0.01 ± 0.01
202.4	2347.9	2.26 ± 0.31	4.02 ± 0.78	140.31 ± 27.37	90.98 ± 17.75	11.14 ± 2.17	6.74 ± 1.31
337.4	1976.6	4.17 ± 0.57	6.24 ± 1.22	183.52 ± 35.80	101.63 ± 19.83	17.00 ± 3.32	8.81 ± 1.72
472.4	1789.2	9.18 ± 1.27	12.45 ± 2.43	307.48 ± 59.98	142.32 ± 27.76	34.25 ± 6.68	14.77 ± 2.88
607.3	1358.2	2.94 ± 0.41	3.03 ± 0.59	56.98 ± 11.11	24.33 ± 4.75	12.95 ± 2.53	2.74 ± 0.53
742.3	1108.4	2.51 ± 0.35	2.11 ± 0.41	30.77 ± 6.00	17.32 ± 3.38	13.07 ± 2.55	1.48 ± 0.29
877.2	46.0	1.15 ± 0.16	0.04 ± 0.01	0.10 ± 0.02	0.05 ± 0.01	0.90 ± 0.18	0.01 ± 0.01
1012.2	113.0	4.06 ± 0.56	0.35 ± 0.07	1.14 ± 0.22	0.50 ± 0.10	3.24 ± 0.63	0.05 ± 0.01
1147.1	368.6	13.20 ± 1.82	3.69 ± 0.72	25.63 ± 5.00	7.84 ± 1.53	19.41 ± 3.79	1.23 ± 0.24
1282.1	533.5	13.53 ± 1.87	5.47 ± 1.07	41.37 ± 8.07	12.37 ± 2.41	29.54 ± 5.76	1.99 ± 0.39
1417.0	350.7	23.01 ± 3.17	6.11 ± 1.19	34.82 ± 6.79	9.72 ± 1.90	29.01 ± 5.66	1.67 ± 0.33
1552.0	407.1	18.39 ± 2.54	5.67 ± 1.11	34.24 ± 6.68	9.27 ± 1.81	27.14 ± 5.29	1.64 ± 0.32
1687.0	440.4	16.17 ± 2.23	5.40 ± 1.05	33.36 ± 6.51	9.03 ± 1.76	26.43 ± 5.16	1.60 ± 0.31
1821.9	517.0	24.38 ± 3.36	9.55 ± 1.86	66.48 ± 12.97	9.45 ± 1.84	27.05 ± 5.28	3.19 ± 0.62
1956.9	538.7	19.68 ± 2.71	8.03 ± 1.57	57.31 ± 11.18	8.21 ± 1.60	22.76 ± 4.44	2.75 ± 0.54

Note. — Numerical results for the mass and energetic quantities as a function of radial distance for the outflowing gas component. Columns are (1) deprojected distance from the nucleus, (2) mass-weighted mean velocity, (3) gas mass in units of 10^5 $M_\odot$, (4) mass outflow rates, (5) kinetic energies, (6) kinetic energy outflow rates, (7) momenta, and (8) momenta flow rates. These results, shown in Figure 3.10, are the sum of the individual radial profiles calculated for each of the semi-annuli (see Figures 3.7 and 3.9). The value at each distance is the quantity contained within the annulus of width δr.

3.7 Discussion

3.7.1 Comparison with Previous Work

In comparison to Mrk 573 and NGC 4151, the outflows in Mrk 34 reach significantly larger distances from the nucleus. However, on average only half of the gas at each location is participating in the outflow. The increased complexity of the kinematics also corresponds to more uncertainty in the proper correction for projection effects. The clear high velocity separations at $r \leq 0\farcs7$ are consistent with our assumptions of radial outflow along the host galaxy disk. At larger radii, the emission line splitting may indicate an "ablation" scenario where pure radial outflow transitions into the ablation of gas off of nuclear spiral arms as discussed in Fischer et al. (2018). In this case, the motion is not purely radial and the projection effects are less severe, and the mass outflow rate and energetic points at all radii > 1.5 kpc should be treated as upper limits.

Our new APO observations also allow us to probe fainter and more extended emission line knots, including those that fall outside of the narrow *HST* slits. These deep exposures reveal evidence of weak, high velocity outflow components that extend to $\sim 2\farcs5$, or deprojected distances of ~ 3.1 kpc. While these weak components likely contain little mass, they indicate the presence of outflows at nearly twice the distance that we detected in Fischer et al. (2018). There is also indication from the APO observations that some outflow or ablation continues out to ~ 5 kpc, with velocities and FWHM that are larger than systemic for a number of components, including the brightest one at PA = 163°. These components are not included in our mass outflow calculations and require high spatial resolution IFU observations to be properly characterized.

It is encouraging for future studies that the emission line ratios derived from the *HST* and APO observations demonstrate quantitative agreement, as the ground-based observations may be obtained more easily. This could indicate that less stringent data requirements may suffice for this type of study; however, high spatial resolution observations are ultimately needed to

constrain the velocity and mass profiles. In addition, it is possible to create photoionization models that sufficiently constrain the physical conditions in the gas for determining outflow rates and energetics with fewer emission lines than were available for our studies in Crenshaw et al. (2015) and Revalski et al. (2018a). Ultimately, enough emission lines to constrain the gas ionization parameter, number and column density, temperature, and reddening are needed to create a complete model. At a practical minimum, this may include: Hγ λ4340, [O III] λ4363, He II λ4686, [O III] λ5007, [O I] λ6300, Hα λ6563, [N II] λ6584, and [S II] $\lambda\lambda 6716, 6731$. However, we caution that constraining the density from [S II] alone can easily bias gas mass estimates when multi-component models are more appropriate. In the case of Mrk 573, the mean model density is > 1 dex higher near the nucleus, corresponding to significantly less mass than that estimated from [S II] alone.

Finally, the dichotomy in the derived line ratios, abundances, temperatures, and densities on either side of the nucleus is intriguing. It is difficult to conceive of a physical model for this stark bimodality and may further indicate that one side of the NLR is exposed to a more heavily filtered SED. This would affect the quantities derived from the emission line diagnostics, as the various models generally assume a particular power-law SED. Alternatively, the bimodality could also be due to a small tilt of the NLR relative to the host galaxy, which is supported by the small but systemically higher E(B-V) values to the SE that visually correspond to a strong dust lane in Figure 3.1. Additional possibilities, including variations in dust content and varying the locations of each ionized component within the spectral extraction, are discussed in §3.4.3.

3.7.2 Comparison with Global Outflow Rates

We refer to single value mass outflow rates that are calculated from mean conditions across the entire NLR as "global" outflow rates. We compare our results with these techniques to explore systematics and better understand the uncertainties that are introduced by various assumptions.

Following the techniques of Nesvadba et al. (2006) and Bae et al. (2017) we calculate the NLR mass using $M = (9.73 \times 10^8\ M_\odot) \times L_{H\alpha,43} \times n_{e,100}^{-1}$, where $L_{H\alpha,43}$ is the Hα luminosity in units of 10^{43} erg s^{-1}, and $n_{e,100}^{-1}$ is the electron density in units of 100 cm^{-3}. Here we scale the [O III] luminosity by the average Hα/[O III] ratio as a proxy for $L_{H\alpha}$. Using an average velocity of 1000 km s^{-1}, we find $\dot{M}_{out} \approx 3 - 63\ M_\odot$ yr^{-1} for $n_e = 3000 - 150$ cm^{-3}, which is the range of our derived [S II] densities. The corresponding NLR mass estimate is $\sim 0.06 - 1.24$ times the value from our models ($\sim 3.3 \times 10^7\ M_\odot$), emphasizing the importance of density choice on the final mass and outflow energetics. A value of $n_e = 100$ cm^{-3} is often adopted in the literature, which may significantly overestimate the mass and energetics of NLR outflows.

Using the findings from Chapter 2 (§2.8.1), we no longer consider geometric methods that employ filling factors to yield a reliable estimate of the gas mass, unless the filling factor is derived for individual objects using a physical tracer of the gas mass, such as emission line modeling or narrow band imaging (Chapter 4).

3.7.3 Implications for Feedback

The outflows in Mrk 34 reach typical galaxy bulge radii and may deliver important feedback to the host galaxy. The global kinetic luminosity ($M = 3.3 \times 10^7\ M_\odot$, $\delta r = 2000$ pc, $V = 1000$ km s^{-1}) of the outflow is $\sim 0.1\%$ of the AGN bolometric luminosity ($L_{bol} \approx 10^{46.2}$ erg s^{-1}), which approaches the $0.5\% - 5\%$ range used in some models of efficient feedback (Di Matteo et al. 2005; Hopkins & Elvis 2010). This result is consistent with the old nuclear stellar population (González Delgado et al. 2001) and lack of current star formation (Wang et al. 2007); however, mass modeling of the galaxy is required to reveal whether or not the outflows are ultimately capable of escaping the gravitational potential of the host galaxy bulge.

Under the idea that the outflows are radiatively driven (Fischer et al. 2017; Wylezalek & Morganti 2018), the mix of outflow and rotational kinematics at all radii could indicate that the coupling efficiency between the ionizing radiation and gas is very sensitive to the physical

conditions in the outflow (Zubovas 2018). The lack of strong high ionization lines seen in the spectra as compared with NGC 4151 and Mrk 573 would lend support to this idea, but a detailed study of the gas acceleration through photoionization models is needed.

Finally, a multiwavelength picture incorporating the UV/X-ray and molecular gas phases would further illuminate the details behind the driving mechanisms (Cicone et al. 2018). NGC 4151 in particular displays ultra-fast outflows, UV/X-ray winds, and NLR outflows (Tombesi et al. 2010, 2011, 2013; Wang et al. 2011; Crenshaw & Kraemer 2012; Crenshaw et al. 2015), some of which display similar mass outflow rates or energetics to the NLR outflows. This is discussed further in §2.8.3.

3.8 Conclusions

Using long-slit spectroscopy, [O III] imaging, and photoionization modeling, we determined spatially resolved mass outflow rates and energetics for the NLR of the QSO2 Mrk 34. This is the first spatially resolved outflow profile for a QSO2, following the results of Crenshaw et al. (2015); Revalski et al. (2018a), and Venturi et al. (2018) for nearby Seyferts. Our conclusions are the following:

1. The outflow contains $M \approx 1.6 \times 10^7$ $M_\odot$ of ionized gas, with a total kinetic energy of $E \approx 1.0 \times 10^{56}$ erg. These are larger than for the NLRs of the lower luminosity galaxies NGC 4151 (Crenshaw et al. 2015) and Mrk 573 (Revalski et al. 2018a).

2. The outflows extend to ~ 2 kpc, reaching a peak mass outflow rate of $\dot{M}_{out} \approx 12.5 \pm 2.4$ $M_\odot$ yr^{-1} at a distance of 470 pc from the SMBH, with evidence of disturbed kinematics extending up to ~ 5 kpc. The resulting mass outflow rates are consistent with in-situ acceleration where host galaxy material in the NLR is accelerated by nuclear radiation.

3. The presence of multiple kinematic components indicates that only a portion of the NLR gas is in outflow and that global outflow rate techniques may overestimate $\dot{M}_{out}$ in these cases. Without photoionization modeling, gas masses may also be overestimated.

4. The presence of rotation and outflow at all radii in this more luminous target may indicate that the coupling efficiency between the radiation and gas, and the ability of the AGN to radiatively drive outflows, is sensitive to the physical conditions in the gas, as well as the luminosity and driving timescale.

Supplementary Diagnostics

We include here additional figures and tables that are referenced throughout this chapter that further illuminate the analysis. In Figure 3.11, we provide the Gaussian profile decomposition for important emission lines at each spatial position in our APO long-slit observations along PA = 163°. Figure 3.12 displays the spatially resolved BPT diagrams for each of the four APO long-slit position angles, with the fluxes of all kinematic components added together. These are further divided into the ratios obtained for each individual Gaussian component at each position angle in Figure 3.13. In Tables 3.10 and 3.11 we provide the emission line ratios for each kinematic component measured in the *HST* and APO spectra, respectively, that were summed to produce the integrated ratios in Tables 3.2 and 3.4.

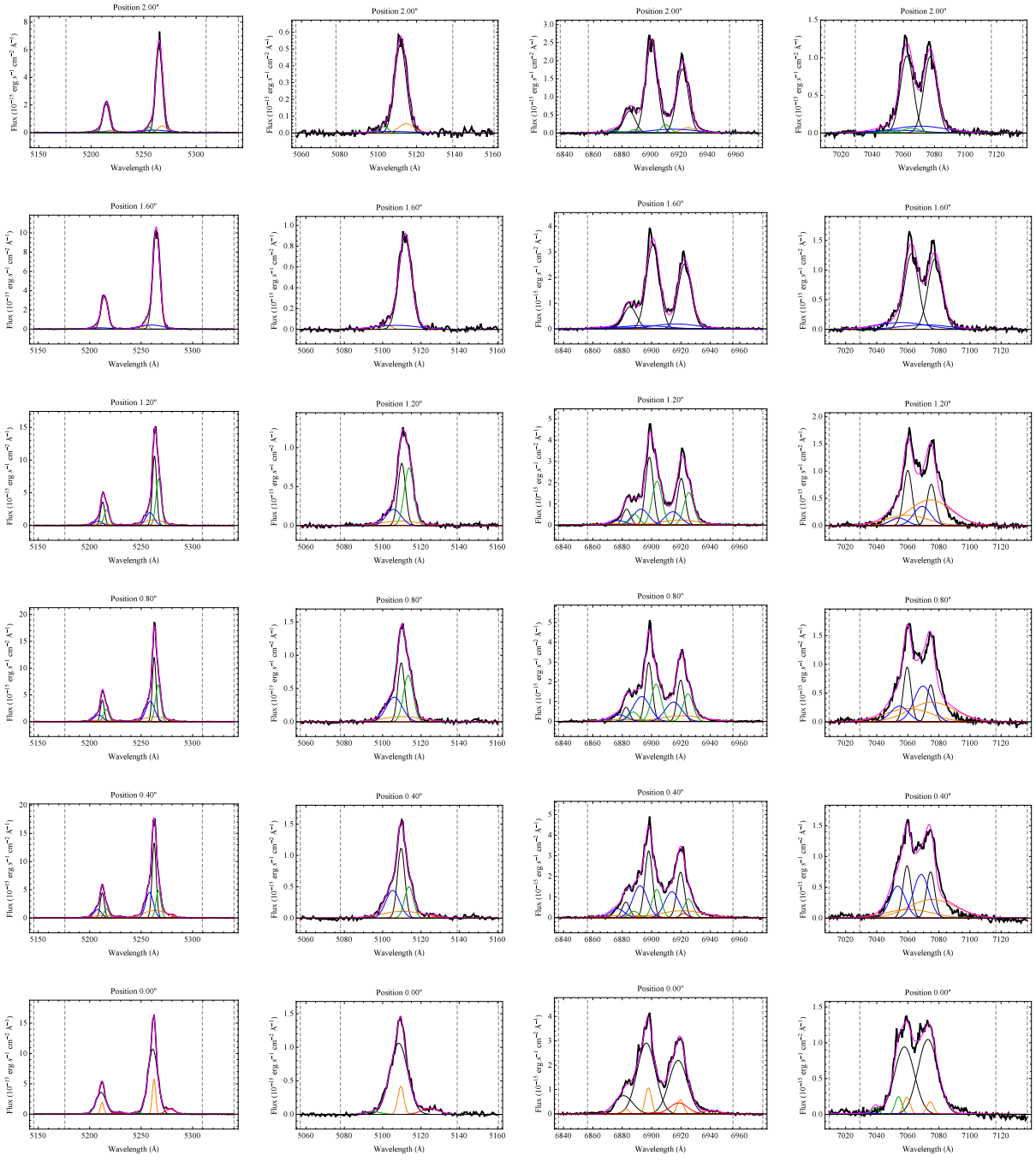

Figure 3.11 Gaussian fits, from left to right, to the [O III], Hβ, [N II]+Hα, and [S II] emission lines for the APO DIS observations along PA = 163°. The components are sorted by peak flux from strongest to weakest: black, orange, blue, green, red, and the total in magenta.

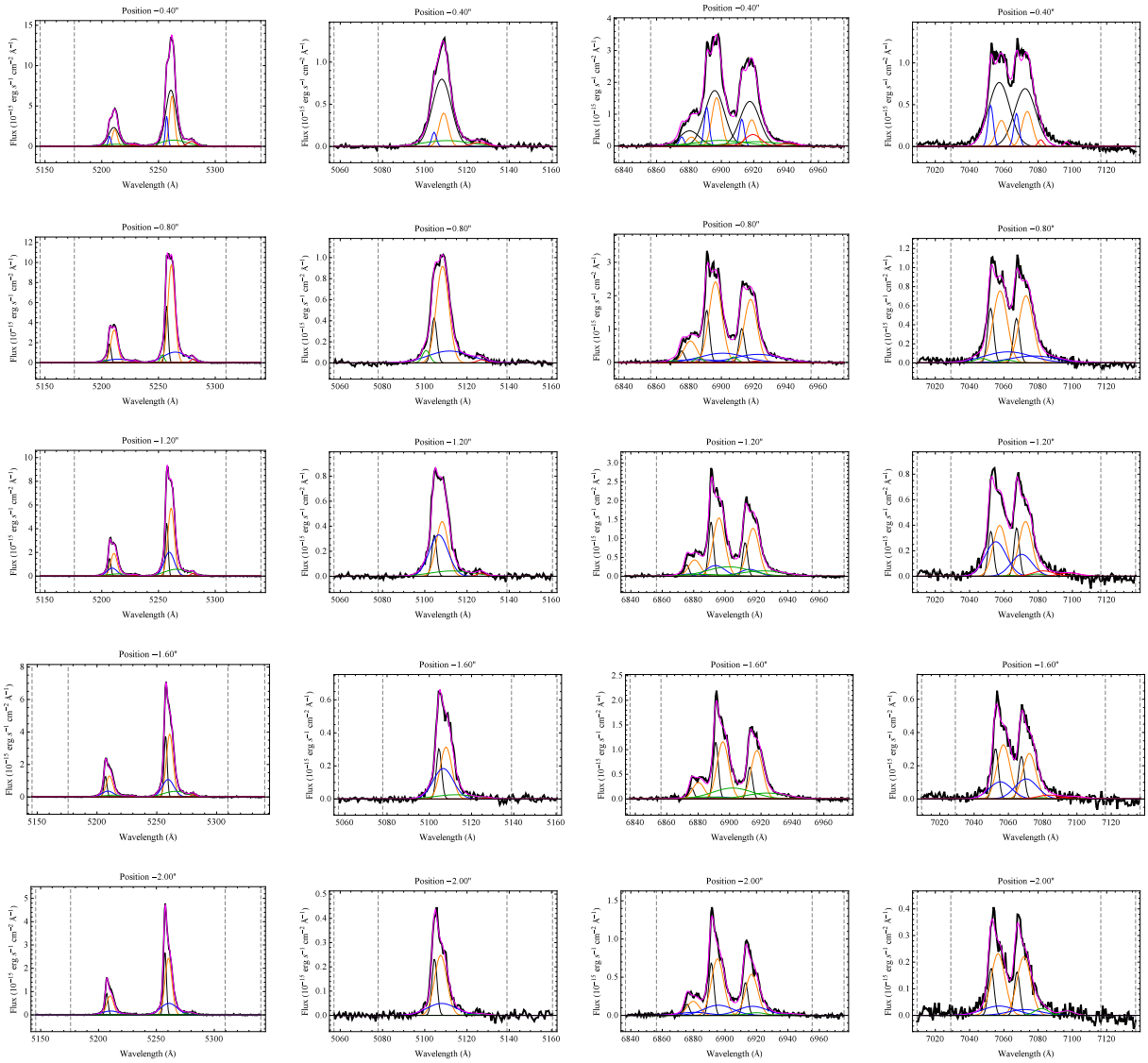

Figure 3.11 *continued.*

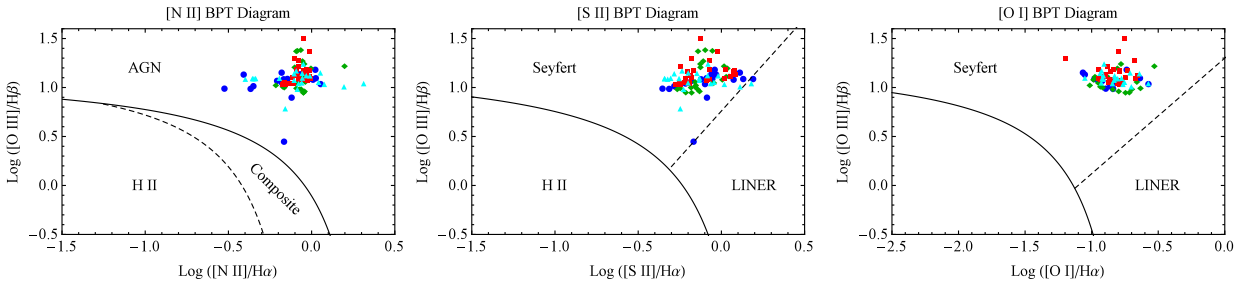

Figure 3.12 BPT ionization diagrams for [N II], [S II], and [O I] using ratios calculated with the fluxes of all kinematic components summed together. The points reach a maximum radial extent of $\sim 8''$ from the nucleus, and symbols are color-coded for each of the four APO DIS position angles: 73° (blue circles), 118° (green diamonds), 163° (red squares), 208° (cyan triangles). The demarcation lines for distinguishing ionization mechanisms are from Kewley et al. (2001, 2006); Kauffmann et al. (2003).

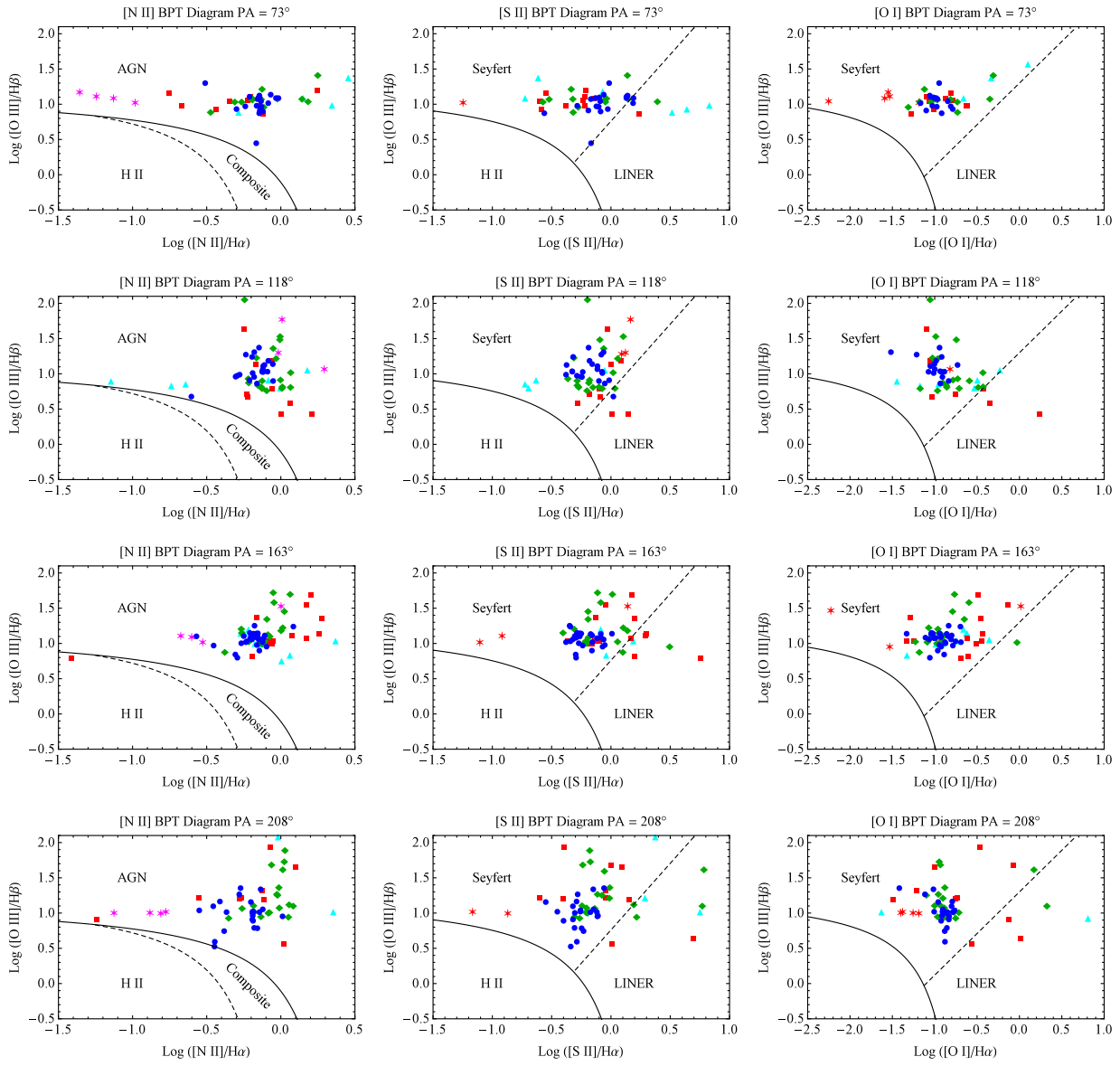

Figure 3.13 BPT ionization diagrams for [N II], [S II], and [O I] for the individual kinematic components for each position angle. The symbols correspond to the peak flux of the kinematic components from strongest to weakest: blue circles, green diamonds, red squares, cyan triangles, magenta stars.

Table 3.10. Observed Emission Line Ratios - Markarian 34 *HST* STIS Spectrum - Components

Component #1	–0.″66	–0.″56	–0.″46	–0.″36	–0.″25	–0.″15	–0.″05	+0.″05	+0.″15	+0.″46	+0.″56	+0.″66
[Ne V] λ3426	... ± ...	0.67 ± 0.54	0.53 ± 0.45	0.72 ± 0.64	... ± ...	... ± ...	0.70 ± 0.47	... ± ...	... ± ...	... ± ...	... ± ...	... ± ...
[O II] λ3728	... ± ...	2.31 ± 1.90	2.02 ± 1.38	1.59 ± 1.03	... ± ...	1.28 ± 1.40	1.29 ± 0.50	1.14 ± 0.47	1.95 ± 4.58	1.09 ± 2.83	1.26 ± 1.38	1.96 ± 1.10
[Ne III] λ3870	... ± ...	0.99 ± 0.81	0.96 ± 0.66	1.00 ± 0.68	0.46 ± 1.00	0.80 ± 0.84	0.43 ± 0.21	0.33 ± 0.16	0.68 ± 1.63	0.64 ± 1.70	0.54 ± 0.62	0.87 ± 0.51
[Ne III] λ3968	... ± ...	... ± ...	0.31 ± 0.22	0.48 ± 0.31	0.49 ± 1.09	0.39 ± 0.46	0.34 ± 0.17	0.37 ± 0.18	... ± ...	... ± ...	... ± ...	0.31 ± 0.26
Hδ λ4102	... ± ...	... ± ...	0.25 ± 0.31	0.30 ± 0.31	... ± ...	... ± ...	0.18 ± 0.21	... ± ...	0.52 ± 1.39	... ± ...	... ± ...	0.32 ± 0.26
Hγ λ4341	... ± ...	0.68 ± 0.58	0.46 ± 0.36	0.36 ± 0.36	... ± ...	0.47 ± 0.52	0.20 ± 0.15	0.31 ± 0.19	... ± ...	0.47 ± 1.24	0.33 ± 0.46	0.38 ± 0.26
[O III] λ4364	... ± ...	... ± ...	... ± ...	... ± ...	... ± ...	... ± ...	... ± ...	... ± ...	... ± ...	0.47 ± 1.22	... ± ...	... ± ...
He II λ4687	... ± ...	0.40 ± 0.38	0.44 ± 0.34	0.32 ± 0.25	... ± ...	... ± ...	... ± ...	... ± ...	0.52 ± 1.46	... ± ...	0.24 ± 0.27	0.36 ± 0.24
Hβ λ4862	... ± ...	1.00 ± 0.27	1.00 ± 0.22	1.00 ± 0.27	1.00 ± 0.70	1.00 ± 0.22	1.00 ± 0.16	1.00 ± 0.21	1.00 ± 0.47	1.00 ± 0.69	1.00 ± 0.42	1.00 ± 0.16
[O III] λ4960	... ± ...	5.03 ± 3.98	4.60 ± 3.10	4.64 ± 2.93	4.79 ± 10.43	4.34 ± 4.41	3.93 ± 1.50	3.52 ± 1.34	4.90 ± 10.93	2.81 ± 7.22	4.43 ± 4.74	4.42 ± 2.38
[O III] λ5008	... ± ...	15.15 ± 11.98	13.85 ± 9.33	13.98 ± 8.82	14.43 ± 31.39	13.05 ± 13.28	11.83 ± 4.50	10.59 ± 4.03	14.74 ± 32.89	8.46 ± 21.75	13.33 ± 14.25	13.30 ± 7.16
[O I] λ6302	... ± ...	... ± ...	... ± ...	... ± ...	... ± ...	... ± ...	... ± ...	... ± ...	... ± ...	... ± ...	0.37 ± 0.82	... ± ...
[N II] λ6549	... ± ...	1.37 ± 1.10	0.75 ± 0.52	0.83 ± 0.53	0.76 ± 1.66	0.69 ± 0.71	0.71 ± 0.28	0.75 ± 0.29	1.57 ± 3.51	... ± ...	0.81 ± 0.88	0.81 ± 0.45
Hα λ6564	... ± ...	4.45 ± 3.55	2.91 ± 2.03	2.88 ± 1.85	... ± ...	2.71 ± 2.77	3.98 ± 1.53	4.16 ± 1.59	8.49 ± 19.00	2.70 ± 6.94	2.63 ± 2.84	2.88 ± 1.60
[N II] λ6585	... ± ...	4.05 ± 3.23	2.22 ± 1.55	2.44 ± 1.57	2.25 ± 4.90	2.03 ± 2.08	2.11 ± 0.81	2.21 ± 0.85	4.63 ± 10.35	1.63 ± 4.18	2.40 ± 2.58	2.40 ± 1.33
[S II] λ6718	... ± ...	0.95 ± 0.77	0.66 ± 0.46	0.68 ± 0.45	0.65 ± 1.41	0.70 ± 0.74	0.82 ± 0.33	0.94 ± 0.36	... ± ...	1.03 ± 2.71	1.28 ± 1.42	0.41 ± 0.29
[S II] λ6732	... ± ...	1.38 ± 1.12	0.79 ± 0.55	0.96 ± 0.64	1.39 ± 3.02	0.46 ± 0.48	0.51 ± 0.21	0.80 ± 0.31	... ± ...	0.87 ± 2.29	0.90 ± 1.00	0.53 ± 0.37
F(Hβ) $\times 10^{-15}$	0.00 ± 0.00	0.33 ± 0.09	0.46 ± 0.10	0.50 ± 0.13	0.20 ± 0.14	0.30 ± 0.07	0.59 ± 0.10	0.64 ± 0.13	0.21 ± 0.10	0.21 ± 0.15	0.37 ± 0.15	0.42 ± 0.07

Component #2	–0.″66	–0.″56	–0.″46	–0.″36	–0.″25	–0.″15	–0.″05	+0.″05	+0.″15	+0.″46	+0.″56	+0.″66
[Ne V] λ3426	... ± ...	0.68 ± 1.15	... ± ...	1.14 ± 3.32	1.90 ± 3.05	... ± ...	... ± ...	... ± ...	... ± ...	... ± ...	... ± ...	... ± ...
[O II] λ3728	1.50 ± 1.60	1.20 ± 2.04	... ± ...	1.66 ± 4.73	2.43 ± 3.88	... ± ...	... ± ...	2.02 ± 3.62	... ± ...	1.20 ± 4.08	1.50 ± 3.17	... ± ...
[Ne III] λ3870	0.82 ± 0.85	0.76 ± 1.29	... ± ...	0.71 ± 2.04	1.20 ± 1.93	... ± ...	... ± ...	0.53 ± 0.96	... ± ...	0.99 ± 3.38	0.76 ± 1.62	... ± ...
[Ne III] λ3968	0.24 ± 0.26	0.86 ± 1.46	... ± ...	... ± ...	... ± ...	... ± ...	... ± ...	... ± ...	... ± ...	0.44 ± 1.53	0.54 ± 1.19	... ± ...
Hδ λ4102	... ± ...	0.49 ± 0.94	... ± ...	... ± ...	... ± ...	... ± ...	... ± ...	... ± ...	... ± ...	... ± ...	... ± ...	... ± ...
Hγ λ4341	0.31 ± 0.40	... ± ...	... ± ...	... ± ...	0.48 ± 0.79	... ± ...	... ± ...	... ± ...	... ± ...	... ± ...	... ± ...	... ± ...
[O III] λ4364	... ± ...	0.21 ± 0.36	... ± ...	... ± ...	... ± ...	... ± ...	... ± ...	... ± ...	... ± ...	0.30 ± 1.02	... ± ...	... ± ...
He II λ4687	0.35 ± 0.43	0.57 ± 1.02	... ± ...	... ± ...	0.85 ± 1.37	... ± ...	... ± ...	... ± ...	... ± ...	0.65 ± 2.28	0.74 ± 1.58	... ± ...
Hβ λ4862	1.00 ± 0.21	1.00 ± 0.58	... ± ...	1.00 ± 1.22	1.00 ± 0.51	... ± ...	... ± ...	1.00 ± 0.98	... ± ...	1.00 ± 0.90	1.00 ± 0.82	... ± ...
[O III] λ4960	3.99 ± 4.12	5.80 ± 9.82	... ± ...	3.43 ± 9.74	4.39 ± 6.93	... ± ...	... ± ...	1.40 ± 2.49	... ± ...	4.48 ± 15.09	4.18 ± 8.75	... ± ...
[O III] λ5008	12.01 ± 12.39	17.46 ± 29.57	... ± ...	10.32 ± 29.33	13.20 ± 20.86	... ± ...	... ± ...	4.22 ± 7.51	... ± ...	13.48 ± 45.43	12.58 ± 26.32	... ± ...
[O I] λ6302	... ± ...	... ± ...	... ± ...	... ± ...	... ± ...	... ± ...	... ± ...	... ± ...	... ± ...	... ± ...	... ± ...	... ± ...
[N II] λ6549	... ± ...	... ± ...	... ± ...	2.20 ± 6.26	0.84 ± 1.32	... ± ...	... ± ...	... ± ...	... ± ...	... ± ...	... ± ...	... ± ...
Hα λ6564	1.88 ± 1.95	1.48 ± 2.51	... ± ...	... ± ...	7.01 ± 11.10	... ± ...	... ± ...	2.76 ± 4.92	... ± ...	3.63 ± 12.23	1.99 ± 4.17	... ± ...
[N II] λ6585	... ± ...	... ± ...	... ± ...	6.49 ± 18.47	2.47 ± 3.90	... ± ...	... ± ...	2.65 ± 4.72	... ± ...	2.58 ± 8.71	1.31 ± 2.74	... ± ...
[S II] λ6718	0.52 ± 0.56	... ± ...	... ± ...	... ± ...	0.86 ± 1.37	... ± ...	... ± ...	... ± ...	... ± ...	... ± ...	... ± ...	... ± ...
[S II] λ6732	... ± ...	... ± ...	... ± ...	... ± ...	0.83 ± 1.31	... ± ...	... ± ...	... ± ...	... ± ...	... ± ...	... ± ...	... ± ...
F(Hβ) $\times 10^{-15}$	0.28 ± 0.06	0.16 ± 0.09	0.00 ± 0.00	0.11 ± 0.13	0.28 ± 0.14	0.00 ± 0.00	0.00 ± 0.00	0.14 ± 0.13	0.00 ± 0.00	0.16 ± 0.15	0.19 ± 0.15	0.00 ± 0.00

Note. — Same as in Table 3.2, but for the individual rotational (#1) and outflow (#2) components.

Table 3.11. Observed Emission Line Ratios - Markarian 34 APO DIS Spectrum - Components

Component #1	−2.″0	−1.″6	−1.″2	−0.″8	−0.″4	0.″0	+0.″4	+0.″8	+1.″2	+1.″6	+2.″0
[S II] λ4072	... ± ...	... ± ...	... ± ...	0.13 ± 0.01	0.08 ± 0.01	0.07 ± 0.01	... ± ...	... ± ...	... ± ...	... ± ...	... ± ...
Hδ λ4101	... ± ...	0.13 ± 0.03	0.15 ± 0.02	0.20 ± 0.02	0.14 ± 0.01	0.14 ± 0.02	0.15 ± 0.01	0.17 ± 0.02	0.20 ± 0.02	0.18 ± 0.05	0.20 ± 0.06
Hγ λ4340	0.26 ± 0.05	0.19 ± 0.02	0.18 ± 0.01	0.34 ± 0.02	0.36 ± 0.01	0.32 ± 0.01	0.34 ± 0.01	0.33 ± 0.01	0.34 ± 0.01	0.35 ± 0.03	0.39 ± 0.04
[O III] λ4363	... ± ...	... ± ...	... ± ...	0.16 ± 0.01	0.12 ± 0.00	0.10 ± 0.00	0.11 ± 0.00	0.12 ± 0.00	0.12 ± 0.00	0.14 ± 0.01	0.16 ± 0.02
He II λ4685	0.18 ± 0.05	0.26 ± 0.03	0.33 ± 0.03	0.20 ± 0.01	0.22 ± 0.01	0.22 ± 0.01	0.26 ± 0.01	0.25 ± 0.01	0.28 ± 0.02	0.24 ± 0.02	0.26 ± 0.03
Hβ λ4861	1.00 ± 0.26	1.00 ± 0.13	1.00 ± 0.15	1.00 ± 0.14	1.00 ± 0.02	1.00 ± 0.02	1.00 ± 0.04	1.00 ± 0.06	1.00 ± 0.04	1.00 ± 0.06	1.00 ± 0.06
[O III] λ4958	3.98 ± 0.62	4.21 ± 0.36	4.67 ± 0.32	4.51 ± 0.21	2.99 ± 0.03	3.46 ± 0.04	4.06 ± 0.06	4.61 ± 0.08	4.57 ± 0.08	3.94 ± 0.12	4.01 ± 0.14
[O III] λ5006	11.99 ± 1.87	12.67 ± 1.08	14.06 ± 0.96	13.56 ± 0.63	8.99 ± 0.09	10.42 ± 0.12	12.21 ± 0.18	13.87 ± 0.25	13.77 ± 0.23	11.84 ± 0.36	12.07 ± 0.41
[N I] λ5199	... ± ...	... ± ...	... ± ...	... ± ...	... ± ...	... ± ...	0.12 ± 0.03	0.15 ± 0.05	0.12 ± 0.04	... ± ...	... ± ...
He I λ5875	... ± ...	0.12 ± 0.02	... ± ...	0.15 ± 0.01	0.10 ± 0.01	0.14 ± 0.01	0.13 ± 0.01	0.15 ± 0.01	0.21 ± 0.03	0.19 ± 0.04	0.28 ± 0.03
[Fe VII] λ6086	... ± ...	... ± ...	... ± ...	... ± ...	0.08 ± 0.01	0.09 ± 0.02	0.07 ± 0.01	0.09 ± 0.02	0.07 ± 0.01	0.08 ± 0.04	0.09 ± 0.05
[O I] λ6300	0.41 ± 0.10	0.60 ± 0.07	0.55 ± 0.05	0.45 ± 0.03	0.36 ± 0.02	0.50 ± 0.03	0.46 ± 0.02	0.52 ± 0.03	0.52 ± 0.03	0.50 ± 0.08	0.51 ± 0.07
[O I] λ6363	0.14 ± 0.03	0.20 ± 0.02	0.18 ± 0.02	0.15 ± 0.01	0.12 ± 0.01	0.17 ± 0.01	0.15 ± 0.01	0.17 ± 0.01	0.17 ± 0.01	0.17 ± 0.03	0.17 ± 0.02
[N II] λ6548	0.84 ± 0.14	0.97 ± 0.08	1.24 ± 0.09	1.09 ± 0.05	0.81 ± 0.02	0.95 ± 0.02	0.90 ± 0.02	1.08 ± 0.03	1.27 ± 0.03	1.30 ± 0.07	1.55 ± 0.08
Hα λ6562	3.94 ± 0.64	5.04 ± 0.44	5.89 ± 0.41	4.92 ± 0.25	2.95 ± 0.06	3.70 ± 0.07	3.89 ± 0.09	4.51 ± 0.10	5.41 ± 0.12	4.98 ± 0.27	6.44 ± 0.32
[N II] λ6583	2.48 ± 0.40	2.85 ± 0.25	3.66 ± 0.26	3.21 ± 0.16	2.38 ± 0.05	2.81 ± 0.05	2.67 ± 0.06	3.18 ± 0.07	3.73 ± 0.08	3.84 ± 0.21	4.56 ± 0.23
[S II] λ6716	1.04 ± 0.18	1.36 ± 0.12	1.48 ± 0.11	1.84 ± 0.10	1.33 ± 0.03	1.23 ± 0.03	1.05 ± 0.04	1.48 ± 0.07	1.75 ± 0.08	1.99 ± 0.17	2.69 ± 0.18
[S II] λ6730	0.97 ± 0.17	1.15 ± 0.10	1.60 ± 0.12	1.51 ± 0.08	1.20 ± 0.03	1.37 ± 0.03	0.93 ± 0.03	1.00 ± 0.04	1.31 ± 0.06	1.85 ± 0.15	2.67 ± 0.18
F(Hβ) $\times 10^{-15}$	0.70 ± 0.18	0.95 ± 0.12	0.94 ± 0.15	1.39 ± 0.19	8.97 ± 0.19	12.33 ± 0.30	5.42 ± 0.23	3.93 ± 0.22	3.96 ± 0.16	7.32 ± 0.42	4.02 ± 0.24

Component #2	−2.″0	−1.″6	−1.″2	−0.″8	−0.″4	0.″0	+0.″4	+0.″8	+1.″2	+1.″6	+2.″0
[S II] λ4072	... ± ...	... ± ...	... ± ...	... ± ...	... ± ...	... ± ...	... ± ...	... ± ...	... ± ...	... ± ...	... ± ...
Hδ λ4101	... ± ...	... ± ...	... ± ...	0.14 ± 0.01	0.16 ± 0.02	0.12 ± 0.02	... ± ...	... ± ...	... ± ...	... ± ...	... ± ...
Hγ λ4340	0.26 ± 0.04	0.17 ± 0.01	0.21 ± 0.01	0.33 ± 0.01	0.27 ± 0.01	0.38 ± 0.02	0.67 ± 0.03	0.71 ± 0.03	... ± ...	... ± ...	... ± ...
[O III] λ4363	... ± ...	0.17 ± 0.01	0.13 ± 0.01	0.10 ± 0.00	... ± ...	... ± ...	... ± ...	... ± ...	... ± ...	... ± ...	... ± ...
He II λ4685	0.26 ± 0.06	0.29 ± 0.02	0.31 ± 0.02	0.25 ± 0.01	0.30 ± 0.02	0.33 ± 0.02	... ± ...	... ± ...	... ± ...	... ± ...	... ± ...
Hβ λ4861	1.00 ± 0.10	1.00 ± 0.06	1.00 ± 0.05	1.00 ± 0.03	1.00 ± 0.09	1.00 ± 0.18	1.00 ± 0.08	1.00 ± 0.11	1.00 ± 0.11	1.00 ± 1.65	1.00 ± 0.44
[O III] λ4958	3.36 ± 0.21	4.21 ± 0.16	4.48 ± 0.10	3.63 ± 0.04	5.37 ± 0.14	4.74 ± 0.22	4.19 ± 0.09	4.01 ± 0.12	4.87 ± 0.18	4.56 ± 1.51	3.01 ± 0.56
[O III] λ5006	10.12 ± 0.65	12.67 ± 0.48	13.47 ± 0.30	10.91 ± 0.13	16.16 ± 0.41	14.26 ± 0.67	12.60 ± 0.28	12.08 ± 0.37	14.67 ± 0.55	13.73 ± 4.55	9.05 ± 1.67
[N I] λ5199	... ± ...	... ± ...	... ± ...	... ± ...	... ± ...	... ± ...	... ± ...	... ± ...	... ± ...	... ± ...	... ± ...
He I λ5875	0.13 ± 0.06	... ± ...	0.10 ± 0.01	0.13 ± 0.01	0.22 ± 0.02	... ± ...	... ± ...	... ± ...	... ± ...	... ± ...	... ± ...
[Fe VII] λ6086	... ± ...	0.11 ± 0.03	0.08 ± 0.02	0.07 ± 0.01	0.10 ± 0.02	... ± ...	... ± ...	... ± ...	... ± ...	... ± ...	... ± ...
[O I] λ6300	0.43 ± 0.09	0.64 ± 0.05	0.58 ± 0.04	0.44 ± 0.02	0.57 ± 0.04	0.39 ± 0.03	1.14 ± 0.06	1.34 ± 0.08	2.02 ± 0.13	... ± ...	1.00 ± 0.23
[O I] λ6363	0.14 ± 0.03	0.21 ± 0.02	0.19 ± 0.01	0.15 ± 0.01	0.19 ± 0.01	... ± ...	... ± ...	... ± ...	... ± ...	... ± ...	... ± ...
[N II] λ6548	1.00 ± 0.08	1.43 ± 0.06	1.33 ± 0.04	0.94 ± 0.02	0.96 ± 0.03	0.64 ± 0.03	1.41 ± 0.04	1.66 ± 0.06	1.90 ± 0.08	... ± ...	1.22 ± 0.23
Hα λ6562	4.03 ± 0.31	4.98 ± 0.21	4.76 ± 0.14	3.54 ± 0.08	5.17 ± 0.16	3.45 ± 0.17	... ± ...	... ± ...	... ± ...	... ± ...	... ± ...
[N II] λ6583	2.94 ± 0.23	4.23 ± 0.18	3.92 ± 0.11	2.78 ± 0.06	2.82 ± 0.09	1.90 ± 0.09	4.15 ± 0.12	4.90 ± 0.17	5.60 ± 0.23	... ± ...	3.59 ± 0.68

Table 3.11 (cont'd)

[S II] λ6716	1.29 ± 0.13	1.43 ± 0.07	1.26 ± 0.04	1.14 ± 0.03	1.09 ± 0.04	0.79 ± 0.04	1.76 ± 0.07	4.12 ± 0.21	4.53 ± 0.27	... ± ...	... ± ...
[S II] λ6730	1.23 ± 0.12	1.21 ± 0.06	1.36 ± 0.05	1.06 ± 0.03	1.46 ± 0.05	0.58 ± 0.03	3.83 ± 0.15	6.08 ± 0.31	11.33 ± 0.67	... ± ...	... ± ...
F(Hβ) ×10^{-15}	1.81 ± 0.18	2.18 ± 0.12	3.09 ± 0.15	6.86 ± 0.19	2.16 ± 0.19	1.66 ± 0.30	2.97 ± 0.23	2.06 ± 0.22	1.40 ± 0.16	0.25 ± 0.42	0.55 ± 0.24

Component #3	–2.″0	–1.″6	–1.″2	–0.″8	–0.″4	0.″0	+0.″4	+0.″8	+1.″2	+1.″6	+2.″0
[S II] λ4072	... ± ...	... ± ...	... ± ...	... ± ...	... ± ...	... ± ...	0.20 ± 0.02	0.16 ± 0.02	0.46 ± 0.05	... ± ...	... ± ...
Hδ λ4101	... ± ...	0.23 ± 0.04	0.21 ± 0.03	... ± ...	0.28 ± 0.04	... ± ...	0.15 ± 0.01	0.23 ± 0.02	0.27 ± 0.03	... ± ...	... ± ...
Hγ λ4340	0.69 ± 0.12	0.58 ± 0.03	0.45 ± 0.02	0.55 ± 0.02	... ± ...	... ± ...	0.37 ± 0.01	0.45 ± 0.02	0.55 ± 0.02	1.07 ± 0.13	... ± ...
[O III] λ4363	... ± ...	... ± ...	... ± ...	... ± ...	... ± ...	... ± ...	0.14 ± 0.01	0.18 ± 0.01	... ± ...	... ± ...	... ± ...
He II λ4685	... ± ...	... ± ...	... ± ...	... ± ...	0.28 ± 0.03	... ± ...	0.20 ± 0.01	0.25 ± 0.01	0.25 ± 0.02	... ± ...	... ± ...
Hβ λ4861	1.00 ± 0.22	1.00 ± 0.06	1.00 ± 0.04	1.00 ± 0.07	1.00 ± 0.40	... ± ...	1.00 ± 0.06	1.00 ± 0.06	1.00 ± 0.08	1.00 ± 0.39	... ± ...
[O III] λ4958	3.44 ± 0.45	2.00 ± 0.08	2.08 ± 0.04	3.22 ± 0.08	7.55 ± 0.84	... ± ...	3.51 ± 0.06	3.49 ± 0.06	3.22 ± 0.09	3.87 ± 0.32	... ± ...
[O III] λ5006	10.37 ± 1.34	6.02 ± 0.23	6.27 ± 0.12	9.69 ± 0.23	22.72 ± 2.54	... ± ...	10.55 ± 0.19	10.51 ± 0.19	9.71 ± 0.26	11.65 ± 0.97	... ± ...
[N I] λ5199	... ± ...	... ± ...	... ± ...	... ± ...	... ± ...	... ± ...	... ± ...	... ± ...	... ± ...	... ± ...	... ± ...
He I λ5875	... ± ...	... ± ...	... ± ...	... ± ...	0.33 ± 0.04	... ± ...	0.26 ± 0.02	0.24 ± 0.02	... ± ...	... ± ...	... ± ...
[Fe VII] λ6086	... ± ...	... ± ...	... ± ...	... ± ...	... ± ...	... ± ...	... ± ...	... ± ...	... ± ...	... ± ...	... ± ...
[O I] λ6300	1.34 ± 0.32	... ± ...	0.29 ± 0.02	1.02 ± 0.06	0.50 ± 0.06	... ± ...	0.27 ± 0.01	0.22 ± 0.01	... ± ...	1.11 ± 0.20	... ± ...
[O I] λ6363	... ± ...	... ± ...	... ± ...	... ± ...	... ± ...	... ± ...	... ± ...	... ± ...	... ± ...	... ± ...	... ± ...
[N II] λ6548	1.11 ± 0.15	... ± ...	0.25 ± 0.01	0.98 ± 0.03	2.29 ± 0.26	... ± ...	1.30 ± 0.03	1.20 ± 0.03	1.39 ± 0.04	2.32 ± 0.22	... ± ...
Hα λ6562	3.65 ± 0.50	... ± ...	1.16 ± 0.03	3.31 ± 0.10	9.74 ± 1.10	... ± ...	4.72 ± 0.12	4.56 ± 0.11	4.87 ± 0.15	4.57 ± 0.43	... ± ...
[N II] λ6583	3.26 ± 0.45	... ± ...	0.75 ± 0.02	2.90 ± 0.09	6.76 ± 0.76	... ± ...	3.85 ± 0.09	3.55 ± 0.08	4.10 ± 0.13	6.83 ± 0.65	... ± ...
[S II] λ6716	... ± ...	0.77 ± 0.04	1.13 ± 0.04	1.42 ± 0.05	4.02 ± 0.46	... ± ...	1.62 ± 0.06	1.01 ± 0.04	0.94 ± 0.05	4.14 ± 0.47	... ± ...
[S II] λ6730	... ± ...	0.91 ± 0.04	0.72 ± 0.02	0.89 ± 0.03	3.24 ± 0.37	... ± ...	2.21 ± 0.08	2.32 ± 0.10	2.35 ± 0.12	2.72 ± 0.31	... ± ...
F(Hβ) ×10^{-15}	0.85 ± 0.18	2.18 ± 0.12	3.67 ± 0.15	2.84 ± 0.19	0.47 ± 0.19	0.00 ± 0.00	3.99 ± 0.23	3.87 ± 0.22	2.03 ± 0.16	1.08 ± 0.42	0.00 ± 0.00

Component #4	–2.″0	–1.″6	–1.″2	–0.″8	–0.″4	0.″0	+0.″4	+0.″8	+1.″2	+1.″6	+2.″0
[S II] λ4072	... ± ...	... ± ...	... ± ...	0.41 ± 0.06	... ± ...	... ± ...	... ± ...	... ± ...	... ± ...	... ± ...	... ± ...
Hδ λ4101	... ± ...	... ± ...	... ± ...	... ± ...	... ± ...	... ± ...	0.11 ± 0.01	0.14 ± 0.01	0.13 ± 0.01	... ± ...	... ± ...
Hγ λ4340	... ± ...	... ± ...	... ± ...	0.55 ± 0.07	... ± ...	... ± ...	0.29 ± 0.01	0.32 ± 0.01	0.32 ± 0.01	... ± ...	... ± ...
[O III] λ4363	... ± ...	... ± ...	... ± ...	... ± ...	... ± ...	... ± ...	... ± ...	0.10 ± 0.00	0.09 ± 0.00	... ± ...	... ± ...
He II λ4685	... ± ...	... ± ...	... ± ...	... ± ...	... ± ...	... ± ...	0.26 ± 0.01	0.25 ± 0.01	0.23 ± 0.02	... ± ...	... ± ...
Hβ λ4861	... ± ...	1.00 ± 0.20	1.00 ± 0.13	1.00 ± 0.37	1.00 ± 0.10	1.00 ± 0.72	1.00 ± 0.08	1.00 ± 0.05	1.00 ± 0.03	... ± ...	1.00 ± 1.04
[O III] λ4958	... ± ...	4.65 ± 0.61	4.64 ± 0.27	2.27 ± 0.28	3.78 ± 0.11	1.89 ± 0.34	3.33 ± 0.08	3.37 ± 0.06	3.27 ± 0.05	... ± ...	3.63 ± 1.58
[O III] λ5006	... ± ...	14.00 ± 1.85	13.97 ± 0.82	6.84 ± 0.85	11.39 ± 0.32	5.68 ± 1.04	10.01 ± 0.23	10.13 ± 0.17	9.85 ± 0.15	... ± ...	10.92 ± 4.74
[N I] λ5199	... ± ...	... ± ...	... ± ...	... ± ...	... ± ...	... ± ...	... ± ...	... ± ...	... ± ...	... ± ...	... ± ...
He I λ5875	... ± ...	... ± ...	... ± ...	... ± ...	... ± ...	... ± ...	... ± ...	0.09 ± 0.01	0.09 ± 0.01	... ± ...	... ± ...
[Fe VII] λ6086	... ± ...	... ± ...	... ± ...	... ± ...	... ± ...	... ± ...	0.17 ± 0.03	0.08 ± 0.01	0.09 ± 0.02	... ± ...	... ± ...
[O I] λ6300	... ± ...	2.80 ± 0.42	1.94 ± 0.16	... ± ...	1.52 ± 0.09	... ± ...	0.44 ± 0.02	0.46 ± 0.02	0.39 ± 0.02	... ± ...	... ± ...

Table 3.11 (cont'd)

[O I] λ6363	... ± ...	... ± ...	... ± ...	... ± ...	... ± ...	... ± ...	0.15 ± 0.01	0.15 ± 0.01	0.13 ± 0.01	... ± ...	... ± ...
[N II] λ6548	... ± ...	2.15 ± 0.29	1.54 ± 0.09	0.63 ± 0.08	... ± ...	... ± ...	0.84 ± 0.02	0.91 ± 0.02	0.95 ± 0.02	... ± ...	2.77 ± 1.21
Hα λ6562	... ± ...	11.74 ± 1.56	7.92 ± 0.49	1.61 ± 0.20	3.41 ± 0.11	... ± ...	3.67 ± 0.10	3.63 ± 0.08	3.76 ± 0.08	... ± ...	3.47 ± 1.51
[N II] λ6583	... ± ...	6.34 ± 0.84	4.55 ± 0.28	1.86 ± 0.23	2.62 ± 0.09	... ± ...	2.47 ± 0.07	2.68 ± 0.06	2.81 ± 0.06	... ± ...	8.18 ± 3.57
[S II] λ6716	... ± ...	... ± ...	... ± ...	... ± ...	... ± ...	1.31 ± 0.24	... ± ...	... ± ...	... ± ...	... ± ...	... ± ...
[S II] λ6730	... ± ...	... ± ...	... ± ...	... ± ...	... ± ...	3.27 ± 0.60	... ± ...	... ± ...	... ± ...	... ± ...	3.86 ± 1.69
F(Hβ) $\times 10^{-15}$	0.00 ± 0.00	0.61 ± 0.12	1.10 ± 0.15	0.52 ± 0.19	1.95 ± 0.19	0.42 ± 0.30	2.89 ± 0.23	4.41 ± 0.22	4.62 ± 0.16	0.00 ± 0.00	0.23 ± 0.24

Component #5	−2.″0	−1.″6	−1.″2	−0.″8	−0.″4	0.″0	+0.″4	+0.″8	+1.″2	+1.″6	+2.″0
[S II] λ4072	... ± ...	... ± ...	... ± ...	... ± ...	... ± ...	... ± ...	... ± ...	... ± ...	... ± ...	... ± ...	... ± ...
Hδ λ4101	... ± ...	... ± ...	... ± ...	... ± ...	... ± ...	... ± ...	... ± ...	... ± ...	... ± ...	... ± ...	... ± ...
Hγ λ4340	... ± ...	... ± ...	... ± ...	... ± ...	... ± ...	... ± ...	... ± ...	... ± ...	... ± ...	... ± ...	... ± ...
[O III] λ4363	... ± ...	... ± ...	... ± ...	... ± ...	... ± ...	... ± ...	... ± ...	... ± ...	... ± ...	... ± ...	... ± ...
He II λ4685	... ± ...	... ± ...	... ± ...	... ± ...	... ± ...	... ± ...	... ± ...	... ± ...	... ± ...	... ± ...	... ± ...
Hβ λ4861	... ± ...	... ± ...	... ± ...	... ± ...	1.00 ± 0.44	1.00 ± 0.30	... ± ...	... ± ...	... ± ...	... ± ...	... ± ...
[O III] λ4958	... ± ...	... ± ...	... ± ...	... ± ...	4.18 ± 0.51	3.38 ± 0.26	... ± ...	... ± ...	... ± ...	... ± ...	... ± ...
[O III] λ5006	... ± ...	... ± ...	... ± ...	... ± ...	12.57 ± 1.52	10.18 ± 0.77	... ± ...	... ± ...	... ± ...	... ± ...	... ± ...
[N I] λ5199	... ± ...	... ± ...	... ± ...	... ± ...	... ± ...	... ± ...	... ± ...	... ± ...	... ± ...	... ± ...	... ± ...
He I λ5875	... ± ...	... ± ...	... ± ...	... ± ...	... ± ...	... ± ...	... ± ...	... ± ...	... ± ...	... ± ...	... ± ...
[Fe VII] λ6086	... ± ...	... ± ...	... ± ...	... ± ...	... ± ...	... ± ...	... ± ...	... ± ...	... ± ...	... ± ...	... ± ...
[O I] λ6300	... ± ...	... ± ...	... ± ...	... ± ...	... ± ...	0.78 ± 0.07	... ± ...	... ± ...	... ± ...	... ± ...	... ± ...
[O I] λ6363	... ± ...	... ± ...	... ± ...	... ± ...	... ± ...	... ± ...	... ± ...	... ± ...	... ± ...	... ± ...	... ± ...
[N II] λ6548	... ± ...	... ± ...	... ± ...	... ± ...	... ± ...	... ± ...	... ± ...	... ± ...	... ± ...	... ± ...	... ± ...
Hα λ6562	... ± ...	... ± ...	... ± ...	... ± ...	10.00 ± 1.22	6.87 ± 0.53	... ± ...	... ± ...	... ± ...	... ± ...	... ± ...
[N II] λ6583	... ± ...	... ± ...	... ± ...	... ± ...	2.13 ± 0.26	2.06 ± 0.16	... ± ...	... ± ...	... ± ...	... ± ...	... ± ...
[S II] λ6716	... ± ...	... ± ...	... ± ...	... ± ...	0.72 ± 0.09	... ± ...	... ± ...	... ± ...	... ± ...	... ± ...	... ± ...
[S II] λ6730	... ± ...	... ± ...	... ± ...	... ± ...	... ± ...	... ± ...	... ± ...	... ± ...	... ± ...	... ± ...	... ± ...
F(Hβ) $\times 10^{-15}$	0.00 ± 0.00	0.00 ± 0.00	0.00 ± 0.00	0.00 ± 0.00	0.43 ± 0.19	1.01 ± 0.30	0.00 ± 0.00	0.00 ± 0.00	0.00 ± 0.00	0.00 ± 0.00	0.00 ± 0.00

Note. — Same as in Table 3.4, but for the individual kinematic components, sorted from strongest to weakest peak flux.

CHAPTER 4

SIMPLIFIED METHODS

4.1 The Search for a Simplified Methodology

The results of this study rest upon our ability to accurately determine the mass of ionized gas that is responsible for producing the observed emission line luminosities. We have generated photoionization models to match the relative emission line strengths and reveal the physical conditions in the gas such as number density, column density, and ionization state. These models capture all of the physical processes that lead to photon emission and allow us to predict the luminosity per unit mass that is emitted by the photoionized gas.

The physical conditions in the gas can vary significantly on small scales that may be unresolved even in our high spatial resolution *HST* STIS observations as evidenced by the wide range of ionized species present in our spectral extractions. The $\sim 0\farcs1$ spatial resolution corresponds to physical scales of $\sim 5 - 100$ pc for the AGN in this study. Any variations of the physical conditions on smaller scales is blended into the single spectrum extracted at each location along the slit. To account for this, we used multicomponent models that allow for multiple density and ionization states, with the predicted emission from all components convolved to match the observed spectrum.

The multicomponent photoionization modeling results represent our best possible determination of the ionized gas mass with the current generation of telescopes and instruments. Using these results as a benchmark, it is then worthwhile to explore various methods of mass determination that are less resource intensive and quantify any differences with our benchmark results. These tests will reveal the effects of various physical assumptions on

the resulting mass estimates and allow us to determine if a simplified method that has less stringent data and modeling requirements may be implemented to determine reasonably accurate ionized gas masses. Without the detailed modeling results for NGC 4151, Mrk 573, and Mrk 34, it would not be possible to estimate the reliability of such techniques.

In Chapters 2 and 3 we briefly explored mass estimates derived from geometric and luminosity-based techniques, which revealed that geometric techniques are subject to strong systematic biases and that luminosity-based techniques that employ a physical tracer of the gas mass produce more promising results. We explore here in more detail the mass estimates that can be obtained from simplified luminosity-based techniques that may employ spectra with fewer emission lines and without the need to generate time-intensive photoionization models on an object by object basis. We assume that the observer has spatially resolved spectroscopy of a bright emission line such as [O III] λ5007 to determine the velocity and extent of the outflowing ionized gas and an emission-line image to determine the luminosity of the gas outside of the spectral slit. Alternatively, IFU spectral observations of the entire NLR at sufficiently high ($\sim 0\farcs1$) spatial resolution would fulfill both of these requirements.

4.2 Theoretical Framework

One of the more common techniques used in the literature is to estimate the gas mass based on the luminosity of a single emission line at constant density. A recombination line such as Hα or Hβ is typically chosen as these are more stable than the forbidden lines across a wide range of physical conditions. When accessible, Hβ is the preferred option as it is less sensitive to collisional effects than Hα and is generally not blended with other strong emission lines. This is important, as this technique is essentially "photon counting" to determine the mass, which assumes that the emission is dominated by pure radiative recombination and neglects other emission processes. This simplifies the analysis and allows for a simple multiplicative factor known as the recombination coefficient to relate the number of photons to the number of hydrogen atoms and thus the total ionized gas mass, i.e. $M \propto L/n_e$.

The main differences between our modeling approach and this single emission line technique are illuminated further by deriving the exact expression that relates the Hβ luminosity to the gas mass. A simplified form of this derivation for pure hydrogen can be found in Peterson (1997), with additional expressions and physical insight gathered from Osterbrock & Ferland (2006). The physical setup is as follows. First, we consider an unresolved region containing discrete gas clouds that each contribute line emission to the observed spectrum. The total mass M in these clouds is given by

$$M = \frac{4\pi}{3}\ l^3\ n_e\ m_p\ N_c \tag{4.1}$$

where l is the radius of a cloud, n_e is the electron density, m_p is the mass of a proton, and N_c is the total number of clouds. This framework establishes the mass by defining the cloud volume ($4\pi l^3/3$) multiplied by the density to get the total number of particles. This result is multiplied by the mass per particle to get the mass of a single cloud, which is then summed over the total number of clouds.

Next, the emission released by these gas clouds is derived from the gas emissivity ($j_{H\beta}$), which is the luminosity per unit volume per solid angle, defined as

$$j_{H\beta} = \frac{1}{4\pi}\ n_e n_p\ \alpha^{eff}_{H\beta}\ h\nu_{H\beta}\ (\mathrm{erg\ s^{-1}\ cm^{-3}\ ster^{-1}}) \tag{4.2}$$

where n_e and n_p are the electron and proton number densities and $\alpha^{eff}_{H\beta}$ is the effective recombination coefficient that describes all transitions from levels $n \geq 4$ that will eventually transition to $n = 2$ and release an Hβ photon. The recombination coefficient is a weak function of temperature due to collisional ionization effects[1], approximately following $\alpha^{eff}_{H\beta} \propto T^{-0.9}$. Exact values for various temperatures can be found in Tables 4.2 and 4.4 of Osterbrock &

[1]The effective recombination coefficient is also a very weak function of density owing to collisional effects, which is increasingly negligible for higher temperatures. Over the density range of $n_H = 10^2 - 10^6$ cm^{-3} the change is $\sim 4.1\%$ at $T = 5,000$ K, $\sim 1.7\%$ at $T = 10,000$ K, and $\sim 0.6\%$ at $T = 20,000$ K. See Table 4.4 in Osterbrock & Ferland (2006).

Ferland (2006). Assuming optically thick (Case B) recombination for several temperatures these values are:

$$\alpha_{H\beta}^{eff} = 5.37 \times 10^{-14} \text{ (cm}^3 \text{ s}^{-1}, \text{ T} = \ 5,000 \text{ K)} \tag{4.3}$$

$$\alpha_{H\beta}^{eff} = 3.03 \times 10^{-14} \text{ (cm}^3 \text{ s}^{-1}, \text{ T} = 10,000 \text{ K)} \tag{4.4}$$

$$\alpha_{H\beta}^{eff} = 2.10 \times 10^{-14} \text{ (cm}^3 \text{ s}^{-1}, \text{ T} = 15,000 \text{ K)} \tag{4.5}$$

$$\alpha_{H\beta}^{eff} = 1.62 \times 10^{-14} \text{ (cm}^3 \text{ s}^{-1}, \text{ T} = 20,000 \text{ K)} \tag{4.6}$$

The emitted luminosity is then the emissivity integrated over all angles ($d\Omega$) and volume (dV).

$$L(H\beta) = \int\int j_{H\beta} \ d\Omega \ dV = \frac{1}{4\pi} \ n_e n_p \ \alpha_{H\beta}^{eff} \ h\nu_{H\beta} \times 4\pi \times \frac{4\pi}{3} \ N_c \ l^3, \tag{4.7}$$

which reduces to

$$L(H\beta) = \frac{4\pi}{3} \ N_c \ l^3 \ n_e n_p \ \alpha_{H\beta}^{eff} \ h\nu_{H\beta}. \tag{4.8}$$

Using the original expression for the total gas mass (Equation 4.1, $M = \frac{4\pi}{3} l^3 n_e m_p N_c$) we can identify the first portion of this expression as M/m_p and write the luminosity as

$$L(H\beta) = \frac{4\pi}{3m_p} M n_p \ \alpha_{H\beta}^{eff} \ h\nu_{H\beta}. \tag{4.9}$$

Solving for the mass and introducing $m_p = m_p^{eff}$ and $n_p = n_p^{eff}$ to account for elements other than hydrogen,

$$M = \left(\frac{L(H\beta)}{\alpha_{H\beta}^{eff} \ h\nu_{H\beta}} \right) \left(\frac{m_p^{eff}}{n_p^{eff}} \right). \tag{4.10}$$

We found that the gaseous abundances of the NLR for our AGN are $Z_{NLR} \approx 1.3 \ Z_\odot$ and taking into account elements heavier than hydrogen yields $m_p^{eff} = \mu m_p \approx 1.4 m_p$ and $n_p^{eff} \approx 1.1 n_e$. The remaining physical quantity in this expression is the energy of an Hβ photon, which is

$$E = h\nu_{H\beta} = (6.626 \times 10^{-27} \text{ erg s}) \times (6.165 \times 10^{14} \text{ Hz}) = 4.085 \times 10^{-12} \text{ erg} \approx 2.55 \text{ eV}. \tag{4.11}$$

Incorporating these constants into Equation 4.10 we arrive at the final expression relating the Hβ luminosity to the ionized gas mass

$$M = 5.21 \times 10^{-13} \left(\frac{L(H\beta)}{\alpha_{H\beta}^{eff} n_e} \right) \text{ (g)}, \tag{4.12}$$

or equivalently,

$$M = 2.62 \times 10^{-46} \left(\frac{L(H\beta)}{\alpha_{H\beta}^{eff} n_e} \right) \text{ ($M_\odot$)}. \tag{4.13}$$

We may assign uncertainties to these expressions by adopting a range of effective recombination coefficients that are appropriate for the range of temperatures observed in the NLRs of nearby AGN. Various studies have derived the electron temperature for statistically significant samples of Seyfert galaxies using the standard [O III] $\lambda\lambda$4363/5007 emission line ratio that is sensitive to the gas electron temperature as shown in Figure 4.1. These grids were originally presented in Chapter 2 and are shown here for clarity.

Reported NLR temperatures span an order of magnitude with $T \approx 5,000 - 50,000$ K (Dors et al. 2015). However, most studies find a mean [O III] emission line temperature of $T \approx 15,000$ K with a standard deviation $\sim 2,500 - 5,000$ K (Bennert et al. 2006; Vaona et al. 2012; Zhang et al. 2013). Owing to the large range of reported temperatures we conservatively adopt the upper limit of this range as the formal uncertainty, yielding a final mean NLR temperature of $T \approx 15,000 \pm 5,000$ K.

As discussed in Chapter 2, it is critical to note that these temperatures probe the [O III] emission line gas that may be hotter and more highly ionized than the [S II] emission line gas that we use to constrain the gas density in one of the following simplified methods. Our photoionization modeling results showed that the [S II] gas is on average $\sim 60\%$ cooler than the [O III] gas, which is in excellent agreement with the observational results of Vaona et al. (2012). If we adopt this temperature for the gas then the effective recombination coefficients increase and the mass estimates will decrease by a similar factor of ~ 1.6.

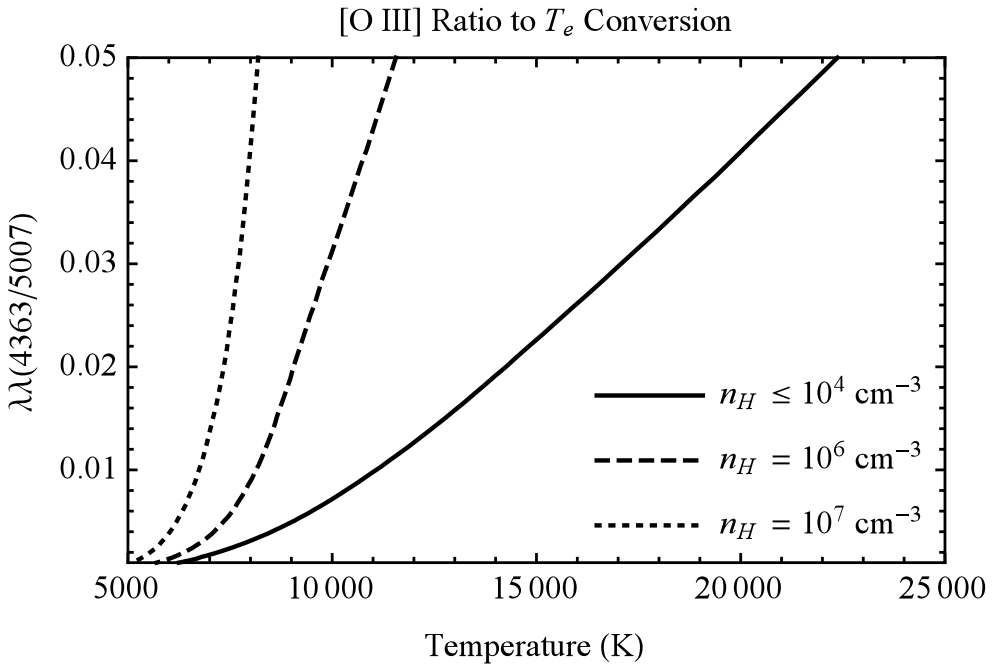

Figure 4.1 The theoretical relationship between the [O III] $\lambda\lambda$4363/5007 emission line ratio and the corresponding electron temperature for several typical NLR densities. These relationships were calculated using a grid of Cloudy photoionization models.

Inserting the effective recombination coefficients that correspond to $T \approx 15,000 \pm 5,000$ K we obtain the useful expressions

$$M = (24.81\ ^{+7.35}_{-7.62}) \left(\frac{L(H\beta)}{n_e}\right)\ (\mathrm{g}), \tag{4.14}$$

and,

$$M = (12.48\ ^{+3.70}_{-3.83} \times 10^{-33}) \left(\frac{L(H\beta)}{n_e}\right)\ (\mathrm{M}_\odot). \tag{4.15}$$

This result is conceptually elegant as it only requires a measurement of the emission line luminosity and the electron density in order to determine the gas mass within any particular region. However, there are still several observational considerations that add an underlying level of complexity in practice. Specifically, deriving the intrinsic Hβ luminosity from the observed flux requires an accurate correction for extinction from dust and geometric dilution. In general, at least two hydrogen or helium recombination lines are required to derive the

reddening (or color excess, i.e. the differential extinction between the photometric B and V bands due to dust), while correcting for geometric dilution requires an accurate estimate of the distance to the galaxy. In addition, deriving a single electron density for all of the emitting material may not be realistic based on the results of our multicomponent models that required multiple density and ionization states at each spatial location. The uncertainties in the above equation are entirely due to the dependence of $\alpha_{H\beta}^{eff}$ on a broad range of temperatures ($T \approx 10,000 - 20,000$ K) if the latter is not well constrained by emission line diagnostics or photoionization models.

4.3 Simplified Analysis

Regardless of the details for various estimates, all luminosity-based techniques require three fundamental parameters to estimate the ionized gas mass and outflows rates. These are 1) the emission line luminosity distribution, 2) the radial outflow velocity, and 3) the gas density. The purpose of deriving a simplified methodology is so that we may apply it to a larger number of galaxies with less stringent spectral requirements. For example, there are a large number of AGN with high quality *HST* STIS spectroscopy utilizing the G430M dispersion grating. This medium dispersion grating allows for precise radial velocity measurements but the narrow spectral range only encompasses the [O III] and in some cases also the Hβ emission lines. These types of data would not be suitable for our detailed modeling process as there are insufficient emission lines to constrain the physical conditions in the gas. However, if a sufficiently accurate simplified technique based on the luminosity of a single line can be found, then the number of AGN that we may derive high spatial resolution gas mass and outflow rate profiles for increases significantly.

With these observational considerations in mind, we may adopt the emission line luminosities and deprojected radial outflow kinematics from our earlier studies as control variables, because these may be determined with equal precision from higher dispersion spectra with a

single emission line. The remaining element to determine is whether or not we can derive an accurate density law profile that reproduces our earlier results.

The goal for this section, then, is to compare the mass and outflow rate profiles that are derived from different density estimates and to compare them with our benchmark results. While numerous methods exist, we consider three cases that are commonly employed in the literature and/or have the most relaxed data requirements. As derived above, we calculate the gas mass using Equation 4.15, which is

$$M = (12.48\ ^{+3.70}_{-3.83} \times 10^{-33}) \left(\frac{L(H\beta)}{n_e} \right)\ (\mathrm{M}_\odot).$$

The Hβ luminosity is approximated by using the [O III] luminosities derived from our [O III] imaging and scaling them by the mean [O III]/Hβ ratio for each galaxy. While a marginal increase in accuracy may be obtainable by using the exact [O III]/Hβ ratio at each location along the slit, the range of [O III]/Hβ ratios across the NLR is approximately constant. The mean [O III]/Hβ ratio for each galaxy is, NGC 4151: [O III]/H$\beta \approx 12$, Mrk 573: [O III]/H$\beta \approx 13$, Mrk 34: [O III]/H$\beta \approx 11$. These averages are accurate to within better than a factor of two at all modeled radii for all three galaxies. This also further relaxes the requirement that a spectrum used with a simplified method need have Hβ present at all locations. Thus the Hβ luminosity at each location is given by

$$L(H\beta) = \left(4\pi D^2 F_{[\mathrm{O\ III}]}\right) \times \left(\frac{F_{\mathrm{H}\beta}}{F_{[\mathrm{O\ III}]}} \right) \times \left(10^{0.4 \cdot R_{\lambda 5007} \cdot E(B-V)}\right) \tag{4.16}$$

where D is the distance to the galaxy assuming all portions of the NLR are at approximately the same distance from us, $F_{[\mathrm{O\ III}]}$ is the measured [O III] λ5007 flux from our images, $R_{\lambda 5007} = 3.57$ is the value of the Galactic reddening curve for [O III] λ5007, and E(B-V) is

the color excess from extinction given by

$$E(B-V) \equiv -\frac{2.5log\left(\frac{F_o}{F_i}\right)}{R_\lambda} = \frac{2.5log\left(\frac{(\mathrm{H}\alpha/\mathrm{H}\beta)_i}{(\mathrm{H}\alpha/\mathrm{H}\beta)_o}\right)}{R_{\mathrm{H}\alpha} - R_{\mathrm{H}\beta}} \tag{4.17}$$

where F_o and F_i are the observed and intrinsic fluxes, respectively. The flux ratios can be expanded to the intrinsic and observed Hα/Hβ ratios and the Galactic reddening values are $R_{\mathrm{H}\alpha} \approx 2.497$ and $R_{\mathrm{H}\beta} \approx 3.687$ (Savage & Mathis 1979; Cardelli et al. 1989), assuming the standard Galactic reddening law applies within both our Galaxy and within the AGN host galaxy. The uncertainties and assumptions regarding the choices of extinction-correction and density profile may have a significant impact on the resulting masses and outflow rates. There are also additional sources of uncertainty that are inherent to both our primary method and these simplified techniques, such as errors in the distance to the galaxy, the geometric model for deprojecting velocities and distances from the SMBH, and the choice of reddening curve. These issues are addressed in detail in Chapter 5.

Finally, we may use the mass derived from Equation 4.15 along with our deprojected radial outflow velocities and spatial bin sizes to calculate the mass outflow rates and energetics as defined in Chapter 2,

$$\dot{M}_{\mathrm{out}} = \left(\frac{Mv}{\delta r}\right). \tag{4.18}$$

Using this framework we now examine techniques for deriving the density law and quantify the resulting mass profiles and outflow rates. We consider three cases with the density calculated based on different physical assumptions in each and present the resulting mass and outflow rate profiles with and without an extinction-correction. The latter is important to understand the effects of neglecting extinction on the final mass, which may be necessary when the available spectra do not include multiple hydrogen or helium lines. For each target the mean color-excess was calculated from the spatially resolved values (Crenshaw et al. 2015; Revalski et al. 2018a,b), resulting in E(B-V) = 0.18, 0.28, and 0.30, for NGC 4151, Mrk 573, and Mrk 34, respectively.

4.3.1 [S II] Density Profile

The first method that we consider is to derive the gas density directly from density sensitive emission lines in the spectrum rather than using them as a first estimate for photoionization models. While there are several density sensitive doublets in the optical, such as [O II] $\lambda\lambda$3726, 3729, [Ar IV] $\lambda\lambda$4711, 4740, and [S II] $\lambda\lambda$6716, 6731, only the [S II] doublet is typically spectrally resolved and has sufficient strength to be useful as a diagnostic tool. As discussed in Chapter 2, the [S II] lines will only probe a single ionization state of the emission line gas and it may be cooler and at a different density than the [O III] emission lines that are used to trace the gas luminosity and kinematics.

The density profile for each object was calculated using the reddening-corrected [S II] $\lambda\lambda$6716, 6731 emission line ratios[2]. These values were obtained from Kraemer et al. (2000a) Tables 1A and 1B for NGC 4151, and Chapter 2 and 3 for Mrk 573 and Mrk 34, respectively. We generated a fine grid of Cloudy photoionization models across a wide range of densities for several typical NLR temperatures and recorded the predicted [S II] emission line ratios. This grid was then used as a reference table to match each [S II] ratio with the corresponding density and to determine the uncertainties that are introduced by a range of temperatures. These grids were originally presented in Chapter 2 and are shown in Figure 4.2 for clarity. In the cases of NGC 4151 and Mrk 34 the [S II] doublet was not detected for a small number of spatial extractions corresponding to an [O III] image flux measurement due to low S/N. At these locations we interpolated the density using the measured values at the next inner and outer radial distances. The resulting density profiles are shown in Figure 4.3.

The [S II] densities tend to be lower at small radii than may be expected from gas with an approximately constant ionization parameter. In general, we would expect the low ionization gas that gives rise to the [S II] emission to be at a higher density compared to the higher ionization gas that is at approximately the same distance from the SMBH, but that does not

[2]While we have used the reddening-corrected emission line ratios throughout this investigation, the small separation of the [S II] doublet allows the observed values to be used with nearly equal accuracy. For typical levels of extinction observed in the NLR the derived densities agree to within $\sim 1\%$.

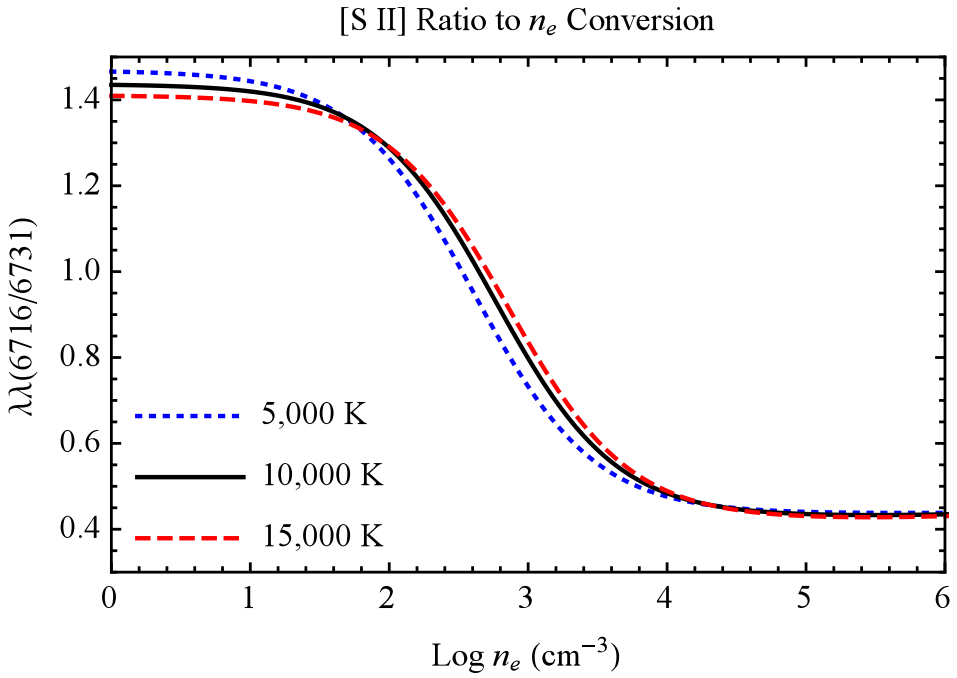

Figure 4.2 The theoretical relationship between the [S II] $\lambda\lambda$6716/6731 emission line ratio and the corresponding electron density for several typical NLR temperatures. These relationships were calculated using a grid of Cloudy photoionization models.

need to be the case when shielding is considered. In that case, the low ionization gas sees a reduced ionizing flux from the central source due to absorption at smaller radii and can have a lower density for a given ionization parameter than is required to maintain continuity with the ionization parameter equation based on the nuclear ionizing flux, Q_{ion}.

These densities were then used with Equation 4.15 to calculate the radial mass distribution for each galaxy. The mass outflow rates were then derived using the deprojected kinematics discussed earlier. The results of this process with and without an extinction correction are shown in Figures 4.4 and 4.5, respectively.

Prior to interpreting these results it is important to note that Mrk 573 is a special case, as we adopted the [S II] density for $R > 175$ pc because there were insufficient emission lines in our *HST* spectra to create detailed photoionization models. Thus there is an expected agreement between the benchmark and simplified results with regard to overall shape, with a

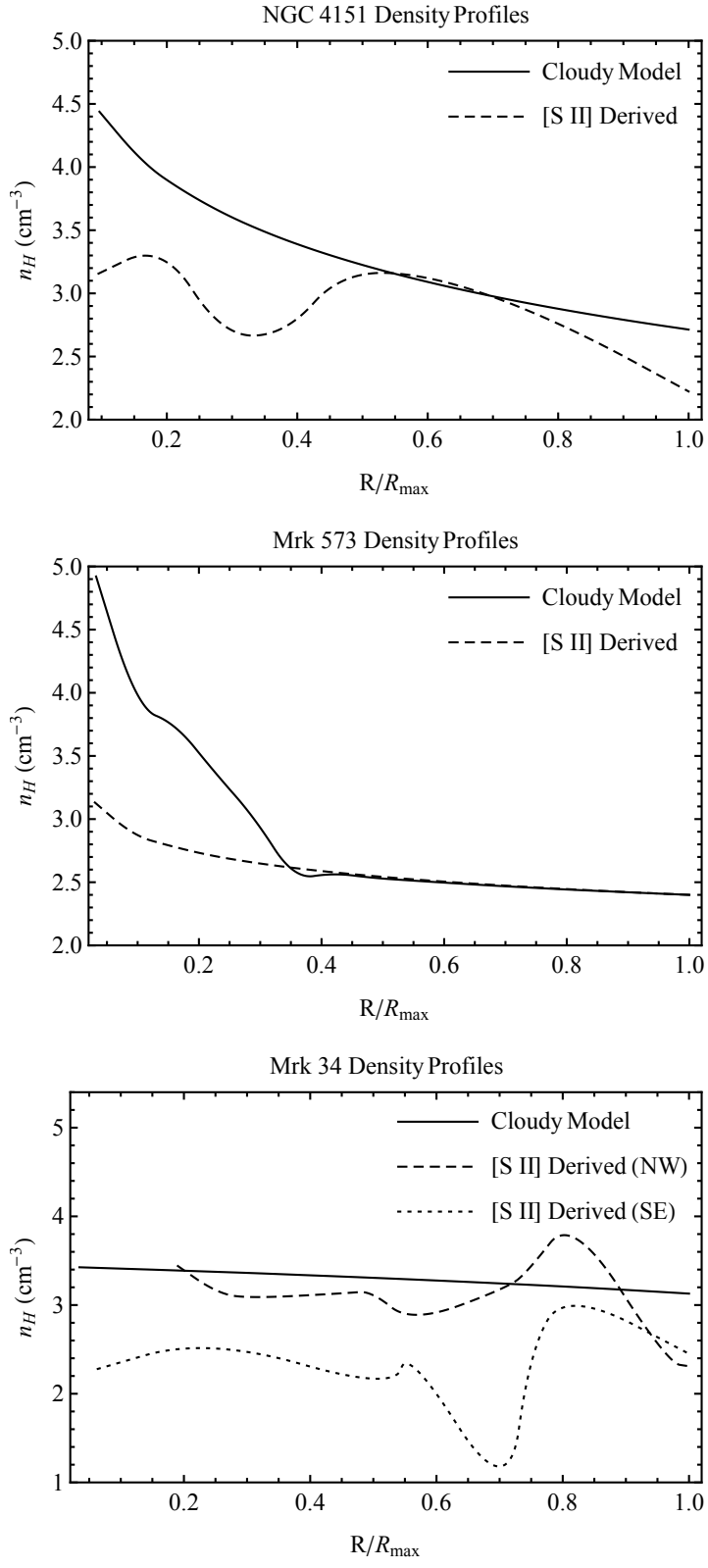

Figure 4.3 The radial density profiles for NGC 4151, Mrk 573, and Mrk 34 from our Cloudy models (solid) and [S II] measurements (dashed). Note that the Cloudy model values are the numerical mean density of all components, which is different from the mass weighted mean density. For Mrk 34, the [S II] density profiles were sufficiently different on either side of the nucleus that we display each individually.

constant offset capturing the difference between using a model derived scale factor versus the constant in Equation 4.15 that assumes pure radiative recombination.

Figures 4.4 and 4.5 show that this technique overestimates the ionized gas mass and outflow rates by large factors at all radii with limited exceptions. This is in agreement with our result from Chapters 2 and 3 where we found that the [S II] density was not representative of all the emission line gas, which required multiple density and ionization states to produce the wide range of ionized species observed in the spectra. A key result is that the [S II] line ratio will generally underestimate the overall density and thus overestimate the gas mass because they are inversely proportional as seen in Equation 4.15. Physically, this is because the more dense material will emit more efficiently ($\propto n_e^2$, see Equation 4.2) and thus can dominate the line luminosity with only a small fraction of the total mass.

It is tempting to conclude that the lack of an extinction-correction provides a superior estimate of the gas mass; however, this is coincidental because the overestimate is partially compensated for by artificially reducing the luminosity. Avoiding an extinction-correction is therefore not recommended, because extinction may vary significantly for different galaxies or across the NLR (Kraemer et al. 2000a; Kraemer & Crenshaw 2000c; Collins et al. 2005).

4.3.2 Constant Density Profile

The second method that we consider is to fix the density at a constant value across the entire NLR. When density diagnostics are not available in spectra this technique is often employed adopting a density of $n_H = 100$ cm^{-3} (Kakkad et al. 2018; Nevin et al. 2018). We examine constant density values of $n_H = 10^2$, 10^3, and 10^4 cm^{-3}, as this range encompasses that observed for the majority of our photoionization model components presented in earlier chapters. As this process also employs Equation 4.15, a lower density will correspond to a higher predicted mass. The results of this process with and without an extinction-correction are shown in Figures 4.6 - 4.7, with the vertical scale expanded in Figures 4.8 - 4.9.

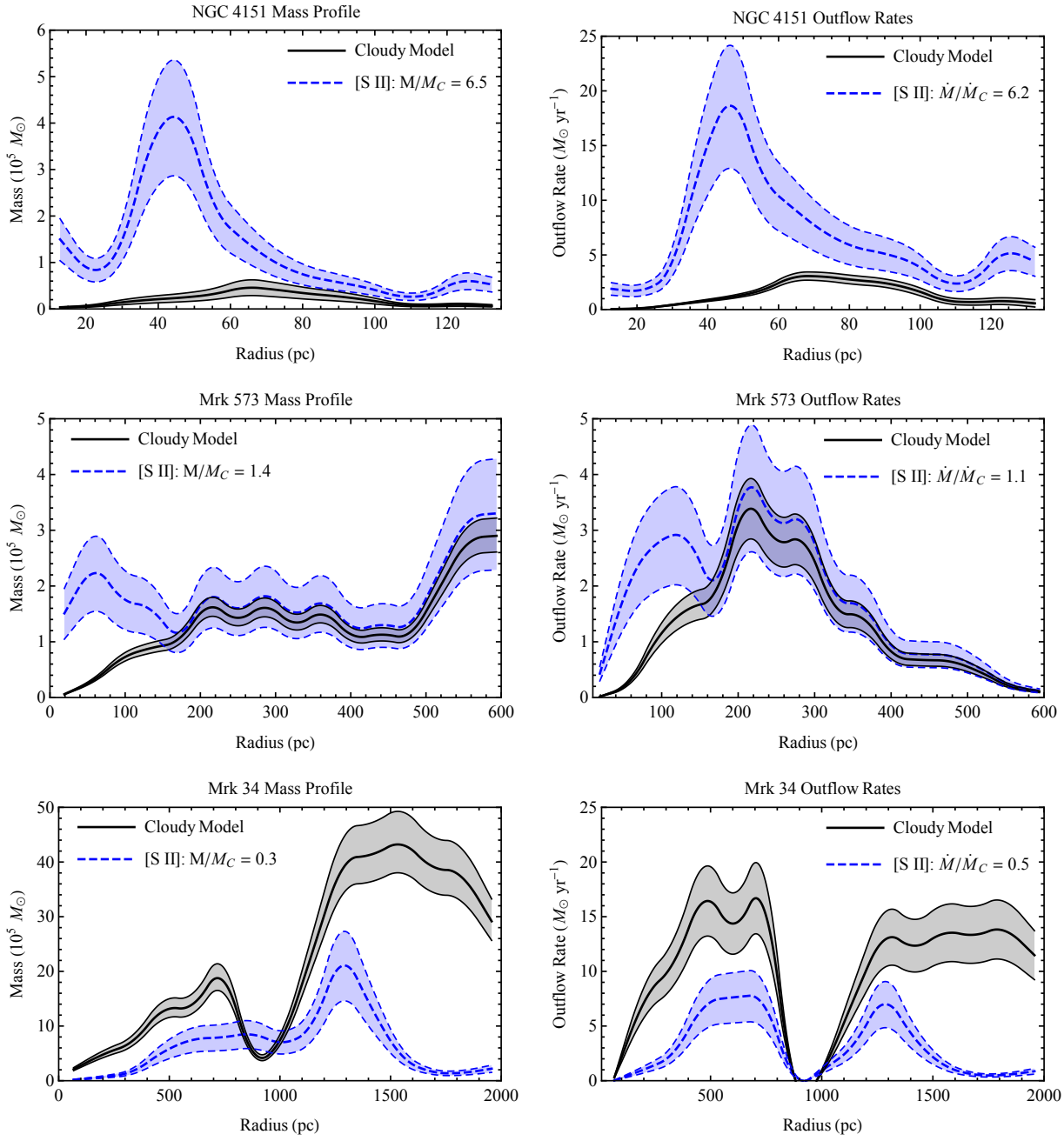

Figure 4.4 Mass and outflow rate profiles for NGC 4151, Mrk 573, and Mrk 34 calculated from Cloudy models (black) and using the density profiles derived from the [S II] line ratios assuming global color-excess values of E(B-V) = 0.18, 0.28, and 0.30, respectively. Regions where the mass is overestimated by the simplified technique correspond to underestimates in the gas density. The precise agreement in profile shape for Mrk 573 at $R > 175$ pc is expected as described in the text. The legend indicates the ratio of the total [S II] to Cloudy derived mass (M/M_C) and peak outflow rates ($\dot{M}/\dot{M}_C$). The uncertainties in the simplified method are dominated by the uncertainty in $\alpha^{eff}_{H\beta}$ due to its dependence on temperature.

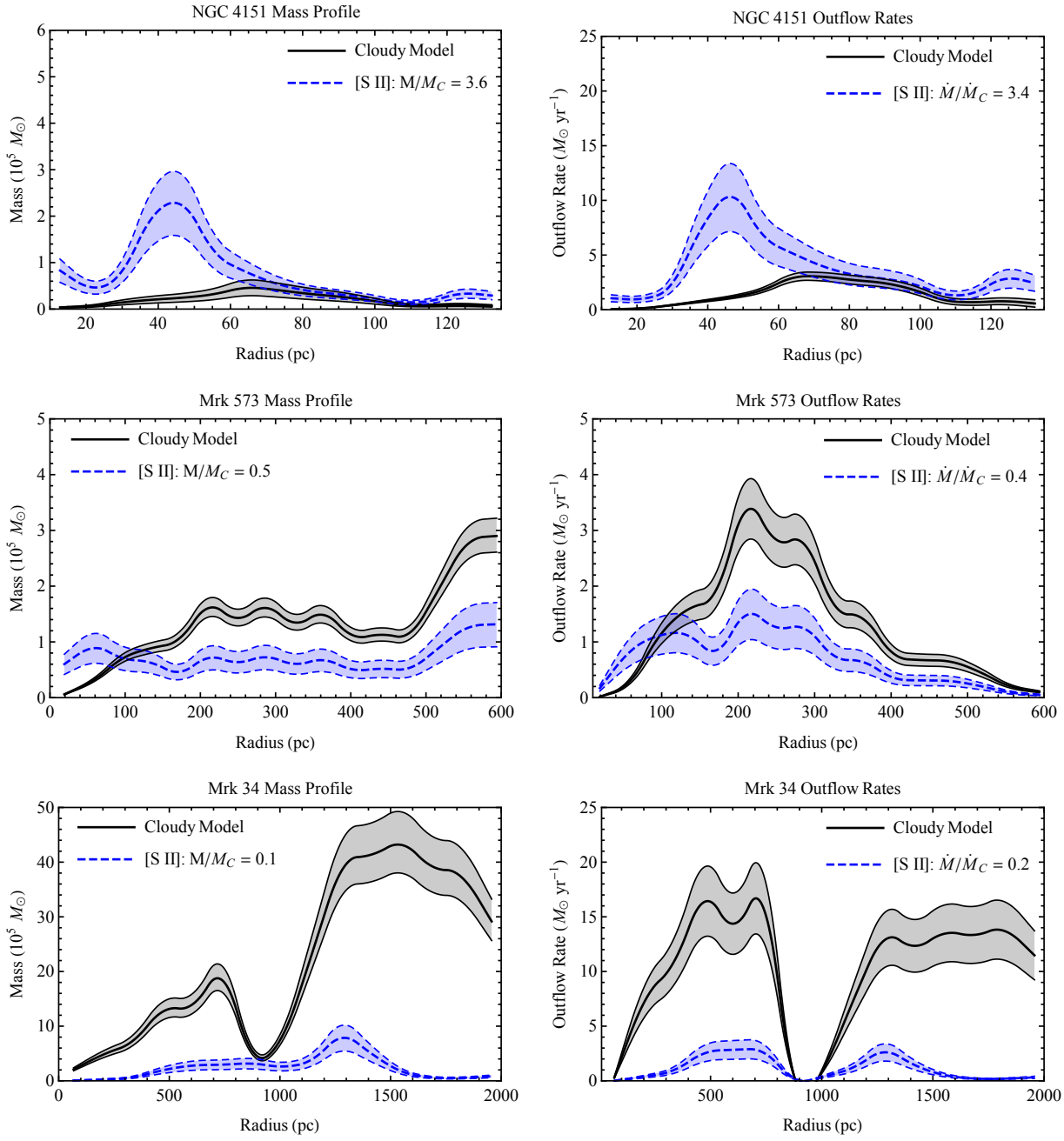

Figure 4.5 The same as Figure 4.4, except assuming a global color-excess of E(B-V) = 0.0 for all galaxies. The display ranges exactly match those of Figure 4.4 for visual comparison. As discussed in the text, adopting E(B-V) = 0.0 is not recommended despite the apparent improved agreement in some cases.

Adopting a constant density of $n_H = 100$ cm^{-3} significantly overestimates the gas mass for all three galaxies by a factor ranging from $\sim 6 - 60$. Adopting a higher density of $n_H = 10^3$ cm^{-3} still overestimates the mass for NGC 4151 and Mrk 34, and as before Mrk 573 must be considered separately for $R > 175$ pc due to the modeling limitations discussed in the previous section. At smaller radii the mass is also overpredicted for Mrk 573 and all three galaxies lend a consistent picture.

These results are consistent with the physical model that the higher density material, which has a much higher emissivity, is contributing a significant fraction of the luminosity with a relatively small fraction of the mass. Similar to the previous case, the simplifying assumptions regarding the density significantly alter the mass and mass outflow rate profiles, while neglecting extinction biases the results by artificially reducing the luminosity. Our results show that the commonly adopted value of $n_H = 100$ cm^{-3} for the NLR is a poor one; assuming a constant value of $n_H = 10^3 - 10^4$ cm^{-3} is an improvement but can still lead to large errors for individual AGN.

4.3.3 Constant Ionization Parameter

The third and final method that we consider is to assume that the ionization parameter of the emission line gas is constant with radius such that $U(r) =$ constant. This will naturally lead to a density profile that decreases $\propto 1/r^2$ with distance from the nucleus if the ionizing luminosity is constant with time, which is consistent with the results of our photoionization models for these AGN[3].

This choice of density profile is physically motivated by the observation that the [O III]/Hβ ratio, which is a strong function of the ionization parameter, is approximately constant across the NLR for each galaxy. An underlying assumption of this method is that the ionized gas mass fraction is traced out equally well by the [O III] emission at all radial distances. This

[3]The luminosity of the AGN may vary significantly with time so long as the time-averaged value is approximately constant. This means that the luminosity could vary around an average value on times scales where the light crossing time is smaller (sub-pc) and larger (tens of kpc) than those probed by our observations of the spatially resolved NLR.

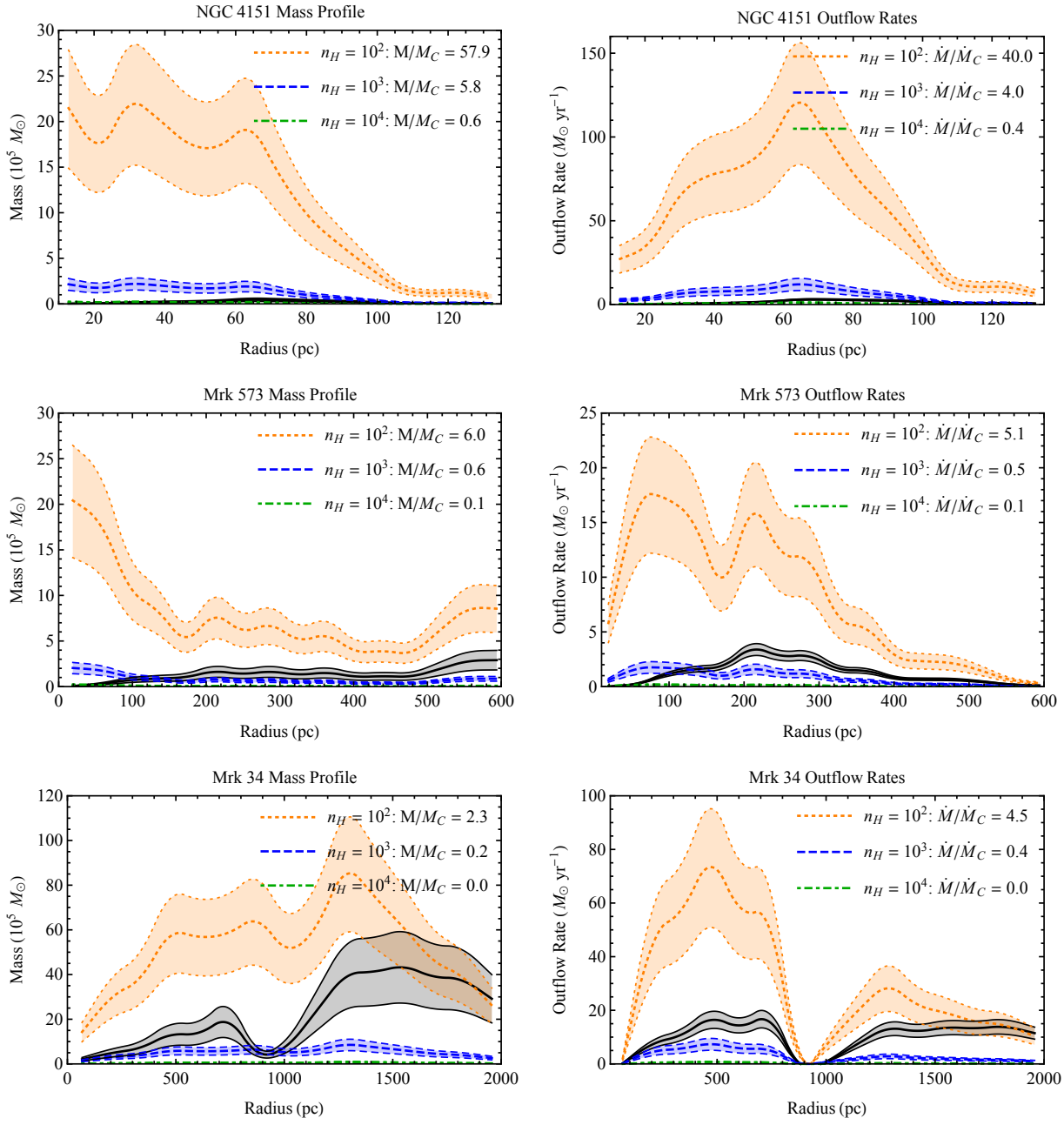

Figure 4.6 Mass and outflow rate profiles for NGC 4151, Mrk 573, and Mrk 34 calculated from Cloudy models (black) and assuming a constant density profile with radius using global E(B-V) values of 0.18, 0.28, and 0.30, respectively. The legend indicates the ratio of the total constant density mass to the Cloudy derived mass (M/M_C) and peak outflow rates ($\dot{M}/\dot{M}_C$). The uncertainties in the simplified method are dominated by the uncertainty in $\alpha^{eff}_{H\beta}$ due to its dependence on temperature.

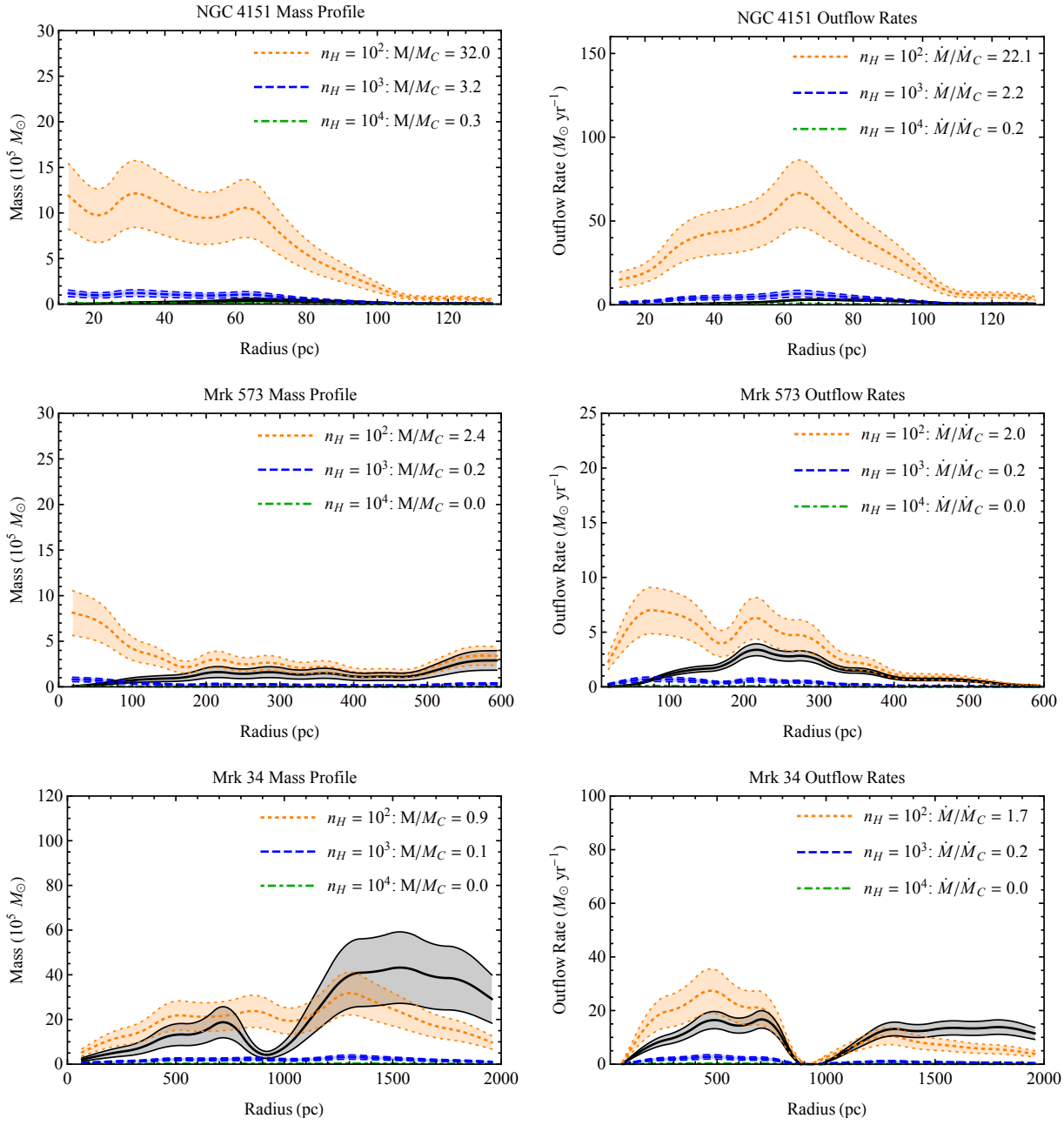

Figure 4.7 The same as Figure 4.6, except assuming a global color-excess of E(B-V) = 0.0 for all galaxies. The display ranges exactly match those of Figure 4.6 for visual comparison. As discussed in the text, adopting E(B-V) = 0.0 is not recommended despite the apparent improved agreement in some cases.

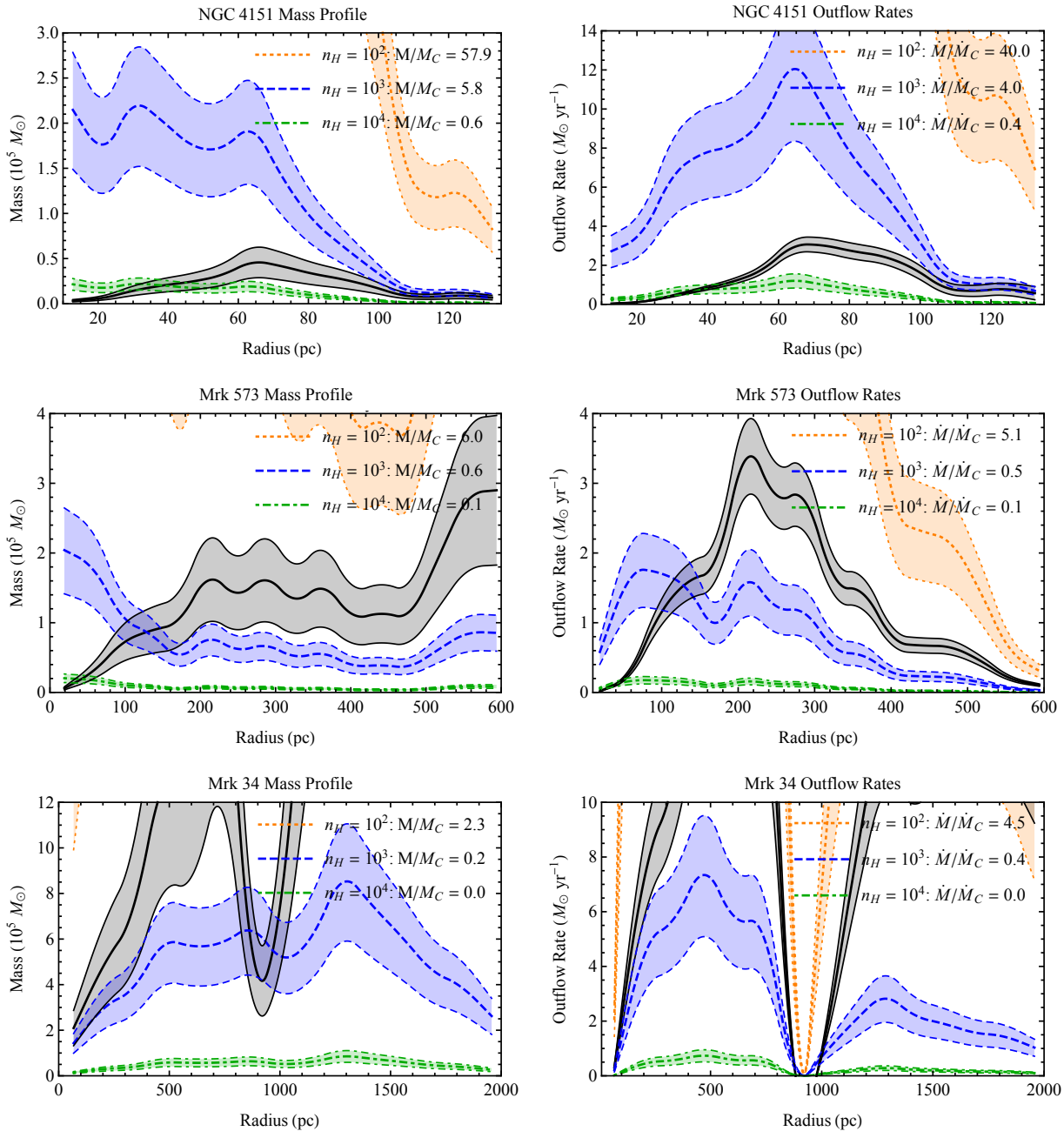

Figure 4.8 The same as Figure 4.6 with the vertical display range decreased by a factor of ~ 10 for easier viewing of the $n_H = 10^3 - 10^4$ cm^{-3} cases.

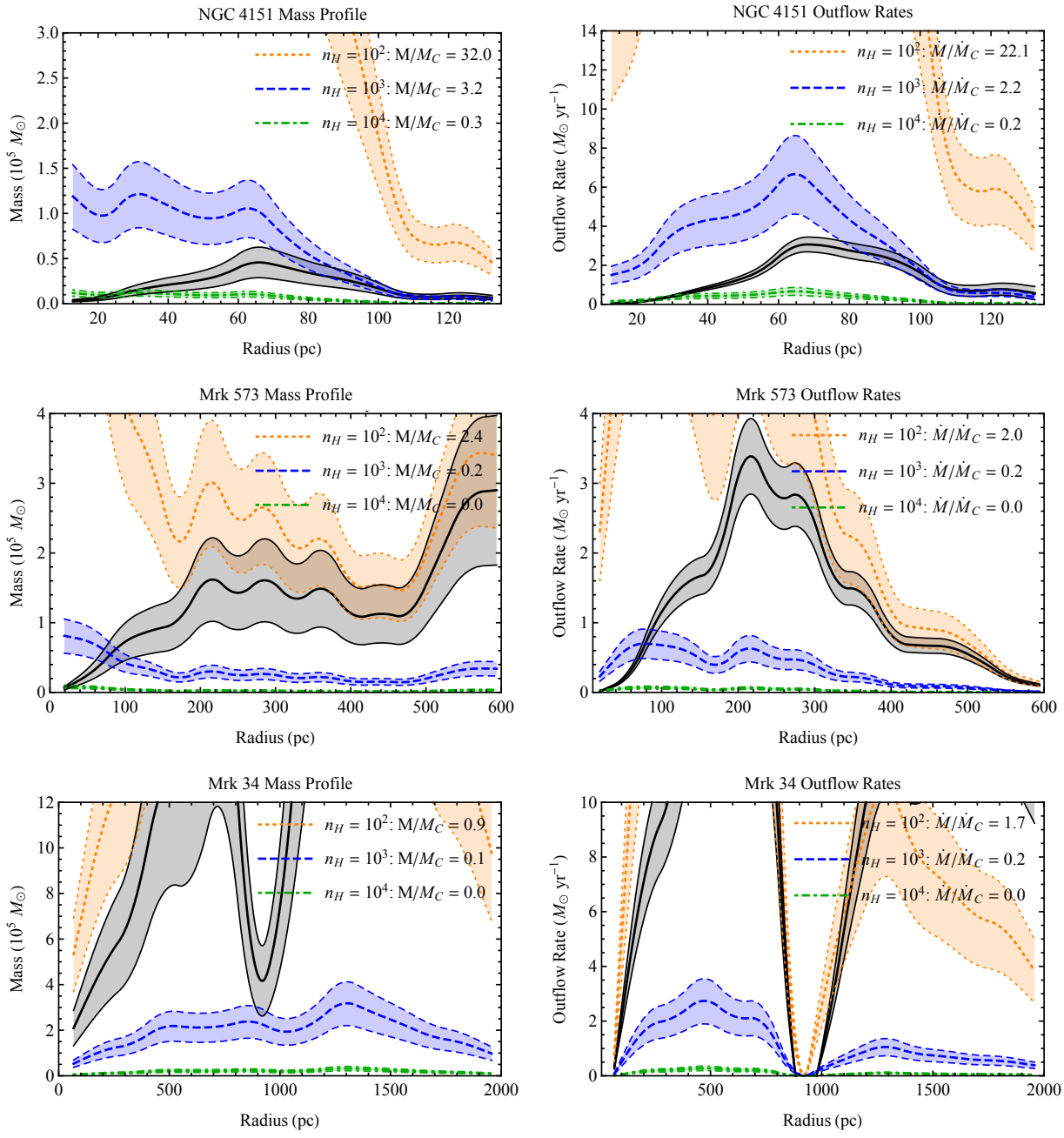

Figure 4.9 The same as Figure 4.7 with the vertical display range decreased by a factor of ~ 10 for easier viewing of the $n_H = 10^3 - 10^4$ cm^{-3} cases.

type of density profile is generally consistent with the medium ionization Cloudy model component for our galaxies.

In this case, we chose various values of the ionization parameter that are known from general Cloudy models to produce the observed [O III]/Hβ ratios and calculated the density at each radial distance using the ionization parameter equation. Specifically,

$$n_H = \left(\frac{Q_{ion}}{4\pi r^2 U c} \right) \tag{4.19}$$

where Q_{ion} is the number of ionizing photons s^{-1} emitted by the AGN assuming no self-absorption at smaller radii, r is the radial distance of the gas from the AGN, U is the ionization parameter, and c is the speed of light.

The critical aspect of this method is to choose an appropriate value of the ionization parameter. A first approximation is to choose a commonly accepted value of $\log(U)$ = -2.0, which will produce [O III]/Hβ ratios comparable to those we observe in our galaxies. It is worth noting that this is a degenerate parameter space, with the same value of [O III]/Hβ possible for multiple ionization parameters if the gas is more or less ionized. This behavior is demonstrated in Figure 4.10 and clearly illustrates the reverse-saddle nature of the degeneracy.

The results for $\log(U)$ = -2.0 are shown in Figures 4.11 - 4.12. This procedure produces a reasonable match for NGC 4151, but firmly disagrees with the benchmark results for Mrk 573 and Mrk 34. To better understand the variations in U that are required to produce an acceptable match we varied the ionization parameter until the total mass between this method and our Cloudy model results were equal. These results are shown in Figure 4.13.

It is clear that even with the ionization parameters chosen to result in equal total mass between the two methods that there are still significant local deviations in the profiles. This indicates that the density profile for all of the ionized gas is not well represented by a $1/r^2$ density law. It may still be the case that the dominant [O III] emission line component follows this density profile; however, it is not representative of the gas mass at all radii. Finally, if

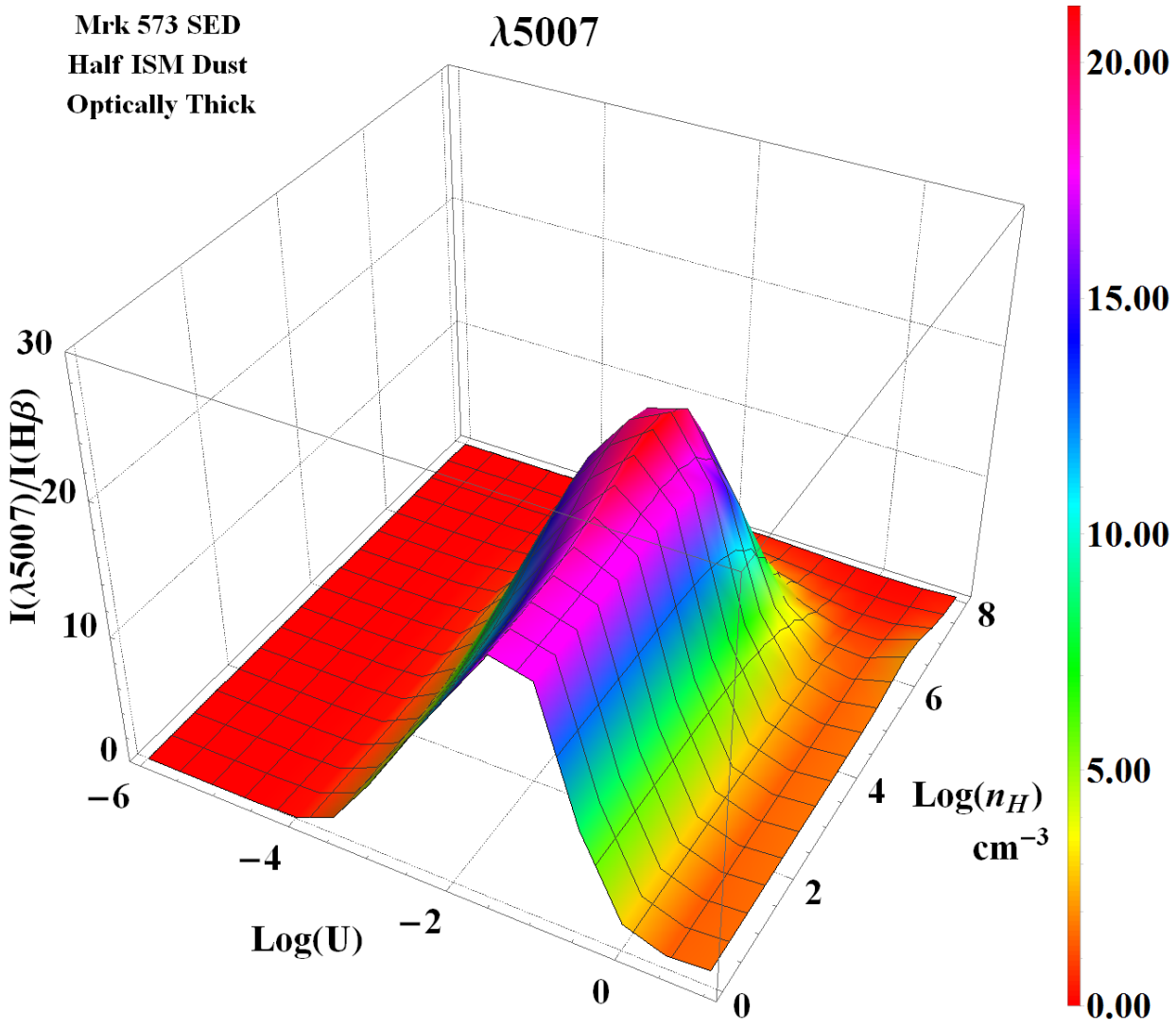

Figure 4.10 The [O III]/Hβ emission line ratio as a function of ionization parameter (U) and density (n_H). Note that it is possible to have the same value of [O III]/Hβ produced under a variety of conditions.

only one emission line is available in the spectrum then there is insufficient information to derive an accurate ionization parameter.

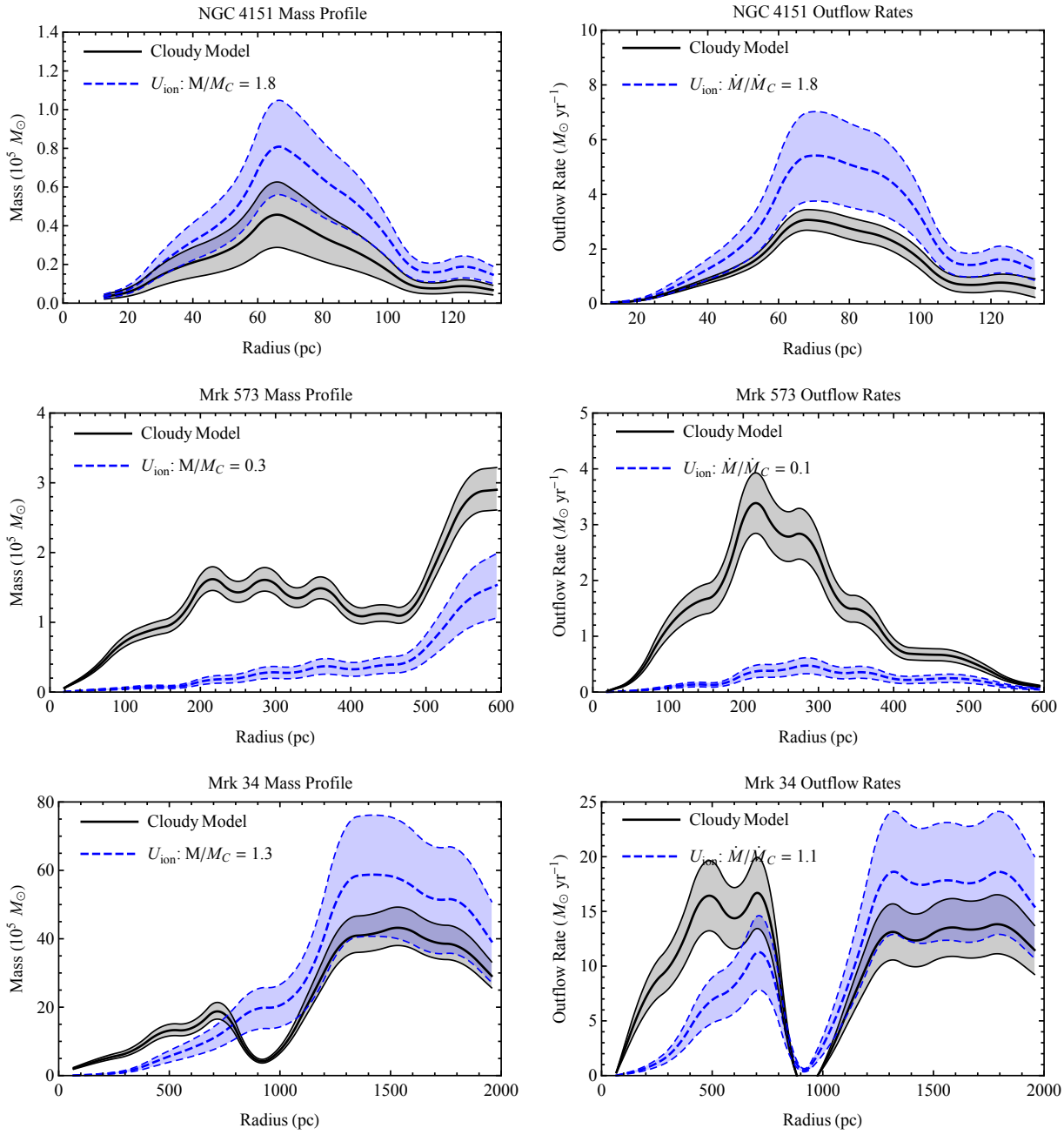

Figure 4.11 Mass and outflow rate profiles for NGC 4151, Mrk 573, and Mrk 34 calculated from Cloudy models (black) and assuming a constant ionization parameter (blue) of log(U) = -2.0 with global color-excess values of E(B-V) = 0.18, 0.28, and 0.30, respectively. The uncertainties in the simplified method are dominated by the uncertainty in $\alpha^{eff}_{H\beta}$ due to its dependence on temperature.

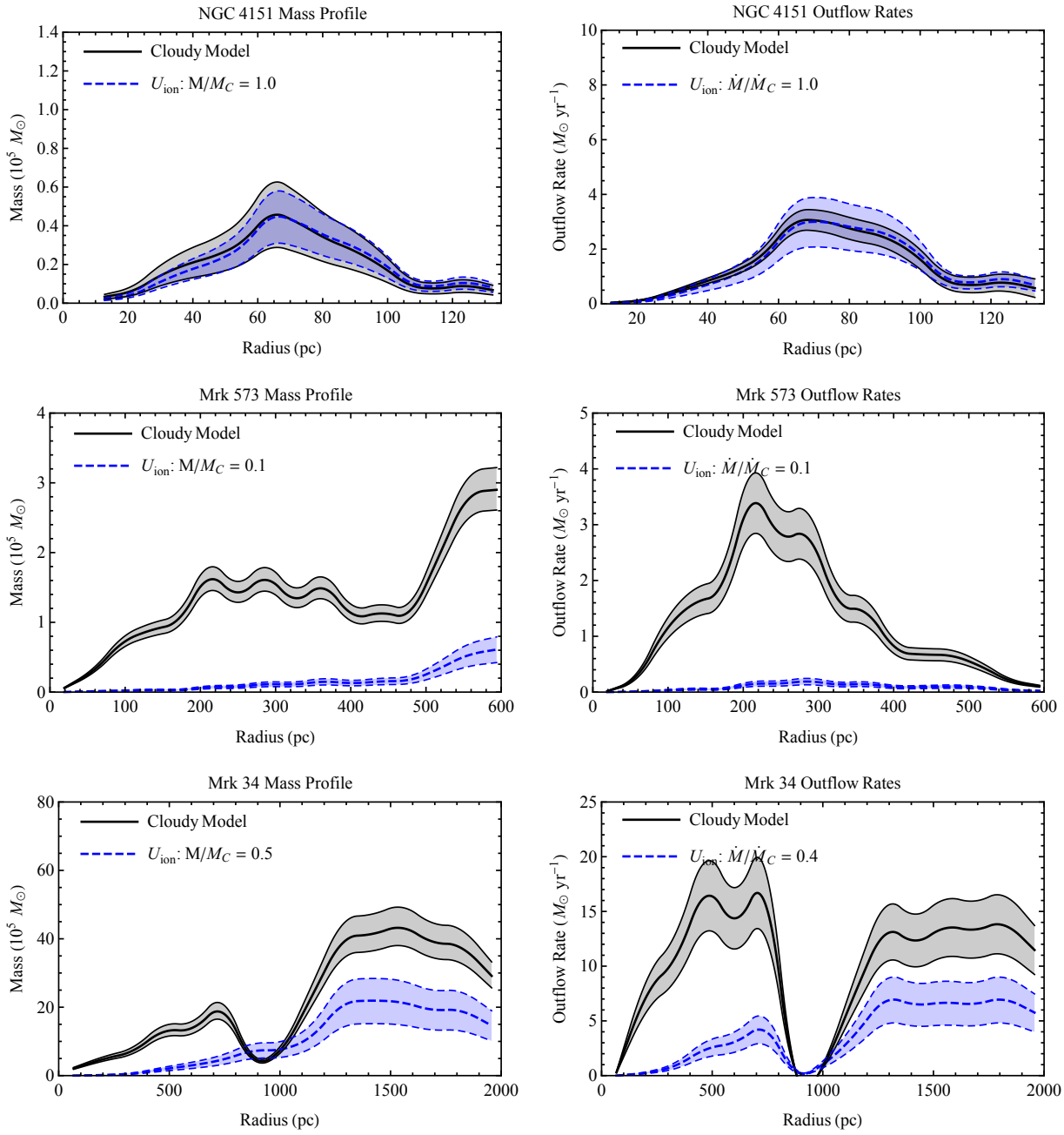

Figure 4.12 The same as Figure 4.11, except assuming a global color-excess of E(B-V) = 0.0 for all galaxies. The display ranges exactly match those of Figure 4.11 for visual comparison.

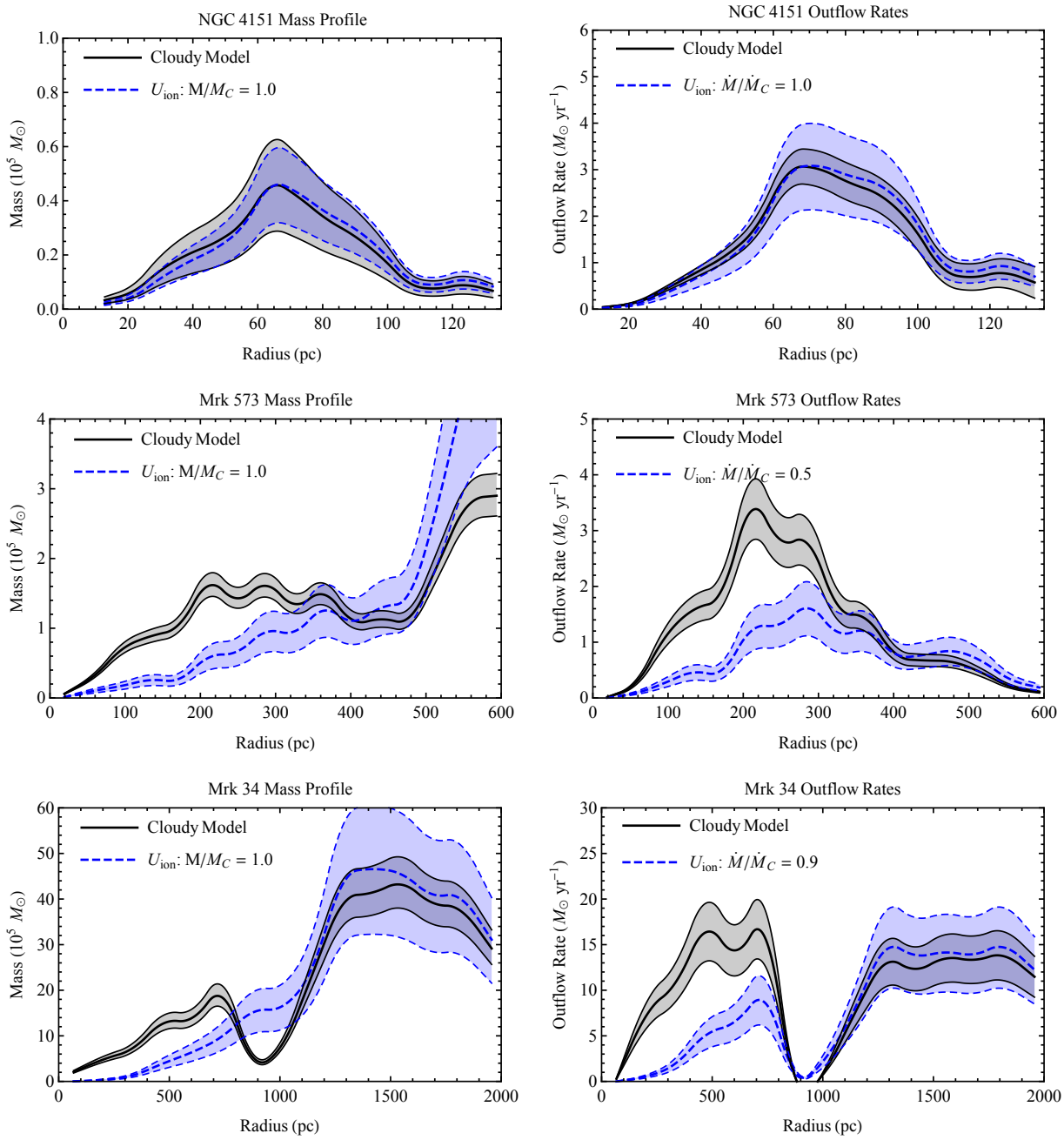

Figure 4.13 Mass and outflow rate profiles for NGC 4151, Mrk 573, and Mrk 34 calculated from Cloudy models (black) and assuming a constant ionization parameter (blue) with global mean E(B-V) values of 0.18, 0.28, and 0.30, respectively. The best fit values of log(U) = -2.245, -1.470, and -2.101 were chosen to bring the total masses between this method and the Cloudy models into agreement. The uncertainties in the simplified method are dominated by the uncertainty in $\alpha^{eff}_{H\beta}$ due to its dependence on temperature.

4.4 Summary of Results

In this chapter we investigated the effects of deriving ionized gas masses and outflow rates using simplified methodologies that are not based on photoionization models. The results of these methods differ from our benchmark results primarily due to 1) the techniques used to derive the density laws and 2) differences in converting the luminosity to mass using a recombination coefficient versus a model derived scale factor that accounts for emission mechanisms other than pure recombination. We also explored the effects of using an average value for reddening and not correcting the luminosities for reddening, which would be the case if suitable recombination lines are unavailable. These results are summarized in Table 4.1, which contains the ratios of the total simplified method masses to Cloudy model masses (M/M_C) as well as the ratios of the peak outflow rates ($\dot{M}/\dot{M}_C$). All of these techniques generally overestimate the gas mass when commonly adopted values are applied.

The common assumption of a constant density profile with $n_H = 10^2$ cm^{-3} produces the worst results, significantly overestimating the gas mass and outflow rates. This trend would also apply to the kinetic luminosities, although the overestimation can be slightly less severe in some cases because it is proportional to $\dot{M}$ rather than M. The conclusion that adopting a density of $n_H = 10^2$ cm^{-3} will overestimate the gas mass has also been noted by others (Perna et al. 2017; Baron & Ménard 2019), and a mean density of $n_H \approx 10^{3.3}$ cm^{-3} produces results that are more consistent with our photoionization modeling. However, there is a significant range of densities present across our objects so adopting a mean NLR gas density is not recommended.

The assumption of a $1/r^2$ density law is satisfactory in some cases and likely traces the density profile of the [O III] emitting component. The largest disagreement is seen for Mrk 573; however, this may be due to the fact that the gas masses at large radii were determined using a density profile derived from the [S II] emission lines as discussed earlier. This technique is worthy of further investigation with a larger sample of objects.

Table 4.1. Summary of Simplified Method Results

Quantity Extinction	$M/M_{\rm Cloudy}$ Mean E(B-V)	$\dot{M}/\dot{M}_{\rm Cloudy}$ Mean E(B-V)	$M/M_{\rm Cloudy}$ E(B-V) = 0	$\dot{M}/\dot{M}_{\rm Cloudy}$ E(B-V) = 0
NGC 4151				
[S II] Ratio	6.5	6.2	3.6	3.4
$n_H = 10^2$	57.9	40.0	32.0	22.1
$n_H = 10^3$	5.8	4.0	3.2	2.2
$n_H = 10^4$	0.6	0.4	0.3	0.2
$U_{ion} = 10^{-2}$	1.8	1.8	1.0	1.0
Mrk 573				
[S II] Ratio	1.4	1.1	0.5	0.4
$n_H = 10^2$	6.0	5.1	2.4	2.0
$n_H = 10^3$	0.6	0.5	0.2	0.2
$n_H = 10^4$	0.1	0.1	<0.1	<0.1
$U_{ion} = 10^{-2}$	0.3	0.1	0.1	0.1
Mrk 34				
[S II] Ratio	0.3	0.5	0.1	0.2
$n_H = 10^2$	2.3	4.5	0.9	1.7
$n_H = 10^3$	0.2	0.4	0.1	0.2
$n_H = 10^4$	<0.1	<0.1	<0.1	<0.1
$U_{ion} = 10^{-2}$	1.3	1.1	0.5	0.4

Note. — NGC 4151: $M_{\rm Cloudy} = 3 \times 10^5\ M_\odot$ and $\dot{M}_{\rm max} = 3.0\ M_\odot\ {\rm yr}^{-1}$. Mrk 573: $M_{\rm Cloudy} = 2 \times 10^6\ M_\odot$ and $\dot{M}_{\rm max} = 3.4\ M_\odot\ {\rm yr}^{-1}$. Mrk 34: $M_{\rm Cloudy} = 3 \times 10^7\ M_\odot$ and $\dot{M}_{\rm max} = 12.5\ M_\odot\ {\rm yr}^{-1}$.

The results of this Chapter suggest that claims of very energetic NLR outflows in nearby AGN that are based on global or simplified techniques should be considered with caution, as also suggested by others (Karouzos et al. 2016; Bischetti et al. 2017; Perna et al. 2017). The [S II] density law method appears to be the most physically motivated as it employs a direct tracer of the gas density, while the assumption of a constant ionization parameter also yields potentially promising results. The differences between the results of these methods and our benchmark results highlights the need for multi-component photoionization models to properly account for the multiphase nature of the optical emission line gas.

CHAPTER 5

DISCUSSION

With the results of the preceding three chapters we may now explore the results as a whole and critically examine the assumptions, implications, open questions, and future investigations that stem from our analysis. First, we explore any remaining assumptions underlying our techniques that were not explicity addressed elsewhere. Following this, we discuss the implications of our results in terms of feedback in nearby AGN and the relevance of these results to higher redshift quasars. The results of this study aid in answering several questions but also lead to new open questions that are worthy of further pursuit. We use these open questions to motivate and focus our future research efforts.

5.1 Assumptions

A goal of this dissertation was to produce the most accurate measurements of ionized gas mass profiles, outflow rates, and energetics as possible with current observations and modeling techniques. Nonetheless, there are invariably still underlying assumptions that must be made in order to progress. We critically examine those assumptions here and attempt to characterize their systematic effects on our results and conclusions.

5.1.1 Galaxy Distances

The variable that may have the largest impact on our overall results is the accuracy of the adopted distances to our active galaxies. We have calculated these distances using Hubble's Law, which determines the distance to a galaxy based on its measured recessional velocity ($D = v/H_0$). This process assumes that a galaxy's motion is dominated by Hubble flow

due to the overall expansion of the universe. However, galaxies also have their own peculiar velocities superimposed on the Hubble flow that may be as large as ~ 600 km s^{-1}. This effect is negligible for galaxies at large distances greater than ~ 85 Mpc ($z \approx 0.02$), introducing an error of less than 10%; however, it can dominate for nearby galaxies.

In the case of this study, Mrk 34 is at a sufficiently large distance that any peculiar velocity will have a negligible affect on the derived distance, while the estimate for Mrk 573 could be in error by as much as $\sim 15\%$ in the most extreme case. The most significant deviation would be for NGC 4151, for which Crenshaw et al. (2015) adopted a distance of $D = 13.3$ Mpc. Subsequent to this study, the distance to NGC 4151 was independently measured to be ~ 16 Mpc using Cepheid variables (Fausnaugh et al., private communication).

Overall, it is clear that the estimated distances for our AGN are accurate to better than 25% in all cases, with Mrk 573 and Mrk 34 the most constrained. A change in the adopted distance for a galaxy would correspond to an increase or decrease of our adopted spatial scale, which would alter the outflow radii and bin sizes used to caculate the outflow rates. If a new distance of D_1 is adopted then compared to the previously used distance of D_2 the spatial scale would change by a factor of (D_1/D_2). In addition, this would also affect our adopted bolometric and Hβ luminosities used to calculate the gas mass profile. In this case, the luminosities would change by a factor of $(D_1/D_2)^2$. While the effects for our targets are likely to be small based on the accuracy of our adopted distances, we have provided all of the kinematic measurements and photoionization modeling results required to recalibrate the mass and outflow rate results should the distance estimates be revised in the future.

5.1.2 Geometric Outflow Model

Next, our results rely upon adopting a geometric model of the host galaxy and outflow orientations in order to deproject the observed radial distances and line-of-sight velocities to their intrinsic values. In the cases of Mrk 573 and Mrk 34 the data supported a coplanar alignment of the host galaxy disk and NLR outflows based on the structure observed in *HST*

imaging. Specifically, the [O III] emission corresponds to arcs of emission that can be traced to inner spiral dust lanes, as well as fueling flows of warm molecular gas in the case of Mrk 573 (Fischer et al. 2017), implying driving of the outflows off of spiral dust lanes within the host galaxy disk. The orientation of the disks were then constrained with either kinematic models of the stellar velocity fields using CO absorption features, or isophotal ellipse fitting to continuum imaging (Fischer et al. 2017, 2018). In the case of NGC 4151, the kinematics were well fit by a biconical outflow model with material flowing along the axes of the bicone (Das et al. 2005). If this system were interpreted under the framework of the disk flow model then the deprojected outflow velocities would be even higher, leading to larger mass outflow rates by up to factors of a few. These models may not be representative of the outflow geometry in all AGN systems and we encourage a detailed comparison of the ionized gas and stellar kinematics on a case by case basis.

5.1.3 Azimuthal Symmetry

Our measured gas kinematics and quantities derived from photoionization modeling are based on the emission that occupies the narrow *HST* STIS long-slit. We then apply the flux-to-mass scale factor that we derived from these observations and models to an *HST* [O III] image of the entire NLR to calculate the ionized gas mass profile. This process requires a fundamental assumption that the quantities derived within the long-slit data are symmetric over all azimuthal angles at each distance, which may not be the case considering the biconical morphology of the NLR. Specifically, the outflow velocity law, density law, and reddening law that are derived within the spectral slit are assumed to hold elsewhere in the NLR.

As a first measure, we quantified the [O III] flux outside of the nominal bicone in each AGN by dividing up our elliptical annuli into smaller azimuthal segments. We generally found that the large solid angle of weaker emission along the bicone minor axis corresponds to a small fraction of the total [O III] luminosity, indicating that the effects of assuming

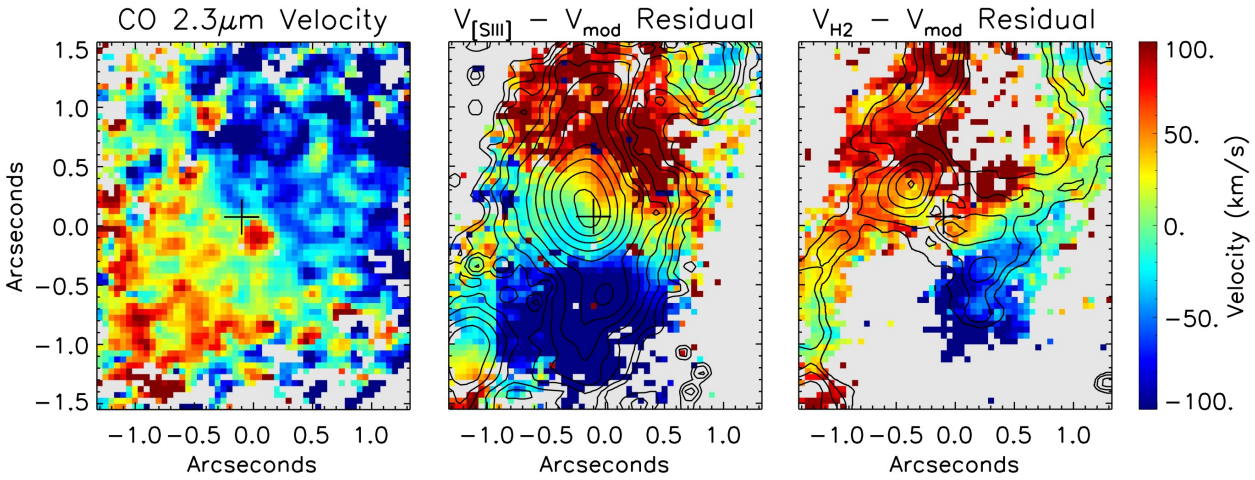

Figure 5.1 The *Gemini* NIFS velocity fields of the stellar disk, ionized gas, and warm molecular gas components, after the subtraction of a rotation model (Fischer et al. 2017, ApJ, 834, 30, doi: 10.3847/1538-4357/834/1/30). Note that the outflow velocity of the ionized gas is approximately constant at all azimuthal angles within the ionizing bicone. © AAS. Reproduced with permission.

azimuthal symmetry will be mitigated. Specifically, for NGC 4151, Mrk 573, and Mrk 34, we adopted bicone half-opening angles of $\theta = 33°$, 38°, and 40°, respectively, resulting in only $\sim$ 31%, 19%, and 20% of the [O III] flux outside of the nominal bicone.

Supplementary studies of these AGN (Das et al. 2005; Storchi-Bergmann et al. 2010; Fischer et al. 2017, see Figure 5.1) indicate that to first order the outflow velocity is not a strong function of azimuthal angle within the ionizing bicone. In addition, while the derived density and reddening laws that are used to calculate the ionized gas masses are unlikely to hold precisely along the NLR minor axis, our supplementary APO DIS observations indicate that this gas is AGN ionized. This material may be susceptible to more foreground reddening; however, this would only result in a minor underestimation of the gas mass along the NLR minor axis, which already corresponds to $\lesssim$ 30% of the total [O III] luminosity.

We further reduced the impact of assuming azimuthal symmetry and improved upon the procedure of Crenshaw et al. (2015) by dividing our elliptical annuli into two sections, modeling each half of the bicone independently. This refinement was particularly important

in the case of Mrk 34 where the density and other physical conditions were strongly bimodal across the NLR bicone.

5.1.4 Extinction Curve

We adopted a Milky Way Galactic extinction curve (Savage & Mathis 1979; Cardelli et al. 1989) to correct the observed emission line ratios that were used to model the ionized gas mass. This assumes that the standard Galactic reddening law applies within both our Galaxy and within the AGN host galaxy. This is unlikely to be the case for all nearby AGN, but is difficult to model without extensive UV spectroscopy. The differences between various extinction curves are largest in the UV such that they have a smaller impact in the optical. In addition, our reddening-corrected emission line ratios from the hydrogen and helium recombination lines agree very well with the model predicted values that are robust and largely unaffected by the specific Cloudy model parameters. The strongest indication of this is the excellent agreement between the reddening-corrected and model predicted He II λ3203 emission line observed in Mrk 573, as it is the shortest wavelength recombination line and furthest in spectral range from the Hα and Hβ emission lines used to derive the reddening.

5.1.5 Ionizing Continuum

Finally, for our Cloudy photoionization modeling we adopted a standard Seyfert power-law SED that has been derived primarily from studies of nearby Type 1 AGN (e.g., Schmitt et al. 1997; Alonso-Herrero et al. 2003; Jin et al. 2012). Due to the obscured nature of Type 2 AGN, their ionizing source cannot be directly detected. We adopted this standard power-law SED and normalized the total luminosity to calibrated measures such as the $2-10$ keV luminosity, which can partially penetrate the torus in most objects. In the case of Mrk 34, the AGN is Compton-thick and even higher energy X-rays were used to model the SED and derive a $2-10$ keV luminosity (Gandhi et al. 2014). This quantity is believed to be isotropic and thus can be used to calculate the bolometric luminosity based on calibrations derived from

Type 1 AGN. The scatter in these relationships are typically factors of $\sim 3-4$ and ultimately affect our estimate of the total number of ionizing photons per second (Q_{ion}) emitted by the AGN that are used in our Cloudy models. This value in conjunction with the deprojected distances were used to constrain the gas density as a function of ionization parameter at each distance. Based on changes in the predicted emission line ratios over small ranges of ionization parameter and thus density, it is likely that changes in Q_{ion} by factors of ~ 2 would hide within the uncertainties of our models. As each of the Cloudy model components may have a different ionization parameter and density, and thus a different mass, quantifying the resulting change in the total gas mass is not straight-forward. However, larger changes in Q_{ion} that may occur if the AGN is changing in luminosity on timescales comparable to the light crossing time of the NLR would be captured, as the best fit models would be unable to reproduce the density sensitive emission line ratios at the ionization parameters required to match their overall strengths relative to the Hβ emission line.

5.2 Implications

5.2.1 Results for Nearby AGN

In the introduction we established several key scientific objectives and questions that we wished to answer in order to gauge the success of our study. We examine the implications of our results here in the context of these objectives.

Objective #1: Quantify the ionized gas mass distributions, mass outflow rates, and outflow energetics of NLR outflows in a sample of AGN that span a range of black hole masses (M_{BH}), bolometric luminosities (L_{bol}) and Eddington ratios (L_{bol}/L_{Edd}). *Do properties of the outflows scale with fundamental AGN parameters?*

We have successfully quantified the ionized gas mass distributions, mass outflow rates, and outflow energetics of the NLR outflows in three nearby AGN, with the analysis for three additional AGN in-progress. Our sample spans a large range in bolometric luminosity; however, a larger sample is needed to cover an appreciable range in black hole mass to

distinguish between luminosity and Eddington ratio effects. Our results indicate that the outflow mass, velocity, radial extent, and energetics are positively correlated with AGN luminosity, while the peak mass outflow rates are approximately constant. However, a larger sample is needed to test these findings and quantify the correlations.

Objective #2: Determine if the NLR outflows are providing effective feedback by constraining the timescale for removing potential star-forming gas from the host galaxy bulge and by comparing our outflow energetics with theoretical models. *Are the outflows energetic enough to measurably impact the host galaxy?*

The mass outflow rates indicate that the ionized gas may be evacuated from the inner bulge on times scales of $\tau \approx M/\dot{M} \sim 10^6$ years. However, recent ALMA observations of Mrk 573 reveal that the nuclear region ($r < 1.4$ kpc) also contains $\sim 10^8$ $M_\odot$ of cold molecular gas (Wiklind et al., private communication). If the ionized gas reservoir is continually replenished through the ionization of the cold molecular gas, then the evacuation timescale for the bulge becomes $\tau \approx M/\dot{M} \sim 10^8$ years, which is comparable to the duty cycle of an AGN. Finally, additional mass modeling of each object similar to that which we completed for Mrk 573 (Fischer et al. 2017) is needed to determine if the outflows reach the escape velocity of the galactic bulge.

We also observe that AGN ionized gas in the ENLR extends to kpc scales in most cases and can encompasses $\sim$ 10 million solar masses of gas. This may inhibit star formation by heating the gas in the galaxy disk and inducing turbulence that prevents collapse into star-forming regions as indicated by high FWHM lines that often extend beyond the outflow regions (Fischer et al. 2018; Revalski et al. 2018b). Examining this in more detail is beyond the scope of this work and requires a careful determination of the AGN duty cycle and star formation timescale, as outflows may cause positive or negative (compression triggered or compression disrupted) feedback. There is evidence that nearby AGN as a whole, including some of our AGN, sit below the Kennicutt-Schmidt law (Wang et al. 2007) that describes the star-formation rate as a function of gas density. This is worthy of further investigation

and would require measuring the star formation rates in these AGN and a matched sample of quiescent galaxies with similar host galaxy types, colors, and gas masses.

Finally, while the outflows do reach benchmark kinetic luminosity values required by some models for effective feedback, these low redshift AGN already have fully assembled bulges. Thus, feedback should be examined in the context of the current impact of the outflows and implications for scaling the relevant physics to higher redshift objects.

Objective #3: Use our spatially resolved measurements to explore the assumptions of simplified gas mass estimate techniques to gauge the reliability and systematic uncertainties of mass outflow rate and energetic measurements in the literature. *Can ionized gas masses be calculated accurately without photoionization modeling?*

The results presented here indicate that global and simplified techniques tend to significantly overestimate ionized gas masses and are subject to strong systematic biases. While we are able to recommend some improvements to these techniques, such as adopting a higher density of $n_H \approx 10^{3.3}$ cm^{-3} for the commonly used constant density method, the uncertainties remain unacceptably large with errors > 1 dex. Ultimately, we were unable to find a satisfactory technique that does not utilize photoionization models to match all of our results. We recommend that literature values of ionized gas masses and outflow rates be interpreted with caution when these methods are adopted, especially when considering claims of very energetic outflows. Ultimately, the optical emission line gas is a multiphase medium that requires modeling of multiple ionization and density states to accurately capture the mass in each component.

5.2.2 Relevance to High Redshift Quasars

A logical extension of the techniques developed here would be to probe outflows in more luminous and higher redshift quasars at the peak of cosmic star formation ($z \approx 2$). When galaxies can be resolved at much higher redshifts where they are in the process of forming, our results may play an important role in properly characterizing the outflows.

Our results indicate that spatially resolved observations are required to accurately quantify the mass outflow properties. Specifically, global techniques that may not resolve the extent of the outflows versus the ionized gas in rotation in the ENLR, or separate gas in outflow versus rotation within the NLR itself, are subject to significant biases that will generally overestimate the gas mass and outflow rates.

Current observations with *HST* allow us to probe outflows in higher redshift quasars, with a practical observational limit of $z \sim 2$ in order to resolve sources (Leung et al. 2017). These types of observations require exceedingly long exposures and generally capture the rest-frame UV emission of the AGN and host galaxy. As an intermediate step we have begun expanding our sample to higher luminosities and redshifts up to $z \approx 0.4$ (e.g. Fischer et al. 2018). The development and launch of next generation observatories such as the Large UV/Optical/IR Surveyor (*LUVOIR*) and *JWST* will provide even more capabilities for exploring spatially resolved outflows at higher redshifts.

5.2.3 Open Questions

The results of this study, as well as the recent results of others, lead to open questions that cannot be answered within the context of our analysis, thus requiring further studies. We highlight the most interesting questions raised by this work.

Is $\dot{M} \approx 3 - 4\ M_{\odot}\ \mathbf{yr}^{-1}$ a universal outflow rate for nearby AGN?

The peak mass outflow rate for these three AGN is approximately the same despite their very different bolometric luminosities and Eddington ratios. This may be coincidental as we have characterized a small number of objects, or may represent a more fundamental property of NLR outflows. Answering the above question will require studying additional objects that also span a range of black hole mass and bulge gravitational potential. Our plans for this type of study are described further in the next section.

Is there a critical bolometric luminosity threshold for bulge clearing?

The maximum outflow extent and ionized gas radius increase monotonically with bolometric luminosity; however, the outflows do not reach scales of several kpc that are typical of galaxy bulges (Oohama et al. 2009). Recent work has begun to solidify the presence of an outflow radius-luminosity relationship that may continue to extend to more distant and higher luminosity sources, keeping in mind that the radial outflow region (the classic NLR) may only be a fraction of the total extent of the ionized gas (the ENLR, Fischer et al. 2018; Kang & Woo 2018). Answering this question will require spatially resolved studies of higher redshift and higher luminosity objects, which we are submitting an *HST* proposal to investigate.

Is radiative driving a ubiquitious outflow launching mechanism?

Modeling of Mrk 573 (Fischer et al. 2017) clearly established that radiative driving was sufficient to explain the observed NLR outflow velocities and that the gas is accelerated in-situ. This conclusion would seem applicable to NGC 4151 and Mrk 34 as well; however, it is unclear then why a large fraction of nearby Seyfert galaxies do not exhibit clear signs of outflow in their NLRs (Fischer et al. 2013, 2014). This could be dependent on the geometry of the system and/or the physical conditions in the gas that are required for effective radiative driving. Answering the above question will require additional radiative driving and mass modeling studies of nearby AGN.

What is the combined impact of multiphase outflows on the host galaxy?

Our results account for the UV/optical emission line gas; however, we do not have a direct measurement of the X-ray emission line gas or cold molecular gas outflow rates and energetics. These gas components could contain more or less mass than the optical emission line gas and play an important role in feedback. Finally, these phases may couple such that the driving of one phase is able to confine or encompass another and compound the evacuation of gas from the bulge. Answering the above question requires detailed multiwavelength studies that are discussed in the next section.

5.3 Future Work

5.3.1 Expanding the Sample

We are currently in the process of deriving spatially resolved mass outflow rates and energetics for NGC 1068, Mrk 3, and Mrk 78. These targets are included in our original sample listed in Table 1.1 and we had hoped to derive a simplified methodology that would allow us to more quickly derive their outflow properties. As discussed in Chapter 4, we were unable to establish a satisfactory procedure and concluded that multicomponent photoionization modeling of individual targets is still the best option for producing accurate results. Therefore, we will continue to analyze these three additional AGN within our original framework and publish their results at a later date.

We have identified four additional targets from the sample of Fischer et al. (2013, 2014) that have the required archival data for our spatially resolved analysis that we now classify as having kinematic signatures of outflow along the galactic disk based on our results for Mrk 573 and Mrk 34, in contrast to the earlier biconical outflow geometry classification scheme. These four galaxies are: NGC 2273, NGC 3393, NGC 5347, and NGC 5643. The physical characteristics of these AGN are presented in Table 5.1, and we will pursue the analysis of these targets as part of a larger scale program in the future.

Finally, we are seeking to build a substantially larger sample by proposing new observations with *HST*. We have examined the *HST* archives for AGN with NLR outflows that already have portions of the required data sets for this analysis. We have identified 14 nearby Seyfert galaxies from the Fischer et al. (2013) sample that have all of the necessary spectroscopy already in the archives and only require an [O III] image. These AGN span a significant range in bolometric luminosity (3.8 dex), Eddington ratio (3.3 dex), black hole mass (2.0 dex), and host galaxy type. This will allow us to measure the range of outflow radii and mass outflow rates that are present in nearby active galaxies and determine their dependence on fundamental AGN and host galaxy parameters.

Table 5.1. Nearby Active Galaxies with Archival *HST* STIS Observations

Catalog Name (1)	Redshift (21 cm) (2)	Distance (Mpc) (3)	Scale (pc/″) (4)	V (mag) (5)	$\log(L_{bol})$ (erg s^{-1}) (6)	$\log(M_{BH})$ ($M_\odot$) (7)	L_{bol}/L_{Edd} (unitless) (8)	Refs. (Col. 6,7) (9)	Analysis Status (10)
NGC 5643	0.0040	16.8	81.5	13.6	43.6	6.4	0.125	3, 5	Future
NGC 2273	0.0061	25.8	124.9	13.5	44.0	7.3	0.040	1, 2	Future
NGC 5347	0.0080	33.4	161.8	12.7	43.8	6.8	0.079	1, 2	Future
NGC 3393	0.0125	52.3	253.7	14.0	45.0	7.7	0.158	3, 4	Future

Note. — Columns are (1) target name, (2) 21 cm redshift from the NASA/IPAC Extragalactic Database, (3) Hubble distance and (4) spatial scale assuming $H_0 = 71$ km s^{-1} Mpc^{-1}, (5) apparent V band magnitude from SIMBAD, (6) bolometric luminosity estimated from [O III] imaging, (7) black hole mass, and (8) the corresponding Eddington ratio. Column (9) gives the references for columns (6) and (7). References are: (1) Woo & Urry 2002, (2) Nelson & Whittle 1995, (3) this work, (4) Beifiori et al. 2012, (5) Goulding et al. 2010.

5.3.2 Multiphase Outflows

The results of our study account for a single gas phase; namely, the optical emission line gas. This naturally leads to questions such as, *what is the relative importance of other outflow phases? What is their combined impact on galaxy bulge scales? Do the phases interact?*

Several studies have suggested that there could be a comparable or larger amount of mass in the more highly ionized X-ray gas (Kraemer et al. 2015; Bogdán et al. 2017), which could therefore have a larger impact than the optical NLR outflows. Other studies find large outflows of molecular gas in ultra-luminous infrared galaxies (Rose et al. 2018; Spence et al. 2018), with evidence for warm molecular outflows in at least some nearby AGN (Fischer et al. 2017).

Our picture of multiphase outflows is incomplete, and we need to conduct a systematic multiwavelength survey of a uniform galaxy sample that employs a consistent methodology for calculating outflow energetics with spatially resolved observations similar to what we developed in Revalski et al. (2018a,b). Through this project, we will take the first steps to connect multiphase outflows by deriving spatially resolved masses, outflow rates, and energetics for

the X-ray emitting gas in nearby active galaxies where we have already quantified the impact of optical NLR outflows. We can adapt our methodology refined for *HST* to archival spectra and imaging in the X-rays from the *Chandra* and *XMM-Newton* space-based observatories to constrain the dynamics of the X-ray gas, and directly compare its impact with the optical outflows. The *Chandra* data can be optimized by applying advanced sub-pixel sampling and deconvolution techniques (Maksym et al. 2017) to approach the spatial resolution of *HST* ($\sim 0\farcs1$). This will be the first comparison of multiphase outflows for a sample of AGN at comparable spatial resolution, employing self-consistent methodology for quantifying outflow impact.

We have selected six nearby AGN with suitable archival *Chandra* and *XMM-Newton* data to accomplish the science goals. These are a subset of galaxies from our optical NLR outflow analysis that possess both high quality optical and X-ray data needed compare the outflow phases. In Table 5.2, we summarize the physical properties and data sets for these targets. We have proposed for deeper *XMM-Newton* observations of Mrk 34, and will propose for new *Chandra* observations for targets without grating data.

All of the data required to complete this project are available, and we highlight example data sets in Figure 5.2. These data show that the X-ray emitting gas has a similar spatial extent to the optical NLR and may contain a similar or larger amount of mass (Kraemer et al. 2015). The similar spatial distribution also suggests a physical connection between the phases that may help to explain the driving mechanisms of AGN outflows (Gómez-Guijarro et al. 2017). We have mapped out powerful outflows of ionized gas in the optical containing millions of solar masses, *but what is the X-ray gas mass? How fast is it outflowing, and what is its dynamic impact?* This project will answer these questions. Our sample spans a range in luminosity, black hole mass, Eddington ratio, and host galaxy type, and will allow us to begin connecting multiphase outflows and understand their impact on galaxy and SMBH evolution. Our scientific objectives are the following:

Table 5.2. Active Galaxy Sample and Archival Data Sets

Galaxy Designation (1)	Redshift (21 cm) (2)	Distance (Mpc) (3)	Scale (pc/″) (4)	log(L_{bol}) (erg s^{-1}) (5)	*Chandra* Imaging (6)	*Chandra* Spectroscopy (7)	*XMM-Newton* Spectroscopy (8)
NGC 4151	0.0033	13.9	67.4	43.9	ACIS	H/LETGS	RGS
MRK 573	0.0172	72.0	349.1	45.5	ACIS	...	RGS
MRK 34	0.0505	207.9	1007.7	46.2	ACIS	...	RGS
NGC 1068	0.0038	16.0	77.6	45.0	ACIS	H/LETGS	RGS
MRK 3	0.0135	56.6	274.5	45.3	ACIS	HETGS	RGS
MRK 78	0.0372	154.2	747.4	44.6	ACIS	...	RGS

Note. — AGN targets from our optical sample (Table 1.1) that have archival *Chandra* and *XMM-Newton* data required for this study. The addition of *Chandra* grating spectroscopy for some objects would allow us to place even tighter constraints on the kinematics and gas mass. Optical modeling is complete for the first three targets and in-progress for the remaining three. Columns are (1) target name, (2) 21 cm redshift from the NASA/IPAC Extragalactic Database, (3) distance and (4) spatial scale assuming $H_0 = 71$ km s^{-1} Mpc^{-1}, (5) bolometric luminosity estimated from [O III] imaging, (6) availability of *Chandra* imaging, (7) availability of *Chandra* grating spectroscopy, and (8) the availability of *XMM-Newton* spectroscopy.

1) Determine the Kinematics of the X-ray Gas: We will use a combination of *Chandra*, *XMM-Newton*, and *HST* spectroscopy to constrain the kinematics of the X-ray gas. With *Chandra* and *XMM-Newton* grating spectroscopy we can constrain the gas velocity centroids and FWHM to within a few hundred km s^{-1}, as the emission lines are often resolved spectroscopically (Kallman et al. 2014; Couto et al. 2016). These measurements will also provide the emission line ratios required for photoionization modeling. We will refine the kinematics using spatially-resolved high-ionization emission lines such as [Fe XIV] in the *HST* long-slit spectra. These lines often show larger velocity offsets than lower-ionization optical emission lines (Schlesinger et al. 2009; Kraemer et al. 2009), and through photoionization modeling we will determine if these lines are produced under the same conditions as the X-ray gas to link their kinematics.

2) Constrain the Physical Conditions with Photoionization Models: We will generate multi-component photoionization models using the Cloudy code (Ferland et al. 2017) to

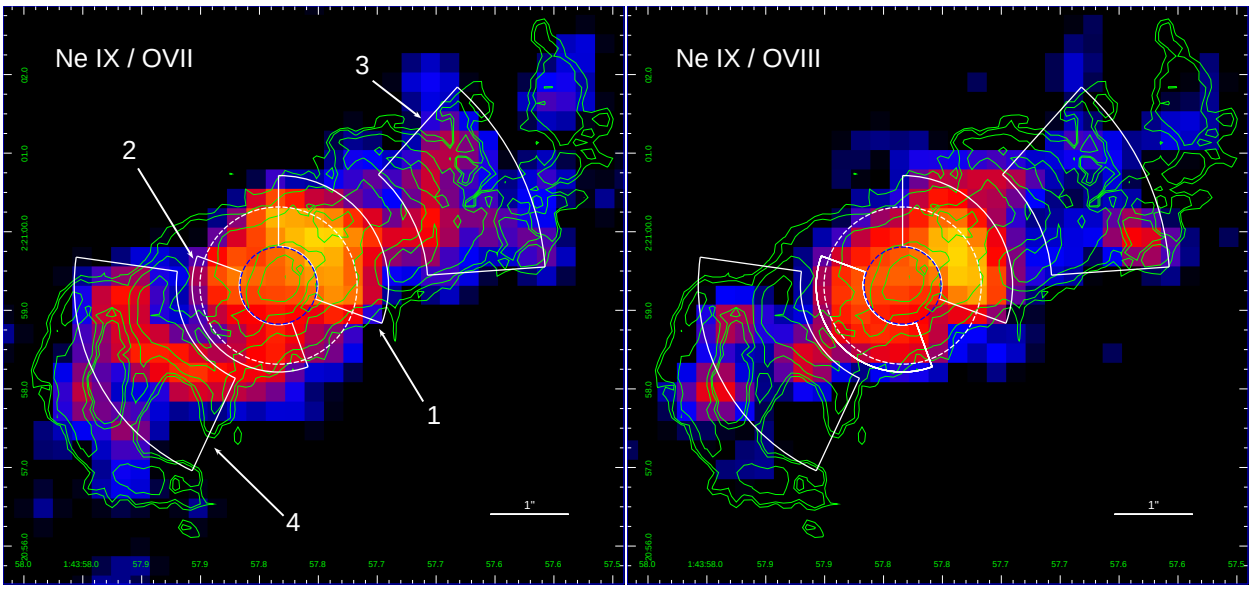

Figure 5.2 An example of the emission line diagnostics that can be used to constrain the physical conditions in the gas as a function of position for Mrk 573 (Paggi et al. 2012, ApJ, 756, 39, doi: 10.1088/0004-637X/756/1/39). The [O III] emission is shown in green contours and regions where spatially resolved fluxes were extracted are numbered. We will derive a flux to mass scale factor from our photoionization models and apply it to an emission line image extracted from the energy-resolved *Chandra* ACIS imaging to determine the radial gas mass profile. © AAS. Reproduced with permission.

match the emission lines in the *Chandra* and *XMM-Newton* spectra, and refine the physical conditions as a function of position using the *Chandra* ACIS imaging to spatially resolve strong emission-line ratios as shown in Figure 5.2. We have already determined all of the model input parameters for NGC 4151, Mrk 573, and Mrk 34 from our optical modeling (Crenshaw et al. 2015; Revalski et al. 2018a,b), and there are several previous studies that will help us to efficiently complete the models (Bianchi et al. 2010; Gonzalez-Martin et al. 2010; Paggi et al. 2012). For targets without high quality *Chandra* grating spectra, we may model the spatially unresolved *XMM-Newton* spectra, which contain a wealth of diagnostic emission lines, and extrapolate the flux to mass scale factor to larger radii using the measured [O III] to soft X-ray flux ratio. In Figure 5.3 we show example *XMM-Newton* spectra and a photoionization model overlay from Kraemer et al. (2015) for the proto-typical Seyfert 2 galaxy NGC 1068.

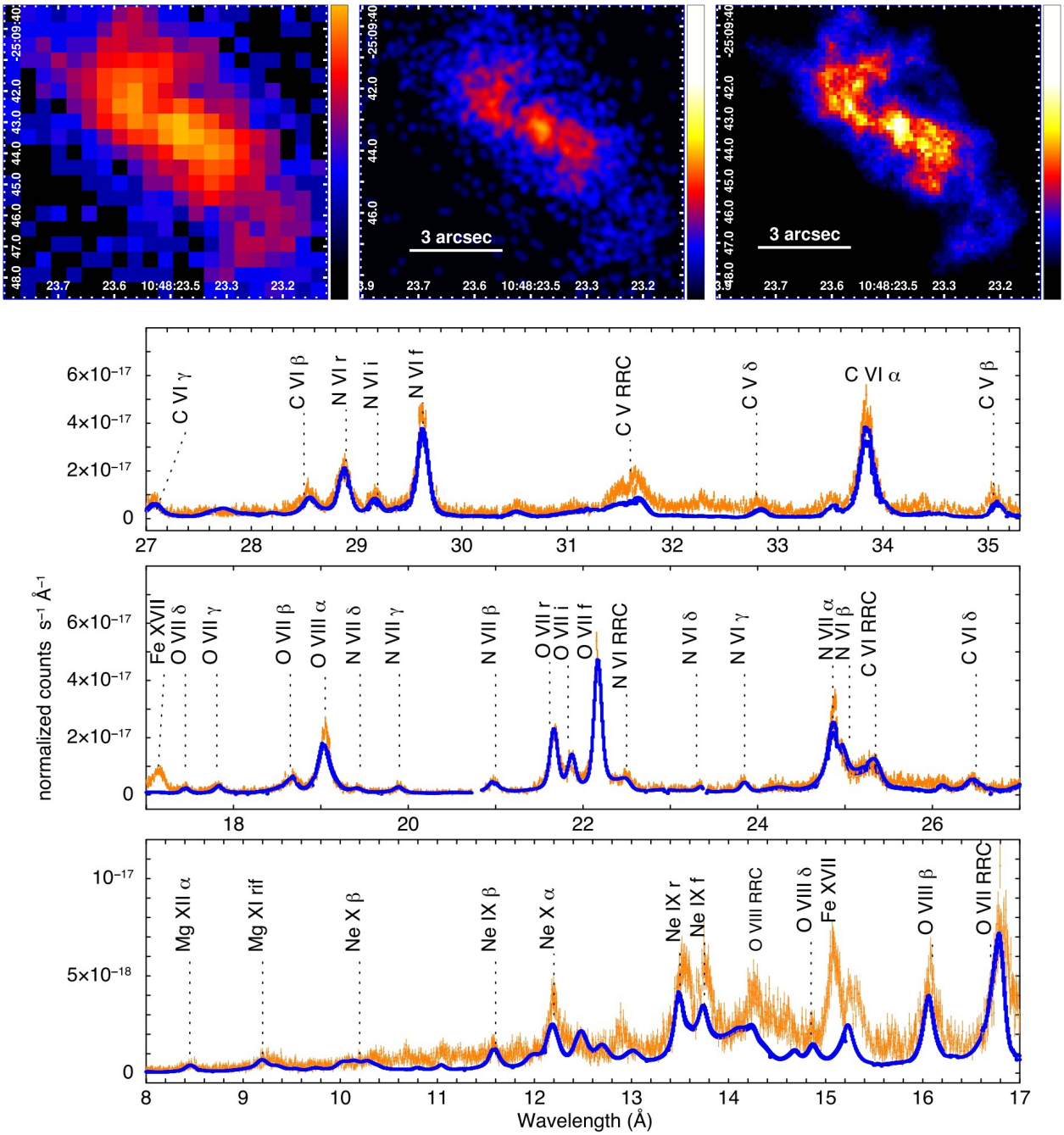

Figure 5.3 The top panel highlights the advanced data treatment techniques used with *Chandra* data to achieve the highest possible spatial resolution ($\sim 0\farcs1$) and compare the optical and X-ray gas at similar spatial scales (Maksym et al. 2017, ApJ, 844, 69, doi: 10.3847/1538-4357/aa78a4). This image shows the raw data for NGC 3393 (left), post re-binning and smoothed (center), and deconvolved from the instrumental point spread function using the EMC2 routine (right). The bottom panels display the *XMM-Newton* RGS spectrum of NGC 1068 from (Kraemer et al. 2015, ApJ, 798, 53, doi: 10.1088/0004-637X/798/1/53) with the data in orange, and the photoionization model prediction in blue. These models will allow us to calculate the X-ray gas mass. © AAS. Reproduced with permission.

3) Calculate the Ionized Gas Mass, Outflow Rates, and Energetics: We can use the output parameters of our Cloudy models to calculate the gas mass at each distance using the same equations that were presented in our optical outflow analysis. In this case, the emission line luminosities will be obtained from *Chandra* ACIS imaging (Figure 5.2).

4) Compare the Impact of the X-ray and Optical Outflows: We will be able to compare the calculated energetics to those we found for the optical NLR gas in Revalski et al. (2018a,b), and those in progress (Revalski et al. 2019, in preparation.). This will answer the questions as to how much mass is contained in the X-ray gas, what its energetic impact is on the host galaxy, and its importance relative to the optical outflows.

The results of this study can provide us with the first spatially resolved, multiphase outflow comparison for a sample of AGN at similar spatial resolution using a self-consistent methodology to determine the gas masses, outflow rates, and energetics. The multiwavelength nature of this investigation is required to determine the relative impact of different outflow phases and reveal if any of them dominate in driving the evolution of the AGN/host galaxy system. These types of studies will be critical moving forward in order to gain a complete understanding of feeding and feedback in active galaxies.

CHAPTER 6

CONCLUSIONS

We provide the first spatially resolved mass outflow and kinetic energy rate measurements for NLR outflows in a small sample of nearby AGN using *HST*. As the interest in spatially resolved outflow properties continues to grow, our results provide important constraints for determining accurate gas masses, outflow rates, and outflow energetics. Our main conclusions are the following:

1. The outflows encompass total ionized gas masses of $M \sim 10^5 - 10^7\ M_\odot$ and reach peak outflow velocities of $v \approx 800 - 2000$ km s^{-1}. The outflows extend to maximum radial distances of $r \approx 0.1 - 2$ kpc from the nucleus, with the gas mass, peak velocity, and radial extent of the outflows positively correlated with increasing AGN luminosity.

2. The mass outflow rates reach maximum values of $\dot{M} \approx 3 - 12\ M_\odot$ yr^{-1} with the outflows carrying total kinetic energies of $E \sim 10^{54} - 10^{56}$ erg. The peak mass outflow rates are similar for all of the targets regardless of AGN luminosity, while the kinetic energies span a wider range that is positively correlated with increasing AGN luminosity.

3. The outflows are capable of delivering significant feedback to their host galaxies on scales of $r \lesssim 2$ kpc by evacuating reservoirs of gas from the galactic bulge with depletion timescales of $\tau \sim 10^6$ years for the ionized gas and $\tau \sim 10^8$ years for both the ionized and molecular gas phases. The calculated outflow rates are consistent with in-situ acceleration where gas within the host galaxy is accelerated at all radii by the nuclear radiation field, rather than a steady nuclear flow.

4. The outflow energetics are consistent with theoretical benchmarks that are required for effective feedback; however, it is important to note that AGN in the local universe have fully established bulges and any comparison with feedback models of high redshift galaxies must be interpreted with care.

5. The mass, kinetic energy, and momentum profiles may be summed radially to obtain enclosed totals for the outflow; however, the spatially resolved rates cannot. When in-situ acceleration is considered then gas is driven at all radii and the total mass reaching the outer boundary is larger than for a nuclear flow. Calculating the evacuated mass requires a time integration that is not equivalent to summing the rates. The average outflow rate and area under the rate curve are invariant to the spatial sampling.

6. The non-rotational kinematics and high gas temperatures ($T \sim 10^4$ K) at large radii indicate that these AGN are capable of driving weak outflows and inducing turbulence on kpc scales that may inhibit star-formation in the host galaxy. The optical emission in the ENLR can contain $M > 10^8$ $M_\odot$ of ionized gas and even more mass may be encompassed in the X-ray emission line gas.

7. Our study accounts for the mass of the UV and optical emission line gas. Additional analysis is required to account for the multiphase nature of the outflows, including the hot X-ray and cold molecular gas. This will require multiwavelength datasets at similar spatial resolution and is possible with the current generation of observatories including the *Chandra* X-ray Observatory and the Atacama Large Millimeter Array.

8. Spatially resolved observations are required to properly constrain the properties of outflows. This includes the velocity profile, luminosity distribution, separation of rotational and outflow kinematics, and the radial extent of the outflowing gas. Global techniques that utilize spatially integrated spectra and provide a single estimate of the gas mass and outflow energetics are susceptible to strong selection effects and systematic biases that can be avoided by utilizing spatially resolved observations.

9. We explored geometric-based and luminosity-based mass estimate techniques and found that luminosity-based methods, which utilize an observable tracer of the gas mass, provide more accurate results. Both techniques require spatially resolved observations to separate the fraction of gas in outflow versus rotation, determine the outflow radius, and to probe changes in the outflow velocity on sub-arcsecond scales. Multicomponent photoionization modeling provides the most precise measurement of the ionized gas mass.

10. The choice of gas density has a profound effect on the derived gas mass. Modeling the optical emission line gas is a multiphase problem that requires multiple density and ionization components to reproduce the emission line ratios. When using a single density, commonly adopted values such as those provided by the [S II] doublet line ratio, or assuming a constant density of $n_H = 100$ cm^{-3}, can overestimate the ionized gas mass for some NLR outflows. If a constant density must be assumed, then a higher value of $n_H \approx 2000$ cm^{-3} produces estimates that are more consistent with our modeling. However, large density variations across the NLR and between AGN indicate that photoionization modeling is strongly preferred.

The results of this dissertation indicate that spatially resolved studies of NLR outflows in multiple wavebands hold great promise for understanding AGN feedback and its effects on the growth and evolution of SMBHs and their galaxies.

REFERENCES

Afanasiev, V. L., Mikhailov, V. P., & Shapovalova, A. I. 1998, Astronomical and Astrophysical Transactions, 16, 257

Afanasiev, V. L., Burenkov, A. N., Shapovalova, A. I., & Vlasyuk, V. V. 1996, IAU Colloq. 157: Barred Galaxies, 91, 218

Event Horizon Telescope Collaboration, Akiyama, K., Alberdi, A., et al. 2019, ApJL, 875, L1

Alexander, T., Sturm, E., Lutz, D., et al. 1999, ApJ, 512, 204

Alonso-Herrero, A., Quillen, A. C., Rieke, G. H., et al. 2003, AJ, 126, 81

Alonso-Herrero, A., Simpson, C., Ward, M. J., & Wilson, A. S. 1998, ApJ, 495, 196

Antonucci, R. 1993, ARA&A, 31, 473

Antonucci, R. R. J., & Miller, J. S. 1985, ApJ, 297, 621

Asplund, M., Grevesse, N., Sauval, A. J., & Scott, P. 2009, ARA&A, 47, 481

Awaki, H., Koyama, K., Inoue, H., & Halpern, J. P. 1991, PASJ, 43, 195

Babcock, H. W. 1953, PASP, 65, 229

Bae, H.-J., Woo, J.-H., Karouzos, M., et al. 2017, ApJ, 837, 91

Bae, H.-J., & Woo, J.-H. 2016, ApJ, 828, 97

Baldwin, J. A., Phillips, M. M., & Terlevich, R. 1981, PASP, 93, 5

Bär, R. E., Weigel, A. K., Sartori, L. F., et al. 2017, MNRAS, 466, 2879

Barbosa, F. K. B., Storchi-Bergmann, T., Cid Fernandes, R., Winge, C., & Schmitt, H. 2009, MNRAS, 396, 2

Baron, D., & Netzer, H. 2019, arXiv:1903.11076

Baron, D., & Ménard, B. 2019, arXiv:1903.01996

Batiste, M., Bentz, M. C., Raimundo, S. I., Vestergaard, M., & Onken, C. A. 2017, ApJL, 838, L10

Baum, S. A., O'Dea, C. P., Dallacassa, D., de Bruyn, A. G., & Pedlar, A. 1993, ApJ, 419, 553

Beifiori, A., Courteau, S., Corsini, E. M., & Zhu, Y. 2012, MNRAS, 419, 2497

Bennert, N., Jungwiert, B., Komossa, S., Haas, M., & Chini, R. 2006, A&A, 456, 953

Begelman, M. C. 2004, Coevolution of Black Holes and Galaxies, 374

Bentz, M. C., Walsh, J. L., Barth, A. J., et al. 2009, ApJ, 705, 199

Bentz, M. C., Denney, K. D., Cackett, E. M., et al. 2006, ApJ, 651, 775

Bian, W., & Gu, Q. 2007, ApJ, 657, 159

Bianchi, S., Chiaberge, M., Evans, D. A., et al. 2010, MNRAS, 405, 553

Binette, L., Wilson, A. S., & Storchi-Bergmann, T. 1996, A&A, 312, 365

Bischetti, M., Piconcelli, E., Vietri, G., et al. 2017, A&A, 598, A122

Bogdán, Á., Kraft, R. P., Evans, D. A., Andrade-Santos, F., & Forman, W. R. 2017, ApJ, 848, 61

Buchner, J., Georgakakis, A., Nandra, K., et al. 2014, A&A, 564, A125

Capetti, A., Axon, D. J., Macchetto, F., Sparks, W. B., & Boksenberg, A. 1996, ApJ, 469, 554

Cardelli, J. A., Clayton, G. C., & Mathis, J. S. 1989, ApJ, 345, 245

Castro, C. S., Dors, O. L., Cardaci, M. V., & Hägele, G. F. 2017, MNRAS, 467, 1507

Cicone, C., Brusa, M., Ramos Almeida, C., et al. 2018, Nature Astronomy, 2, 176

Ciotti, L., & Ostriker, J. P. 2001, ApJ, 551, 131

Collins, N. R., Kraemer, S. B., Crenshaw, D. M., Bruhweiler, F. C., & Meléndez, M. 2009, ApJ, 694, 765

Collins, N. R., Kraemer, S. B., Crenshaw, D. M., et al. 2005, ApJ, 619, 116

Combes, F. 2015, Galaxies in 3D across the Universe, 309, 182

Comerford, J. M., Barrows, R. S., Greene, J. E., & Pooley, D. 2017, ApJ, 847, 41

Costa, T., Sijacki, D., & Haehnelt, M. G. 2014, MNRAS, 444, 2355

Couto, J. D., Kraemer, S. B., Turner, T. J., & Crenshaw, D. M. 2016, ApJ, 833, 191

Crenshaw, D. M., Fischer, T. C., Kraemer, S. B., & Schmitt, H. R. 2015, ApJ, 799, 83

Crenshaw, D. M., & Kraemer, S. B. 2012, ApJ, 753, 75

Crenshaw, D. M., Schmitt, H. R., Kraemer, S. B., Mushotzky, R. F., & Dunn, J. P. 2010, ApJ, 708, 419

Crenshaw, D. M., Kraemer, S. B., & George, I. M. 2003, ARA&A, 41, 117

Crenshaw, D. M., Kraemer, S. B., Boggess, A., et al. 1999, ApJ, 516, 750

Cresci, G., & Maiolino, R. 2018, Nature Astronomy, 2, 179

Das, V., Crenshaw, D. M., Hutchings, J. B., et al. 2005, AJ, 130, 945

Davies, R. L., Groves, B., Kewley, L. J., et al. 2016, MNRAS, 462, 1616

De Robertis, M. M., & Osterbrock, D. E. 1986, ApJ, 301, 727

Di Matteo, T., Springel, V., & Hernquist, L. 2005, Nature, 433, 604

Diniz, M. R., Riffel, R. A., Riffel, R., et al. 2017, MNRAS, 469, 3286

de Vaucouleurs, G., de Vaucouleurs, A., Corwin, H. G., et al. 1995, VizieR Online Data Catalog, 7155

Dopita, M. A., Shastri, P., Davies, R., et al. 2015, ApJS, 217, 12

Dors, O. L., Cardaci, M. V., Hägele, G. F., et al. 2015, MNRAS, 453, 4102

Dors, O. L., Cardaci, M. V., Hägele, G. F., & Krabbe, Â. C. 2014, MNRAS, 443, 1291

Draine, B. T. 2011, Physics of the Interstellar and Intergalactic Medium by Bruce T. Draine. Princeton University Press, 2011. ISBN: 978-0-691-12214-4

Draine, B. T. 2003, ARA&A, 41, 241

Dressel, L. 2012, Wide Field Camera 3, HST Instrument Handbook

Durré, M., & Mould, J. 2019, ApJ, 870, 37

Durré, M., & Mould, J. 2018, ApJ, 867, 149

Erkens, U., Appenzeller, I., & Wagner, S. 1997, A&A, 323, 707

Fabian, A. C. 2012, ARA&A, 50, 455

Falcke, H., Wilson, A. S., & Simpson, C. 1998, ApJ, 502, 199

Ferland, G. J., Chatzikos, M., Guzmán, F., et al. 2017, RMxAA, 53, 385

Ferland, G. J., Porter, R. L., van Hoof, P. A. M., et al. 2013, RMxAA, 49, 137

Ferland, G. J., & Osterbrock, D. E. 1986, ApJ, 300, 658

Ferland, G. J., & Mushotzky, R. F. 1982, ApJ, 262, 564

Ferrarese, L., & Merritt, D. 2000, ApJL, 539, L9

Feroz, F., Hobson, M. P., Cameron, E., & Pettitt, A. N. 2013, arXiv:1306.2144

Feroz, F., Hobson, M. P., & Bridges, M. 2009, MNRAS, 398, 1601

Feroz, F., & Hobson, M. P. 2008, MNRAS, 384, 449

Ferruit, P. 2002, Revista Mexicana de Astronomia y Astrofisica Conference Series, 13, 183

Ferruit, P., Wilson, A. S., Falcke, H., et al. 1999, MNRAS, 309, 1

Feruglio, C., Fiore, F., Carniani, S., et al. 2015, A&A, 583, A99

Fiore, F., Feruglio, C., Shankar, F., et al. 2017, A&A, 601, A143

Fischer, T. C., Kraemer, S. B., Schmitt, H. R., et al. 2018, ApJ, 856, 102

Fischer, T. C., Machuca, C., Diniz, M. R., et al. 2017, ApJ, 834, 30

Fischer, T. C., Crenshaw, D. M., Kraemer, S. B., Schmitt, H. R., & Turner, T. J. 2014, ApJ, 785, 25

Fischer, T. C., Crenshaw, D. M., Kraemer, S. B., & Schmitt, H. R. 2013, ApJS, 209, 1

Fischer, T. C., Crenshaw, D. M., Kraemer, S. B., Schmitt, H. R., & Trippe, M. L. 2010, AJ, 140, 577

Förster Schreiber, N. M., Genzel, R., Newman, S. F., et al. 2014, ApJ, 787, 38

Gandhi, P., Lansbury, G. B., Alexander, D. M., et al. 2014, ApJ, 792, 117

Gebhardt, K., Bender, R., Bower, G., et al. 2000, ApJL, 539, L13

Genzel, R., Förster Schreiber, N. M., Rosario, D., et al. 2014, ApJ, 796, 7

Gofford, J., Reeves, J. N., McLaughlin, D. E., et al. 2015, MNRAS, 451, 4169

González Delgado, R. M., Heckman, T., & Leitherer, C. 2001, ApJ, 546, 845

Gómez-Guijarro, C., González-Martín, O., Ramos Almeida, C., Rodríguez-Espinosa, J. M., & Gallego, J. 2017, MNRAS, 469, 2720

Gonzalez-Martin, O., Acosta-Pulido, J. A., Perez Garcia, A. M., & Ramos Almeida, C. 2010, ApJ, 723, 1748

Goulding, A. D., Alexander, D. M., Lehmer, B. D., & Mullaney, J. R. 2010, MNRAS, 406, 597

Guainazzi, M., Matt, G., & Perola, G. C. 2005, A&A, 444, 119

Hamann, F., Korista, K. T., Ferland, G. J., Warner, C., & Baldwin, J. 2002, ApJ, 564, 592

Hamann, F., & Ferland, G. 1999, ARA&A, 37, 487

Haniff, C. A., Ward, M. J., & Wilson, A. S. 1991, ApJ, 368, 167

Haniff, C. A., Wilson, A. S., & Ward, M. J. 1988, ApJ, 334, 104

Häring, N., & Rix, H.-W. 2004, ApJL, 604, L89

Harrison, C. M., Costa, T., Tadhunter, C. N., et al. 2018, Nature Astronomy, 2, 198

Harrison, C. M. 2017, Nature Astronomy, 1, 0165

Harrison, C. M., Alexander, D. M., Mullaney, J. R., & Swinbank, A. M. 2014, MNRAS, 441, 3306

Heckman, T. M., & Best, P. N. 2014, ARA&A, 52, 589

Heckman, T. M., Ptak, A., Hornschemeier, A., & Kauffmann, G. 2005, ApJ, 634, 161

Heckman, T. M., Kauffmann, G., Brinchmann, J., et al. 2004, ApJ, 613, 109

Henkel, C., Peck, A. B., Tarchi, A., et al. 2005, A&A, 436, 75

Hopkins, P. F., & Elvis, M. 2010, MNRAS, 401, 7

Hopkins, P. F., Hernquist, L., Cox, T. J., et al. 2005, ApJ, 630, 705

Imanishi, M., Ichikawa, K., Takeuchi, T., et al. 2011, PASJ, 63, 447

Jackson, N., & Beswick, R. J. 2007, MNRAS, 376, 719

Janssen, A. W., Christopher, N., Sturm, E., et al. 2016, ApJ, 822, 43

Jensen, J. J., Hönig, S. F., Rakshit, S., et al. 2017, MNRAS, 470, 3071

Jin, C., Ward, M., & Done, C. 2012, MNRAS, 425, 907

Joye, W. A., & Mandel, E. 2003, Astronomical Data Analysis Software and Systems XII, 295, 489

Juan de Dios, L., & Rodríguez, M. 2017, MNRAS, 469, 1036

Kakkad, D., Groves, B., Dopita, M., et al. 2018, A&A, 618, A6

Kakkad, D., Mainieri, V., Padovani, P., et al. 2016, A&A, 592, A148

Kallman, T., Evans, D. A., Marshall, H., et al. 2014, ApJ, 780, 121

Kang, D., & Woo, J.-H. 2018, ApJ, 864, 124

Karouzos, M., Woo, J.-H., & Bae, H.-J. 2016, ApJ, 833, 171

Kauffmann, G., Heckman, T. M., Tremonti, C., et al. 2003, MNRAS, 346, 1055

Kay, L. E. 1994, ApJ, 430, 196

Keel, W. C. 1980, AJ, 85, 198

Kewley, L. J., Maier, C., Yabe, K., et al. 2013a, ApJL, 774, L10

Kewley, L. J., Dopita, M. A., Leitherer, C., et al. 2013b, ApJ, 774, 100

Kewley, L. J., Groves, B., Kauffmann, G., & Heckman, T. 2006, MNRAS, 372, 961

Kewley, L. J., Dopita, M. A., Sutherland, R. S., Heisler, C. A., & Trevena, J. 2001, ApJ, 556, 121

Khachikian, E. Y., & Weedman, D. W. 1974, ApJ, 192, 581

Khalatyan, A., Cattaneo, A., Schramm, M., et al. 2008, MNRAS, 387, 13

King, A., & Pounds, K. 2015, ARA&A, 53, 115

Kinney, A. L., Antonucci, R. R. J., Ward, M. J., Wilson, A. S., & Whittle, M. 1991, ApJ, 377, 100

Kirkpatrick, A., Alberts, S., Pope, A., et al. 2017, ApJ, 849, 111

Kormendy, J., & Ho, L. C. 2013, ARA&A, 51, 511

Koski, A. T. 1978, ApJ, 223, 56

Kraemer, S. B., Sharma, N., Turner, T. J., George, I. M., & Crenshaw, D. M. 2015, ApJ, 798, 53

Kraemer, S. B., Crenshaw, D. M., Trippe, M. L., Schmitt, H. R., & Meléndez, M. 2010, Co-Evolution of Central Black Holes and Galaxies, 267, 401

Kraemer, S. B., Trippe, M. L., Crenshaw, D. M., et al. 2009, ApJ, 698, 106

Kraemer, S. B., Schmitt, H. R., & Crenshaw, D. M. 2008, ApJ, 679, 1128-1143

Kraemer, S. B., Crenshaw, D. M., Gabel, J. R., et al. 2006, ApJS, 167, 161

Kraemer, S. B., George, I. M., Crenshaw, D. M., et al. 2005, ApJ, 633, 693

Kraemer, S. B., Crenshaw, D. M., Hutchings, J. B., et al. 2000a, ApJ, 531, 278

Kraemer, S. B., & Crenshaw, D. M. 2000b, ApJ, 532, 256

Kraemer, S. B., & Crenshaw, D. M. 2000c, ApJ, 544, 763

Kraemer, S. B. 1985, Ph.D. Thesis

Krügel, E. 2008, An introduction to the physics of interstellar dust. ISBN 9781584887072

Laha, S., Tyndall, N. B., Keenan, F. P., et al. 2017, ApJ, 841, 3

Laha, S., Guainazzi, M., Chakravorty, S., Dewangan, G. C., & Kembhavi, A. K. 2016, MNRAS, 457, 3896

Leung, G. C. K., Coil, A. L., Azadi, M., et al. 2017, ApJ, 849, 48

Liu, Z. W., Zhang, J. S., Henkel, C., et al. 2017, MNRAS, 466, 1608

Liu, G., Zakamska, N. L., Greene, J. E., Nesvadba, N. P. H., & Liu, X. 2013, MNRAS, 436, 2576

MacAlpine, G. M. 1988, PASP, 100, 65

Madau, P., & Dickinson, M. 2014, Annual Review of Astronomy and Astrophysics, 52, 415

Magorrian, J., Tremaine, S., Richstone, D., et al. 1998, AJ, 115, 2285

Mahoro, A., Pović, M., & Nkundabakura, P. 2017, MNRAS, 471, 3226

Maksym, W. P., Fabbiano, G., Elvis, M., et al. 2017, ApJ, 844, 69

Maksym, W. P., Fabbiano, G., Elvis, M., et al. 2016, ApJ, 829, 46

Malkan, M. A., Gorjian, V., & Tam, R. 1998, ApJS, 117, 25

Martini, P., Pogge, R. W., Ravindranath, S., & An, J. H. 2001, ApJ, 562, 139

McElroy, R., Croom, S. M., Pracy, M., et al. 2015, MNRAS, 446, 2186

McMaster, M., & et al. 2008, Wide Field and Planetary Camera 2, HST Instrument Handbook

Meléndez, M., Heckman, T. M., Martínez-Paredes, M., Kraemer, S. B., & Mendoza, C. 2014, MNRAS, 443, 1358

Meléndez, M., Kraemer, S. B., Armentrout, B. K., et al. 2008a, ApJ, 682, 94-103

Meléndez, M., Kraemer, S. B., Schmitt, H. R., et al. 2008b, ApJ, 689, 95-107

Mou, G., Wang, T., & Yang, C. 2017, ApJ, 844, 30

Moy, E., & Rocca-Volmerange, B. 2002, A&A, 383, 46

Mullaney, J. R., & Ward, M. J. 2008, MNRAS, 385, 53

Müller-Sánchez, F., Comerford, J., Stern, D., & Harrison, F. A. 2016, ApJ, 830, 50

Müller-Sánchez, F., Prieto, M. A., Hicks, E. K. S., et al. 2011, ApJ, 739, 69

Nagao, T., Maiolino, R., & Marconi, A. 2006, A&A, 447, 863

Nagao, T., Kawabata, K. S., Murayama, T., et al. 2004a, AJ, 128, 109

Nagao, T., Kawabata, K. S., Murayama, T., et al. 2004b, AJ, 128, 2066

Nagao, T., Murayama, T., Shioya, Y., & Taniguchi, Y. 2003, AJ, 125, 1729

Nagar, N. M., & Wilson, A. S. 1999, ApJ, 516, 97

Nair, P. B., & Abraham, R. G. 2010, ApJS, 186, 427

Nelson, C. H., & Whittle, M. 1995, ApJS, 99, 67

Nesvadba, N. P. H., Lehnert, M. D., Eisenhauer, F., et al. 2006, ApJ, 650, 693

Nevin, R., Comerford, J. M., Müller-Sánchez, F., Barrows, R., & Cooper, M. C. 2018, MNRAS, 473, 2160

Nevin, R., Comerford, J., Müller-Sánchez, F., Barrows, R., & Cooper, M. 2016, ApJ, 832, 67

Netzer, H. 2015, ARA&A, 53, 365

Netzer, H. 2009, MNRAS, 399, 1907

Oh, K., Sarzi, M., Schawinski, K., & Yi, S. K. 2011, ApJS, 195, 13

Oke, J. B. 1990, AJ, 99, 1621

Oohama, N., Okamura, S., Fukugita, M., Yasuda, N., & Nakamura, O. 2009, ApJ, 705, 245

Osterbrock, D. E., & Ferland, G. J. 2006, Astrophysics of gaseous nebulae and active galactic nuclei, 2nd. ed. by D.E. Osterbrock and G.J. Ferland. Sausalito, CA: University Science Books, 2006

Osterbrock, D. E. 1981, ApJ, 249, 462

Osterbrock, D. E. 1978, Proceedings of the National Academy of Science, 75, 540

Padovani, P., Alexander, D. M., Assef, R. J., et al. 2017, Astronomy and Astrophysics Reviews, 25, 2

Paggi, A., Wang, J., Fabbiano, G., Elvis, M., & Karovska, M. 2012, ApJ, 756, 39

Peterson, B. M., Ferrarese, L., Gilbert, K. M., et al. 2004, ApJ, 613, 682

Peterson, B. M. 1997, An Introduction to Active Galactic Nuclei, Publisher: Cambridge, New York Cambridge University Press, 1997, 238 p. ISBN 0521473489

Perna, M., Lanzuisi, G., Brusa, M., Cresci, G., & Mignoli, M. 2017, A&A, 606, A96

Piro, L., de Rosa, A., Matt, G., & Perola, G. C. 2005, A&A, 441, L13

Pogge, R. W., & Martini, P. 2002, ApJ, 569, 624

Pogge, R. W., & De Robertis, M. M. 1995, ApJ, 451, 585

Pogge, R. W., & De Robertis, M. M. 1993, ApJ, 404, 563

Rafter, S. E., Crenshaw, D. M., & Wiita, P. J. 2009, AJ, 137, 42

Raimann, D., Storchi-Bergmann, T., González Delgado, R. M., et al. 2003, MNRAS, 339, 772

Ramos Almeida, C., Pérez García, A. M., & Acosta-Pulido, J. A. 2009a, ApJ, 694, 1379

Ramos Almeida, C., Levenson, N. A., Rodríguez Espinosa, J. M., et al. 2009b, ApJ, 702, 1127

Ramos Almeida, C., Pérez García, A. M., Acosta-Pulido, J. A., & González-Martín, O. 2008, ApJL, 680, L17

Revalski, M., Crenshaw, D. M., Kraemer, S. B., et al. 2018, ApJ, 856, 46, Paper I

Revalski, M., Dashtamirova, D., Crenshaw, D. M., et al. 2018, ApJ, 867, 88, Paper II

Reyes, R., Zakamska, N. L., Strauss, M. A., et al. 2008, AJ, 136, 2373

Reynaldi, V., Guainazzi, M., Feinstein, C., & Combi, J. A. 2012, Boletin de la Asociacion Argentina de Astronomia La Plata Argentina, 55, 341

Riffel, R. A., Storchi-Bergmann, T., & Winge, C. 2013, MNRAS, 430, 2249

Riffel, R. A., & Storchi-Bergmann, T. 2011a, MNRAS, 411, 469

Riffel, R. A., & Storchi-Bergmann, T. 2011b, MNRAS, 417, 2752

Riffel, R. A., Storchi-Bergmann, T., Dors, O. L., & Winge, C. 2009, MNRAS, 393, 783

Riffel, R., Pastoriza, M. G., Rodríguez-Ardila, A., & Maraston, C. 2007, ApJL, 659, L103

Riffel, R., Rodríguez-Ardila, A., & Pastoriza, M. G. 2006, A&A, 457, 61

Riley, A. 2017, Space Telescope Imaging Spectrograph Instrument Handbook

Rodríguez-Ardila, A., Prieto, M. A., Viegas, S., & Gruenwald, R. 2006, ApJ, 653, 1098

Rosario, D. J., Whittle, M., Nelson, C. H., & Wilson, A. S. 2008, Mem. Soc. Astron. Italiana, 79, 1217

Rosario, D. J. V. 2007, Ph.D. Thesis

Rose, M., Tadhunter, C., Ramos Almeida, C., et al. 2018, MNRAS, 474, 128

Ruiz, J. R., Crenshaw, D. M., Kraemer, S. B., et al. 2005, AJ, 129, 73

Rupke, D. 2018, Galaxies, 6, 138

Rupke, D. S. N., Gültekin, K., & Veilleux, S. 2017, ApJ, 850, 40

Savage, B. D., & Mathis, J. S. 1979, ARA&A, 17, 73

Scannapieco, E., & Oh, S. P. 2004, ApJ, 608, 62

Schawinski, K., Thomas, D., Sarzi, M., et al. 2007, MNRAS, 382, 1415

Schlesinger, K., Pogge, R. W., Martini, P., Shields, J. C., & Fields, D. 2009, ApJ, 699, 857

Schmitt, H. R., Donley, J. L., Antonucci, R. R. J., Hutchings, J. B., & Kinney, A. L. 2003a, ApJS, 148, 327

Schmitt, H. R., Donley, J. L., Antonucci, R. R. J., et al. 2003b, ApJ, 597, 768

Schmitt, H. R., & Kinney, A. L. 2000, ApJS, 128, 479

Schmitt, H. R., Kinney, A. L., Calzetti, D., et al. 1997, AJ, 114, 592

Schnorr-Müller, A., Storchi-Bergmann, T., Robinson, A., Lena, D., & Nagar, N. M. 2016, MNRAS, 457, 972

Schnorr-Müller, A., Storchi-Bergmann, T., Nagar, N. M., et al. 2014, MNRAS, 437, 1708

Schönell, A. J., Jr., Storchi-Bergmann, T., Riffel, R. A., & Riffel, R. 2017, MNRAS, 464, 1771

Schönell, A. J., Riffel, R. A., Storchi-Bergmann, T., & Winge, C. 2014, MNRAS, 445, 414

Schurch, N. J., Warwick, R. S., Griffiths, R. E., & Sembay, S. 2003, MNRAS, 345, 423

Seab, C. G., & Shull, J. M. 1983, ApJ, 275, 652

Seyfert, C. K. 1943, ApJ, 97, 28

Shipley, H. V., Papovich, C., Rieke, G. H., Brown, M. J. I., & Moustakas, J. 2016, ApJ, 818, 60

Shipley, H. V., Papovich, C., Rieke, G. H., et al. 2013, ApJ, 769, 75

Silk, J. 2013, ApJ, 772, 112

Snow, T. P., & Witt, A. N. 1996, ApJL, 468, L65

Spence, R. A. W., Tadhunter, C. N., Rose, M., & Rodríguez Zaurín, J. 2018, MNRAS, 478, 2438

Spinoglio, L., Benedettini, M., de Troia, G., et al. 2000, ISO Beyond the Peaks: The 2nd ISO Workshop on Analytical Spectroscopy, 456, 261

Springob, C. M., Haynes, M. P., Giovanelli, R., & Kent, B. R. 2005, ApJS, 160, 149

Stasińska, G., Cid Fernandes, R., Mateus, A., Sodré, L., & Asari, N. V. 2006, MNRAS, 371, 972

Stoklasová, I., Ferruit, P., Emsellem, E., et al. 2009, A&A, 500, 1287

Storchi-Bergmann, T., & Schnorr-Müller, A. 2019, Nature Astronomy, 3, 48

Storchi-Bergmann, T., Lopes, R. D. S., McGregor, P. J., et al. 2010, MNRAS, 402, 819

Storchi-Bergmann, T., Fernandes, R. C., & Schmitt, H. R. 1998a, ApJ, 501, 94

Storchi-Bergmann, T., Schmitt, H. R., Calzetti, D., & Kinney, A. L. 1998b, AJ, 115, 909

Storchi-Bergmann, T., Wilson, A. S., Mulchaey, J. S., & Binette, L. 1996, A&A, 312, 357

Sturm, E., González-Alfonso, E., Veilleux, S., et al. 2011, ApJL, 733, L16

Terao, K., Nagao, T., Hashimoto, T., et al. 2016, ApJ, 833, 190

Tody, D. 1993, Astronomical Data Analysis Software and Systems II, 52, 173

Tody, D. 1986, Proc. SPIE, 627, 733

Tombesi, F., Cappi, M., Reeves, J. N., et al. 2013, MNRAS, 430, 1102

Tombesi, F., Cappi, M., Reeves, J. N., & Braito, V. 2012, MNRAS, 422, L1

Tombesi, F., Cappi, M., Reeves, J. N., et al. 2011, ApJ, 742, 44

Tombesi, F., Cappi, M., Reeves, J. N., et al. 2010, A&A, 521, A57

Tran, H. D. 2001, ApJL, 554, L19

Tsvetanov, Z., & Walsh, J. R. 1992, ApJ, 386, 485

Tsvetanov, Z., Tadhunter, C., Perez, E., & Gonzalez-Delgado, R. 1989a, European Southern Observatory Conference and Workshop Proceedings, 32, 19

Tsvetanov, Z. 1989b, European Southern Observatory Conference and Workshop Proceedings, 32, 251

Ulvestad, J. S., & Wilson, A. S. 1984, ApJ, 278, 544

Unger, S. W., Pedlar, A., Axon, D. J., et al. 1987, MNRAS, 228, 671

Urry, C. M., & Padovani, P. 1995, PASP, 107, 803

Vaona, L., Ciroi, S., Di Mille, F., et al. 2012, MNRAS, 427, 1266

van Dokkum, P. G. 2001, PASP, 113, 1420

van Hoof, P. A. M., Weingartner, J. C., Martin, P. G., Volk, K., & Ferland, G. J. 2004, Asymmetrical Planetary Nebulae III: Winds, Structure and the Thunderbird, 313, 380

van Hoof, P. A. M., Weingartner, J. C., Martin, P. G., Volk, K., & Ferland, G. J. 2001, Spectroscopic Challenges of Photoionized Plasmas, 247, 363

Veilleux, S., Cecil, G., & Bland-Hawthorn, J. 2005, ARA&A, 43, 769

Veilleux, S., Goodrich, R. W., & Hill, G. J. 1997, ApJ, 477, 631

Veilleux, S., & Osterbrock, D. E. 1987, ApJS, 63, 295

Venturi, G., Nardini, E., Marconi, A., et al. 2018, A&A, 619, A74

Villar-Martín, M., Arribas, S., Emonts, B., et al. 2016, MNRAS, 460, 130

Wang, J., Fabbiano, G., Elvis, M., et al. 2011, ApJ, 742, 23

Wang, J.-M., Chen, Y.-M., Yan, C.-S., Hu, C., & Bian, W.-H. 2007, ApJL, 661, L143

Weingartner, J. C., Draine, B. T., & Barr, D. K. 2006, ApJ, 645, 1188

Weingartner, J. C., & Draine, B. T. 2001, ApJS, 134, 263

Whittle, M., Pedlar, A., Meurs, E. J. A., et al. 1988, ApJ, 326, 125

Whittle, M. 1985, MNRAS, 216, 817

Wilson, A. S., Binette, L., & Storchi-Bergmann, T. 1997, ApJL, 482, L131

Wilson, A. S., Ward, M. J., & Haniff, C. A. 1988, ApJ, 334, 121

Woo, J.-H., & Urry, C. M. 2002, ApJ, 579, 530

Woodgate, B. E., Kimble, R. A., Bowers, C. W., et al. 1998, PASP, 110, 1183

Wylezalek, D., & Morganti, R. 2018, Nature Astronomy, 2, 181

Wylezalek, D., Schnorr-Müller, A., Zakamska, N. L., et al. 2017, MNRAS, 467, 2612

Wylezalek, D., & Zakamska, N. L. 2016, MNRAS, 461, 3724

Xanthopoulos, E. 1996, MNRAS, 280, 6

Yang, G., Brandt, W. N., Alexander, D. M., et al. 2019, MNRAS, 485, 3721

Zhang, D. 2018, Galaxies, 6, 114

Zhang, Z. T., Liang, Y. C., & Hammer, F. 2013, MNRAS, 430, 2605

Zubovas, K. 2018, MNRAS, 479, 3189

Zubovas, K., & Bourne, M. A. 2017, MNRAS, 468, 4956

Zubovas, K., & King, A. 2012, ApJL, 745, L34